

**Department of Biochemical Engineering**

**University College London**

**A combined modelling and experimental  
characterisation of *Chlamydomonas reinhardtii*  
under monochromatic LED illumination**

A thesis submitted for the degree of Doctor of Philosophy

**Victor Sanchez Tarre**

*Para Isabel, Satur y Holly, con amor.*

# Abstract

---

Industrial biotechnology is currently synonymous with heterotrophic processes that rely on bacterial, yeast, insect or mammalian cells to biosynthesise products of interest. Microalgae are of substantial biotechnological interest due their polyphyletic nature which grants them access to a wide array of high-value metabolites and their ability to grow under a variety of trophic strategies, including phototrophy. Despite significant process development and optimisation efforts, the full potential of these photosynthetic organisms has yet to be realised.

One of the most impactful process parameters when cultivating microalgae is light. It is essential for phototrophic growth and remains highly influential on mixotrophic growth. Indoor cultivations relying on artificial light allow full control of illumination conditions. The advent of LED lights has lowered the costs and improved the flexibility of such installations. Specifically, the spectral composition of LED lights can be accurately and dynamically tailored to the needs of the culture. Spectral composition is known to exert regulatory control over the cell cycle and can affect the cell's biochemical make up.

The effects of illumination strategy on the model microalgae *Chlamydomonas reinhardtii* were characterised at three different levels (a) growth kinetics, (b) biochemical composition and, (c) transcriptional activity at key carbon nodes. To obtain the transcriptional data, RNA extraction protocols were compared and optimised. Additionally, a suite of candidate reference genes was validated to ensure accurate gene expression normalisation was possible in reverse transcriptase quantitative real-time polymerase chain reaction (RT-qPCR) studies. The growth kinetics and biochemical composition data obtained served as inputs for a previously published genome scale metabolic model. An algorithm was developed to approximate the default biomass composition in the model to experimental data in an effort to increase the fidelity of the simulations. The flux distributions obtained thereafter helped to describe the distinct metabolic fingerprints created under different trophic and illumination strategies.

# Impact statement

---

The research described in this thesis aims to serve as the baseline for both academia and industry and enable the incorporation of monochromatic illumination strategies in microalgal cultivation strategies.

Given the drive towards high-value products from microalgae in the industrial biotechnology industry, the use of artificial illumination is destined to become more widespread. As such setting the baseline for the effects of narrow spectral band illumination on a model microalga like *Chlamydomonas reinhardtii* is bound to benefit future uses of artificial illumination in microalgae cultivation.

The novel reference genes identified and validated to be stable across different colours of light and types of growth can now be used in future studies to understand the gene expression of *C. reinhardtii* when grown under different colours of light. This could help accelerate product development by uncovering previously unattainable insights.

The biomass optimisation algorithm developed is applicable to any genome scale metabolic model and therefore its impact spread beyond the metabolic modelling of microalgae to that of any microorganism. As well as impacting industrial biotechnology, the algorithm can be used in human cancer models to improve the fidelity of disease evolution simulations and hence inform therapy development.

## **Declaration of authenticity**

---

I, Victor Sanchez Tarre confirm that the work presented in this thesis is my own. Where information has been derived from other sources, I confirm that this has been indicated in the thesis.

# Acknowledgments

---

First and foremost, I would like to thank my parents for giving me the opportunity to reach this point. Sin vuestro apoyo incondicional durante todos estos años no podría estar escribiendo esta frase hoy. Gracias de corazón.

To Holly, I would like to admire your resilience and companionship throughout this journey. Thank you.

To Alex, thank you for your time, advice and never ending patience. I have become the researcher I am today in great measure thanks to you. Ευχαριστώ.

This journey started all the way back in September of 2015. After four years of studying at UCL I was a new student for the third and last time. I can say without a shadow of a doubt that the peers I met throughout my journey are amongst the people I most admire in this world. Max, there is little you don't know by now and I must thank you for always setting an example with your kaiser excellence. Thank you for introducing me to the wonderful world of boardgames and for always entertaining my platinum tongue ideas regardless of how pointless they might have been. Jay and Roman thank you for all the fun, it would not have been the same without you both. To the rest of the vineyard office, keep working hard, the end will arrive eventually!

This has been the most demanding experience of my life. I can safely say that I did not know what real effort meant before embarking on this adventure. It has been a pleasure.

# Table of Contents

---

<b>Abstract</b>		<b>3</b>
<b>Impact statement</b>		<b>4</b>
<b>Acknowledgements</b>		<b>6</b>
<b>Table of contents</b>		<b>7</b>
<b>Nomenclature</b>		<b>9</b>
<b>List of Figures</b>		<b>11</b>
<b>List of Tables</b>		<b>18</b>
<b>Chapter 1</b>	<b>Introduction</b>	<b>20</b>
	1.1 Aim & Objectives	23
<b>Chapter 2</b>	<b>Outline of relevant scientific literature</b>	<b>26</b>
	2.1 Phototrophic cell biology	26
	2.2 Microalgal cultivation	43
	2.3 Metabolic modelling	55
<b>Chapter 3</b>	<b>The effects of illumination and trophic strategy on cell physiology and biochemical composition in <i>Chlamydomonas reinhardtii</i></b>	<b>66</b>
	3.1 Introduction	66
	3.2 Aim & Objectives	68
	3.3 Materials and experimental methods	69
	3.4 Growth kinetics and cell physiology in phototrophic and mixotrophic batch cultures	78
	3.5 Biochemical composition in phototrophic and mixotrophic batch cultures	116
	3.6 Conclusions	121
<b>Chapter 4</b>	<b>Development of reliable tools for the evaluation of key physiological differences at the transcriptional level in <i>C. reinhardtii</i></b>	<b>123</b>
	4.1 Introduction	123
	4.2 Aim & Objectives	126

	4.3 Materials and experimental methods	126
	4.4 RNA extraction optimisation	130
	4.5 Expression Stability	134
	4.6 Gene expression under different illumination and trophic strategies	137
	4.7 Conclusions	153
<b>Chapter 5</b>	<b>Model based analysis of the diverse metabolic phenotypes that arise in <i>C. reinhardtii</i> under a variety of trophic and illumination strategies</b>	<b>154</b>
	5.1 Introduction	154
	5.2 Aim & Objectives	159
	5.3 Methodology	160
	5.4 Biomass equation optimisation	177
	5.5 Multivariate analysis of experimental conditions after BMO processing	197
	5.6 Conclusions	203
<b>Chapter 6</b>	<b>Conclusions &amp; Future directions</b>	<b>207</b>
	6.1. Advanced characterisation of the effects of illumination and trophic strategy on microalgae cultivation	208
	6.2 Advanced metabolic modelling of microalgal metabolism	209
	6.3 Concluding remarks	210
<b>Bibliography</b>		<b>211</b>
<b>Appendix I</b>		<b>251</b>
<b>Appendix II</b>		<b>252</b>
<b>Appendix III</b>		<b>254</b>
<b>Appendix IV</b>		<b>259</b>
<b>Appendix V</b>		<b>260</b>



# Nomenclature

---

$a$	Effective bandwidth lower limit ( $\mu\text{mol}_{\text{ph}} \text{m}^{-2} \text{s}^{-1}$ )
$b$	Effective bandwidth upper limit ( $\mu\text{mol}_{\text{ph}} \text{m}^{-2} \text{s}^{-1}$ )
$c$	Optimisation objective weight vector of a linear programming optimisation problem
$C_a^b$	Effective bandwidth coefficient ( $\mu\text{mol}_{\text{ph}} \text{m}^{-2} \text{s}^{-1}$ )
$C_c$	Carotenes concentration ( $\mu\text{g}C_c \text{mL}^{-1}$ )
$\text{Chl}_a$	Chlorophyll a concentration ( $\mu\text{gChl}_a \text{mL}^{-1}$ )
$\text{Chl}_b$	Chlorophyll b concentration ( $\mu\text{gChl}_b \text{mL}^{-1}$ )
$C_{jh}$	Stoichiometric coefficient of constituent $j$ in experimental condition $h$ ( $\text{g gDCW}^{-1}$ )
$C_{kih}$	Sum of the stoichiometric coefficients of all constituents in a macromolecular group ( $\text{g gDCW}^{-1}$ )
$C_s$	Substrate concentration ( $\text{mmol L}^{-1}$ )
$C_x$	Xanthophylls concentration ( $\mu\text{g}C_x \text{mL}^{-1}$ )
$E_{ih}$	Sum of macromolecular groups ( $\text{g gDCW}^{-1}$ )
$\text{gC}$	Grams of carbon in metabolite (w/w)
$\text{GC}_h$	Ghost carbon fraction in condition $h$ ( $\text{g gDCW}^{-1}$ )
$\text{GC}_{vih}$	Proportion of GC in condition $h$ attributable to $V_{ih}$ macromolecular group
$G_i$	See $C_{kih}$
$G_{ih,\text{LB}}$	Macromolecular group $h$ contribution to biomass dry weight, lower bound ( $\text{g gDCW}^{-1}$ )
$G_{ih,\text{UB}}$	Macromolecular group $h$ contribution to biomass dry weight upper bound ( $\text{g gDCW}^{-1}$ )

$L(\lambda)$	Photon flux as a function of wavelength ( $\mu\text{mol}_{\text{ph}} \text{m}^{-2} \text{s}^{-1} \text{nm}^{-1}$ )
$MW_j$	Molecular weight of constituent $j$ ( $\text{mol g}^{-1}$ )
$q_s$	Specific uptake rate of substrate ( $\mu\text{mol } 1000\text{cells}^{-1} \text{h}^{-1}$ )
$r_s$	Volumetric uptake rate of substrate ( $\mu\text{mol L}^{-1} \text{h}^{-1}$ )
$S$	Stoichiometric matrix of a genome scale metabolic model
$\text{Total}_{\text{Chl}}$	Total chlorophyll concentration ( $\mu\text{gTot}_{\text{Chl}} \text{mL}^{-1}$ )
$v$	Flux vector of a genome scale metabolic model
$V_{ih}$	Average quantity of macromolecule $i$ in experimental condition $h$ ( $\text{g gDCW}^{-1}$ )
$v^{\text{lb}}$	Lower bound for metabolic flux rate ( $\text{mmol gDCW}^{-1} \text{h}^{-1}$ )
$v^{\text{ub}}$	Upper bound for metabolic flux rate ( $\text{mmol gDCW}^{-1} \text{h}^{-1}$ )
$Y_{\text{C}/\text{NH}_4^+}$	Observed yield of cells on ammonium ( $\text{cells pmolNH}_4^{+ -1}$ )
$Y_{\text{X}/\text{NH}_4^+}$	Observed yield of biomass on ammonium ( $\text{gX mmolNH}_4^{+ -1}$ )
$Z$	Optimisation objective of a linear programming optimisation problem
$\mu_{\text{max}}$	Maximum specific growth rate ( $\text{h}^{-1}$ )

# List of Figures

<b>Figure 2.1</b>	Evolutionary relationships of the different microalgal lineages thought to have evolved from various symbiotic events. Example species belonging to each phylum are listed. (Adapted from Merchant et al. 2007).	27
<b>Figure 2.2</b>	Schematic diagram of the <i>Chlamydomonas reinhardtii</i> cell structure. Major organelles are labelled and the inner cross section of the flagellum is detailed (From Merchant et al. 2007).	30
<b>Figure 2.3</b>	Overview of the <i>Chlamydomonas reinhardtii</i> cell cycle. A vegetative cell grows until it reaches a critical size and loses its flagella. After which it enters several cycles of DNA replication and cell division within a sporangium formed from the original mother cell's cell wall. Once daughter cells reach a critical size the S/M cycles cease, flagella regrow and sporangin is released so the daughter cells can hatch. G1, growth phase; S/M, DNA replication / mitosis; H, hatching.	33
<b>Figure 2.4</b>	Schematic diagram of photosynthesis light dependent reactions. (A) Linear electron flow; (B) Cyclic electron flow. PSII, photosystem II; Pq, plastoquinol/plastoquinone; Cyt, cytochrome b6f complex; Pc, plastocyanin; PSI, photosystem I; Fd, ferredoxin. Adapted from www.khanacademy.com.	37
<b>Figure 2.5</b>	<i>C. reinhardtii</i> light absorption profile compared to LED illumination sources. (A) LED illumination sources of differing peak wavelength; (B) <i>C. reinhardtii</i> optical absorption cross section measured under different LED illumination sources during continuous turbidostat cultures at 1500 $\mu\text{molph m}^{-2} \text{s}^{-1}$ . $I_{ph}/\lambda$ , normalised photon flux for each wavelength ( $\mu\text{mol m}^{-2} \text{s}^{-1} \text{nm}^{-1}$ ) ; $ax \lambda$ , biomass absorbance cross section ( $\text{m}^2 \text{g}^{-1}$ ). Adapted from Mooij et al. 2016.	39
<b>Figure 2.6</b>	Metabolic pathway diagram comparing the assimilation of uptaken acetate into central carbon metabolism via the tricarboxylic (TCA) cycle and the glyoxylate cycle. Orange arrows highlight reactions where acetate and or acetyl co-enzyme A are involved. Grey arrows highlight $\text{CO}_2$ release. Purple arrows highlight the production of reducing equivalents NADH and FADH <sub>2</sub> . (A) acetyl Co-A synthase; (B) acetate kinase; (C) phosphate acetyltransferase; (1) citrate synthase; (2) aconitase; (3) isocitrate dehydrogenase; (4) $\alpha$ -ketoglutarate dehydrogenase; (5) succinyl-CoA synthetase; (6) succinate dehydrogenase (7) fumarate hydratase; (8) malate dehydrogenase; (9) isocitrate lyase; (10) malate synthase.	42
<b>Figure 2.7</b>	(a) Medium scale raceway pond for research purposes (b) Cyanotech facility, Hawaii, USA.	44

<b>Figure 2.8</b>	The stoichiometric matrix, $S$ . The matrix is made up of $m$ metabolites and $n$ reactions. Each matrix element ( $s_{ij}$ ) in $S$ is therefore a stoichiometric coefficient of the $i$ th metabolite in the $j$ th reaction. 1, reaction product; 0, metabolite does not participate in this reaction; -1, reaction substrate.	59
<b>Figure 2.9</b>	Full summary of the flux balance analysis methodology. (a) Reconstruction of an annotated genome sequence into a metabolic network; (b) The stoichiometric matrix formed by $n$ reactions and $m$ metabolites ( $m \times n$ ); (c) Definition of the quasi-steady state assumption; (d) Definition of the objective function, made up of weighted contribution, $c$ , of chosen reaction fluxes, $v$ ; (e) Solving the defined linear problem to maximise the objective function $Z$ . Taken from Orth, Thiele and Palsson, (2010).	62
<b>Figure 3.1</b>	Normalised spectra of white, red (640-670nm) and blue (440-480 nm) light, supplied at equivalent photon flux, by the LEDs incorporated in the ALGEM bioreactor system.	71
<b>Figure 3.2</b>	<i>C. reinhardtii</i> OD 750 nm vs dry cell weight (DCW - g/L) measurements across all experimental conditions studied. Each point represents the average of three technical replicates. Error bars of $\pm 1$ SD are smaller than plotted point.	74
<b>Figure 3.3</b>	<i>C. reinhardtii</i> batch growth kinetics under a variety of trophic and illumination strategies. (A and C) Autotrophic growth in M8a; (B and D) mixotrophic growth in M8a.Ac. (A and B) Biomass Concentration (measured at OD 750) (C and D) Cell concentration (Cells $\mu$ L <sup>-1</sup> ). W, white LED light; R, red LED light; B, blue LED light. Biological duplicates (N=2) plotted.	82
<b>Figure 3.4</b>	Normalised <i>C. reinhardtii</i> OD750 : Cell concentration ratio under a variety of trophic and illumination strategies. W, white LED light; R, red LED light; B, blue LED light. A, autotrophic medium (M8a); X, mixotrophic medium (M8a.Ac).	84
<b>Figure 3.5</b>	<i>C. reinhardtii</i> nutrient uptake kinetics under a variety of trophic and illumination strategies. (A) Ammonium uptake in autotrophic growth in M8a; (B and C) Ammonium and acetate uptake respectively in mixotrophic growth in M8a.Ac. W, white LED light; R, red LED light; B, blue LED light. Biological duplicates (N=2) plotted	90
<b>Figure 3.6</b>	<i>C. reinhardtii</i> cell size distribution at two time-points of a batch culture under white light and a variety of trophic strategies. (A) 48 hours of batch culture corresponding to the mid-exponential growth phase; (B) 136 hours of batch culture corresponding to the late stationary phase. W, autotrophic culture in M8a; WX, mixotrophic culture in M8a.Ac. Single representative sample plotted (N=1).	98

<b>Figure 3.7</b>	<i>C. reinhardtii</i> cell size distribution at two time-points of a batch culture under red LED light and a variety of trophic strategies. (A) 48 hours of batch culture corresponding to the mid-exponential growth phase; (B) 136 hours of batch culture corresponding to the late stationary phase. R, autotrophic culture in M8a; RX, mixotrophic culture in M8a.Ac. Single representative sample plotted (N=1).	99
<b>Figure 3.8</b>	<i>C. reinhardtii</i> cell size distribution at two time-points of a batch culture under blue LED light and a variety of trophic strategies. (A) 48 hours of batch culture corresponding to the mid-exponential growth phase; (B) 136 hours of batch culture corresponding to the late stationary phase. B, autotrophic culture in M8a; BX, mixotrophic culture in M8a.Ac. Single representative sample plotted (N=1).	100
<b>Figure 3.9</b>	<i>C. reinhardtii</i> cell size distribution at two time-points of a batch culture under a variety of illumination strategies in autotrophic M8a media. (A) 48 hours of batch culture corresponding to the mid-exponential growth phase; (B) 136 hours of batch culture corresponding to the late stationary phase. W, white LED light; R, red LED light; B, blue LED light. Single representative sample plotted (N=1).	101
<b>Figure 3.10</b>	<i>C. reinhardtii</i> cell size distribution at two time-points of a batch culture under a variety of illumination strategies in mixotrophic M8a.Ac media. (A) 48 hours of batch culture corresponding to the mid-exponential growth phase; (B) 136 hours of batch culture corresponding to the late stationary phase. WX, white LED light; RX, red LED light; BX, blue LED light. Single representative sample plotted (N=1).	102
<b>Figure 3.11</b>	<i>C. reinhardtii</i> carbohydrate fraction as a percentage of biomass dry weight (w/w) over time. (A) Phototrophic batch cultures in M8a. (B) Mixotrophic batch cultures in M8a.Ac. Biological replicates plotted individually (Flask A – squares. Flask B – circles) Average plotted as a continuous line. W, white LED light; R, red LED light; B, blue LED light.	106
<b>Figure 3.12</b>	<i>C. reinhardtii</i> lipid fraction as a percentage of biomass dry weight (w/w) over time. (A) Phototrophic batch cultures in M8a. (B) Mixotrophic batch cultures in M8a.Ac. Biological replicates plotted individually (Flask A – squares. Flask B – circles) Average plotted as a continuous line. W, white LED light; R, red LED light; B, blue LED light.	109
<b>Figure 3.13</b>	<i>C. reinhardtii</i> protein fraction as a percentage of biomass dry weight (w/w) over time. (A) Phototrophic batch cultures in M8a. (B) Mixotrophic batch cultures in M8a.Ac. Biological replicates plotted individually (Flask A – squares. Flask B – circles) Average plotted as a continuous line. W, white LED light; R, red LED light; B, blue LED light.	111

<b>Figure 3.14</b>	<i>C. reinhardtii</i> pigment fraction as a percentage of biomass dry weight (w/w) over time. (A) Phototrophic batch cultures in M8a. (B) Mixotrophic batch cultures in M8a.Ac. Biological replicates plotted individually (Flask A – squares. Flask B – circles) Average plotted as a continuous line. W, white LED light; R, red LED light; B, blue LED light.	114
<b>Figure 3.15</b>	<i>C. reinhardtii</i> chlorophyll content and composition during an entire batch culture. (A,B) Chlorophyll content as a percentage of total biomass. (C,D) Chlorophyll a to chlorophyll b ratio. The two biological replicates (n=2) are indicated by squares (Flask 1) and circles (Flask 2) respectively. Solid lines indicate the average across the biological replicates for each condition. Black symbols and lines used for white light; Red symbols and lines used for red light 640-670nm; Blue symbols and lines used for blue light 440-480nm.	115
<b>Figure 4.1</b>	Initial RNA extraction optimisation study focusing on the cell lysis step. RNA was extracted from <i>C. reinhardtii</i> cell pellets (5 x 10 <sup>6</sup> cells; N=3).	131
<b>Figure 4.2</b>	Gel electrophoresis of <i>C. reinhardtii</i> RNA extractions employing different lysis techniques. (gDNA, genomic DNA; 18S, 18S rRNA; 16S, 16S rRNA).	132
<b>Figure 4.3</b>	RNA extraction optimisation study focusing on the cell lysis step. RNA was extracted from <i>C. reinhardtii</i> cell pellets (5 x 10 <sup>6</sup> cells; N=3).	133
<b>Figure 4.4</b>	RNA purity analysis. (A) Comparison between Trizol extraction performed in 2 mL Eppendorf tubes and RNA extraction performed with RNeasy spin column kit. (Both extractions N=1) (B) Comparison between Trizol extraction performed in 2 mL MaXtract tubes and RNA extraction performed with RNeasy spin column kit (Trizol extraction N=5; RNeasy extraction N=1). RNA was extracted from <i>C. reinhardtii</i> cell pellets (5 x 10 <sup>6</sup> cells).	134
<b>Figure 4.5</b>	Mean C <sub>q</sub> of candidate reference genes studied. (n = 6, error bars represent minimum and maximum C <sub>q</sub> ).	136
<b>Figure 4.6</b>	Carbon fixation related gene expression in the exponential growth phase. Average Ribulose biphosphate carboxylase small subunit (RBCS) gene expression from 16 h – 48 h (n = 4, error bars represent SEM, different error bar labels indicate statistically significant differences between conditions, p < 0.05). W: white light, R: red light 640-670nm, B: blue light 440-480nm, A: phototrophic growth in M8a, X: mixotrophic growth in M8a.Ac.	140

<b>Figure 4.7</b>	An overview of acetate metabolism in <i>C. reinhardtii</i> and gene expression monitored at key carbon nodes of acetate metabolism. (A) The various subcellular locations and metabolic pathways acetate can be catabolised in. Gene expression of enzymes involved in reactions highlighted in orange and redox cofactors highlighted in purple. (B-D) Average gene expression from 16 h – 48 h of fumarate hydratase (FUM1), malate synthase (MAS1) and 3-oxoacyl-[acyl-carrier-protein] synthase (KAS2) respectively (n = 4, error bars represent SEM, different error bar labels indicate statistically significant differences between conditions, $p < 0.05$ ). W: white light, R: red light 640-670nm, B: blue light 440-480nm, A: phototrophic growth in M8a, X: mixotrophic growth in M8a.Ac.	144
<b>Figure 4.8</b>	Summary of average gene expression level compared across multiple light and media conditions. The colour scale is normalised in each row as the data reflects average fold change in gene expression and is not directly comparable between genes (n = 4). W: white light, R: red light 640-670nm, B: blue light 440-480nm, A: phototrophic growth in M8a, X: mixotrophic growth in M8a.Ac.	149
<b>Figure 4.9</b>	Average gene expression of (A) ribulose biphosphate carboxylase small subunit – RBCS, (B) heat-shock protein 70A – HSP70A and (C) ATP synthase subunit alpha (atpA) respectively, from 16 h – 48 h (Exponential Phase, n = 4, error bars represent SEM) and 136 h (Stationary Phase) (n = 2, error bars represent min and max expression). W: white light, R: red light 640-670nm, B: blue light 440-480nm, A: phototrophic growth in M8a, X: mixotrophic growth in M8a.Ac.	152
<b>Figure 5.1</b>	Derivation of light reactions in iRC1080. The photon flux from wavelengths a to b is normalized by the total visible photon flux from 380 to 750 nm to yield the effective spectral bandwidth coefficient C. The coefficients for each range are compiled into a single prism reaction for a given light source, representing the composition of emitted light as defined by photon-utilizing metabolic reactions. Equation variables are defined at the top of the figure (Adapted from Chang et al., 2011).	163
<b>Figure 5.2</b>	Complete GeM processing workflow. The original iRC1080 model is first curated and reduced. This is followed by updating of the biomass equation using the BMO algorithm. Finally, the model is carbon constrained using ccFVA and the processed iRC1080 is ready for multivariate analysis.	172
<b>Figure 5.3</b>	Solution space percentage coverage (Sariyar et al., 2006) as a function of number of samples.	174

<b>Figure 5.4</b>	Schematic overview of PCA and data pre-processing. A) MC samples matrices of size p-by-n (p samples and n reactions) of different simulations. As an example, WA constrained with the original biomass equation (grey) and WA constrained with the newly generated biomass equation (green) are combined into a single matrix. This operation is scalable to any number of experimental conditions. B) Randomizing the full sample matrix by scrambling rows and creation of a sample ID vector (x-by-1) that maintains the connection of each sample to the original matrix it belongs to. C) Data is mean centred and scaled. D) Evaluation of the covariance matrix from the processed samples matrix. E) Singular-value decomposition. F) Loadings are used to project the original mean centred and scaled data onto a new hyperplane where the axes correspond to the generated principal components.	176
<b>Figure 5.5</b>	<i>C. reinhardtii</i> biomass composition (g gDCW-1) at 16 hours of autotrophic batch culture in M8a under a variety of illumination strategies. (A) Original autotrophic growth iRC1080 biomass equation; (B, D, F) Experimental data for WA, RA and BA respectively; (C,E,G) BMO generated data for WA, RA and BA respectively.	181
<b>Figure 5.6</b>	<i>C. reinhardtii</i> biomass composition (g gDCW-1) at 16 hours of mixotrophic batch culture in M8a.Ac under a variety of illumination strategies. (A) Original mixotrophic growth iRC1080 biomass equation; (B, D,F) Experimental data for WX, RX and BX respectively; (C,E,G) BMO generated data for WX, RX and BX respectively.	182
<b>Figure 5.7</b>	PCA score plots of all experimental conditions. A total of 1x106 points are plotted on each graph with 5x105 points per condition. OGBM scores are shown in grey and BMO scores are shown in green. All scores are plotted on principal component 1 (PC1) and principal component 2 (PC2). (-A) Autotrophic growth in M8a; (-X) Mixotrophic growth in M8a.Ac; (W-) White LED light; (R-) Red LED light; (B-) Blue LED light.	185
<b>Figure 5.8</b>	Principal component contribution to total variance. All data plotted were retrieved from the PCA of WA OGBM / WA BMO flux samples. (A) Cumulative variance described by each principal component. (B) The individual contribution of each of the first 10 principal components to the total variance of the flux sample data.	186



<b>Figure 5.9</b>	Top loadings analysis. All data plotted were retrieved from the PCA of WA OGBM / WA BMO flux samples. (A) Normalised absolute loadings of principal component 1 (PC1). Loadings with an absolute magnitude at least 70% of the largest loading in PC1 were considered highly influential in the separation of WA OGBM and WA BMO score clusters. (B) Loadings plot where PC1 loadings considered highly influential are termed high loadings and highlighted inside red boxes.	189
<b>Figure 5.10</b>	Top loadings analysis. All data plotted were retrieved from the PCA of WA OGBM / WA BMO flux samples. (A-D) Loadings plots where highlighted loadings belong to biomass precursor (pBM) synthesis related subsystems; (A) Carbohydrate pBM synthesis related subsystems; (B) Pigments pBM synthesis related subsystems; (C) Lipids pBM synthesis related subsystems; (D) Protein pBM synthesis related subsystems.	191
<b>Figure 5.11</b>	Top loadings bar chart. All data plotted were retrieved from the PCA of WA OGBM / WA BMO flux samples. All 54 top loadings of the 16 non biomass precursor (nBM) synthesis related subsystems found in PC1. PPP, pentose phosphate pathway; 1C, 1-carbon by folate metabolism.	196
<b>Figure 5.12</b>	PCA score plots of autotrophic growth simulations under a variety of illumination conditions using BMO algorithm generated biomass equations. A total of $1.5 \times 10^6$ points are plotted with $5 \times 10^5$ points per condition. WA BMO scores are shown in grey; RA BMO scores are shown in red; BA BMO scores are shown in blue. All scores are plotted on principal component 1 (PC1) and principal component 2 (PC2). (-A) Autotrophic growth in M8a; (W-) White LED light; (R-) Red LED light; (B-) Blue LED light.	198
<b>Figure 5.13</b>	PCA score plots of mixotrophic growth simulations under a variety of illumination conditions using BMO algorithm generated biomass equations. A total of $1.5 \times 10^6$ points are plotted with $5 \times 10^5$ points per condition. WX BMO scores are shown in light grey; RX BMO scores are shown in orange; BX BMO scores are shown in light blue. All scores are plotted on principal component 1 (PC1) and principal component 2 (PC2). (-X) mixotrophic growth in M8a.Ac; (W-) White LED light; (R-) Red LED light; (B-) Blue LED light.	199
<b>Figure I.1</b>	Disparity in published <i>C. reinhardtii</i> GeM biomass equation compositions.	251
<b>Figure IV.1</b>	<i>C. reinhardtii</i> carbohydrate fraction as a percentage of biomass dry weight (w/w) at 48 hours of batch culture. (A) Phototrophic batch cultures in M8a. (B) Mixotrophic batch cultures in M8a.Ac. Biological replicates plotted individually (Flask A – 1. Flask B – 2). W, white LED light; R, red LED light; B, blue LED light.	259

# List of Tables

<b>Table. 2.1</b>	Main design types of closed photobioreactors.	46
<b>Table. 3.1</b>	Reference guide to the experimental conditions studied in this thesis. W, white LED light; R, red LED light; B, blue LED light. A, autotrophic medium (M8a); X, mixotrophic medium (M8a.Ac) see section 3.3.1 for media compositions.	78
<b>Table. 3.2</b>	<i>C. reinhardtii</i> biomass concentration at 136 hours of culture derived from the linear relationship between OD750 and dry cell weight plotted in Figure 3.1. W, white LED light; R, red LED light; B, blue LED light. A, autotrophic medium (M8a); X, mixotrophic medium (M8a.Ac) see section 3.3.1 for media compositions.	81
<b>Table. 3.3</b>	Maximum biomass growth rate ( $\mu_{max}$ ) of <i>C. reinhardtii</i> cultured under different illumination and trophic strategies. Values calculated according to Equation 3.1. W, white LED light; R, red LED light; B, blue LED light. A, autotrophic medium (M8a); X, mixotrophic medium (M8a.Ac).	85
<b>Table. 3.4</b>	Acetate uptake rate in <i>C. reinhardtii</i> cultures grown in M8a.Ac medium. Values calculated according to equation 3.1. W, white LED light; R, red LED light; B, blue LED light. A, autotrophic medium (M8a); X, mixotrophic medium (M8a.Ac).	86
<b>Table. 3.5</b>	Observed yield of biomass on ammonium ( $gX\ gNH_4^{+1}$ ) and observed yield of cells on ammonium ( $1 \times 10^6 cells\ mgNH_4^{+1}$ ) in phototrophic and mixotrophic cultures under white red and blue LED light. Calculated according to Equation 3.5 and 3.6 respectively.	88
<b>Table. 3.6</b>	Comparison of two methods for measuring cell weight. Method 1 measured cell weight from a known culture volume. Method 2 calculated cell weight from the sum of macromolecular components.	93
<b>Table. 3.7</b>	Cell weight percentage difference between 48h and 136h compared between different cell weight analysis methods.	94
<b>Table 3.8</b>	Average <i>C. reinhardtii</i> cell concentration between 88 and 136 hours of culture under a variety of trophic and illumination strategies. W, white LED light; R, red LED light; B, blue LED light. A, autotrophic medium (M8a); X, mixotrophic medium (M8a.Ac) see section 3.3.1 for media compositions. Individual flask (N) data reported for 2 timepoints (n) (n = 2, N = 1).	95
<b>Table. 4.1</b>	List of candidate reference genes monitored in this study with RT-qPCR.	129
<b>Table. 5.1</b>	Custom PRISM reactions for iRC1080. Stoichiometry derived using Chang et al. 2011 methodology and ALGeM LED spectra.	162

<b>Table. 5.2</b>	Classification of iRC1080 biomass equation constituent metabolites into the macromolecular groups that make up <i>C. reinhardtii</i> biomass.	166
<b>Table. 5.3</b>	<i>C. reinhardtii</i> biomass composition (g gDCW <sup>-1</sup> ) at 16 hours of batch culture under a variety of trophic and illumination strategies. The original autotrophic and mixotrophic biomass equations are compared to the experimental data and the BMO algorithm generated biomass equations. Only variable macromolecular groups (as defined in Table 5.2) are displayed.	183
<b>Table. 5.4</b>	Top loadings and subsystems distribution in the first two principal components (PC1 and PC2) of the PCA performed on autotrophic and mixotrophic growth under white, red and blue LED illumination.	200
<b>Table. II.1</b>	FBA constraints used to simulate autotrophic conditions under different illumination conditions.	252
<b>Table. II.2</b>	FBA constraints used to simulate mixotrophic conditions under different illumination conditions.	253
<b>Table. III.1</b>	Original autotrophic and mixotrophic growth biomass equations in iRC1080.	254
<b>Table. V.1</b>	All 161 biomass precursor synthesis related reactions identified in the top loadings of PCA of WA OGBM / WA BMO.	260

# CHAPTER 1

---

## *Introduction*

The advent of modern industrial biotechnology was the latter part of the 20<sup>th</sup> century when advancements in fermentation technologies and recombinant gene expression techniques combined to enable the production of highly purified enzyme preparations in large quantities. Today industrial biotechnology is the cornerstone of the biopharmaceutical industry and it plays an important role in a wide variety of other sectors like agriculture, environmental remediation, specialty chemicals, detergents and textiles. Industrial biotechnology enables these sectors to implement green chemistry solutions and focus on corporate social responsibility. The combined revenues from industrial biotechnology operations across Europe and the US reached US\$139 billion in 2016 (EY, 2017) and the global market size of monoclonal antibodies alone is expected to reach between US\$137-200 billion by 2022 (Grilo and Mantalaris, 2019). Continued growth and expansion of these sectors means opportunities in industrial biotechnology have the potential to become profitable investments.

While mammalian and stem/T-cell culture systems are dominating the market in terms of annual revenue, shifts in legislation and the push towards a more sustainable, environmentally friendly economy have shifted focus towards crop, fungal and algae based processes (Gavrilescu and Chisti, 2005; Gupta, Sharma and Beg, 2013; Mohan *et al.*, 2016). Microalgae are a highly diverse phylogenetic group of eukaryotic single celled organisms with photosynthetic capabilities (Blaby-Haas and Merchant, 2019) which can grow in culture with only light, water, CO<sub>2</sub> and salts. Therefore, they represent an opportunity to cheaply produce many of the commercially relevant products derived from the industrial biotechnology sectors mentioned above.

Mass cultivation research efforts have trended around whole biomass products for human consumption, biofuels and more recently high-value metabolites and recombinant proteins. Mainly industrial but also research efforts have veered away from

biofuels in recent years due to their low potential for short- and mid-term success (Majidian *et al.*, 2018). Microalgae and products thereof are often touted as sustainable and renewable replacements for fossil fuel fractional distillation derivatives. Whilst this is in theory possible, staying true to environmentally friendly labels becomes increasingly expensive at the scales required for commodity products like biofuels, bioplastics, and whole biomass products. Operating industrial scale open systems increases the amount of concentrated CO<sub>2</sub> required to sustain optimal levels in the culture and increases the risk of contamination. Additionally, the sustainability of the process can be questionable if an efficient nitrogen biofixation capacity is not co-developed alongside the microalgal bioprocess in question (Chisti, 2013). Meanwhile, large closed systems incur added costs and the complexity of designing efficiently illuminated photobioreactors (Blanken *et al.*, 2013). In both types of system low yields lead to high water content that is energetically expensive to deal with in downstream processing (Fasaei *et al.*, 2018).

Although high bioprocessing costs might be prohibitive for the algae based production of commodity chemicals, other classes of products like high-value specialty chemicals, bioactive metabolites and recombinant proteins for industrial or biopharmaceutical applications are still actively pursued due to their excellent prospects (Dyo and Purton, 2018). However, these applications are still struggling to reach the technology transfer threshold required to leave the lab bench and reach industrial viability. Such barriers to profitability have been surmounted in other biotechnology sectors by incremental and disruptive developments alike. For example the monoclonal antibody (mAb) industry has grown exponentially since its inception by trending away from murine mAbs towards humanised, chimeric and fully human mAbs (Grilo and Mantalaris, 2019). More recently in the area of cell and gene therapy, two autologous chimeric antigen T-cell therapies are already being commercialised, but their manufacturing costs are prohibitive. To circumvent this, Phase I clinical trials for allogeneic therapies are underway and their promise to unlock economies of scale may enhance the prospects of this type of therapies (Panagopoulou and Rafiq, 2019). The near future of industrial production in microalgae may veer towards high-value products manufactured indoors at moderate scale where a high degree of control can be exerted

over the culture. This type of medium-scale manufacturing will benefit from advances in upstream bioprocessing control that enhance productivity. To that end, culture illumination presents itself as an easy to control critical process parameter that can be adjusted to influence microalgal physiology, gene expression and metabolism as desired.

Artificial illumination is one of the main cost drivers in indoor closed systems (Blanken *et al.*, 2013). Light emitting diodes (LEDs) are cheaper, more energy efficient, more durable, and offer a higher degree of design flexibility and control compared to fluorescent and halogen lamps (Schulze *et al.*, 2014). Their advantages over traditional light sources make them a superior choice for indoor microalgae bioprocess installations. LEDs allow for simple control of intensity, spectrum and frequency of photons delivered to a photobioreactor. While pH and temperature can be controlled to a certain extent in closed photobioreactors, their narrow operating windows to maintain optimal biomass production levels leave comparatively less room for optimisation than light. Therefore, optimisation of LED illumination is essential to reap the maximum potential from microalgal cultures.

The photosynthetically active radiation (PAR) region lies on the visible light portion of the electromagnetic spectrum between 400 to 700 nm. LEDs can produce narrow peak light with a spectral composition spanning < 10nm making it possible to study the effects of discrete portions of the PAR region on microalgae. Studies utilising monochromatic light and light blends to grow crop plants have shown that light spectrum has significant impact on plant morphology and growth (Pattison *et al.*, 2018). Similarly, spectral composition has been shown to impact microalgae biochemical composition, morphology and cell cycle (Oldenhof, Zachleder and Van Den Ende, 2004a; Baer *et al.*, 2016; Wagner, Steinweg and Posten, 2016; Xu and Harvey, 2019b).

The requirements of the industry, as well as the trends in upstream bioprocessing outlined above position LED illumination strategies as a crucial process parameter to optimise for cost-effective manufacturing of high value products from microalgae. Our understanding of metabolic responses to different illumination strategies is rudimentary, therefore the need arises to fully characterise the effects of

monochromatic illumination on the biochemical composition, gene expression and metabolic response of microalgae.

## **1.1. Aim & Objectives**

The aim of this thesis is to characterise the effects of narrow band monochromatic illumination on microalgae under different trophic strategies. A combined experimental and modelling approach is utilised to develop understanding at the physiological, metabolic and gene expression level. The experimental data acquired are used to constrain a genome scale metabolic model that is used to analyse key differences in metabolic responses under the explored conditions. The results presented herein can be used to inform microalgal process design and optimisation efforts particularly around the benefits and trade-offs of wavelength customisation.

The above aim has been broken down into a series of scientific objectives outlined below.

### **1. Outline of relevant scientific literature (Chapter 2)**

The scientific literature relevant to the topics discussed in this thesis is covered in Chapter 2. The cellular biology of microalgae and phototrophic metabolism are introduced followed by the utilisation of artificial illumination in microalgae cultivation. Subsequently, metabolic modelling is introduced with a focus on stoichiometric models and microalgal applications.

### **2. The effects of illumination and trophic strategy on cell physiology and biochemical composition in *Chlamydomonas reinhardtii* (Chapter 3)**

The microalgae *Chlamydomonas reinhardtii* is employed in Chapter 3 and the remainder of this thesis as a baseline for green microalgal physiology and metabolism due to its status as a model organism. Batch cultures of *C. reinhardtii* illuminated with white and monochromatic light emitting diodes (LEDs) are characterised. Two growth modes are studied: photoautotrophic and mixotrophic. Biomass productivity, nutrient consumption, cell size and macromolecular composition of the biomass are studied. The differences

identified from these analyses validate the original hypothesis that constant illumination with narrow wavelength LEDs has significant effects on *C. reinhardtii* physiology and metabolism.

### **3. Development of reliable tools for the evaluation of key physiological differences at the transcriptional level in *Chlamydomonas reinhardtii* (Chapter 4)**

To obtain a deeper understanding of the physiological and metabolic differences observed in Chapter 3, these conditions were evaluated at the transcriptional level using reverse transcriptase quantitative real-time polymerase chain reaction (RT-qPCR). To enable this study, a robust RNA extraction protocol is developed and optimised. Additionally, ten candidate reference genes are evaluated for their suitability under the experimental conditions of Chapter 3. These tools are combined to obtain high quality RNA and perform high-fidelity RT-qPCR assays on four central carbon metabolism genes and an additional two genes with promoter and/or 3'/5'-untranslated region (UTR) previously utilised to express recombinant proteins in *C. reinhardtii*. These assays can be used as a proxy to study the carbon flux patterns in carbon fixation, the TCA cycle, the glyoxylate cycle and fatty acid synthesis under both autotrophic and mixotrophic conditions during the exponential growth phase of a batch culture.

### **4. Model based analysis of the diverse metabolic phenotypes that arise in *C. reinhardtii* under a variety of trophic and illumination strategies (Chapter 5)**

In Chapter 5, a previously published genome scale metabolic reconstruction (GeM), iRC1080 (Chang *et al.*, 2011) is utilised to perform a detailed analysis of the underlying metabolic reconfiguration/response required to enable/realise the macroscopic and transcriptomic changes observed in Chapters 3 & 4 respectively. A key challenge that limits the use of GeMs to study diverse environmental and phenotypic conditions is their reliance on a predefined, fixed biomass composition which has either been derived under a very narrow set of experimental conditions or more frequently has been carried over from



a related organism. To overcome this key limitation, a novel algorithm is developed to fine-tune the biochemical composition of GeMs, based on proximal analysis data. This significantly increases the accuracy of GeMs when used to study phenotypically disparate conditions. Finally, a combination of Flux Balance Analysis (FBA), Monte Carlo sampling and Multivariate Analysis (MVA) techniques are employed to identify key metabolic differences between a set of diverse trophic and illumination strategies.

## **5. Concluding remarks and future research directions (Chapter 6)**

Chapter 6 contains a discussion summarising the main scientific outcomes of this thesis. Finally, a series of future research directions are proposed to build upon the knowledge gained herein. The value added of targeted metabolomic studies on a particular macromolecular group like lipids is discussed in the context of new illumination strategies derived from insights of this thesis. The application of the biomass optimisation algorithm developed in Chapter 5 to other microalgae GeMs is also posited.

## CHAPTER 2

---

### *Outline of relevant scientific literature*

A contemporary context for the original work presented in this thesis is set in this chapter through the critical review of relevant scientific literature. The foundations of microalgal physiology are discussed in section 2.1. An appraisal of microalgal cultivation modes with a focus on the effects of different illumination strategies serves to highlight the potential for light to be harnessed as a tuneable process factor to maximise bioprocessing objectives. Finally, in section 2.3 previous applications of microalgal constraint-based metabolic modelling and the insights this type of modelling can provide are discussed.

#### **2.1. Phototrophic cell biology**

Microalgae are responsible for ~50% of carbon fixation worldwide (Field *et al.*, 1998) and they occupy a wide variety of ecological niches, which has given rise to the over 40,000 published species, with at least the same amount thought to be undiscovered (Guiry, 2012). The massive phenotypic and genotypic diversity found in phytoplankton is explained by their evolutionary history. Ancestral prokaryotes with photosynthetic capabilities, known as cyanobacteria, mark the beginning of the journey towards contemporary photosynthetic diversity. They appeared in the early Proterozoic, circa 1.8 billion years ago and their photosynthetic mechanism remains essentially unchanged. The evolution of photosynthetic capabilities is postulated to have been propitiated, much like the advent of eukaryotes, from an endosymbiotic event (Martino *et al.*, 2007; Merchant *et al.*, 2007).

In this case, endosymbiosis refers to the event where a unicellular organism absorbs another unicellular organism and the resulting entity displays physiological traits previously unique to each individual. According to this theory, primary endosymbiosis resulted in a primitive eukaryotic ancestor with photosynthetic capabilities. Further evolution resulted in four distinct phyla Chlorophytae,

Glaucophytae, Rhodophytae and Streptophytae (Figure 1.1). Meanwhile diatoms are postulated to have emerged from a secondary endosymbiotic event (Bowler, Vardi and Allen, 2010).

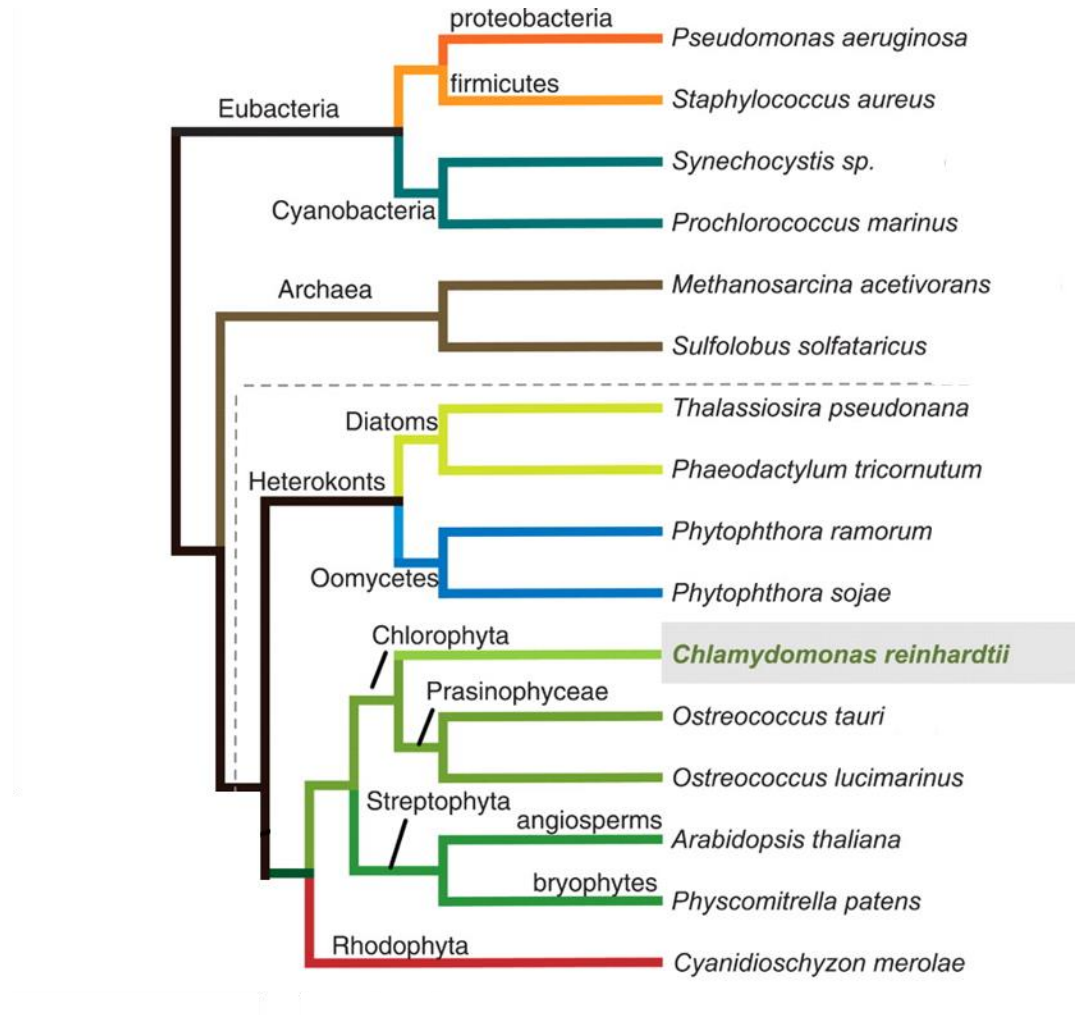


**Figure 2.1** Evolutionary relationships of the different microalgal lineages thought to have evolved from various symbiotic events. Example species belonging to each phylum are listed. (Adapted from Merchant et al. 2007).

Cyanobacteria and the phyla that evolved thereafter can be classified by the membrane structure enclosing their photosynthetic apparatus. On one extreme, prokaryotes lack such structure and their thylakoid membranes are in direct contact with the cytosol, usually stretching along the geometry of the cell (Vothknecht and Westhoff, 2001). Glaucophytes are fresh water microalgae hypothesised to be in between cyanobacteria and eukaryotic photosynthetic organisms (Yusa, Steiner and

Löffelhardt, 2008). A peptidoglycan layer surrounds the cyanelle (Herdman and Stanier, 1977), isolating it from the cytosol but not quite forming the so-called envelope found in red and green algae. Furthermore red and green algae each have characteristic thylakoid membrane topologies and light-harvesting pigment compositions (Wellburn, 1987).

Within this large diversity, *Chlamydomonas reinhardtii* is one of if not the most thoroughly studied species of eukaryotic microalgae (Harris, 2001; Pröschold, Harris and Coleman, 2005; Rasala and Mayfield, 2010). It was first described in 1888 (Dangeard, 1888) and belongs to a subgroup of the class Chlorophyceae (Pröschold *et al.*, 2001). *C. reinhardtii* cellular structure and metabolism are reviewed in detail in the following sub-sections.

### **Cell structure**

*Chlamydomonas* species have two flagella that sprout from the anterior side of the cell and are connected to the basal bodies. They are equal in length and are crucial for the physiology and metabolism of the cell as they enable phototactic (Buder, 1919) and chemotactic (Ermilova, Zalutskaya and Gromov, 1993; Ermilova *et al.*, 1996) responses. Without flagella, cells lose a major competitive advantage in the water column and cannot reposition to maximise light absorption or nutrient uptake opportunities. When grown on solid agar-media flagella may not develop however this key structural component is recovered when the cells are transferred to liquid medium (Harris, 2013).

The extensive diversity of microalgal taxa is exemplified by the different types of cell walls that have evolved across them. For example, diatoms are covered by a hard shell composed primarily of silica (Finkel *et al.*, 2005), whilst prasinophytes, a taxon of green marine microalgae are surrounded by thousands of scales primarily composed of neutral and acidic sugars (Domozych *et al.*, 2012) and some species like *Dunaliella salina* lack a rigid cell wall completely (Oren-Shamir, Pick and Avron, 1990). The *Chlamydomonas reinhardtii* cell wall is composed of two types of crystalline glycoproteins, hydroxyproline-rich glycoproteins and glycine-rich glycoproteins (Goodenough and Heuser, 1985). Foundational studies spanning from the early 70s to

the 90s uncovered the structural make-up of the cell wall (Roberts, 1974; Adair and Snell, 1990). Although originally described as a seven layer ultrastructure (layers named W1-W7), it is now commonly accepted that the electron transparent layers W3 and W5, are spaces rather than true wall components. Nevertheless, the remaining layers are described with the original nomenclature. Hydroxyproline-rich glycoproteins are essential for correct assembly of the cell wall ultrastructure in *C. reinhardtii* as evidenced by a recent RNA interference study showing that silencing of a prolyl 4 hydroxylase gene resulted in a *C. reinhardtii* phenotype lacking layers W2, W4 and W6 (Keskiäho *et al.*, 2007). Wall-deficient mutants were first isolated in the 70s (Davies and Plaskitt, 1971) and have since become invaluable as they allow for the use of low-cost simple methods for recombinant DNA transfection (Kindle, 1990; Madagan, 1998).

As all eukaryotic cells, *C. reinhardtii* cells have membrane bound organelles including a nucleus with a well differentiated nucleolus enveloped by a double membrane. The nuclear envelope is continuous with the endoplasmic reticulum where proteins are synthesized and one or several Golgi apparatuses are characteristically found in proximity as well (Harris, 2013).

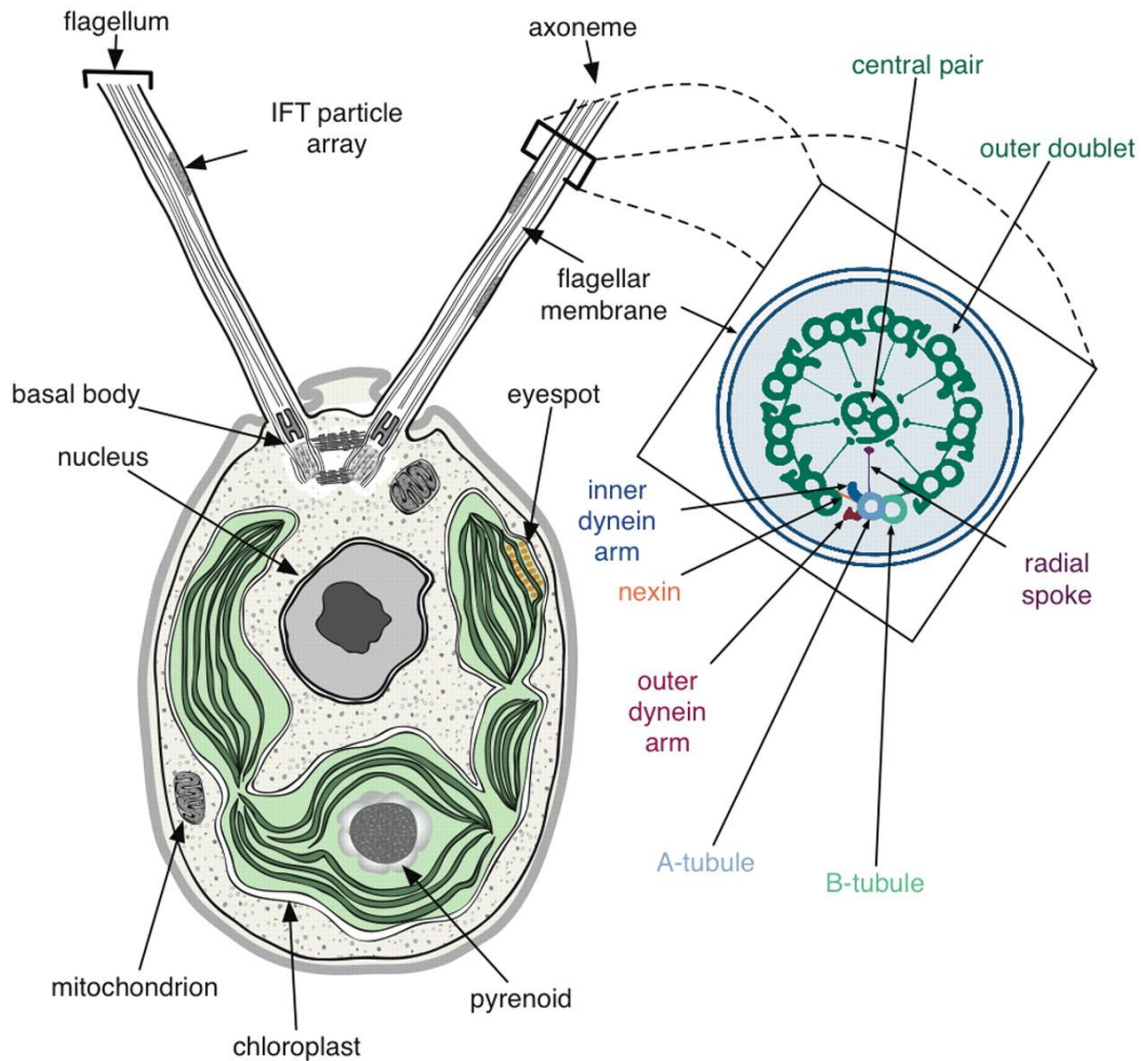


**Figure 2.2** Schematic diagram of the *Chlamydomonas reinhardtii* cell structure. Major organelles are labelled, and the inner cross section of the flagellum is detailed (From Merchant *et al.* 2007).

The morphology of mitochondria varies depending on the growth regime the cells are subjected to, exemplifying the metabolic plasticity of this organism. Cells grown photoautotrophically, particularly under continuous light, are more prone to develop elongated and connected mitochondria that differ from the classical small, single-unit organelle usually found in other organisms (Arnold and Schimmer, 1972). The classical morphology is more common in mixotrophically grown cells. Curiously mitochondria change morphology throughout the cell cycle. Small units come together to form elongated and branched mitochondria which diffuse to smaller units further along the cell cycle (Blank and Arnold, 1980; Gaffal, 1987).

Peroxisomes are a specialised type of organelle and play a central role in mixotrophic metabolism although their rigorous existence as specialised microbodies in *C. reinhardtii* had been a matter of debate until recently. Lauersen and colleagues (2016) identified the subcellular localisation of isoform specific enzymes for 5 out of the 6 associated with the glyoxylate cycle (Lauersen *et al.*, 2016). Fatty acid  $\beta$ -oxidation has also been shown to occur within *C. reinhardtii* peroxisomes (Kong *et al.*, 2017).

The number of peroxisomes per cell may vary with time and growth conditions but the number of chloroplasts per cell is always one. The chloroplast is a cup shaped membrane bound organelle which surrounds the nucleus. Like the nucleus the chloroplast membrane is an envelope formed by an outer and an inner membrane. The chloroplast lumen also known as the stroma contains soluble enzymes and chloroplast ribosomes. Three distinct elements can be found within the chloroplast lumen: the pyrenoid, the eyespot and several stacks of thylakoid membranes.

The pyrenoid was thought to be composed of two enzymes (a) ribulose-1,5-bisphosphate carboxylase/oxygenase large and small subunits (rubisco; *rbcl*; RBCS); (b) rubisco activase (RCA1) (Vladimirova, Markelova and Semenenko, 1982; McKay, Gibbs and Vaughn, 1991). Recently it has been proposed that a third protein component, Essential Pyrenoid Component 1 (EPYC1) is also present in relatively large quantities with ratios of ~1:6 and ~1:1 with *rbcl* and RBCS respectively (Mackinder *et al.*, 2016). The fact that key structural components are still being discovered for such a prominent cellular component shows how much is still to be learned about *Chlamydomonas reinhardtii* and microalgal cell structure in general.

The eyespot acts as a cell antenna and is directly responsible for co-ordinating responses to light like phototaxis. It is connected to the flagella at the distal extremities of the flagellar roots towards the central part of the cell. At least two layers of dense hexagonal pigment granules composed mainly of carotenoids and rhodopsins are intercalated by thylakoid membranes (Harris, 2013). The photoreceptors found in the eyespot are so sensitive that even absorption of single photons can cause changes in swimming direction (Hegemann and Marwan, 1988). Net positive and negative phototaxis can be observed in response to changes in the relative position of the light

source (Harris, 2001). The receptor responsible for phototaxis in *C. reinhardtii* is rhodopsin (Foster and Smyth, 1980). Interestingly a blue and red-light regulated photoreceptor protein, CrCRYa, has been recently discovered in *C. reinhardtii* (Beel *et al.*, 2012). This newfound cryptochrome is the first evidence of red-light regulated metabolism in the model algae. The discovery of CrCRYa means other red light-regulated photoreceptors might yet remain undiscovered in *C. reinhardtii*. Such red/far-red light activated photoreceptors are typically referred to as phytochromes and are common in both higher plants like *Arabidopsis thaliana* (Clack, Mathews and Sharrock, 1994) and cyanobacteria like *Fremyella diplosiphon* (Wiltbank and Kehoe, 2016).

### Cell cycle

*Chlamydomonas reinhardtii* is a haploid microalgae species with a nuclear genome made up of 17 chromosomes (Merchant *et al.*, 2007; Blaby *et al.*, 2014); it additionally has multiple copies of its single plastome chromosome in the chloroplast (Turmel, Lemieux and Lee, 1980). *C. reinhardtii* cells can exist in two distinct states, under nutrient replete conditions cells will be in a haploid vegetative state and reproduce by multiple fission (Bišová and Zachleder, 2014). Vegetative is commonly used to differentiate cells that are actively growing and dividing from inert spores. Under nutrient depleted or other harsh environmental conditions like extremely low temperatures, *C. reinhardtii* can form diploid zygospores that are able to survive extreme environments and ensure the future proliferation of the organism (Harris, Stern and Witman, 2009). *C. reinhardtii* zygospores must germinate into haploid gametes before sexual reproduction via meiosis can occur (see Beck and Haring, 1996; Umen and Goodenough, 2001; Suzuki and Johnson, 2002; Sekimoto, 2017).

Cell proliferation in the experiments described in this thesis is assumed to be predominantly via multiple fission of vegetative cells and is described in further detail here. Multiple fission is comprised of 4 distinct phases namely, growth (G1), DNA replication (S), mitosis (M) and hatching (Figure 2.3). During G1, under optimal growth conditions, the *C. reinhardtii* cell volume can increase by more than 10 times (Cross, 2020). Rapid transitions between the S and M phases lead to the production of a variable number of daughter cells,  $2^n$  where  $n$  is the number of complete S/M cycles, depending



on the final cell size at the end of G1. This means that a single vegetative *C. reinhardtii* cell can spawn 2, 4, 8 or 16 daughter cells.

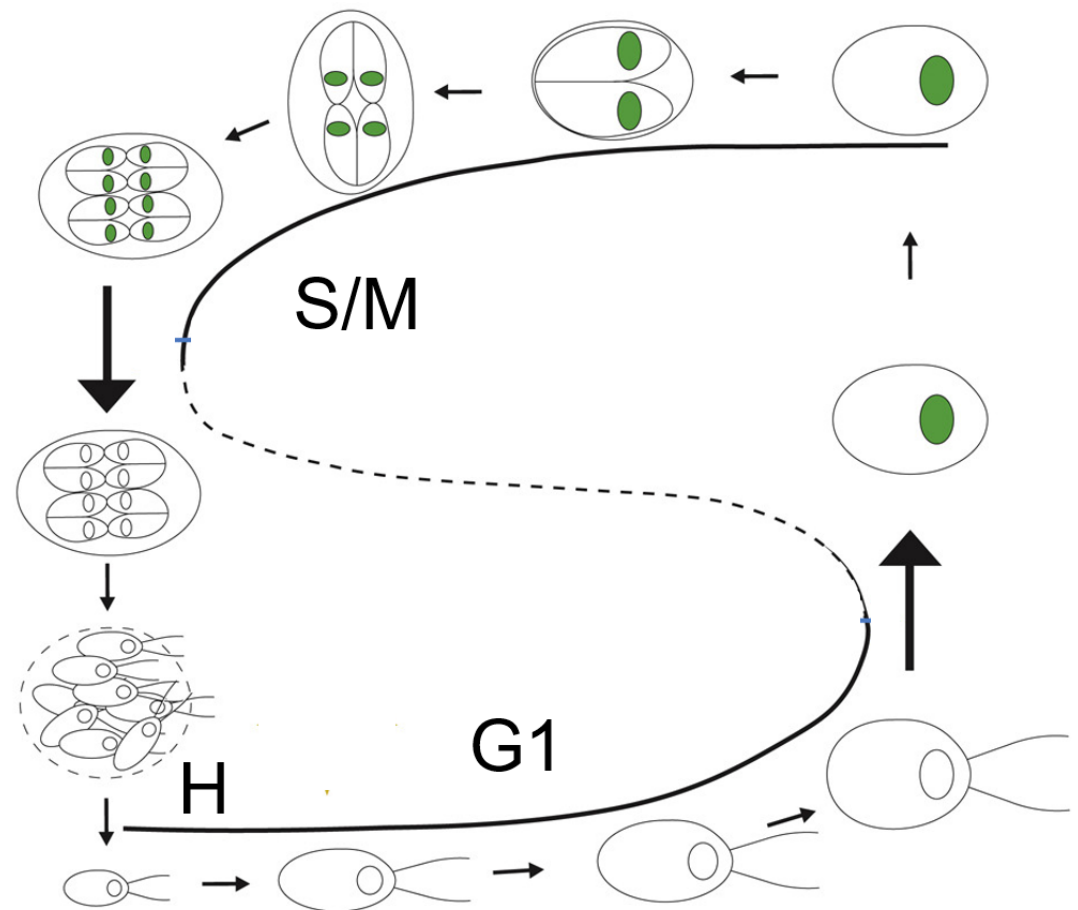


**Figure 2.3** Overview of the *Chlamydomonas reinhardtii* cell cycle. A vegetative cell grows until it reaches a critical size and loses its flagella. After which it enters several cycles of DNA replication and cell division within a sporangium formed from the original mother cell's cell wall. Once daughter cells reach a critical size the S/M cycles cease, flagella regrow and sporangin is released so the daughter cells can hatch. G1, growth phase; S/M, DNA replication / mitosis; H, hatching.

The cell is said to reach a commitment point during G1 after which it will complete at least one S/M cycle. This cell cycle commitment point was speculated to be composed of a sizer mechanism preventing small cells from entering S/M phases and an

endogenous timer linked to the natural diel cycle (Donnan and John, 1983). However, more recent studies have shown the influence of light intensity and growth rate to be the driving factors behind the length of G1 (Matsumura, Yagi and Yasuda, 2003; Vitova *et al.*, 2011). Therefore, the time-point considered as the commitment point and subsequent cell division are postulated to be independent of an endogenous timer. A mechanistic model proposed by Heldt and colleagues (2020) describes the effect of light extending the duration of G1 and vegetative cells as being either in a permissive or non-permissive state for cell division (Heldt *et al.*, 2020). Consensus with the model predictions has been found in a gene expression study looking at cyclin-dependent kinase and other classical cell-cycle regulator pathways (Cross, 2020).

Interestingly, in both multiple fission and sexual reproduction, *C. reinhardtii* eventually loses its cell wall. In multiple fission this is caused at the end of the cell cycle when the daughter cells hatch out of the sporangium formed from the original mother cell's cell wall. Sporangin is the enzyme responsible for the cell wall breakdown, localised to daughter cell flagella (Kubo *et al.*, 2009). On the other hand, during sexual reproduction of *C. reinhardtii* gametes, gametolysin is released into the culture media by the microalgal cells promoting the shedding of the cell wall and aiding in the attachment of two gametes mediated by agglutinins (Matsuda *et al.*, 1985).

### **Cell metabolism**

Metabolism is the amalgamation of all the biochemical reactions occurring in tandem inside a living cell (Stephanopoulos, Aristidou and Nielsen, 1998). It describes (a) catabolism, the breakdown of molecules or molecular complexes into smaller molecules thus releasing energy, and (b) anabolism, the utilisation of lower energy molecules and the energy released by the breakdown of ATP to build higher energy more complex molecules like DNA, lipids, polysaccharides and proteins which make-up the biomass of living organisms.

*Chlamydomonas reinhardtii* is a facultative phototroph species of microalgae. It can grow (a) autotrophically in light with CO<sub>2</sub> as the sole carbon source, (b) mixotrophically in light with acetate as the main source of (organic) carbon and (c) heterotrophically in the dark with acetate as the main source of (organic) carbon. The

metabolic plasticity of microalgae makes them highly versatile microorganisms able to survive in a wide variety of environmental conditions. The following sub-sections detail the metabolic pathways that enable autotrophic and mixotrophic growth in *C. reinhardtii* and their connection to cellular physiology and biomass composition.

### **Photosynthesis – Light dependent reactions**

Photosynthesis plays an important role in autotrophic and mixotrophic growth. It can be divided into two main stages (a) the light dependent reactions and (b) carbon fixation also referred to as the Calvin-Benson cycle. The three net products of the light dependent reactions of photosynthesis are oxygen, ATP and NADPH. Light is absorbed at the two types of photosystem (PS) found in the thylakoid membrane of the chloroplast, PSI and PSII. Photosystems are protein-pigment complexes made up of specialised proteins like light harvesting complex proteins (LHCPs), light harvesting pigments (chlorophylls) and accessory pigments (carotenoids). These components are assembled into peripheral light harvesting antennae that funnel absorbed light energy in the form of excited state electrons to the photochemical reaction centres of each photosystem. Excited electrons travel down the electron transport chain in the thylakoid membrane in either linear electron flow (LEF) or cyclic electron flow (CEF).

Linear electron flow starts with absorption of photons by the proximal antenna complexes of PSII which funnel an excited electron to the primary electron donor P680 forming the unstable form P680\*. This form of the primary electron donor transfers a high-energy electron to the primary acceptor molecule pheophytin a which in a quasi-instantaneous transition passes the electron on to a plastoquinone molecule at site Q<sub>A</sub> and finally the electron reaches a plastoquinone molecule at site Q<sub>B</sub>. Meanwhile the electron-deficient P680<sup>+</sup> is reduced by the oxidation of water to O<sub>2</sub> catalysed by the oxygen evolving complex (OEC). Once the plastoquinone at Q<sub>B</sub> is fully reduced to plastoquinol, it leaves PSII and reaches the cytochrome b<sub>6</sub>f complex where it is fully oxidised, resulting in a net transfer of protons into the thylakoid lumen supporting the build-up of a proton gradient from the lumen down to the stroma. The electron donated from plastoquinol eventually reaches plastocyanin and/or cytochrome c<sub>6</sub>. Both these electron donors can release an electron to the primary electron acceptor in PSI, P700.

However, by the time the electron has travelled down the electron transport chain from PSII to PSI, it is at a lower energy state. Therefore, the electron transfer from P700 to ferredoxin is catalysed by the absorption of another photon. Ultimately ferredoxin enables NADP<sup>+</sup> reductase to catalyse the reduction of NADP<sup>+</sup> into the coveted NADPH, the source of reducing power required for inorganic carbon fixation (Figure 2.4A). Redox reactions throughout the electron transport chain produce a net accumulation of H<sup>+</sup> in the thylakoid lumen. This H<sup>+</sup> travels down a concentration gradient through ATP synthase driving oxidative phosphorylation. All in all, LEF produces ATP and NADPH in a 2.6:2 ratio (Takahashi *et al.*, 2013).

Cyclic electron flow does not produce NADPH as the excited electrons at P700\* in PSI are donated back to plastoquinone and the cytochrome b<sub>6</sub>f complex as opposed to ferredoxin (Figure 2.4B). Net ATP production is maintained as the redox reactions (upstream of PSI) responsible for the build-up of H<sup>+</sup> are unaffected. This type of electron flow is controlled by the reducing potential of the chloroplast stroma. It can be thought of as a complimentary supply of ATP to the LEF derived ATP, completing the strict 3.2:2 ratio of ATP:NADPH required by the Calvin Benson cycle (Takahashi *et al.*, 2013). Additionally and Environmental conditions like high light (Nama *et al.*, 2019) and lack of certain nutrients (sulphur –; phosphorous, (Kamalanathan *et al.*, 2016)) cause reactions at the acceptor side of PSI to become limiting, triggering a large increase in proton potential within the chloroplast lumen. The excess H<sup>+</sup> that is not ported through ATP synthase is instead employed in non-photochemical quenching of chlorophyll fluorescence (Peers *et al.*, 2009), a photoprotective mechanism resulting in the de-excitation of chlorophyll and overall reduced photosynthetic yield. CEF is also thought to have a regulatory role in hydrogen production as *C. reinhardtii* CEF-impaired mutants have been found to overproduce hydrogen under sulphur deprivation conditions in comparison to wildtype (Tolleter *et al.*, 2011).

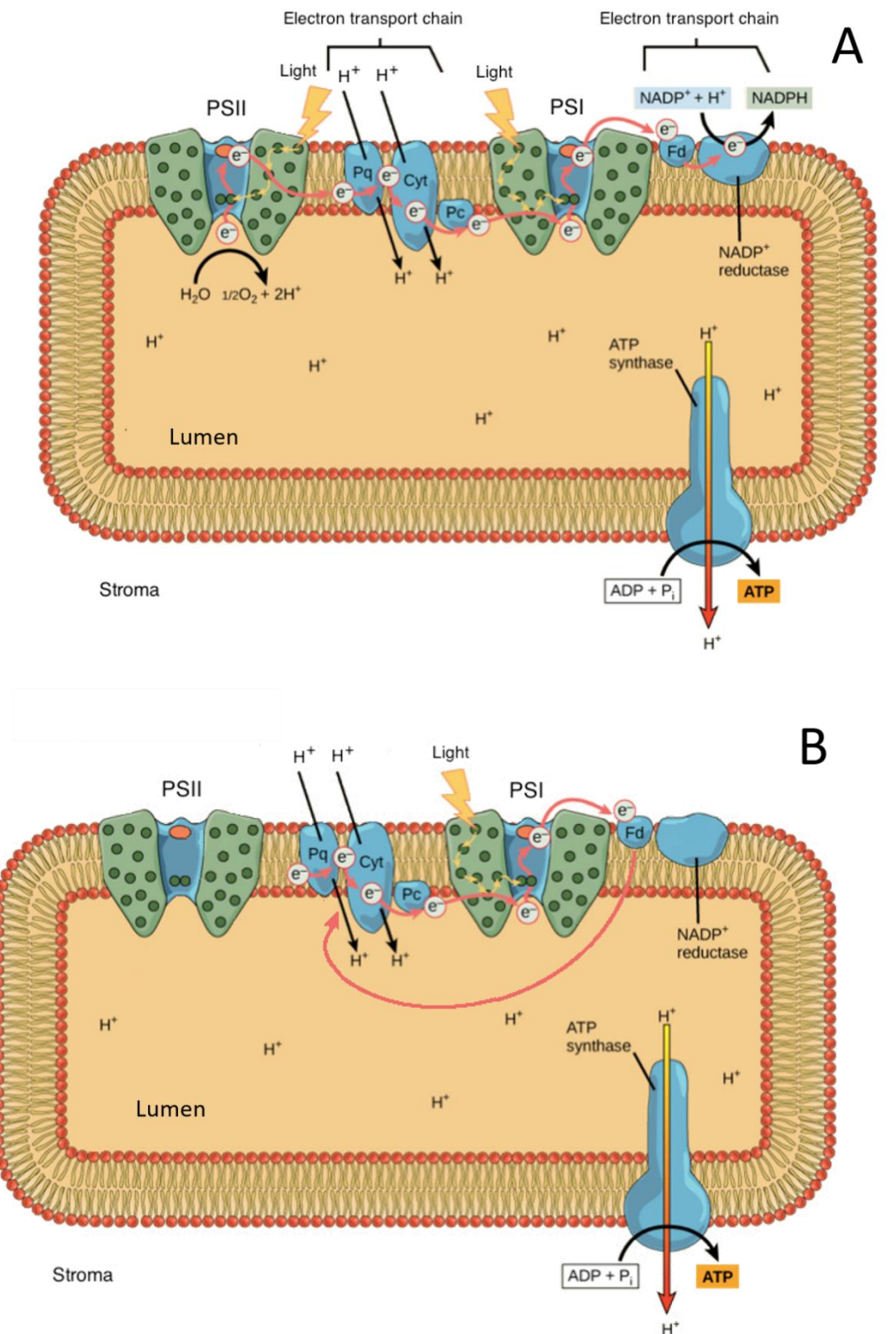


**Figure 2.4** Schematic diagram of photosynthesis light dependent reactions. (A) Linear electron flow; (B) Cyclic electron flow. PSII, photosystem II; Pq, plastoquinol/plastoquinone; Cyt, cytochrome b6f complex; Pc, plastocyanin; PSI, photosystem I; Fd, ferredoxin. Adapted from [www.khanacademy.com](http://www.khanacademy.com).

Photosynthetically active radiation (PAR) is comprised of the range of wavelengths within the visible light spectrum that can drive the light dependent reactions of photosynthesis (400 to 700 nm). The energy carried by a photon is directly proportion to its electromagnetic frequency (Equation 2.1) and can be calculated by Equation 2.2:

$$f = \frac{c}{\lambda} \quad (\text{Eq. 2.1})$$

$$E = \frac{hc}{\lambda} \quad (\text{Eq. 2.2})$$

Where  $E$  is photon energy in  $\text{W m}^{-2}$ ;  $h$  is the Plank constant;  $c$  is the speed of light in a vacuum  $\text{m s}^{-1}$ ;  $\lambda$  is the wavelength in  $\text{m}$ ; and  $f$  is the electromagnetic frequency of a photon in  $\text{Hz}$ .

In terms of energy flux, photons with different wavelengths are different from each other (Equation 2.1 & 2.2). However, all photons in the PAR range can drive photosynthetic reactions therefore when referring to PAR range photons, photosynthetic photon flux (PPF,  $\mu\text{mol}_{\text{ph}} \text{m}^{-2} \text{s}^{-1}$ ) is the more common unit of measure. Although all photons within the PAR range can drive photosynthetic reactions, they are not all absorbed equally. For example blue photons (400-500 nm) can be absorbed by ‘non-active’ secondary photoprotective pigments like the anthocyanins produced in deciduous trees’ leaves (Gould, 2004). In microalgae, carotenoids are very common secondary pigments that can absorb blue light. The efficiency of energy transmission between carotenoids and chlorophylls towards the photosystem reaction centres can be lower than between chlorophyll molecules (30-90% compared to up to 100%; (Cope, Snowden and Bugbee, 2014)). Such processes result in a loss of absorbed energy from blue light photons and therefore a lower yield on photon flux (YPF). Differentiating between absorbed photons of different wavelengths can be done by calculating the action spectrum of photosynthesis (rate of oxygen evolution divided by rate of rate of photon energy received; (McCree, 1971). To understand YPF for photons of different wavelengths, photon energy per wavelength and action spectrum can be combined with the absorption cross section of the microalgal cell ( $a_{x\lambda}$ , Figure 2.5A).

The  $a_{x\lambda}$  of *C. reinhardtii* grown in continuous turbidostat mode under different illumination conditions ( $1500 \mu\text{mol}_{\text{ph}} \text{m}^{-2} \text{s}^{-1}$  of Warm white-, yellow-, deep red-, orange-red- and blue- light emitting diodes) has been shown to not vary significantly (Figure 2.5B, (Mooij *et al.*, 2016)). This suggests that under non limiting light the wavelength of absorbed photons is not of major importance in quantum terms.

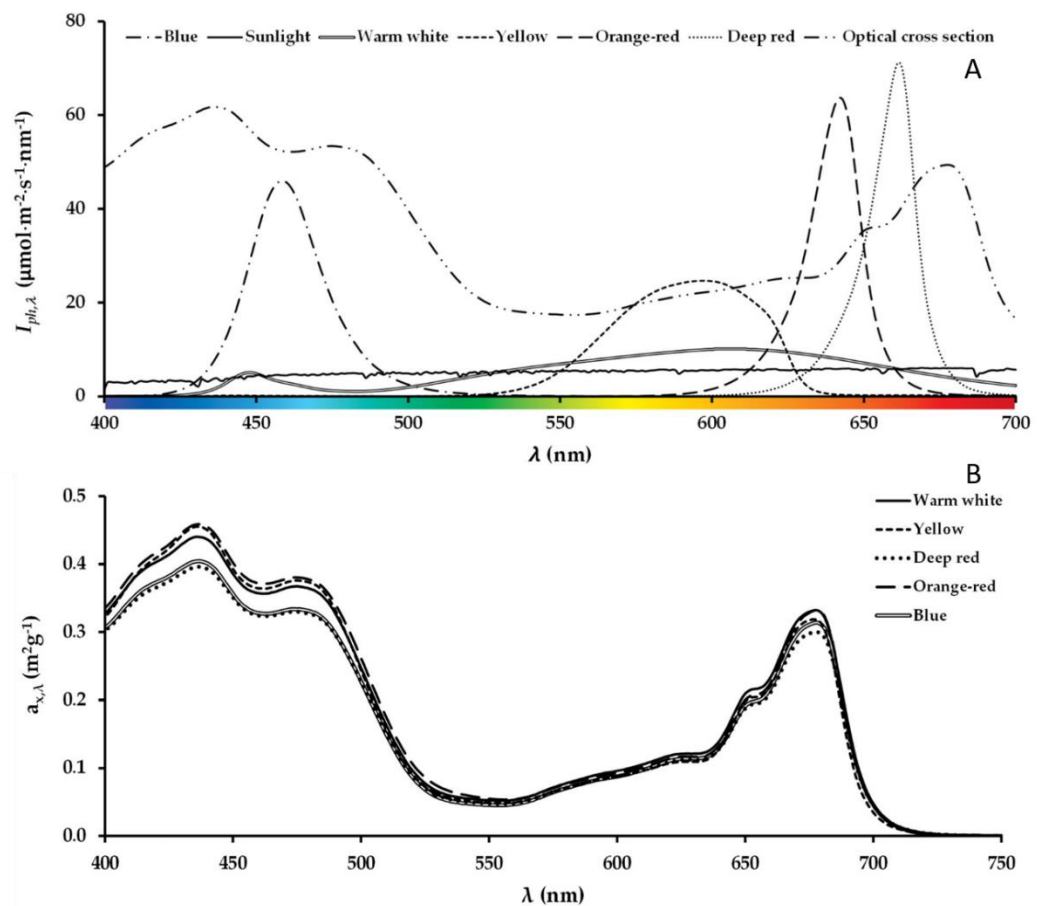


**Figure 2.5** *C. reinhardtii* light absorption profile compared to LED illumination sources. (A) LED illumination sources of differing peak wavelength; (B) *C. reinhardtii* optical absorption cross section measured under different LED illumination sources during continuous turbidostat cultures at  $1500 \mu\text{mol}_{\text{ph}} \text{m}^{-2} \text{s}^{-1}$ ).  $I_{ph,\lambda}$ , normalised photon flux for each wavelength ( $\mu\text{mol} \text{m}^{-2} \text{s}^{-1} \text{nm}^{-1}$ );  $a_{x,\lambda}$ , biomass absorbance cross section ( $\text{m}^2 \text{g}^{-1}$ ). Adapted from Mooij *et al.* 2016.

### Redox balance and photoprotective mechanisms

Light-driven electron flux down the electron transport chain (ETC) of the chloroplast produces reducing power in the form of NADPH and energy-providing ATP

to power cellular activity. However, it also produces a dangerous by-product in the form of dioxygen which can receive energy from a chlorophyll molecule in its triplet excited state and become a harmful reactive oxygen species (ROS) molecule (S. K. Wang *et al.*, 2014). As ever, cellular homeostasis depends on the balance of interconnected metabolic processes functioning in unison. Under environmentally favourable conditions, the reducing power generated in the chloroplast ETC is used to power anabolic reactions and the redox balance of the ETC is maintained ensuring the clearance of dioxygen and ROS. However, the plastoquinone pool can become over-reduced under unfavourable conditions, such as high light or nutrient deprivation, as the electrons produced cannot be unloaded leading to a stall in the proton gradient build-up across the membrane and no more ATP being produced (Allen, 2003). Such an over-reduced state can lead to the accumulation of harmful ROS and put the cell into a hyperoxidant state (Hansberg and Aguirre, 1990).

Various cellular responses have evolved over time to maintain the redox balance in the chloroplast ETC under unfavourable conditions like nutrient deprivation and excess light. These include negative phototaxis, alternative electron flows, heat-dissipation mechanisms known collectively as non-photochemical quenching, and production of antioxidants (all reviewed in Erickson, Wakao and Niyogi (2015)). Some of the cellular responses observed in the experiments presented in this thesis like the differences in cell size between illumination conditions may be explained as differentiation responses to avoid a hyperoxidant state and are further discussed in Chapter 3.

Respiration via the mitochondrial alternative oxidase (AOX) forms part of such photoprotective mechanisms. It mediates non-energy conserving respiration by transferring electrons from ubiquinone directly to molecular oxygen (Finnegan, Soole and Umbach, 2004). It's function in plants like *Sauromatum guttatum* is linked to thermogenic responses that help volatilise it's scent to better attract pollinating insects (McIntosh, 1994). In plant pathogenic fungi like *Botrytis cinerea* it has been shown to be involved in virulence as well as vegetative development functions (Lin *et al.*, 2019). Considering that AOX mediated respiration does not produce a net yield of ATP it can be seen as a wasteful sink of photosynthetically harvested electrons in microalgae.



However, it's importance for photoprotection as a reducing power sink has been demonstrated in *C. reinhardtii* AOX mutants that struggle to survive under high light conditions (Kaye *et al.*, 2019). In light of this information, photosynthetic efficiency optimisation efforts are better directed at the source of the problem, which is the oversaturation of the light harvesting apparatus, for example with reduced antenna-size mutants that have reduced specific light absorption capacity (Perrine, Negi and Sayre, 2012).

### **Carbon assimilation**

CO<sub>2</sub> fixation is essential in autotrophic growth as it is the sole source of organic carbon required to generate new biomass. The ATP and NADPH produced in photosynthesis are the fuel molecules required to drive CO<sub>2</sub> fixation in the chloroplast. This happens in the Calvin-Benson cycle and can be broken down into three stages (a) carbon fixation, (b) triose reduction and (c) ribulose biphosphate (RuBP) regeneration.

In *C. reinhardtii* mixotrophic metabolism, inorganic carbon fixation in the chloroplast is complemented by organic carbon assimilation by converting acetate to acetyl coenzyme-A (CoA). This can be achieved by two ways (a) in a single step via acetyl CoA synthetase (ACS) and (b) in two steps catalysed by acetate kinase (ACK) and phosphate acetyltransferase (PAT). Three isoforms have been found in *C. reinhardtii*; initially ACS2 located in the chloroplast (Terashima *et al.*, 2010) and, more recently ACS1 thought to be localised to the mitochondria exclusively and ACS3 located in peroxisomes (Lauersen *et al.*, 2016). The strong evidence for ACS presence in the specialised peroxisomes suggests the single step conversion of acetate to acetyl-CoA via ACS is the preferred pathway for acetate assimilation in *C. reinhardtii*. Four out of the remaining five enzymes (citrate synthase, CIS2; isocitrate lyase, ICL1; malate synthase, MAS1, malate dehydrogenase, MDH) that make up the glyoxylate cycle were also localised to peroxisomes recently (Lauersen *et al.*, 2016) cementing the centrality of the peroxisome in acetate assimilation.

The glyoxylate cycle is a shortened version of the tricarboxylic acid (TCA) cycle where the two CO<sub>2</sub> evolving steps (ketoglutarate to succinyl-CoA, Figure 2.6(3) and

succinyl-CoA to fumarate Figure 2.6(6)) and the linking reactions between them are bypassed to net a positive gain in organic carbon incorporated into cellular metabolism. In the glyoxylate cycle isocitrate is converted into glyoxylate and succinate (Figure 2.6(9)). The glyoxylate cycle can yield a succinate molecule for every two acetate substrates. Organic carbon assimilated as succinate is available for central carbon metabolism for example feeding into the TCA cycle as a substrate of succinate dehydrogenase (Figure 2.6 (6)).

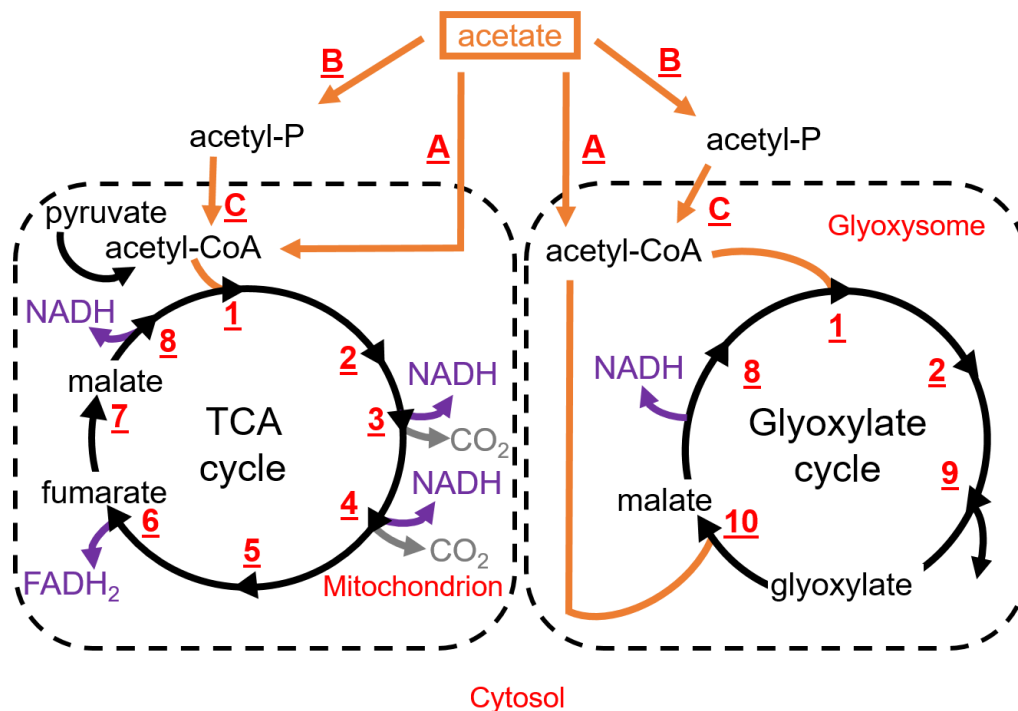


**Figure 2.6** Metabolic pathway diagram comparing the assimilation of uptaken acetate into central carbon metabolism via the tricarboxylic (TCA) cycle and the glyoxylate cycle. Orange arrows highlight reactions where acetate and or acetyl co-enzyme A are involved. Grey arrows highlight CO<sub>2</sub> release. Purple arrows highlight the production of reducing equivalents NADH and FADH<sub>2</sub>. (A) acetyl Co-A synthase; (B) acetate kinase; (C) phosphate acetyltransferase; (1) citrate synthase; (2) aconitase; (3) isocitrate dehydrogenase; (4) α-ketoglutarate dehydrogenase; (5) succinyl-CoA synthetase; (6) succinate dehydrogenase (7) fumarate hydratase; (8) malate dehydrogenase; (9) isocitrate lyase; (10) malate synthase.

*Chlamydomonas reinhardtii* is a facultative phototroph therefore it does not necessarily require light to grow if an organic carbon source like acetate is available.

Photosynthetic CO<sub>2</sub> fixation and net O<sub>2</sub> evolution are reduced in mixotrophic conditions as a metabolic re-configuration takes place and reliance on photosynthesis becomes less important for producing new biomass. Heifetz and colleagues (2000) observed a ~50% decrease in the fraction of carbon biomass resulting from photosynthesis when growing *C. reinhardtii* under saturating illumination conditions in the presence of acetate (Heifetz *et al.*, 2000). The investigators found no decrease in PSII efficiency as measured by chlorophyll fluorescence indicating that the reduced O<sub>2</sub> evolution observed is not necessarily due to a damaged electron transport chain; and more likely due to a reconfiguration of metabolism resulting in increased CEF (Chapman *et al.*, 2015) in the presence of acetate. More recently, a study by Roach and colleagues (2013) employing spin-trapping electron paramagnetic resonance spectroscopy (Chapman and Dodd, 1971) showed in-vitro and in-vivo that acetate treated PSII favoured direct non-radiative charge recombination events that cause photoinhibition and reduced O<sub>2</sub> production (Roach, Sedoud and Krieger-Liszkay, 2013). Additionally, acetate conversion to acetyl-CoA requires ATP and is therefore in direct competition with photosynthetic CO<sub>2</sub> fixation. Overall this metabolic plasticity and reconfiguration in the presence of acetate provide potential avenues for metabolic engineering to re-direct carbon flow towards biotechnologically relevant objectives like terpenoid (Wichmann, Baier, Wentnagel, Kyle J. Lauenstein, *et al.*, 2018) and recombinant protein (Fields, Ostrand and Mayfield, 2018) production.

## **2.2. Microalgal cultivation**

### **Open culture systems**

Large scale microalgae culture systems fall into two main categories: open-systems and closed-systems. Open-systems are based in natural water basins, artificial non-mixed ponds and artificial mixed ponds (circular / raceway ponds) and are almost exclusively installed outdoors. Raceway ponds are the most common open-system used in industry. Figure 2.7 shows the typical configuration of these systems. A closed oval shaped loop allows recirculation of the culture around the system. Culture depth is usually 100 – 300 mm (Williams and Laurens, 2010). In principle these artificial raceway ponds are a simple, relatively low cost option for large scale culture. However, the risk

of contamination limits the species that are suitable for this type of cultivation. Poor mixing results in sub-optimal light utilization and their open nature leads to massive evaporative losses. Illumination is dependent on sunlight which limits their geographical location and increases yield variability. Rainfall can also dilute nutrient and biomass content in the culture. Typically, CO<sub>2</sub> demand is only met by atmospheric CO<sub>2</sub>, which is sufficient to sustain growth, but is nowhere near the optimum. Submerged gas spargers can be utilised to meet CO<sub>2</sub> demand throughout the pond.



**Figure 2.7.** (a) Medium scale raceway pond for research purposes (b) Cyanotech facility, Hawaii, USA.

Productivity is sacrificed in favour of lower capital expenditure costs and simplicity. The risk of contamination and the engineering barriers to controlling environmental parameters like temperature and mixing make this system unlikely to be worthwhile in the long-term. More modern iterations of the design improve power efficiency by replacing the paddle wheel with a propeller (Chiaramonti *et al.*, 2013) or driving re-circulation via aeration (Ketheesan and Nirmalakhandan, 2012). The low concentration of CO<sub>2</sub> in atmospheric air (0.04% v/v) is limiting for microalgae growth. This has been proven by the use of industrial flue gas with a CO<sub>2</sub> concentration (10% v/v) orders of magnitude larger than air successfully increasing CO<sub>2</sub> fixation rates in open raceway ponds growing *Chlorella vulgaris* from 8.92 to 102.66 mg CO<sub>2</sub> per litre per day concomitantly improving volumetric biomass yield by four fold (Yadav, Dubey and Sen, 2020). Improved CO<sub>2</sub> supply has also been engineered whereby the gas is pumped into a 1.5m sump in the pond and allowed to bubble towards the surface (Park, Craggs and Shilton, 2011). These improvements may drive down the cost per kilogram of biomass, but open-systems are still a long way away from providing the necessary control and

reproducibility needed to make a robust bioprocess. This has proven to be acceptable for nutraceutical applications (see *Chlorella* sp, *Spirulina platensis* and *Dunaliella salina*) however as commercial applications of microalgae veer towards higher value products, and require highly controlled environments, closed-systems may be favoured by industry.

### **Closed culture systems**

Closed systems are typically referred to as photobioreactors (PBRs). The main difference with open-systems is that the microalgal culture is not in direct contact with the atmosphere. This reduces the risk of contamination by preventing direct exchange with the surrounding environment. Open systems also require less pumping, this translates into lower power consumption costs and mitigates risk of biomass shearing. Different types of pumps have been found to have detrimental effects on biomass growth so the choice of pump is critical for success (Brindley Alías *et al.*, 2004). Although PBRs are not insusceptible to contamination, their potential to remain axenic is a clear advantage over open-systems as it allows cultivation of non-extremophile species like *C. reinhardtii* which have shown promise in recombinant protein expression (Gimpel *et al.*, 2015).

PBR design categories are summarised in Table 2.1. PBRs can be made of glass or transparent plastic to allow light to travel through the reactor wall. The simplest design involves a polyethylene bag (sleeve) hung from a support. Mixing in these bags occurs by air bubbling. These are used in hatcheries and are also utilised by several companies involved in the nutraceuticals and cosmeceuticals industry (GreenSea, 2016; NOVAgreen, 2016). They are usually operated with some head-space where gas exchange can occur. PBRs can also be single phase whereby the whole reactor is filled with medium and gas exchange occurs in a separate gas exchanger. Lastly, mixing can be promoted by air bubbling as in sleeves or by a pumping system.

**Table 2.1.** Main design types of closed photobioreactors.

Category	
(i)	Flat or tubular
(ii)	Horizontal, inclined, vertical or spiral
(iii)	Manifold or serpentine
(iv)	Hybrid
(v)	Floating
(vi)	Biofilm

As well as offering a smaller risk of contamination, PBRs offer a highly controlled environment. Key operating parameters like temperature,  $ppCO_2$  and  $ppO_2$ , pH and light intensity can all be controlled on-line and optimised for productivity. Conventional stainless steel vessels have a surrounding cooling jacket for temperature control. Due to the number of different PBR designs and their varied surface to volume ratios, there is no conventional way of controlling temperature. A common approach is to house the PBR in a greenhouse with appropriate air vents and a fan system that maintains a constant room temperature. Additionally, as demonstrated in a 5 m<sup>3</sup> horizontal-tubular PBR operated in the south of France, temperature control systems can be linked with a water spraying system that nebulises water over the PBR achieving evaporative cooling (Muller-Feuga *et al.*, 2012). Alternatively, partial immersion of a tubular PBR (25m<sup>3</sup>) in a temperature controlled water basin can be used to maintain a low temperature as applied by the company Aquasearch in Hawaii, US (Huntley and Redalje, 2007). Internal heat exchangers can be used in flat-panel PBRs as shown by Tredici & Rodolfi (2004) and Hu & Sommerfeld (2010).

### Nutrient deficiency

Inorganic nutrient deficiencies are employed in microalgal cultivations as a means to induce stress responses in microalgal cells that result in the accumulation of desirable molecules like triacylglycerides (TAGs) or photoprotective secondary pigments (J Msanne *et al.*, 2012). Starving *C. reinhardtii* cells of nitrogen, sulphur, phosphorous or magnesium has been shown to trigger increased neutral lipid accumulation (Çakmak *et al.*, 2014). Under industrial conditions, transesterification of these neutral lipids yields

two immiscible liquid fractions of glycerol and the methyl esters that can be further refined into biodiesel (Chisti, 2007).

The field of microalgae-based biofuels traces its academic roots to the 1940s (Harder and von Witsch, 1942) and has certainly gathered a lot of attention throughout the past decades (Raheem *et al.*, 2018). The spike in oil prices during the mid-2000s can be attributed as one of the causes for the large increase in venture capital and state funding available for biofuels research, particularly in the United States of America, where a plethora of companies were founded with the intention of commercialising microalgae-based biofuels (Su *et al.*, 2017). However, commercial success has not yet materialised and many of these companies are now either defunct or have pivoted towards valorised biomass production and high-value products. A review on stakeholder outlooks concluded that many years of intensive research and a favourable investment environment are still needed to reach commercialisation (Oltra, 2011).

A prolific researcher, Professor. Michael A. Borowitzka lamented the lack of learning from past failures exemplified in recent literature in his concluding remarks of a chapter detailing the history of energy from microalgae (Michael A Borowitzka, 2013). Ultimately, although inorganic nutrient deprivation is effective in triggering the accumulation of storage molecules, it has a negative effect on growth rate and biomass productivity, which is detrimental for commercial operations aiming at maximising productivity. With this in mind nutrient feeding strategies that maximise biomass production and are able to trigger the specific response required must be developed (Markou, Chatzipavlidis and Georgakakis, 2012).

Another process parameter that has been shown to affect *C. reinhardtii* growth kinetics and cell morphology is pressure. Wagner and Posten (2017) found lower than atmospheric pressure conditions affected *C. reinhardtii* growth rate negatively, increased carbon dioxide uptake rates and did not discernibly affect oxygen production rates or cell viability (Wagner and Posten, 2017). These experiments were performed in the context of determining the suitability of *C. reinhardtii* as a source of oxygen during space missions. On a more down to earth note, the authors also investigated the effects of sudden pressure changes, in the range of 300 millibars, as might be experienced

during mass culture pumping in large scale installations. The lack of detrimental effects is promising for the use of *C. reinhardtii* in large scale industrial bioprocesses where the cells may traverse several pump-valve intersections.

The effectiveness of employing stressful conditions to trigger the over-production of valuable metabolites in microalgae cannot be overstated. Although biofuels have not yet realised their commercial potential, other microalgal commercial ventures, particularly secondary pigment production, rely on successfully controlling such stress responses during upstream bioprocessing to maximise product yield. For example, natural astaxanthin is a coveted antioxidant for use in the aquaculture and nutraceutical industries. It can be produced, by many species of green microalgae under a plethora of different environmental stresses like high salinity and low pH (Orosa *et al.*, 2001).

The green microalgae species *Haematococcus pluvialis* is a prodigious astaxanthin producer. The most suitable combination of environmental stressors has been demonstrated to be high light intensity combined with inorganic nitrogen deprivation in mixotrophic growth media (Orosa *et al.*, 2001). A recent study by Focsan (2017) and colleagues has brought us a step closer to understanding the mechanism behind the unique photoprotective properties of astaxanthin. They used electron paramagnetic resonance (EPR) among other techniques to show the superior oxidation potential of astaxanthin and its esters compared to other carotenoids like  $\beta$ -carotene as well as its inability to aggregate in ester form (Focsan, Polyakov and Kispert, 2017). Although its photoprotective ability is unquestionable, research by Fábregas (2003) *et al.* demonstrated that the triggering factor for astaxanthin production is inorganic nitrogen deprivation and the resulting growth arrest. They suggested high light irradiance acts as a stimulant for nitrogen consumption, rather than a direct trigger of astaxanthin production. They also found that maximal specific astaxanthin level per cell was independent of cell density. However, the rate of astaxanthin accumulation was faster under high light conditions, indicating that astaxanthin accumulation rate is dependent on specific light availability (Fábregas *et al.*, 2003).

High light intensity can also be detrimental to microalgal productivity. For example, in the production of hydrogen with *C. reinhardtii* it was found that 300  $\mu\text{mol}_{\text{ph}}$



$\text{m}^{-2} \text{s}^{-1}$  in combination with sulphur starvation were detrimental due to excessive photosystem II (PS II) photodamage, whereas a slightly lower light intensity of  $200 \mu\text{mol}_{\text{ph}} \text{m}^{-2} \text{s}^{-1}$  was optimal (Pyo Kim *et al.*, 2006). The requirement of residual PS II activity during the anaerobic  $\text{H}_2$  production phase and its sensitivity to high irradiance explains the negative impact exerted by too much light (Antal *et al.*, 2003). The synergistic and detrimental effects of high light irradiance in combination with other stressors, alongside its direct correlation with biomass productivity make light a complex critical process parameter (CPP).

### **Illumination in closed culture systems**

Closed-system photobioreactors (PBRs) typically have higher capital expenditure costs than open cultivation systems. As such, they are not typically employed for commercial production of nutraceuticals except in heterotrophic fermentations for specialty  $\omega$ -3 oil production (Winwood, 2013). However, closed PBRs provide a more controllable environment in which batch to batch variability and risk of batch failure are lower compared to open systems (Richardson *et al.*, 2014). Due to the considerable innovation and engineering effort required to develop these systems, companies do not advertise their manufacturing set-up very often. However, a potential indicator of the recent increase in interest in these systems is the number of patents that mention them. A Google Patents® search for patents containing the terms “closed photobioreactor” found 3,054 results as of 02/02/2016. The same search, filtering results for patent priority date before 02/02/2010 found 1,603 results and only 149 results were found when filtering with a priority date of 02/02/2000. The exhaustive literature review performed in this work did not find any published experimental studies of large scale microalgae cultivation with artificial illumination. From a theoretical perspective, a published techno-economic analysis found the use of artificial illumination at commercial scale increases the costs by  $25.3 \$ \text{kgDCW}^{-1}$  (Blanken *et al.*, 2013) and recommends to avoid artificial illumination except when producing exceptionally lucrative goods. A life cycle assessment comparing sunlight and artificially illuminated production of astaxanthin in *H. pluvialis* found that the increased productivity achieved with artificial illumination of flat panel bioreactors resulted in the bioprocess setup with the lowest environmental impact across all categories evaluated (Pérez-López *et al.*,

2014). The lack of published materials in this topic does not invalidate the potential benefits and rewards to be reaped from optimising illumination strategy in microalgal cultivation as demonstrated by the flourishing of commercially successful vertical farming applications in the horticulture industry (Kalantari *et al.*, 2017; Al-Kodmany, 2018).

### **Illumination customisation approaches**

The US food and drug administration's (FDA) principles of quality by design (QbD) describe the criticality of product attributes and process parameters as a continuum rather than a binary state (FDA, 2011). These principles have been globalised by the international council for harmonisation's Q8/Q9/Q10 directives (ICH, 2006, 2009b, 2009a) and are currently required for the successful development of any biopharmaceutical manufacturing process. The ICH Q8 directive defines critical quality attributes (CQAs) as "a physical, chemical, biological, or microbiological property or characteristic that should be within an appropriate limit, range or distribution to ensure the desired product quality" and critical process parameters (CPPs) as "a process parameter whose variability has an impact on a critical quality attribute and therefore should be monitored or controlled to ensure the process produces the desired quality".

This language is commonly used in the biopharmaceutical development space, but it can be applied to any bioprocessing project. Thus, the process parameters of a microalgal culture can be appraised too. The intrinsic connection between CQAs and CPPs means their number and criticality will be unique to each bioprocess. However, most if not all process parameters can be evaluated for their impact on CQAs of any product. The impact of certain parameters on product quality attributes has previously studied in a systematic manner. For example, the heat tolerance of photosynthesis at elevated temperatures (35-45°C) was studied in a *C. reinhardtii* mutant with impaired plastidic fatty acid desaturation properties (Sato *et al.*, 1996). This study found that PSII in thylakoid membranes with a higher proportion of desaturated lipids had a higher heat tolerance than the wild type (Sato *et al.*, 1996). The effect of temperature on lipid profile for biofuel production was studied in *C. reinhardtii* at temperatures ranging from 17-38°C. and 32°C was found to produce the best lipid profile (James *et al.*, 2013). The

effects of temperature fluctuation are of great importance in outdoor cultures. A review focusing on the effects of global warming across different potential microalgal cultivation sites was written by Ras and colleagues (2013). The effects of pH on hydrogen photoproduction were studied in sulphur deprived *C. reinhardtii* cultures between pH 6.5 – 8.2. The optimum pH for H<sub>2</sub> evolution was 7.3-7.9 and it coincided with the optimal pH for residual activity of PSII, essential for H<sub>2</sub> production. A wide range of pH values, from pH 5 – 10, was tested for growth and lipid accumulation in the marine microalgae *Nannochloropsis salina* and pH 8 and 9 were both found to be equally good (Bartley *et al.*, 2014). On the other hand the fresh water species *Chlorella sorokiniana* was found to have the highest growth rate and lipid profile for biofuel production at pH 6 (Qiu *et al.*, 2017).

This thesis argues that light should be considered as a CPP of all microalgal manufacturing bioprocesses operated in autotrophic or mixotrophic mode. Its essentiality to drive photosynthetic reactions and enable inorganic carbon fixation makes it all important. Additionally, it is a very complex parameter as it is multifaceted with many important aspects to be taken into account. Photon flux density also called light intensity is one of the most commonly studied attributes of light with respect to microalgal cultivation. Light dark cycles have been studied in terms of diel cycle, which is the portion of time over a 24 hour period that the culture is illuminated or left in the darkness, and in terms of flashing light, when light dark cycles are continuous at a high frequency. Finally, light spectrum customisation is achieved with light filters or artificial light sources like LEDs and serves to control the wavelength of photons reaching the culture. The following subsection summarises studies found in the literature for each of these attributes with a specific focus on light spectrum customisation.

Photon flux density (PFD) commonly referred to as light intensity has a big influence on the light distribution within a photobioreactor. Light intensities reported in literature span a wide range from low light conditions at 50  $\mu\text{mol}_{\text{ph}} \text{m}^{-2} \text{s}^{-1}$  (Wagner, Steinweg and Posten, 2016) to high light conditions of up to 2500  $\mu\text{mol}_{\text{ph}} \text{m}^{-2} \text{s}^{-1}$  (S. K. Wang *et al.*, 2014). Generally as light intensity increases so will microalgal growth rate up to a saturation point, after which further increases in intensity will have no effect on growth rate (Carvalho *et al.*, 2011). Conversely, extremely high light intensities can be

detrimental to growth due to photodamage of the chloroplast ETC and chloroplast ETC over-reduction, although the deleterious effects of high light are mitigated in mixotrophic conditions (Fischer, Wiesendanger and Eggen, 2006). Increasing light intensity has been found to shorten the duration of the cell cycle of *C. reinhardtii* from 73 to 10h and the average number of daughter cells per mother cell increased from 2 to 14 (Bonente *et al.*, 2012).

Diurnal cycles have profound evolutionary links with microalgal metabolism due to natural sunlight day/night cycles. A transcriptomic study of *C. reinhardtii* with samples taken every 3 hours of a 12/12 light/dark cycle revealed close correlation of at least 80% of measured transcripts from all parts of cellular metabolism with the light dark period (Zones *et al.*, 2015). The differences between light/dark cycle and constant illumination strategies have not been systematically studied in *C. reinhardtii* from a bioprocessing perspective. A study on *Neochloris abundans* concluded that the cell cycle synchronisation provided by cultivation in a constant length light/dark cycle was beneficial to biomass accumulation (de Winter *et al.*, 2017) although a higher amount of starch per gDCW was found in continuously illuminated cultures probably due to the lack of dark phase oxidative respiration. Different lengths of light/dark cycle durations were investigated in *Tetradismus obliquus*. Cell division was again synchronised by the light/dark cycle however it was not affected by the length of the light phase as cell division was found to start ~14 hours after the start of the day regardless of the length of the day. (León-Saiki *et al.*, 2018)

### **Narrow wavelength illumination**

The effects of spectral composition on microalgal physiology have been reported for a variety of species. An obvious candidate for this area of research is *H. pluvialis* due to its overproduction of astaxanthin under stress (Fábregas *et al.*, 2003). This red microalga was cultivated in a two-stage continuous light regime with red LEDs employed during the growth phase and a switch to blue LEDs used to induce astaxanthin production once the required biomass concentration was reached (Lababpour *et al.*, 2004). In 55 mL cultures, at an incident light intensity of  $3.8\text{-}12\ \mu\text{mol}_{\text{ph}}\ \text{m}^{-2}\ \text{s}^{-1}$  this two-

stage illumination strategy demonstrated the potential of light quality control during a bioprocess to easily have a major impact on culture productivity.

Another natural candidate for spectral composition experiments is *Dunaliella salina* which similarly to *H. pluvialis* can overproduce a valuable antioxidant,  $\beta$ -carotene, when placed under stressful culture conditions (Borowitzka and Borowitzka, 1990). *D. salina* cultures grown in nutrient replete media and illuminated with high intensity red light ( $1000 \mu\text{mol}_{\text{ph}} \text{m}^{-2} \text{s}^{-1}$ ) grow at the same rate as white and blue light illuminated cultures and yield a higher  $\beta$ -carotene content (Xu and Harvey, 2019a). *D. salina* naturally produces two stereoisomers of  $\beta$ -carotene, an *all-trans* form, and a *9-cis* form with much higher antioxidant activity making it more valuable for pharmaceutical applications. The *9-cis:all-trans*  $\beta$ -carotene ratio has been found to be 5 times higher after 48 hours in red light illuminated cultures compared to blue light illuminated cultures (Xu and Harvey, 2019b). The influence of red light on  $\beta$ -carotene production and isomerisation is hypothesised to be effected by red light controlled phytochrome regulation of phytoene synthase and  $\beta$ -carotene isomerases (Xu and Harvey, 2019b).

Rather than focusing on a single light wavelength, some spectral composition studies have explored the effects of light combinations on microalgal physiology. Baer (2016) and colleagues mixed red, green and blue LED lights in different proportions, at a constant photo flux of  $100 \mu\text{mol}_{\text{ph}} \text{m}^{-2} \text{s}^{-1}$  to explore 15 unique spectral compositions and their effects on the biomass productivity of *C. reinhardtii*. Additionally, phycobiliprotein production in *Galdieria sulphuraria* and *Porphyridium purpureum* was also recorded. As expected from such an array of species, the optimum light blends for biomass productivity were different for each of them. The optimum red:green:blue (R:G:B) light ratio for *C. reinhardtii* was reported to be 80:10:10 and the biomass productivity rate under this spectral composition was 176% better than a 20:40:40 control. Interestingly the optimal R:G:B light ratio for biomass productivity matched the optimal R:G:B light ratio for phycobilin production in *P. purpureum* but not in *G. sulphuraria* (Baer *et al.*, 2016). Matching the optimum conditions for biomass production with those of the product of interest is a great step towards maximising bioprocess yield.

Red and blue light blends were compared to white, red, blue and green LED illumination conditions in a study that calculated photo conversion efficiency (PCE) in *C. reinhardtii* phototrophic cultures illuminated at different photon flux densities (Wagner, Steinweg and Posten, 2016). The authors found the highest PCE was achieved with a 90:10 ratio of red light photons to blue light photons at the lowest photon flux density used in the study  $25 \mu\text{mol}_{\text{ph}} \text{m}^{-2} \text{s}^{-1}$ . Additionally, the authors found  $150 \mu\text{mol}_{\text{ph}} \text{m}^{-2} \text{s}^{-1}$  to be saturating for the photosynthetic apparatus of the microalgae, causing PCE values to be very similar between the different illumination conditions tested (Wagner, Steinweg and Posten, 2016). Although the study found significant differences in cell size and pigment composition between the different illumination conditions, the same calorific value was attributed to all conditions for the calculation of PCE. The results might therefore not reflect the true energetic value of the biomass under different light conditions given the plasticity of macromolecular biomass groups in microalgae.

An alternative approach for correlating biomass productivity to biomass specific light absorption in *C. reinhardtii* cultures was taken by de Mooij (2016) and colleagues. Their continuous culture turbidostat approach tested different monochromatic lights at a fixed light intensity of  $1500 \mu\text{mol}_{\text{ph}} \text{m}^{-2} \text{s}^{-1}$ , where the dilution rate was a function of light intensity transmitted through the culture. By maintaining the biomass concentration in the reactor high enough that the transmitted light intensity remained constant at  $10 \mu\text{mol}_{\text{ph}} \text{m}^{-2} \text{s}^{-1}$ , they ensured the rate of photosynthesis was maintained higher than the rate of respiration in the cell culture. This is known as the photosynthetic compensation point and ensures maximal photosynthetic productivity can be achieved (Takache *et al.*, 2010). Their results show that yellow light had the lowest biomass specific light absorption rate, hence the lowest amount of light energy dissipation as heat, and it resulted in the highest biomass productivity (Mooij *et al.*, 2016). White light showed very similar absorption efficiency and biomass productivity as yellow light. Meanwhile, red and blue monochromatic lights resulted in the lowest biomass productivity figures. This was attributed to their high biomass specific light absorption rate leading to oversaturation of the photosystems and a waste of absorbed light energy dissipated as heat (Mooij *et al.*, 2016). Interestingly, the dilution rate for blue light was the highest even though biomass concentration remained low, indicating a very low PCE

under those illumination conditions. The authors hypothesise that different colours of light can be effectively used to control the degree of over-saturation in a microalgal culture, preventing extensive photodamage and maximising biomass productivity.

### **2.3. Metabolic modelling**

A cell culture process is comprised of at least two interacting systems: the cell population and the medium it is growing in which is effectively the surrounding environment. These two systems interact with each other making cell culture processes very complicated. The cell population is composed of a heterogeneous mixture of cells at different stages of the cell cycle. Within each individual cell, homogeneity is not guaranteed as metabolites will have particular localisations. In microalgae, the chloroplast is a large, membrane rich organelle which is typically localized at one pole of the cell as found in *C. reinhardtii*; making one pole of the cell rich in membrane lipids whilst the other pole may house the nucleus and its dense mixture of nucleic acids. Catabolic and anabolic processes consume substrates and produce secondary metabolites and heat respectively. Thus, over time, the cells affect the extracellular environment and medium composition. Substrate consumption may affect an acid-base equilibrium in the medium which in turn has an effect on medium pH and consequently cell growth kinetics. An example of this is when ammonium is used as the nitrate source in microalgal media. Ammonium uptake results in a decrease in pH in non-adequately buffered media (Scherholz and Curtis, 2013). Many biochemical interactions occur inside any given cell at any moment in time. These are coupled to regulation and control mechanisms, increasing the complexity of the intracellular environment even further. These mechanisms allow cellular adaptation to change in the environment further increasing the heterogeneity of the system.

The cellular environment is not simple either. It may be comprised of several phases, has a changing chemical composition over time and its temperature, pH and rheological properties are subject to change too. The medium can consist of two immiscible liquid phases or, more typically, a liquid phase with gas bubbles running through it. The medium's composition varying over time can also be due to reactions between accumulated products and other media components. Viscosity also plays an

important role in high cell density cultures where gas mass transfer may be negatively impacted as the culture progresses. Due to reactor geometry and mixing, local environments may exist within the reactor. These local environments will impact cell growth kinetics differently than the bulk of the medium. As PBR design is not standardised and all closed systems have a degree of customisation, particular growth regimes may not be reliable across designs.

Complicating things further, microalgal cell culture processes have an additional factor to take into account that is not required for heterotrophic cultures: light. Under nutrient saturation conditions, light can become a limiting factor for microalgal productivity (Kirk, 1994). Light intensity is quantitatively described as photon flux density (PFD), measured in  $\mu_{mol}$  of photons.  $m^{-2}. s^{-1}$ . It can negatively impact productivity at both extremes of the intensity range. An early description of the relationship between light irradiance and specific growth rate  $\mu_i$  by Goldman (1979) concluded that PFDs below the compensation light irradiance point ( $I_k / I_c$  depending on publication) are not sufficient for  $CO_2$  fixation and cell maintenance, thus stunting growth. At the other end of the spectrum, when irradiance is very high, photo-inhibition can cause overproduction of  $O_2$  free radicals and cellular damage (Belay and Fogg, 1978).

As mentioned above, local environments with sub-optimal conditions may form within the PBR and light is no exception. Even with relatively short path lengths, self-shading becomes an issue in PBRs as the cells closer to the surface absorb most of the incident light thus creating an inwards light gradient that finishes with a virtually dark zone at the end of the light path. This light gradient and its effect on photosynthetic efficiency (PE) must be accurately described in the model with appropriate mathematical expressions to ensure model accuracy.

The previous paragraphs aim to illustrate the complexity of cell culture processes and the interactions between their different systems and factors. Given their complexity, it is not trivial to attempt to describe them mathematically in full detail. Therefore, assumptions and controlled parameters are used to simplify them into more tractable mathematical problems.



Models describing cellular processes were classified by Fredrickson et al. (1970) as having structure or lack thereof, and being segregated or unsegregated, thus creating four sub-categories. Structure can describe both the physical and biochemical properties of the system being modelled. The cell can be physically structured by compartmentalisation of processes for example localizing particular reactions to their respective organelles. Biochemical structure is understood as the description of the cell contents as varied biochemical species that react with each other to form other species. Segregated models account for the heterogeneity encountered in cell populations (Bertuccio *et al.*, 2015). On the other hand, unsegregated models treat all cells as equals thus veering towards the “average cell” definition model (Schuetz, Kuepfer and Sauer, 2007).

Such biological models can also be discretised into stochastic or deterministic models and static or dynamic models. A model is considered stochastic when its inputs take into account the inherent variability of the modelled system through a probabilistic distribution. On the other hand, deterministic models rely on experimentally verified cause and effect relationships and therefore tend to be limited towards the most probable outcomes. Static models employ algebraic equations to describe cellular processes as they are at a particular instance in time whilst dynamic models are formed by a series of differential algebraic equations that can be resolved over time. Overall, dynamic models can account for the kinetics of a biological system over time but are more computationally demanding than static models.

The various mathematical approaches developed to model cell culture processes are briefly reviewed in Table 1 of Bordbar *et al.*, (2014). Constraint based modelling is the main focus of the remainder of this chapter as it was employed to characterise the impact of different illumination and trophic strategies on the metabolic phenotype of *C. reinhardtii*.

### **2.3.1. Constraint based modelling – Flux balance analysis**

The type of metabolic modelling performed in this thesis is flux balance analysis (FBA), a constraint based modelling approach used for large genome-scale metabolic network models (GeMs) (Orth, Thiele and Palsson, 2010). The advent of next generation

sequencing has propelled genome annotation efforts (Reijnders *et al.*, 2014). These sequences can be used to build constraint-based models, known as GEMs, describing all metabolic reactions known in an organism. Generating GEMs was once a laborious and painstakingly long process, highly dependent on manual curation, however, automation platforms are now widely available to improve and streamline model development (Agren *et al.*, 2013; Hamilton and Reed, 2014). In 2010 there were metabolic models available for 35 different organisms and that number has grown even bigger in recent years with several microalgal species models included (Baroukh *et al.*, 2015; Broddrick, 2016).

Flux balance analysis is centred around metabolic stoichiometry and mass balance. A stoichiometric matrix (Figure 2.8) is used in FBA to constraint the maximum and minimum number of metabolites that can flow through the metabolic network. Additionally, the amount of metabolic flux allowed to flow through the reactions described in the metabolic network can be constrained with upper and lower bounds. The combination of these two types of constraints defines the rate at which metabolites are produced and consumed within the network (McCloskey, Palsson and Feist, 2013). The final component of FBA is the objective function, an optimisation objective subject to the previously mentioned mass balance and flux constraints that can be maximised or minimised to find the optimum fluxes of all reactions in the network.

		Reactions				
		1	2	3	...	$n$
Metabolites	A	1	1	0		
	B	0	-1	0		
	C	1	1	0		
	...					
	$m$					

**Figure 2.8** The stoichiometric matrix,  $\mathbf{S}$ . The matrix is made up of  $m$  metabolites and  $n$  reactions. Each matrix element ( $s_{ij}$ ) in  $\mathbf{S}$  is therefore a stoichiometric coefficient of the  $i^{th}$  metabolite in the  $j^{th}$  reaction. 1, reaction product; 0, metabolite does not participate in this reaction; -1, reaction substrate.

Flux balance analysis is performed under the quasi-steady state assumption as follows:

$$\frac{dX_i}{dt} = \sum_{j=1}^n S_{i,j} v_j, \text{ for } i = 1, \dots, m \quad (\text{Eq. 2.3})$$

Where  $dX_i/dt$  is the  $m \cdot i$  column vector of time derivatives of all intracellular metabolites,  $S_{i,j}$  is the stoichiometric coefficient for the  $i$ th metabolite and  $j$ th reaction and  $v_j$  is the reaction rate of the  $j$ th reaction. In simplified terms:

$$\frac{dX}{dt} = \mathbf{S} \cdot \mathbf{v} \quad (\text{Eq. 2.4})$$

Where  $dX/dt$  is the change of all metabolites over time,  $\mathbf{S}$  is the stoichiometric matrix and  $\mathbf{v}$  the reaction flux vector. As mentioned above, FBA is performed under the quasi-steady state assumption, whereby the timescale of  $dX/dt$  becomes negligible in comparison to the rate of reaction term  $\mathbf{S}\mathbf{v}$  (Orth, Thiele and Palsson, 2010) as follows:

$$\mathbf{S} \cdot \mathbf{v} = 0 \quad (\text{Eq. 2.5})$$

Biological systems tend to have more reactions than metabolites, this makes FBA problems underdetermined and results in them having multiple solution instead of a unique solution (Kiparissides and Hatzimanikatis, 2017). Three main types of constraints can be added into a GeM to reduce the number of possible solutions (a) physio-chemical constraints, (ii) spatial or topological constraints, (c) environmental constraints for a particular experimental condition (d) regulatory constraints (Price, Reed and Palsson, 2004).

Linear programming (LP) is typically used when solving an FBA problem (Lewis *et al.*, 2010) to obtain solution to an optimisation problem where the objective is formulated as a set of weights for each reaction in the model ascribed to be maximised or minimised:

$$Z = c \cdot v \quad (\text{Eq. 2.6})$$

Where Z is the optimisation objective; c represents a weighted vector of coefficients for all the fluxes described by Z and v a vector of the corresponding fluxes.

In FBA, it is assumed that cells gear their metabolism towards a singular, overarching metabolic objective such as maximisation of biomass or ATP (Price, Reed and Palsson, 2004). This can be formulated as a linear programming (LP) optimisation problem:

$$\min/\max (Z) \quad (\text{Eq 2.7})$$

$$s.t. \quad S \cdot v = 0 \quad (\text{Eq 2.8})$$

$$v^{ub} \geq v \geq v^{lb} \quad (\text{Eq 2.9})$$

Where Z corresponds to the flux or fluxes through the reaction or reactions that conform the optimisation objective subject to mass balance (Eq. 2.8) and inequality (Eq. 2.9) constraints. The set of inequality constraints described in Equation 2.9 determines the minimum or lower bound ( $v^{lb}$ ) and the maximum or upper bound ( $v^{ub}$ ) of flux permissible through each reaction.

During growth in nutrient replete conditions and in the absence of any extrinsic stress factors, cell proliferation is a universal evolutionary pressure shared by all living organisms. As such, the biomass equation is a commonly used objective function in FBA simulations (Senger, 2010; Chapman *et al.*, 2015). An overview of the steps described above can be found in Figure 2.9.

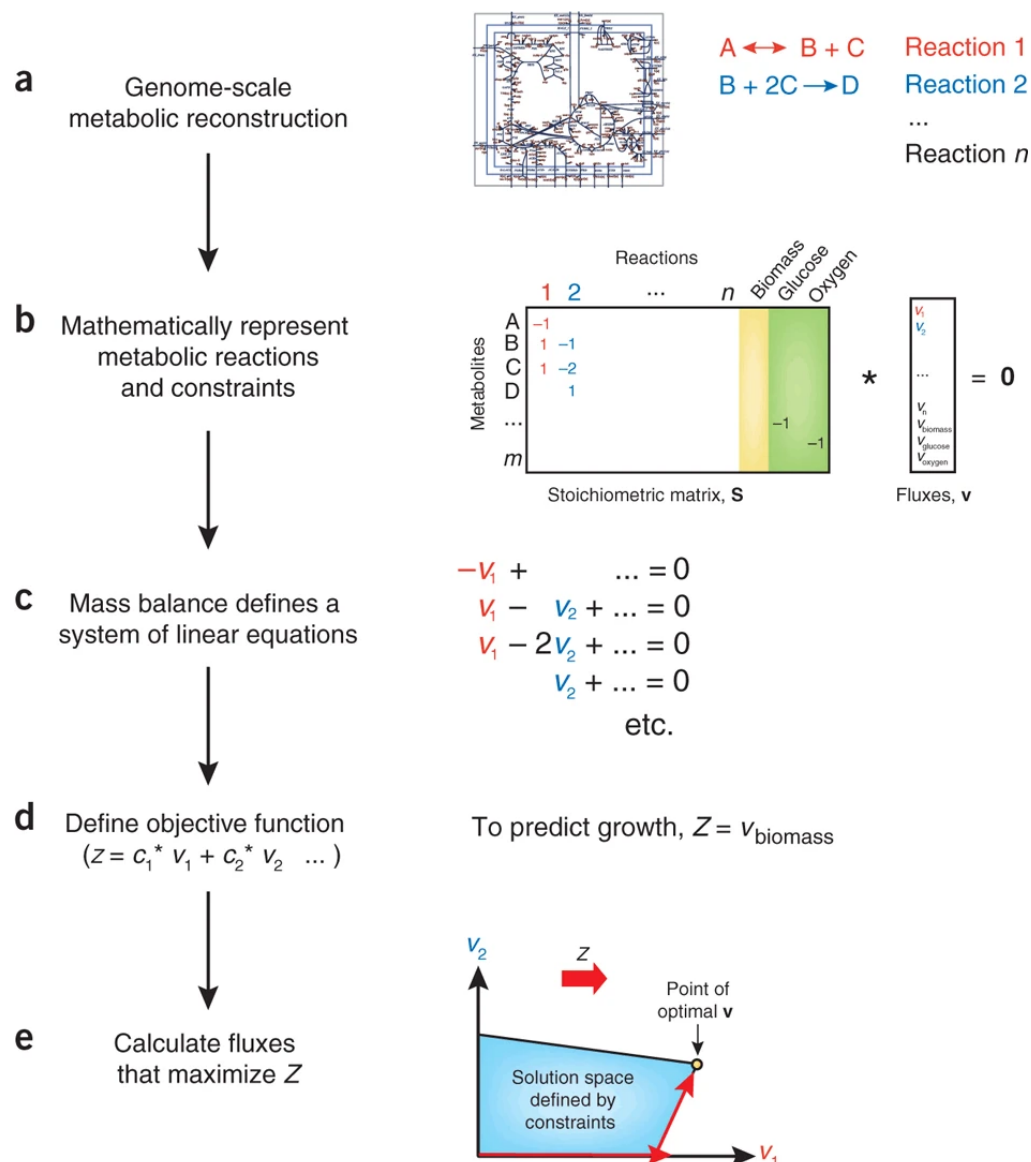


**Figure 2.9** Full summary of the flux balance analysis methodology. (a) Reconstruction of an annotated genome sequence into a metabolic network; (b) The stoichiometric matrix formed by  $n$  reactions and  $m$  metabolites ( $m \times n$ ); (c) Definition of the quasi-steady state assumption; (d) Definition of the objective function, made up of weighted contribution,  $c$ , of chosen reaction fluxes,  $v$ ; (e) Solving the defined linear problem to maximise the objective function  $Z$ . Taken from Orth, Thiele and Palsson, (2010).

### 2.3.2. Microalgae FBA

#### GeM light input

Flux balance analysis (FBA) is an established modelling technique used to simulate the intracellular flux distribution of cells growing in steady or semi-steady state with a genome scale metabolic model (GEM) (Orth, Thiele and Palsson, 2010). Modelling phototrophic metabolism with FBA has been limited by the difficulty of accurately describing the amount of light absorbed by the modelled organism (Baroukh *et al.*, 2015). A non-mechanistic approach to constrain the light reactions of a phototrophic GEM is typically applied by explicitly defining the bounds for the growth rate and CO<sub>2</sub> uptake rate reactions alongside any other reactions for which experimentally determined uptake and secretion rates are available. Once the multi-dimensional solution space has been constrained in this manner, the objective function of the optimisation problem is postulated as a minimisation of the flux through the light reaction (Shastri and Morgan, 2005; Hendry *et al.*, 2016). The underlying assumption of this approach is that only the required light energy to produce enough ATP to fuel the measured rate of carbon fixation is metabolised by the microalgal cell. However, this results in the flux of photon utilising reactions to be linearly dependent on the stoichiometry of ATP maintenance defined in the GEM.

The stoichiometry of ATP maintenance in a GEM is the sum of the ATP demanded by growth associated and non-growth associated processes. Non-growth associated ATP maintenance encompasses all biomass substrate polymerisation processes as well as formation of nucleic acids. Non-growth associated ATP maintenance.

A mechanistic approach was used to develop the light absorption reactions in iRC1080 - the *C. reinhardtii* GEM employed in this chapter (Chang *et al.*, 2011). The aim of the authors was to accurately differentiate the stoichiometry of light photons absorbed according to the spectral distribution of the light source modelled. This is achieved by first defining the effective spectral bandwidth of each photon utilising reaction in the model. Specific metabolites are assigned to each bandwidth, grouping certain portions of the photosynthesis active radiation (PAR) range. Each light source is then assigned its unique reaction, termed "PRISM\_light\_source\_x". The stoichiometry

of these reactions is defined by the ratio of photon flux at the determined wavelength range and the total photon flux emitted by the light source (Chang *et al.*, 2011). Two additional conversion factors are included to account for dimensions and optical properties of the cell.

Attempts to achieve greater fidelity with respect to photo-metabolism have taken the mechanistic approach utilised by Chang *et al.* (2011) a step further by taking into account the chlorophyll-normalised optical absorption cross-section (Broddrick *et al.*, 2019). Doing so enables the clear definition of effective absorption and voids the need to include the conversion factors mentioned above. This approach has also been used for purely kinetic simulations in *Chlamydomonas reinhardtii* and *Chlorella sorokiniana* models (Blanken *et al.*, 2016). The GEM study by Broddrick *et al.* (2019) also included a stoichiometric description of photodamage and the metabolic costs to repair the D1 subunit of photosystem II. Additionally, it incorporated the unique energy transfer efficiencies of each photosynthetic pigment. This approach could be applied to GEMs of other photosynthetic organisms provided the physiological information for the experimental conditions studied is available in the literature or can be obtained experimentally (Tibocha-Bonilla *et al.*, 2018).

### **Application of FBA with microalgae GeMs**

The first microalgal genome scale metabolic reconstruction ever completed was a central carbon metabolism model of *Chlamydomonas reinhardtii*. The metabolic network is comprised of 484 metabolic reactions and 458 intracellular metabolites (Boyle and Morgan, 2009). The biomass equation was derived from experimental data included in the publication. The authors simulated growth under nutrient replete conditions in all three possible trophic modes (a) autotrophic, (b) mixotrophic and (c) heterotrophic. The authors observed that carbon efficiency is higher in autotrophic and mixotrophic conditions than in heterotrophic conditions. Although its biomass equation only contains macromolecules and its lipid metabolism is not as detailed as models published after it, it is a useful reconstruction, with several intracellular compartments simulating organelles, which can be used to simulate several growth conditions.



The biomass reaction of microalgal GeMs has been used as an objective function in several FBA studies. The effects of light absorption and CO<sub>2</sub> uptake rate on oleic acid production in *Chlorella protothecoides* were explored with a combined FBA and <sup>13</sup>C metabolic flux study comparing photoautotrophic and heterotrophic growth conditions (Wu *et al.*, 2015). Both techniques highlighted the low activity of the tricarboxylic acid (TCA) cycle in phototrophic conditions and its high activity in heterotrophic conditions contributing to a better understanding of oleaginous algae metabolism. Chapman and colleagues studied the effects of acetate on photosynthesis, their predictions matched experimental observations of photosynthetic downregulation and increased flux through cyclic electron flow reactions during mixotrophic growth (Chapman *et al.*, 2015, 2017). Evaluation of metabolic configurations in microalgae is a common application of FBA GeM and has been further reviewed by Baroukh *et al.* (2015) and Tibocha-Bonilla *et al.* (2018).

The inability of FBA to capture the variations in flux over time during light/dark cycles has prompted researchers wanting to study such scenarios to employ dynamic flux balance analysis (dFBA). This implementation of FBA combines traditional constraint-based modelling with some form of kinetic modelling. Flassig and colleagues combined kinetic equations describing average biomass specific light intensity, the lower bound of nitrate uptake as well as several pigment accumulation dynamics; with a modified version of the *C. reinhardtii* GeM iRC1080 to predict β-carotene accumulation (Flassig *et al.*, 2016). Their validated model was then used to predict optimum light intensity and nitrogen feeding rate for a fed-batch culture. The optimal conditions predicted by the model were validated in a an experiment that yielded 2.1 times higher β-carotene per gDCW the standard fed-batch conditions (Flassig *et al.*, 2016). This study demonstrates the great potential for metabolic modelling to be employed in the optimisation of illumination and trophic strategies for microalgal cultivation.

## CHAPTER 3

---

### *The effects of illumination and trophic strategy on cell physiology and biochemical composition in *Chlamydomonas reinhardtii**

#### 3.1. Introduction

Microalgae are found in highly diverse habitats ranging from hypersaline water reserves like the Dead Sea (Oren, 2014) to fresh water (Celewicz-Gołdyn and Kuczyńska-Kippen, 2017) and soil (Sack *et al.*, 1994; Pushkareva, Johansen and Elster, 2016). Each habitat presents its own seasonal and even daily variations in environmental conditions. In order to maintain their competitive advantage under uncontrollable environmental changes, microalgae have evolved great metabolic plasticity. The ability to grow and reproduce following diverse trophic strategies is key for survival of microalgal species. *Chlamydomonas reinhardtii* can grow phototrophically by producing the ATP and reducing equivalents required to fix carbon dioxide into bioavailable organic carbon skeletons via the Calvin-Benson cycle; it can also grow mixotrophically whereby the reliance on photosynthetically fixed carbon diminishes as an organic carbon source is readily available; and it can also grow heterotrophically in the absence of light provided a suitable organic carbon source is available (Harris, 2009).

*Chlamydomonas reinhardtii* growth under different trophic strategies relies on alternative sets of metabolic pathways (Johnson and Alric, 2012, 2013). It follows that physiological differences can be expected to affect culture productivity. For example, recombinant production of the sesquiterpene bisabolene, a biotechnologically relevant biodiesel precursor, in *C. reinhardtii* was found to be 2.8 times higher in mixotrophic conditions compared to phototrophic conditions (Wichmann, Baier, Wentnagel, Kyle J Lauersen, *et al.*, 2018). Although mixotrophic conditions are often associated with higher productivity, this can be due to autotrophic cultures having poor light conditions

leading to early photo-limitation; and the lack of pH control in most flask-based autotrophic microalgae experiments published in literature, coupled with better buffering of commonly employed mixotrophic media like tris-acetate phosphate medium (TAP) compared to minimal media (Scherholz and Curtis, 2013).

Light is a critical process parameter in both phototrophic and mixotrophic growth conditions. This chapter focuses on evaluating the effects of lights with different narrow-wavelength distributions on the physiology of *C. reinhardtii*. The productivity of this microalgae under several colours of high intensity narrow wavelength LED illumination has been examined in phototrophic conditions with continuous cultures under yellow light resulting in the highest biomass productivity, although it required supplementation with minimal amount of blue photons (Mooij *et al.*, 2016). Such supplementation of yellow light with blue light brings the resulting wavelength distribution closer to that of white LED light and hints at the importance of blue LED light regulation in key cellular processes.

*Chlamydomonas reinhardtii*'s vegetative cell cycle produces a variable number of daughter cells as explained in detail in Chapter 2 (Donnan and John, 1983). This flexibility means multiple fission can be affected by environmental conditions such as wavelength distribution of the incident light source. Cultivation studies using halogen lamps and narrow band glass filters to irradiate *C. reinhardtii* cells with only red or blue photons showed that, under blue light, cells reached a larger size before starting to divide compared to red light (Oldenhof, Zachleder and Van Den Ende, 2006). Interestingly, shifting from blue to red illumination once cells had attained a larger size than would be possible under red light precipitated cell division, suggesting direct regulation of cell division by blue light (Oldenhof, Zachleder and Van Den Ende, 2006).

The biomass of microalgae can be valorised in different ways ranging from commercialising full biomass products to fractionation and purification to retain only the desired component (Borowitzka, 1999). Modifying the biomass composition of *C. reinhardtii* to maximise the production of a desired product can be achieved by altering macronutrient availability such as reduced nitrogen to increase neutral lipid accumulation (Siaut *et al.*, 2011) and reduced sulphur to induce biohydrogen production

(Ghirardi *et al.*, 2000). In the case of lipid production, acetate availability has been shown to improve lipid productivity (Davey *et al.*, 2014). Given the inferred regulatory effects of narrow band illumination on cellular metabolism as well as the centrality of light quality to microalgal biomass production it can be hypothesised that this CPP can be used to modify the biomass composition of *C. reinhardtii*. However, when it comes to the effects of narrow peak illumination on the biomass composition of *C. reinhardtii* there is a clear gap in the literature. The batch culture experiments described and discussed in this chapter are an initial attempt to define the characterised space of *C. reinhardtii* batch cultivations with respect to the effect of two CPPs, light spectral composition and trophic growth strategy, on typical bioprocessing objectives.

### 3.2. Aim & Objectives

The aim of this chapter is to characterise and compare the effect of narrow band illumination at two extremes of the photosynthetically active radiation (PAR) range on the physiology of *C. reinhardtii* in batch cultures with two different trophic strategies (phototrophic and mixotrophic). This can be broken down into the following scientific objectives:

- Evaluate the effect of wavelength and trophic strategy on *C. reinhardtii* growth and nutrient uptake kinetics periodically for 136 hours
- Evaluate the effect of wavelength and trophic strategy on *C. reinhardtii* cell size in the exponential growth and stationary phases of a batch culture
- Evaluate the effect of wavelength and trophic strategy on *C. reinhardtii* macromolecular composition in terms of total soluble carbohydrates, lipids, proteins and pigments periodically for 136 hours
- Form hypotheses to explain the differences observed in *C. reinhardtii* growth and nutrient uptake kinetics alongside the changes observed in biochemical composition and cell size during a batch culture through the holistic lens of interconnected cellular metabolism

### 3.3. Materials and experimental methods

Batch culture experiments were carried out to characterise the impact of different illumination and trophic strategies on the growth kinetics, biochemical composition and cell size distribution of *C. reinhardtii*. All experiments were carried out in biological duplicates due to resource constraints using an ALGEM Environmental Modelling Lab scale Photobioreactor (Algenuity, Bedfordshire, UK). This flask bioreactor system provides a robustly stable culture environment maximising experimental replicability. Analytical measurements were performed in triplicates to maximise the accuracy of the limited biological replicates available. The following sections describe the materials and experimental methods employed throughout all batch culture experiments reported in this thesis.

#### 3.3.1. Cell culture

*Chlamydomonas reinhardtii* strain 11/32c was obtained from the Culture Collection of Algae and Protozoa (CCAP; Oban, Scotland). All batch culture experiments reported in this thesis were carried out in duplicate in 1L Erlenmeyer flasks with a 500 mL working volume. The flasks were housed inside an ALGEM Environmental Modelling Lab scale Photobioreactor (Algenuity, Bedfordshire, UK) at 25°C. Cultures were grown under continuous illumination at  $400 \mu\text{mol}_{\text{ph}} \text{m}^{-2} \text{s}^{-1}$  for the duration of the experiment. Experimental cultures were maintained at 25°C, continuously aerated at  $3 \text{ mL L}^{-1} \text{min}^{-1}$  with an aquarium pump (Airtek, Germany) and 5% CO<sub>2</sub>-enriched air was supplied on demand to maintain pH at  $7 \pm 0.1$  by automatic opening/closing of a solenoid valve. All experimental cultures were inoculated at a starting concentration of approximately  $1 \times 10^6 \text{ cells mL}^{-1}$ .

Two different media were utilised in the experiments described in this thesis. Phototrophic growth, defined as promoting growth exclusively from the uptake of photons and exogenous inorganic carbon was achieved with modified M8a media (Kliphuis *et al.*, 2010), hereby referred to as M8a. The nitrogen source used was ammonium, diluted to the same concentration found in commonly used TAP media (Sager and Granick, 1953) of 7.48 mM. Mixotrophic growth, defined as growth resulting

from a combination of phototrophic mechanisms and the catabolism of exogenous organic carbon was achieved with M8a enriched with acetic acid and Tris base added to concentrations of 17 mM and 20 mM respectively. The concentrations of these additions were chosen to replicate the commonly used Tris-acetate phosphate (TAP) medium. Mixotrophic growth medium will hereby be referred to as M8a.Ac.

### **Stock maintenance and seed cultures**

Liquid stock cultures in 25 mL T-flasks (Corning®, Merck, Germany) with a 5 mL working volume of M8a were stored in a KWBF illuminated incubator (Binder, Germany). The temperature was maintained at 20°C and illumination ran through a 12 hours on / 12 hours off diel cycle at  $100 \mu\text{mol}_{\text{ph}} \text{m}^{-2} \text{s}^{-1}$ . Liquid stock cultures were diluted with fresh media into sterile T-flasks every 4 to 6 weeks. Seed cultures were inoculated with 3 mL of stock culture in 400 mL of fresh M8a for phototrophic and M8a.Ac for mixotrophic experiments. Incident light intensity for all seed cultures was linearly increased during the first 48h until  $400 \mu\text{mol}_{\text{ph}} \cdot \text{m}^{-2} \cdot \text{s}^{-1}$  and was subsequently kept constant for up to 84h. Identical pH control, temperature and gas flow conditions as described above for experiment cultures were used as well as condition specific wavelength selection. This was done to ensure seed cultures were pre-acclimatised to the experimental conditions with the objective of minimising the lag phase after inoculation.

### **Illumination conditions**

The emission spectra of white, red (640-670nm) and blue (440-480 nm) light, supplied at equivalent photon flux, by the LEDs incorporated in the ALGEM bioreactor system is shown in Figure 3.1. These can be compared directly with Figure 2.5 to understand the overlap between the emission spectra of the LED lights employed in the experiments described in this thesis and the absorption spectra of *C. reinhardtii* cells as reported in literature. The main light absorbing pigments in *C. reinhardtii* are chlorophyll a and b which absorb maximally in the blue region at 372nm and 392nm respectively and in the red region at 642nm and 626nm respectively (Milne *et al.*, 2015).

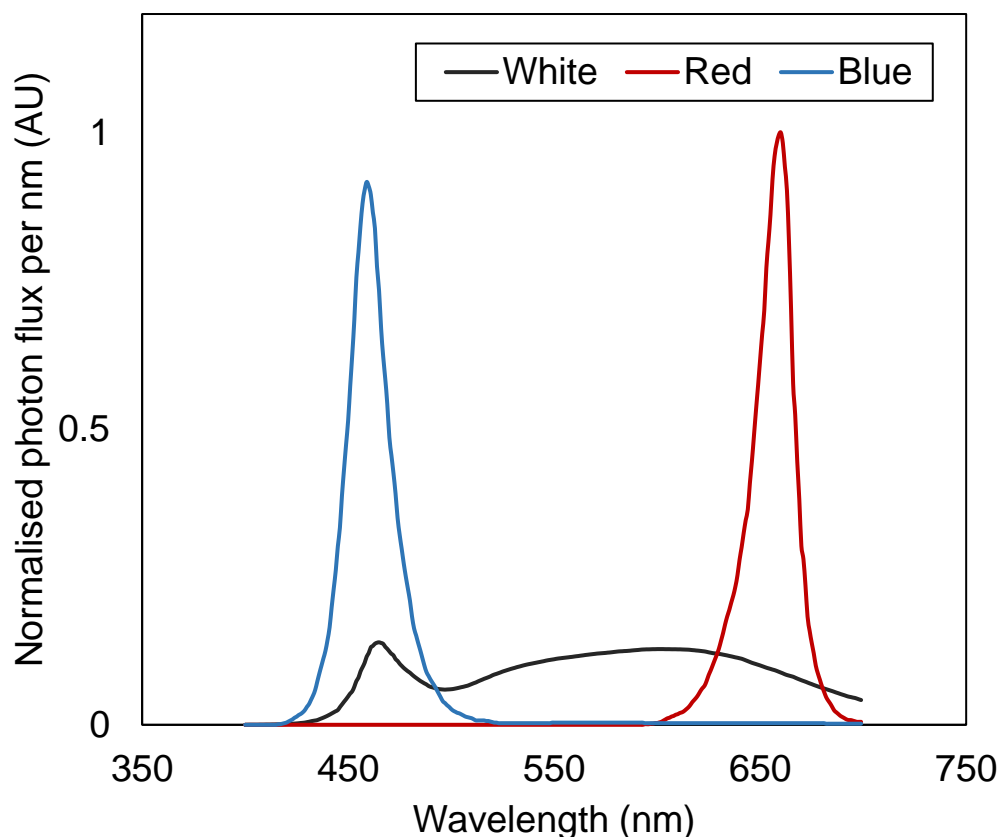


**Figure 3.1.** Normalised spectra of white, red (640-670nm) and blue (440-480 nm) light, supplied at equivalent photon flux, by the LEDs incorporated in the ALGEM bioreactor system.

### 3.3.2. Sampling and analysis

#### Culture productivity

Culture productivity was evaluated through optical density, cell concentration and dry cell weight measurements. Optical density (OD) at 750 nm was measured as the amount of light scattered by cells in suspension in a GENESYS 10S UV/Vis Spectrophotometer (ThermoScientific) blanked with distilled water. The higher the cell concentration, the more light is scattered before reaching the detector. When the OD measured was higher than 0.6, a 1 in 10 dilution was performed and the measurement was re-done to account for the loss of linearity in the relationship between particle

concentration and light attenuation at high concentrations. Cell concentration was manually counted with a Bright-Line haemocytometer (Merck, US) under a light microscope (Carl Zeiss, Germany). Cell samples were diluted in distilled water and Lugol's solution (Sigma-Aldrich) for immobilisation. Dry cell weight was measured by filtering a known volume of culture on a pre-weighed 47mm glass microfiber GF/C filter (Sigma-Aldrich) under a gentle vacuum. Distilled water was filtered over the sample to wash off inorganic salts. The filters were dried for 24h at 70°C and weighed again. Dry cell weight was also measured by centrifuging a known volume of culture in a pre-weighed 2 mL Eppendorf tube. The supernatant was discarded, and the pellet was freeze-dried in a LyoStar 3 (BPS) freeze dryer. Following freeze drying, the tube was re-weighed.

The maximum specific growth rate was calculated between 0 hours of batch culture and 48 hours of batch culture from OD750 measurements as per equation 3.1:

$$\mu_{max} = \frac{\ln (OD750_{48h} - OD750_{0h})}{t_{48h} - t_{0h}} \quad (\text{Eq. 3.1})$$

Where  $\mu_{max}$  is the maximum specific growth rate between 0 and 48 hours of batch culture.

### **Cell weight**

Two approaches were employed to estimate cell weight. Measured cell weight was calculated from the weight difference of a GF/C filter before and after filtering a known volume of culture and drying for 24h in a 70°C oven. The dry cell weight per unit volume of culture measured was processed as per equation 3.2:

$$\text{cell weight} = \frac{\text{dry cell weight per unit volume of culture}}{\text{cell concentration per unit volume of culture}} \quad (\text{Eq. 3.2})$$



The second method was the sum of macromolecular components, this assumes a cell is composed of only the components measured carbohydrates, lipids, pigments and proteins, as well as nucleic acids, values for which were obtained from literature (Chang *et al.*, 2011).

$$\begin{aligned} & \text{(Approach 2)} \\ \text{cell weight} &= \sum \text{Macromolecular components} \end{aligned} \tag{Eq. 3.3}$$

Where macromolecular components is the total carbohydrates, lipids, pigments and proteins measured + DNA/RNA fraction obtained from literature (Chang *et al.*, 2011)

Given the small sample volume available in these experiments and the good correlation of OD750 nm data and dry cell weight measurements (Figure 3.2) from all the experimental conditions explored in this thesis, OD750nm data and cell concentration were employed to convert the time series of macromolecular component picogram per cell data to picogram per picogram of dry cell weight.

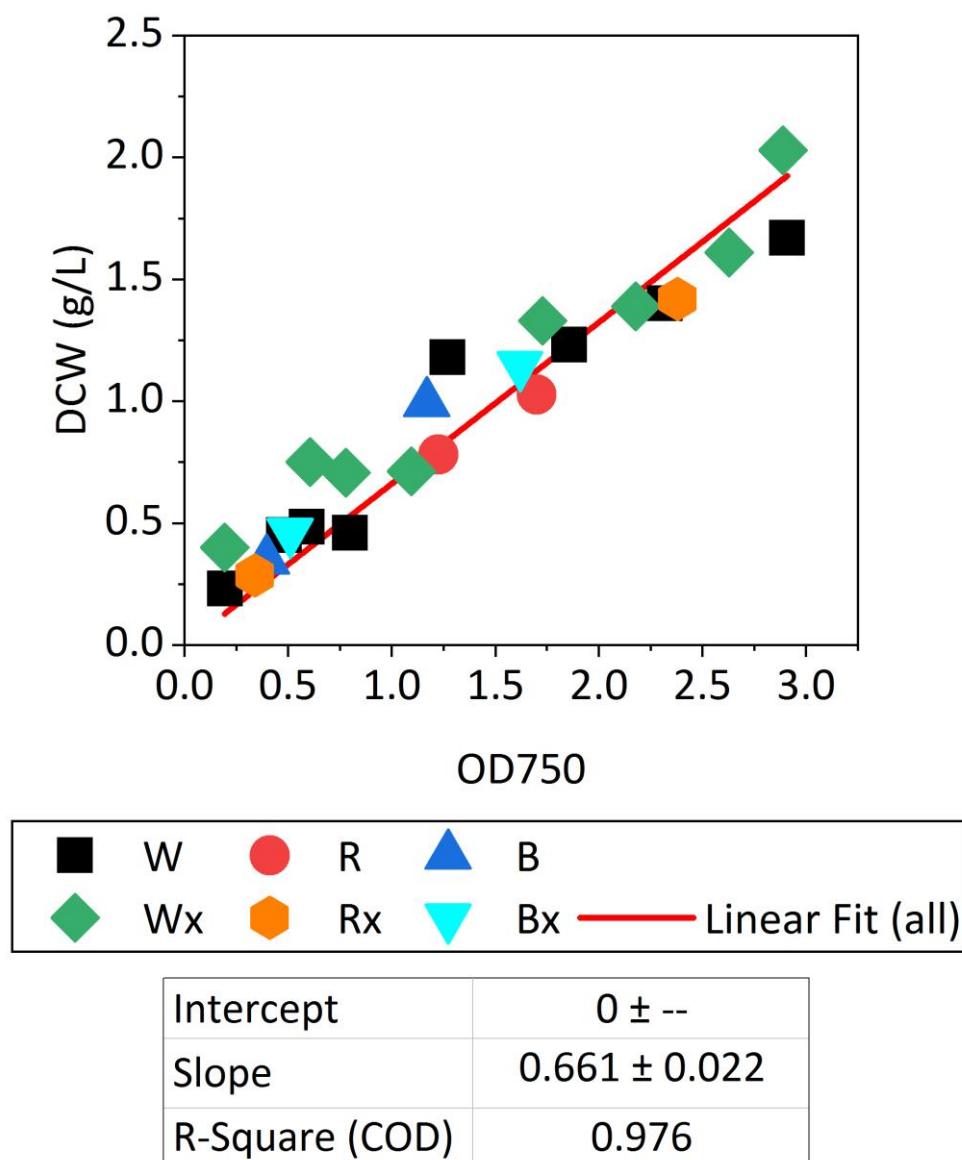


**Figure 3.2.** *C. reinhardtii* OD 750 nm vs dry cell weight (DCW - g/L) measurements across all experimental conditions studied. Each point represents the average of three technical replicates. Error bars of  $\pm 1$  SD are smaller than plotted point.

The slope of the linear fit was used to convert OD 750 nm values to dry cell weight as per equation 3.4:

$$X = 0.661 \cdot OD750 \quad (\text{Eq. 3.4})$$

Where  $X$  is dry cell weight ( $\text{g}\cdot\text{L}^{-1}$ ) and OD750 is the OD750 nm measurement.

### Extracellular nutrient analysis

The concentration of extracellular ammonium and acetate was measured on a customised CubianXC system (Optocell, Germany). 2 mL culture aliquots were centrifuged at 10,000 g for 1 minute and the supernatant was syringe filtered into a 2 mL Eppendorf tube and stored at  $-20^{\circ}\text{C}$  prior to analysis. The chemistry of the spectrophotometric detection of ammonium involves its combination with  $\alpha$ -ketoglutarate and NADPH in the presence of glutamate dehydrogenase (GLDH) to yield glutamate and NADP<sup>+</sup>. This reaction results in a decrease in absorbance at 340 nm for which a calibration is automatically performed by the instrument. The acetate assay chemistry is proprietary (Optocell, Germany).

The observed biomass yield on ammonium was calculated using equation 3.5:

$$Y_{X/S} = \frac{X_{136h} - X_{0h}}{S_{136h} - S_{0h}} \quad (\text{Eq. 3.5})$$

Where  $Y_{X/S}$  is the observed biomass yield on substrate ( $\text{gDCW}\cdot\text{g}_{\text{substrate}}^{-1}$ ).

The observed cell yield on substrate was calculated for  $\text{NH}_4^+$  and acetate using equation 3.6:

$$Y_{C/S} = \frac{C_{136h} - C_{0h}}{S_{136h} - S_{0h}} \quad (\text{Eq. 3.6})$$

Where  $Y_{C/S}$  is the observed cell yield on substrate with units of  $1 \times 10^6$  cells  $\text{mg}_{\text{substrate}}^{-1}$ . Observed substrate yields calculated were  $\text{NH}_4^+$  and acetate.

### Pigments analysis

The pigment quantity per cell was determined by spectrophotometric measurements after dimethylformamide (DMF) extraction. 1 mL culture aliquots were spun down at 12,000 g and  $4^{\circ}\text{C}$ . Pellets were stored at  $-80^{\circ}\text{C}$  for up to 3 months prior to analysis. Solvent resistant BRAND® UV cuvettes (Merck, Darmstadt, Germany) were

employed. Equations 3.7 to 3.9 (Inskip and Bloom, 1985) were used to calculate the chlorophyll a, chlorophyll b and total chlorophyll ( $\mu\text{g}_{\text{pigment mL}^{-1}}$ ) in the sample. Carotenoid content ( $\mu\text{g}_{\text{pigment mL}^{-1}}$ ) was calculated using equation 3.10 (Wellburn, 1994):

$$Chl_a = 12.70A_{664.5} - 2.79A_{647} \quad (\text{Eq. 3.7})$$

$$Chl_b = 20.70A_{647} - 4.62A_{664.5} \quad (\text{Eq. 3.8})$$

$$Total_{chl} = 17.90A_{647} + 8.08A_{664.5} \quad (\text{Eq. 3.9})$$

$$C_c + C_x = \frac{1000A_{480} - 2.14Chl_a - 70.16Chl_b}{245} \quad (\text{Eq. 3.10})$$

$Chl_a$  stands for chlorophyll a,  $Chl_b$  stands for chlorophyll b and  $Total_{chl}$  stands for total chlorophyll.  $C_c$  stands for carotenes fraction of carotenoids and  $C_x$  stands for xanthophylls fraction of carotenoids.

### Carbohydrates assay

The carbohydrate quantity per cell ( $\text{pg}_{\text{carbohydrate cell}^{-1}}$ ) was determined with a modified version of the Phenol-Sulfuric acid (PHS) method (Dubois *et al.*, 1956). The assay was scaled down to process smaller amounts of biomass in 200  $\mu\text{L}$  tubes. Aliquots containing  $5 \times 10^6$  cells were spun down at 12,000 g and 4°C. Pellets were stored at -80°C prior to analysis. The method's chemistry is as follows. Sulphuric acid hydrolysis breaks down carbohydrates into their monomeric subunits. Mixed with 5% phenol solution (w/v) and concentrated sulphuric acid (98%) (v/v) a coloured aromatic complex between the reducing sugar and phenol is formed. The quantity of aromatic complex formed can be calculated by measuring the absorbance of the resulting mixture at 485 nm and comparing it to glucose standards.

### Lipids assay

The lipids fraction of the biomass' biochemical composition was determined with a modified version of the Sulpho-Phospho-Vanillin (SPV) method (Van Handel, 1985). After performing a manual cell count as described above, aliquots containing  $5 \times 10^6$  cells were spun down at 12,000 g and 4°C. Pellets were stored at -80°C for up to 3 months prior to analysis. The method's chemistry is as follows. Lipids are extracted in a methanol:dichloromethane (MeOH:DCM; 1:1 v/v) system. An aliquot of the extract is

evaporated in a microwell plate. Concentrated sulphuric acid and high temperature are used to oxidize the extracted lipids into water soluble sulfonic acid derivatives. After cooling, a vanillin-phosphoric acid solution is added to produce a chromophore. The quantity of chromophore formed can be calculated by measuring the absorbance of the resulting mixture at OD 540 nm and comparing it to rapeseed oil standards.

### **Proteins assay**

The proteins fraction of the biomass' biochemical composition was determined with a modified version of the Lowry assay (Lowry *et al.*, 1951; Slocombe *et al.*, 2013). After performing a manual cell count as described above, aliquots containing  $5 \cdot 10^6$  cells were spun down at 12,000 g and 4°C. Pellets were stored at -80°C for up to 3 months prior to analysis. The method's chemistry is as follows. Protein is extracted using heat (95°C) and trichloroacetic acid (TCA). Copper ions in Lowry D solution form bonds with the peptide bonds of the extracted proteins under alkaline conditions. This results in monovalent copper cations that react with the added Folin-Ciocalteu's reagent to produce a chromophore. The quantity of chromophore formed can be calculated by measuring the absorbance of the resulting mixture at OD 600 nm and comparing it to bovine serum album (BSA) standards.

### **Cell size distribution**

Cell size distribution was measured from fresh samples on a CASY (Merck, US). The measurement principle of the instrument relies on aspirating cells through a capillary tube with a pore that has a pulsed low voltage field going between two platinum electrodes. The electrolyte-filled pore has a defined electrical resistance which changes by the displacement of electrolyte caused by the passage of cells. The change in electrical resistance corresponds to the volume of the cell which is modelled as a perfect sphere. A diameter-linear size distribution is calculated from the linear-volume distribution originally measured by the instrument.

### **Experimental condition nomenclature**

To facilitate the reader's experience throughout this Chapter and the rest of this Thesis, experimental conditions will be referred to as a combination of the illumination

and trophic strategy employed. For example, cells grown under white LED illumination in autotrophic M8a medium will be referred to as *WA*. Conversely, cells grown under red LED illumination in mixotrophic M8a.Ac media will be *RX* and so on for a total of six possible combinations of illumination and trophic strategy (Table 3.1).

**Table 3.1.** Reference guide to the experimental conditions studied in this thesis. W, white LED light; R, red LED light; B, blue LED light. A, autotrophic medium (M8a); X, mixotrophic medium (M8a.Ac) see section 3.3.1 for media compositions.

		LED light		
		White	Red	Blue
Growth media	M8a	<b>WA</b>	<b>RA</b>	<b>BA</b>
	M8a.Ac	<b>WX</b>	<b>RX</b>	<b>BX</b>

## 3.4. Results

### 3.4.1. Growth kinetics and cell physiology in phototrophic and mixotrophic batch cultures

Under phototrophic conditions, there is no organic carbon source in the medium and all organic carbon available to the cell is produced in the chloroplast by carbon fixation (Raven, 1974). Light is the main driver of carbon fixation as the photons supplied to the microalgal cell enable the generation of the ATP required for the Calvin-Benson cycle via oxidative phosphorylation in the chloroplast. When the wavelength, and therefore the energy of the photons supplied changes, so does the availability of photons throughout the culture volume. The biomass concentration and the absorption profile of the cell in conjunction with the light's spectral composition determine the spectral composition and photon availability across the culture volume. Since *C. reinhardtii* cells do not absorb photons evenly across the photosynthetically active

radiation (PAR) range it follows that the amount of light absorbed in a culture will be different depending on the light's spectral composition.

Culture productivity was evaluated by daily measurements of OD 750 nm and cell concentration as explained in section 3.3.2. Figure 3.3 shows the growth profiles of *C. reinhardtii* batch cultures for the six experimental conditions studied (WA, RA, BA, WX, RX and BX). Trophic growth mode was either phototrophic (M8a medium) or mixotrophic (M8a.Ac medium) and constant LED illumination was either white, red or blue as detailed in section 3.3.1. When evaluating cell growth kinetics, it is important to distinguish between OD 750 nm measurements (Figure 3.3 A & B) and cell concentration measurements (Figure 3.3 C & D). Optical density measurements at 750nm are a more accurate approximation of biomass concentration, commonly measured as dry cell weight (gDCW L<sup>-1</sup>). This is due to cellular volume not being considered by cell concentration measurements, whereas OD 750 nm data are affected by both cellular volume and number. On the other hand, cell concentration measurements allow the tracking of changes to cell cycle duration and the derivation of other significant properties such as cell weight. The existing literature on the effects of narrow wavelength illumination on the cell cycle and cell size of microalgae (Wilhelm, Kramer and Wild, 1985; Oldenhof, Zachleder and Van Den Ende, 2006; Kim *et al.*, 2014) justifies such a holistic approach to the evaluation of growth dynamics.

Tracking culture productivity with both metrics is particularly important when comparing different growth conditions that might affect cell physiology as they can help to determine the causes of any observed changes in product yield. These can be either a change in biomass productivity, biomass specific product yield or a combination of both. However, a change in one may affect the other and the trade-off must be evaluated against the bioprocess objective. In a batch versus fed-batch comparison study of green fluorescent protein (GFP) production in *C. reinhardtii*, total GFP produced was higher in the fed-batch strategy due the higher biomass concentration achieved (Fields, Ostrand and Mayfield, 2018). However, the cell specific GFP content was statistically significantly higher in the batch culture ( $p < 0.05$ ). This was accompanied by a morphological change that increased the cell weight of fed-batch grown *C. reinhardtii* and is a good example of process parameters affecting cell physiology and product yield.

In all microalgal bioprocesses, and especially when the product will be ingested or otherwise come into contact with humans, the importance of total product produced is undeniable however in many cases it will be equalled or superseded by product quality (Michael A. Borowitzka, 2013). Given the likelihood of cell dimensions and cell cycle to differ between these experiments, it is important to characterise both OD 750 nm and cell concentration profiles.

### **Biomass accumulation**

*Chlamydomonas reinhardtii* batch cultures grown in autotrophic conditions (Figure 3.3 A & C) had an average final biomass concentration of WA (1.33 gDCW L<sup>-1</sup>), RA (1.10 gDCW L<sup>-1</sup>), BA (0.775 gDCW L<sup>-1</sup>) at 136 hours as measured by the dry biomass method described in section 1.3.2. A one factor ANOVA followed by Tukey's HSD test determined there was a statistically significant difference between each condition's final biomass concentration (N=4,  $p < 0.05$ ). This is in agreement with previous studies comparing monochromatic illumination to white LED lights that found maximum biomass productivity is achieved with balanced light spectra similar to white LED light (Baer *et al.*, 2016; Mooij *et al.*, 2016).

When *C. reinhardtii* is grown in acetate containing media like M8a.Ac, its metabolism shifts to mixotrophy and the influence of photosynthesis on biomass productivity is comparatively reduced (Heifetz *et al.*, 2000). No statistically significant difference was found in the final biomass concentration of WX (1.51 gDCW L<sup>-1</sup>) and RX (1.33 gDCW L<sup>-1</sup>) cultures (N=4,  $p < 0.05$ ), supporting the above (Figure 3.3 B & D). The relatively poor performance under blue light seen in phototrophic cultures was improved in BX (1.03 gDCW L<sup>-1</sup>), although this was not enough to bring it to parity with the other two light conditions.



**Table 3.2.** *C. reinhardtii* biomass concentration at 136 hours of culture derived from the linear relationship between OD750 and dry cell weight plotted in Figure 3.2. W, white LED light; R, red LED light; B, blue LED light. A, autotrophic medium (M8a); X, mixotrophic medium (M8a.Ac) see section 3.3.1 for media compositions.

		WA	RA	BA	WX	RX	BX
<b>Average Biomass concentration from 88 - 136 h (gDCW L<sup>-1</sup>)</b>	Culture 1	1.35	1.12	0.78	1.55	1.22	0.97
	Culture 2	1.31	1.08	0.77	1.48	1.44	0.94

Overall, the results from autotrophic and mixotrophic conditions show that blue light is sub-optimal for batch cultivation of *C. reinhardtii* under constant illumination at constant photon flux with a relatively deep light path. One of the reasons for this is the poor efficiency with which *C. reinhardtii* utilises the energy (ATP) and reducing power (NADPH) from photosynthesizing blue light to produce new biomass via carbon fixation as reported by De Mooij (2016) and colleagues in continuous cultures. The low biomass productivity observed in BA cultures is partially remedied in BX due to the reliance on heterotrophic acetate metabolism.

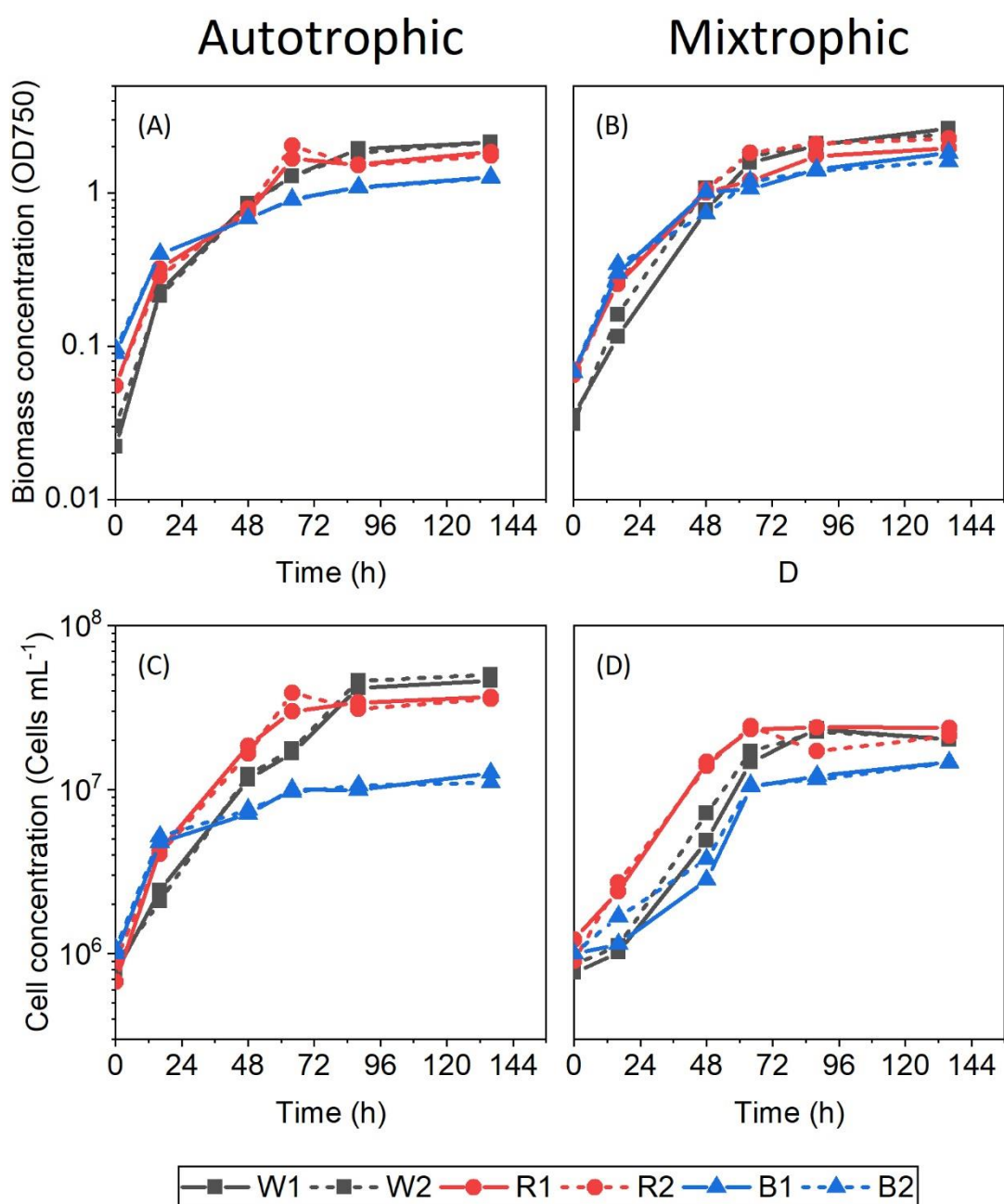


**Figure 3.3.** *C. reinhardtii* batch growth kinetics under a variety of trophic and illumination strategies. (A and C) Autotrophic growth in M8a; (B and D) mixotrophic growth in M8a.Ac, black arrow indicates acetate depletion from the culture medium. (A and B) Biomass Concentration (measured at OD 750) (C and D) Cell concentration (Cells·mL<sup>-1</sup>). W, white LED light; R, red LED light; B, blue LED light. Biological duplicates (N=2) plotted.

The influence of LED light colour on final cell concentration followed a similar trend as OD 750 nm in both trophic modes studied suggesting that OD 750 nm and cell concentration are analogous to each other and either could be used as a proxy for dry cell weight. However, the correlation between these two variables is dependent on cell physiology remaining constant. It can be deduced from Figure 3.3 that the cell physiology of *C. reinhardtii* does not remain constant between the two trophic modes studied. The OD 750 nm growth profiles for each LED light colour are similar between autotrophic and mixotrophic cultures, however this does not hold true for cell concentration.

The normalised ratio of OD 750 nm to viable cell concentration can be used to identify changes in the cell mass to cell number relationship between different trophic strategies (Figure 3.4). Consequently, cells grown under blue LED light were found to remain largely unaffected by trophic mode selection, whilst larger changes were observed for cells grown under white and red LED light. Furthermore, the final biomass in terms of OD 750 nm for each light was statistically significantly higher in mixotrophic than phototrophic conditions ( $N=4$ ,  $p < 0.05$ ). In terms of cell concentration under white and red LED light, this relationship was inverted, with phototrophic cultures producing a significantly larger final cell yield ( $N=4$ ,  $p < 0.05$ ). Blue light producing lower final biomass and cell yields indicates that it is sub-optimal for growing *C. reinhardtii* in batch cultures with a constant illumination strategy.

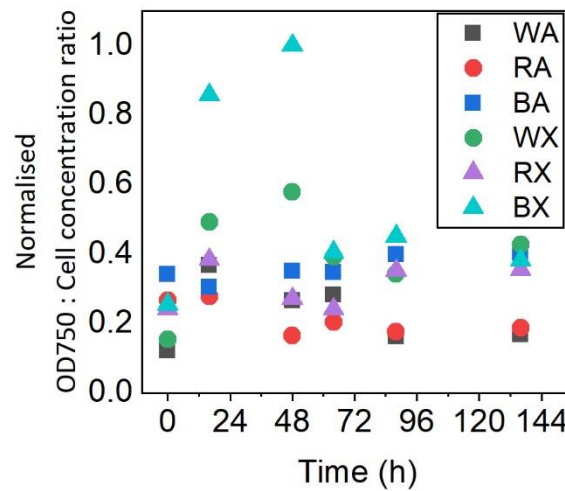


**Figure 3.4.** Normalised *C. reinhardtii* OD750 : Cell concentration ratio under a variety of trophic and illumination strategies. W, white LED light; R, red LED light; B, blue LED light. A, autotrophic medium (M8a); X, mixotrophic medium (M8a.Ac).

### Maximum specific growth rate

The maximum specific growth rate ( $\mu_{\max}$ ) calculated from OD 750 nm measurements (Equation 3.1) during the exponential growth phase is a measure of biomass productivity. The inclusion of organic carbon in mixotrophic cultures had the biggest positive effect on  $\mu_{\max}$  in BX where a 28% increase was observed (as calculated from the average of the values for individual flasks presented in Table 3.3). Meanwhile in WX and RX the difference in  $\mu_{\max}$  between trophic strategies was -5% and 3% respectively. These results indicate that under constant environmental conditions where wavelength distribution of available light is not limiting (temperature, pH and light intensity) trophic strategy has little impact on  $\mu_{\max}$  in batch cultures. This observation matches previously published results across a range of acetate concentrations and at a relatively high irradiance ( $600 \mu\text{mol}_{\text{ph}} \text{m}^{-2}\text{s}^{-1}$ ) (Heifetz *et al.*, 2000). Electron paramagnetic resonance (EPR) spectroscopy has shown that cells grown in a mixotrophic regime produce fewer reactive oxygen species due to a direct effect of acetate on the quantum state of photosystem-II (PSII) (Roach, Sedoud and Krieger-Liszkay, 2013). Roach and colleagues (2013) they hypothesised that acetate replaces the bicarbonate associated to the non-heme iron atom in photosystem II particles changing

the environment of the two secondary quinone acceptors positively impacting charge recombination events and photoinhibition in the chloroplast. Blue light photons carry more energy and can cause photoinhibition at lower irradiances than red or white light (Yan *et al.*, 2016). The lower productivity of BA cultures could be due to higher photoinhibition. This would be reduced in the presence of acetate and could explain the increased  $\mu_{\max}$  observed in BX cultures.

**Table 3.3** Maximum biomass growth rate ( $\mu_{\max}$ ) of *C. reinhardtii* cultured under different illumination and trophic strategies. Values calculated according to Equation 3.1. W, white LED light; R, red LED light; B, blue LED light. A, autotrophic medium (M8a); X, mixotrophic medium (M8a.Ac).

		WA	RA	BA	WX	RX	BX
$\mu_{\exp}$	Culture 1	0.076	0.054	0.042	0.064	0.055	0.056
(h <sup>-1</sup> )	Culture 2	0.069	0.056	0.040	0.074	0.058	0.050

White light resulted in the highest  $\mu_{\max}$  on average, followed by red light and finally blue light (Table 3.3). This suggests that at moderate light intensities a combination of wavelengths is more beneficial for fast growth than a narrow portion of the PAR range alone.

### Nutrient uptake

The stationary phase is reached when the rate of cell proliferation is equal to the rate of cell death (Doran, 2013). This can be triggered by a growth factor becoming limiting. RA and BA cultures reached the stationary phase after 64 hours of cultivation whilst WA cultures reached it after 88 hours (Figure 3.3 C). Ammonia was fully depleted in WA cultures by the time they reached stationary phase. In contrast, there were

measurable amounts of ammonia left in RA and BA cultures when they reached the stationary phase. However, the levels reached could be low enough to become limiting, partially explaining the earlier transition to stationary phase under red and blue light in autotrophic conditions. Meanwhile WX, RX and BX cultures all reached the stationary phase after 64 hours of culture. This synchronisation could be linked to the depletion of acetate occurring at the same time under all three lights (Figure 3.5 C). Once the main organic carbon source is depleted from the medium, cells could theoretically switch to phototrophic growth and continue proliferating. The rate of acetate consumption in mixotrophic cultures ( $q_{ac}$ , Table 3.4) was nearly identical under all studied wavelengths irrespective of the observed biomass growth rate. Values calculated based on acetate concentrations between  $t_1 = 0h$  and  $t_2 = 48h$ .

**Table 3.4** Acetate uptake rate in *C. reinhardtii* cultures grown in M8a.Ac medium. Values calculated according to equation 3.1. W, white LED light; R, red LED light; B, blue LED light. A, autotrophic medium (M8a); X, mixotrophic medium (M8a.Ac).

		WX	RX	BX
$q_{Ac}$ (mM h <sup>-1</sup> )	Flask 1	0.363	0.369	0.370
	Flask 2	0.361	0.370	0.370

Nitrogen uptake is a key physiological parameter to monitor in microalgal cultures as it is an essential nutrient with key roles in protein, lipid and nucleic acid metabolism and therefore has a big influence on culture productivity (Fernandez, Llamas and Galvan, 2009). The nitrogen source in both autotrophic and mixotrophic cultures was ammonium, its uptake profile is displayed in Figure 3.5 A&B. Maximum nitrogen uptake rate ( $V_{maxN}$ ) has been found to scale isometrically with cell volume over several orders of magnitude and different species of microalgae (Marañón *et al.*, 2013). The authors concluded that the limiting factors for  $\mu_{max}$  are cell size and the conversion of nutrients into biomass rather than  $V_{maxN}$ . This is logical as availability of intracellular N is not the only limiting factor during cell growth and other metabolic pathways like oxidative

phosphorylation or the Calvin cycle can become the bottleneck to increased  $\mu_{\max}$  too. The depletion rate of ammonia followed a similar trend across all illumination modes for mixotrophically grown cultures (Figure 3.5 B) with ammonia concentration falling below detection limits after 68 hours of culture. In contrast, the concentration profile of ammonia in phototrophically grown cultures was found to vary with light colour. Ammonium was depleted after 64h in white light, 88h in red light and not at all in blue light reaching a minimum value of 0.5 mM at the end of the experiment. A closer observation of the experimental trends (Figure 3.5 A&B) indicates that the difference in ammonia depletion between WA and RA is likely overestimated due to time between experimental measurements and highlights a flaw in experimental design that could be remedied by reducing the time interval between extracellular nutrient measurements thus obtaining a more precise time of ammonia depletion.

To quantify the differences in nitrogen assimilation into biomass, the observed yield of biomass on ammonium ( $Y_{X/NH_4^+}$ ) and the observed yield of cells on ammonium ( $Y_{C/NH_4^+}$ ) at the beginning of the stationary phase were calculated (Table 3.5). The onset of the stationary phase, indicated by the cessation of net cell division, did not necessarily coincide with the exhaustion of ammonium in the media. In WA and WX cultures, ammonium was exhausted after up to 64h whilst the stationary phase begun after 88h. In RA cultures ammonium was exhausted after up to 64h whilst in RX it was exhausted after up to 88h, meanwhile the stationary phase began after 64h in both trophic modes. This suggests that N was not the first growth-limiting factor in RX cultures. Under blue light, ammonium was only exhausted in BX whilst in BA the average final concentration remained at 0.57 mM. Additionally, it was hard to differentiate between exponential, linear and stationary phase in the growth profile of BA experiments as growth under this light was sub-optimal and a clear sigmoid profile was not apparent (Figure 3.3 A).

The same total amount of ammonium was consumed under white and red light in both trophic modes as concentration dipped below the limit of quantification between 64 – 88 hours into the culture. By the end of the experiment there were still quantifiable levels of ammonium in the medium of BA cultures of 0.57 mM. Although the same amount of ammonium was consumed across all conditions except blue phototrophic, there were statistically significant differences in final biomass yield and final cell yield

between trophic modes (under the same light).  $Y_{X/NH_4^+}$  and  $Y_{C/NH_4^+}$  reflect those differences and emphasise the differing nitrogen requirements of *C. reinhardtii* under the conditions studied.

**Table 3.5.** Observed yield of biomass on ammonium ( $Y_{X/NH_4^+}$ , gX gNH<sub>4</sub><sup>+1</sup>) and observed yield of cells on ammonium ( $Y_{C/NH_4^+}$ , 1x10<sup>6</sup>cells mgNH<sub>4</sub><sup>+1</sup>) in phototrophic and mixotrophic cultures under white red and blue LED light. Calculated according to Equation 3.5 and 3.6 respectively.

$\lambda$	Trophic mode	$Y_{C/NH_4}$ (1x10 <sup>6</sup> cells mgNH <sub>4</sub> <sup>+1</sup> )			$Y_{X/NH_4}$ (gX gNH <sub>4</sub> <sup>+1</sup> )		
		Flask 1	Flask 2	Average	Flask 1	Flask 2	Average
W	A	414	449	432	12.8	12.6	12.7
R	A	329	322	325	10.8	10.3	10.6
B	A	115	98	107	7.72	7.48	7.6
CV(%)		57.6			24.9		
W	X	185	207	196	16.0	16.1	16.0
R	X	191	179	185	10.6	12.8	11.7
B	X	153	131	142	11.3	9.77	10.5
CV(%)		16.4			22.7		

Coefficients of variation (CV) from the observed yield values in Table 3.5 show that the biggest variance in  $Y_{C/NH_4}$  between illumination strategies within a trophic mode was 57.6%. In mixotrophically grown cultures, the CV of  $Y_{C/NH_4}$  was only 16.4%, suggesting that the influence of light colour on  $Y_{C/NH_4}$  was less pronounced in this trophic mode. This matches the conclusions drawn from Figure 3.5 and suggests a different nitrogen utilisation per cell in WA, RA and BA cultures. This could be due to changes in cell size leading to differences in volume specific N requirements (Marañón *et al.*, 2013) or changes in cellular metabolism resulting in a different macromolecular composition under each light. The CVs calculated for  $Y_{X/NH_4}$  in phototrophic and mixotrophic mode were 24.9% and 22.7% respectively.  $Y_{X/NH_4}$  did not follow the same pattern of variation between lights in each trophic mode as  $Y_{C/NH_4}$  and instead the variation remained similar between modes. This suggests that the differences observed in  $Y_{C/NH_4}$  are mainly due to cell size differences between the trophic modes and not due



to a re-routing of assimilated N causing biochemical composition differences between the same light in each trophic mode. This holds true for white and blue light as they both have the largest and smallest observed yield values respectively (Table 3.5). However, RX cultures had a  $Y_{X/NH_4}$  closer to the BA/BX average than the WA/WX average. A hypothesis can be formulated here considering whether RX cultures had a different biochemical composition than RA cultures. Biochemical composition differences are studied in the following sections.

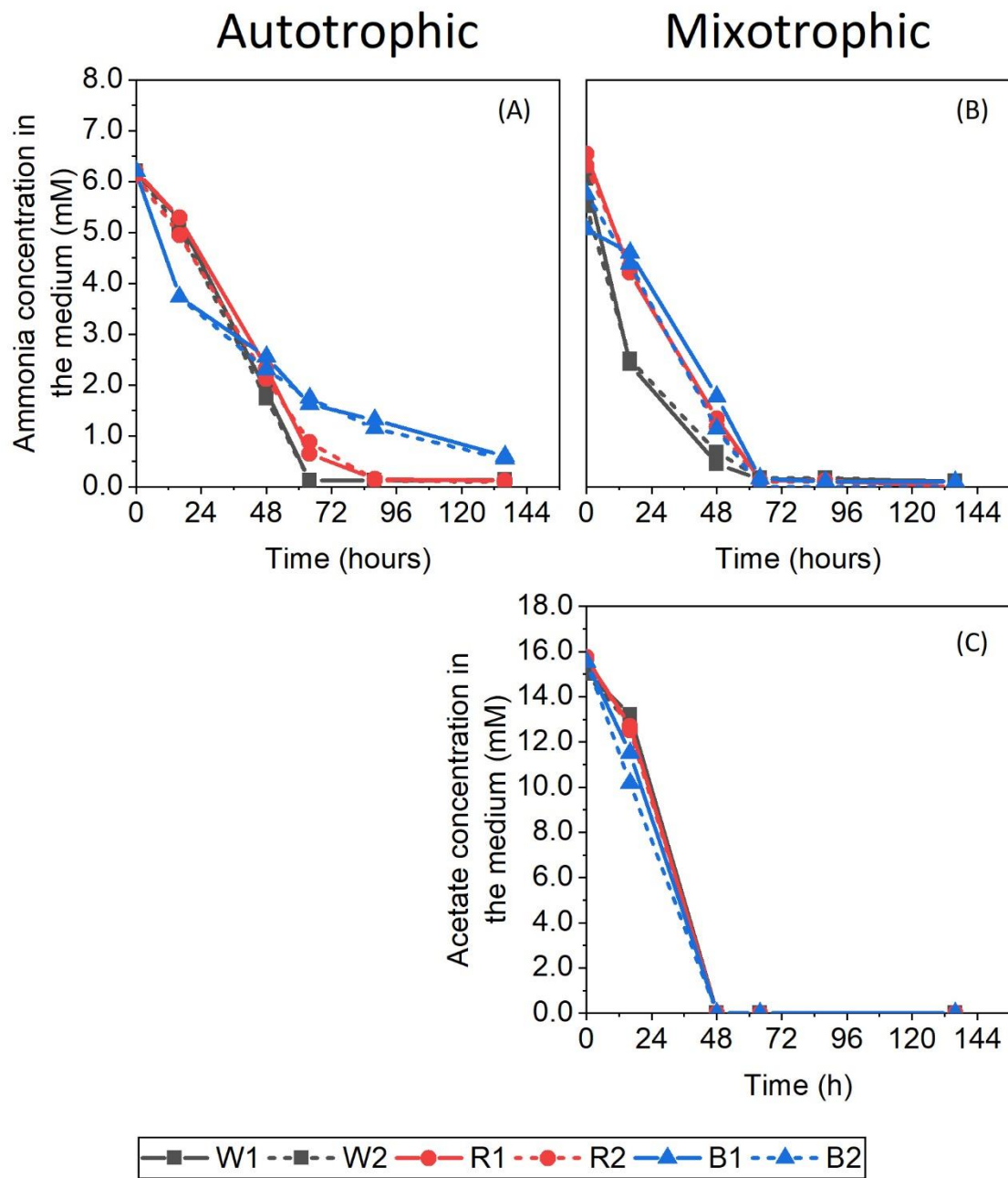


**Figure 3.5** *C. reinhardtii* nutrient uptake kinetics under a variety of trophic and illumination strategies. (A) Ammonium uptake in autotrophic growth in M8a; (B and C) Ammonium and acetate uptake respectively in mixotrophic growth in M8a.Ac. W, white LED light; R, red LED light; B, blue LED light. Biological duplicates (N=2) plotted.

### Cell weight

The two methods employed to estimate cell weight (Section 3.3.2) do not produce the exact same value for each sample analysed as can be seen in Table 3.6. This can be

due to accumulated errors from cell concentration measurements, dry biomass measurements and measurement errors in the biochemical assays themselves. Additionally, it must be pointed out that the ash content of the cells was not experimentally measured. Published ash values for *C. reinhardtii* cultivated in a variety of experimental conditions are very similar between conditions in each paper but vary significantly between publications. Values from 4% to 20% of dry biomass weight have been reported (Kliphuis *et al.*, 2011; Kebelmann *et al.*, 2013). This might be due to the typically small culture volumes involved in these studies affecting the amount of biomass available for ash measurements. Sample volume has been found to be a determinant factor in ash measurement reproducibility in microalgae (Liu, 2019). G

The measured biomass and the sum of macromolecular components methods do not equate to each other, and this can lead to speculation on the validity of the macromolecular assay measurements. However, both methods of cell weight measurement correlate well in most instances across all experimental conditions at two different growth phases, improving our confidence on the validity of the macromolecular assays. Firstly, the samples analysed can be divided into four cases specified by culture time and trophic mode. Within each case, the cell weight ranking between lights remains the same with both methods in three out of four cases. The discordant case is samples from 48h in mixotrophic conditions. Here, cell weight calculated from measured dry cell weight suggests cells grown under red light are heavier than cells grown under blue light and the opposite is true when cell weight is calculated from the sum of macromolecular components. However, in this comparison, cells grown under red light had the biggest percentage difference in cell weight between the two methods, 49.1%. This larger discrepancy suggests at least one of the two measurements had higher inaccuracy than average. The additional steps required to calculate a cell weight value from the addition of macromolecular components result in a larger compounded error and therefore the cell weight calculated with this method is likely to be an outlier.

Secondly, the percentage change in cell weight from 48h to 136h is comparable for most samples across both methods (Table 3.6). Only mixotrophic cultures under red and blue light show larger discrepancies between the two methods. In the case of red

light mixotrophic cultures this is likely due to the accumulated error in the sum of macromolecular components at 48h. In the case of blue mixotrophic light, examining the differences between time points for each method, the differences are similar in magnitude but opposite in direction. According to the measured dry cell weight method, the cells decreased in weight between 48h and 136h whereas the opposite is true according to the sum of macromolecular components method. This equates to a 19.6% absolute difference in Table 3.7 even though the difference between time points in each method is around 10% only. The two very distinct methods of measuring cell weight agreed well, thus increasing the validity of proximal analyses discussed in this chapter.

**Table 3.6.** Comparison of two methods for estimating cell weight. Method 1 measured cell weight from a known culture volume. Method 2 calculated cell weight from the sum of macromolecular components.

Condition	48h			136h		
	Measured dry cell weight (pgDCW cell <sup>-1</sup> )	Sum of macromolecular components (pg cell <sup>-1</sup> )	Percentage difference between methods (%)	Measured dry cell weight (pgDCW cell <sup>-1</sup> )	Sum of macromolecular components (pg cell <sup>-1</sup> )	Percentage difference between methods (%)
WA	60.8	45.9	24.5%	29.5	25.3	14.2%
RA	38.9	33.9	12.9%	39.4	32.3	18.1%
BA	67.7	54.3	19.8%	48.7	41.4	15.0%
WX	105	81.0	23.0%	57.7	47.0	18.6%
RX	72.4	36.9	49.1%	40.2	26.0	35.2%
BX	65.6	50.1	23.7%	61.5	56.8	7.69%

**Table 3.7.** Cell weight percentage difference between 48h and 136h compared between different cell weight analysis methods.

Condition	Measured dry cell weight	Sum of macromolecular components	Absolute percentage difference between methods (%)
	Cell weight percentage difference between 48h and 136h (%)		
WA	-51.5%	-44.9%	6.60%
RA	1.29%	-4.72%	6.01%
BA	-28.1%	-23.8%	4.31%
WX	-45.0%	-42.0%	3.07%
RX	-44.5%	-29.5%	14.9%
BX	-6.25%	13.4%	19.6%

### Average cell size distribution

Statistically significant differences were found between the average final cell concentrations of WA ( $4.60 \times 10^6$  cells mL<sup>-1</sup>), RA ( $3.44 \times 10^6$  cells mL<sup>-1</sup>) and BA ( $1.11 \times 10^6$  cells mL<sup>-1</sup>) cultures (N=4,  $p < 0.05$ ) as seen in Table 3.8. In contrast, the final cell weight in phototrophic mode was highest under blue light followed by red light and finally white light 3.2). Final cell concentration and cell weight were inversely proportional to each other in phototrophic mode. If cell density remained constant, the changes in cell weight would be proportional to changes observed in cell size as per equation 3.11.

**Table 3.8.** Average cell concentration at 136 hours of culture under a variety of trophic and illumination strategies. W, white LED light; R, red LED light; B, blue LED light. A, autotrophic medium (M8a); X, mixotrophic medium (M8a.Ac) see section 3.3.1 for media compositions. Individual flask (N) data reported for 2 timepoints (n) (n = 2, N = 1).

		WA	RA	BA	WX	RX	BX
<b>Average cell concentration from 88 - 136h (10<sup>7</sup> cells mL<sup>-1</sup>)</b>	Culture 1	4.53	3.44	1.11	2.17	2.16	1.32
	Culture 2	4.60	3.43	1.06	2.15	2.10	1.33

$$\rho = \frac{m}{V} \quad (\text{Eq. 3.11})$$

Where  $\rho$  is density of a cell,  $m$  is mass of a cell and  $V$  is the volume of a cell.

Cell weight decreased from 48h to 136h in all cultures except in RA and BX cultures where it remained stable. For those conditions where cell weight decreased (WA, BA, WX, RX), the average percentage decrease was of 42.3% when measured from a known

volume of culture versus 35.0% when measured as the sum of macromolecular components (Table 3.7).

Cell weight is an important physical property in bioprocessing as it is tightly linked to macromolecular composition and cell size (Chapman and Gray, 1981). Macromolecular composition is particularly important in microalgal bioprocesses where several classes of macromolecules or even the entirety of the cellular mass are often the product of interest. The shear sensitivity of a cell determines its resilience during culture and the ease of product recovery during downstream processing (Voulgaris *et al.*, 2016). Shear sensitivity is a function of many properties, including cell size (Rayat, Micheletti and Lye, 2010; Rayat *et al.*, 2016). Therefore, modelled cell viability or cell disruption rate in a particular unit operation could be affected by changes in cell size. Cell size distribution (CSD) was measured to improve our understanding of the factors causing cell weight differences under the conditions studied.

All the cell size distributions of cells grown under white and red light approximate a narrow peak normal distribution. Comparing the mode between 48h and 136h of all white and red light conditions (Figure 3.6 and Figure 3.7), the average percentage difference is only -4%. Assuming a constant  $\rho$ , the CSDs do not reflect the large percentage cell weight decreases seen from 48h to 136h either (Figure 3.6 and Figure 3.7). A similar analysis is not advisable for cells grown under blue light as their CSDs are closer to a bimodal distribution indicating at least two distinct cell populations with different cell sizes.

The same CSD data was plotted grouped by trophic mode in Figure 3.9 and Figure 3.10 to accentuate the differences observed in cell size between lights at each time point. The increased similarity in cell size distribution at 136h seen in mixotrophic cultures (Figure 3.10) compared to phototrophic cultures (Figure 3.9) is a similar trend to that observed in the final cell concentration data (Table 3.8). Both point towards a dampening of the differential effects of wavelength selection on *C. reinhardtii* metabolism in mixotrophic growth conditions. This is a step towards rejecting the null hypothesis that impact of wavelength selection is the same in phototrophic and mixotrophic growth conditions. From a bioprocessing optimisation perspective,



wavelength selection should have a higher priority in phototrophic cultivations. However, mixotrophic metabolism also relies on photosynthesis to produce the ATP necessary for acetate assimilation (Johnson and Alric, 2012) and the potential benefits from a customised wavelength strategy should not be ignored.

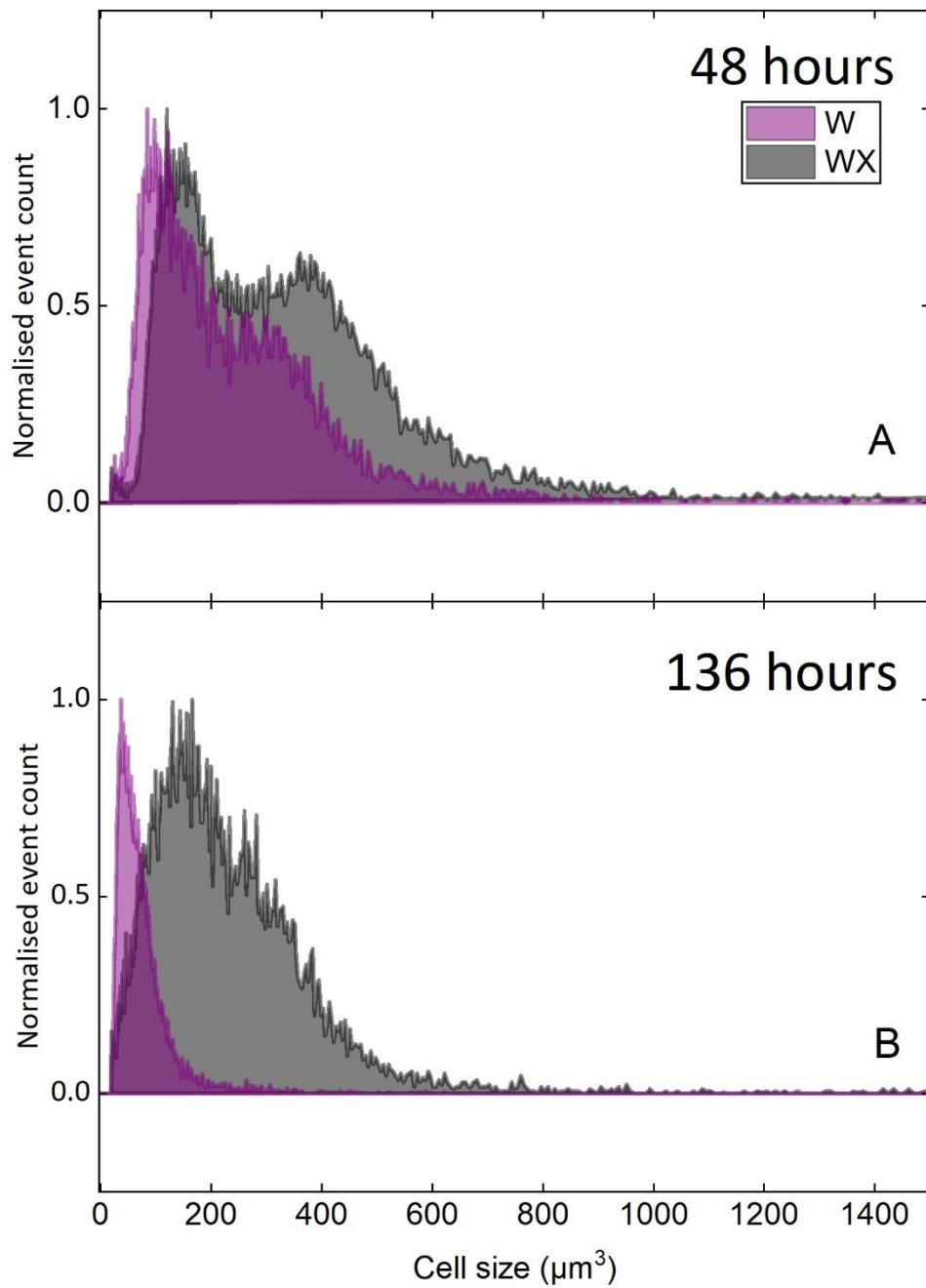


**Figure 3.6** *C. reinhardtii* cell size distribution at two time-points of a batch culture under white LED light and a variety of trophic strategies. (A) 48 hours of batch culture corresponding to the mid-exponential growth phase; (B) 136 hours of batch culture corresponding to the late stationary phase. W, autotrophic culture in M8a; WX, mixotrophic culture in M8a.Ac. Single representative sample plotted (N=1).

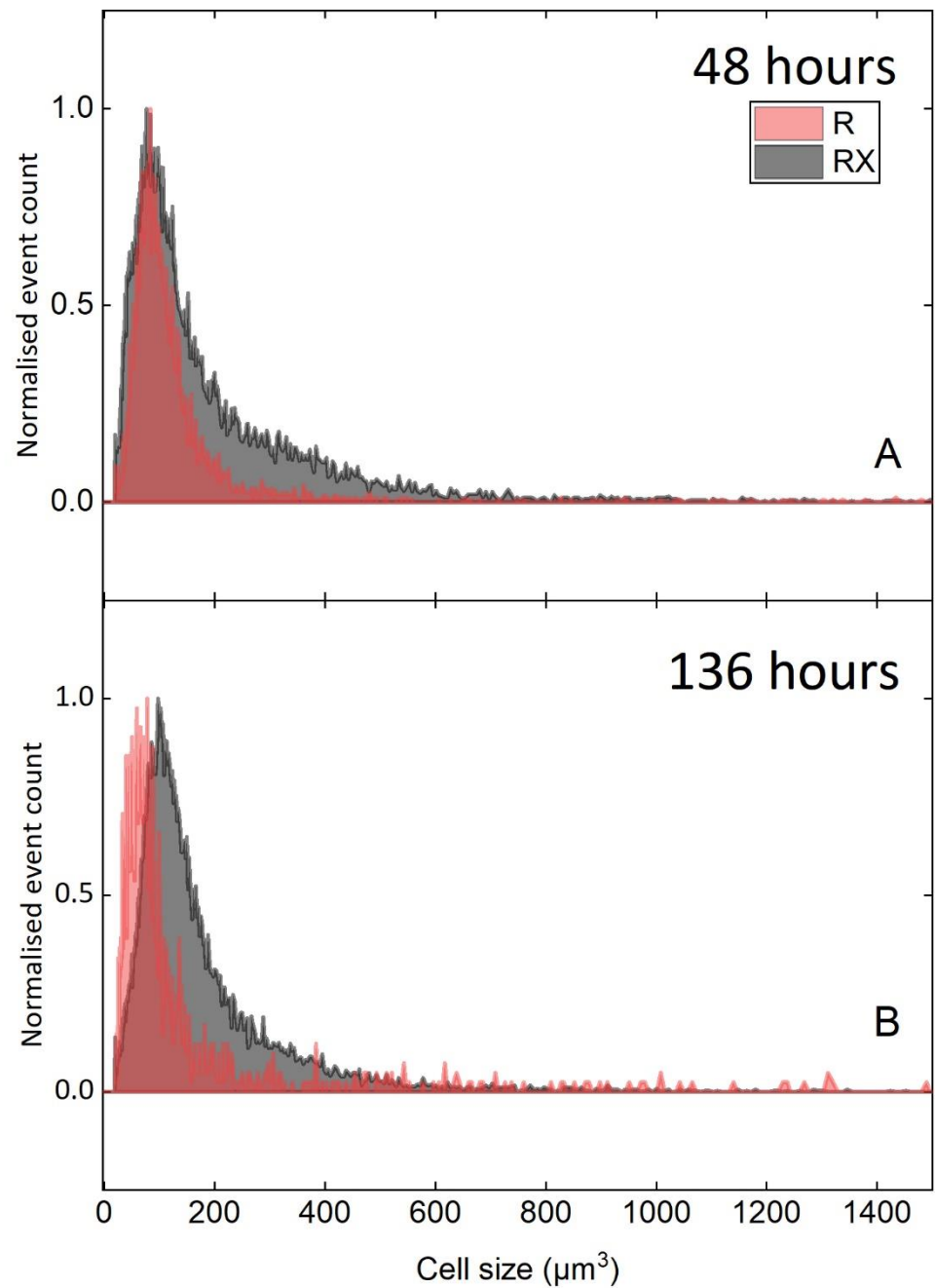


**Figure 3.7.** *C. reinhardtii* cell size distribution at two time-points of a batch culture under red LED light and a variety of trophic strategies. (A) 48 hours of batch culture corresponding to the mid-exponential growth phase; (B) 136 hours of batch culture corresponding to the late stationary phase. R, autotrophic culture in M8a; RX, mixotrophic culture in M8a.Ac. Single representative sample plotted (N=1).

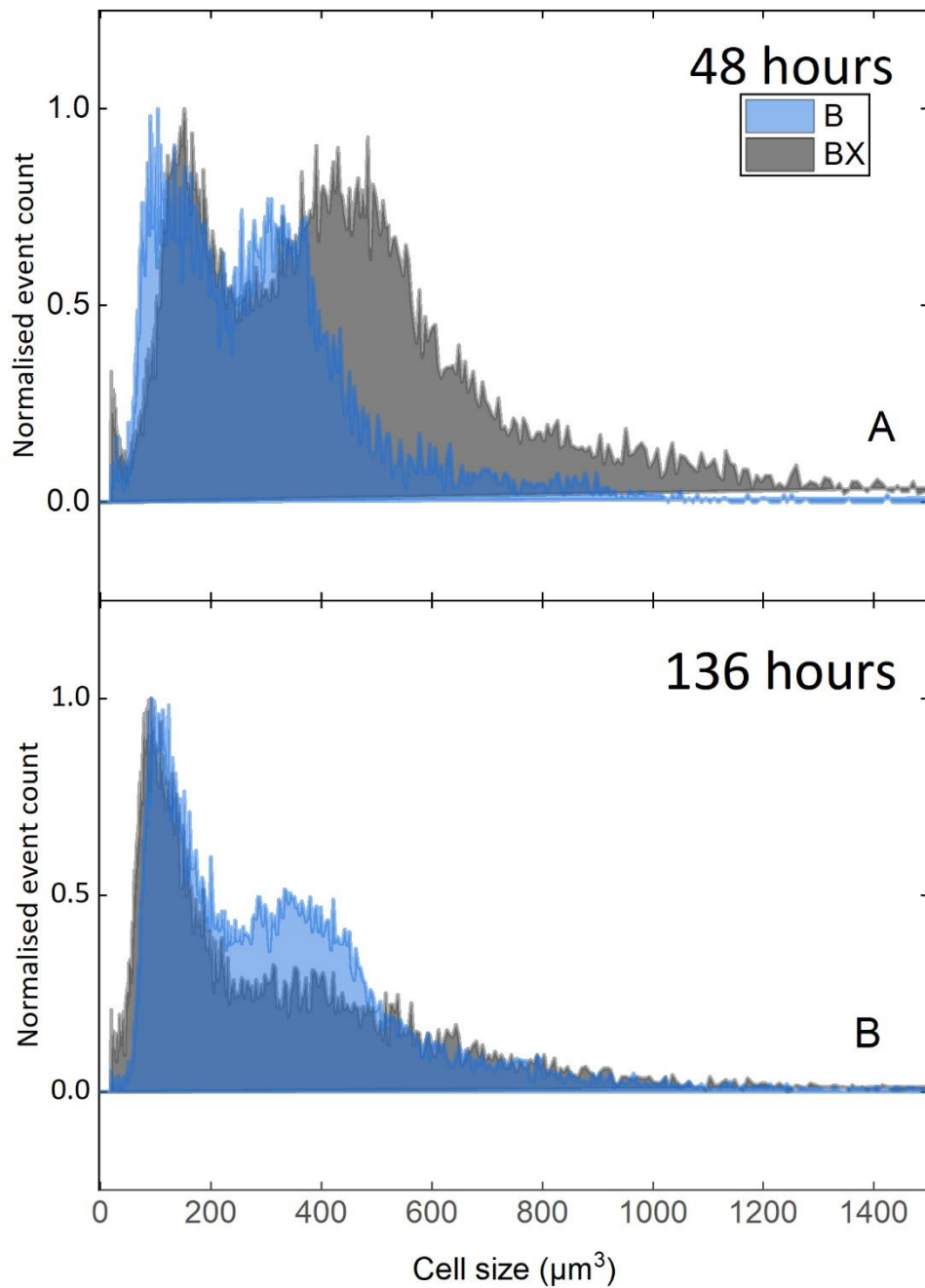


**Figure 3.8.** *C. reinhardtii* cell size distribution at two time-points of a batch culture under blue LED light and a variety of trophic strategies. (A) 48 hours of batch culture corresponding to the mid-exponential growth phase; (B) 136 hours of batch culture corresponding to the late stationary phase. B, autotrophic culture in M8a; BX, mixotrophic culture in M8a.Ac. Single representative sample plotted (N=1).

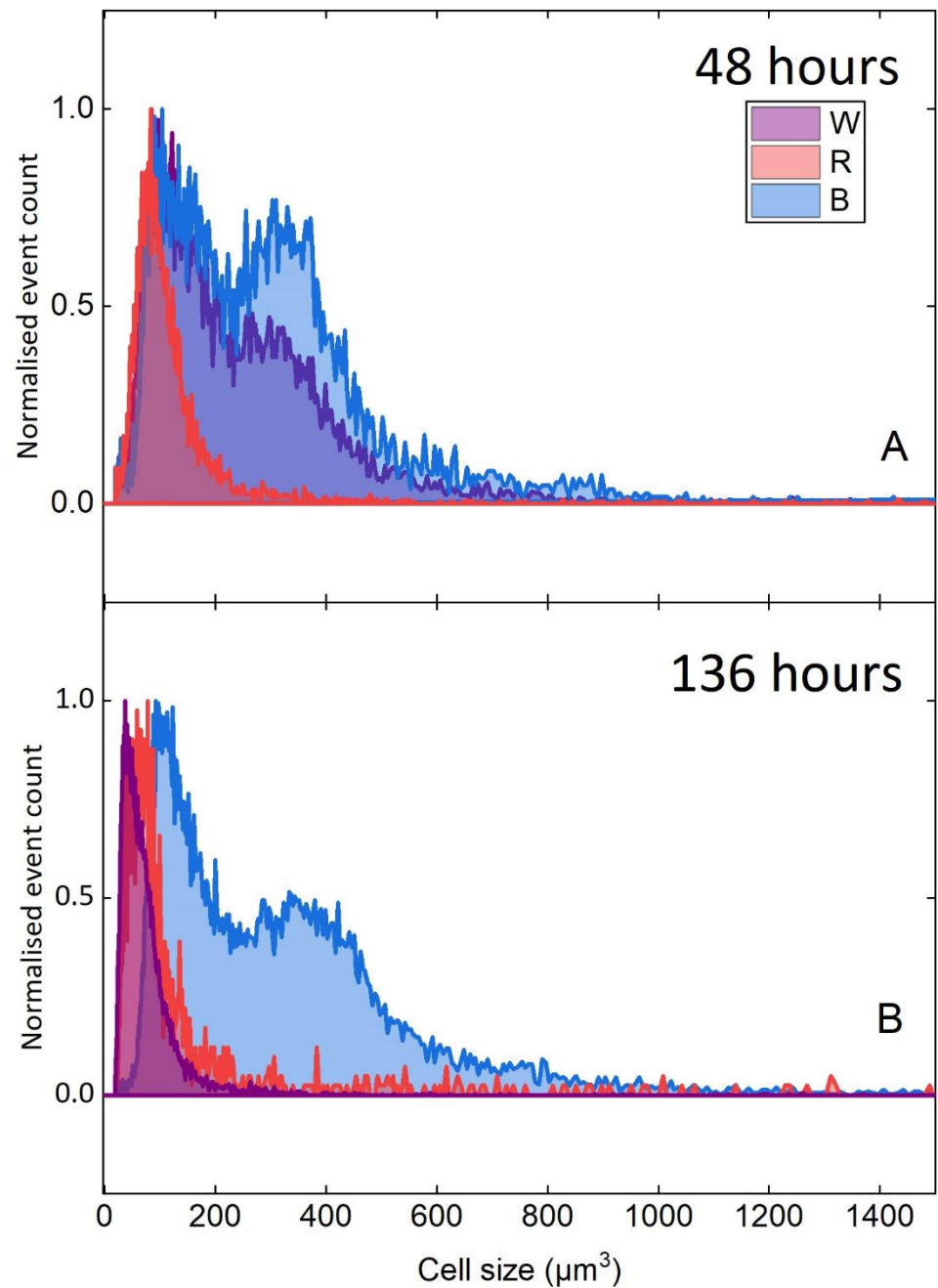


**Figure 3.9.** *C. reinhardtii* cell size distribution at two time-points of a batch culture under a variety of illumination strategies in autotrophic M8a media. (A) 48 hours of batch culture corresponding to the mid-exponential growth phase; (B) 136 hours of batch culture corresponding to the late stationary phase. W, white LED light; R, red LED light; B, blue LED light. Single representative sample plotted (N=1).

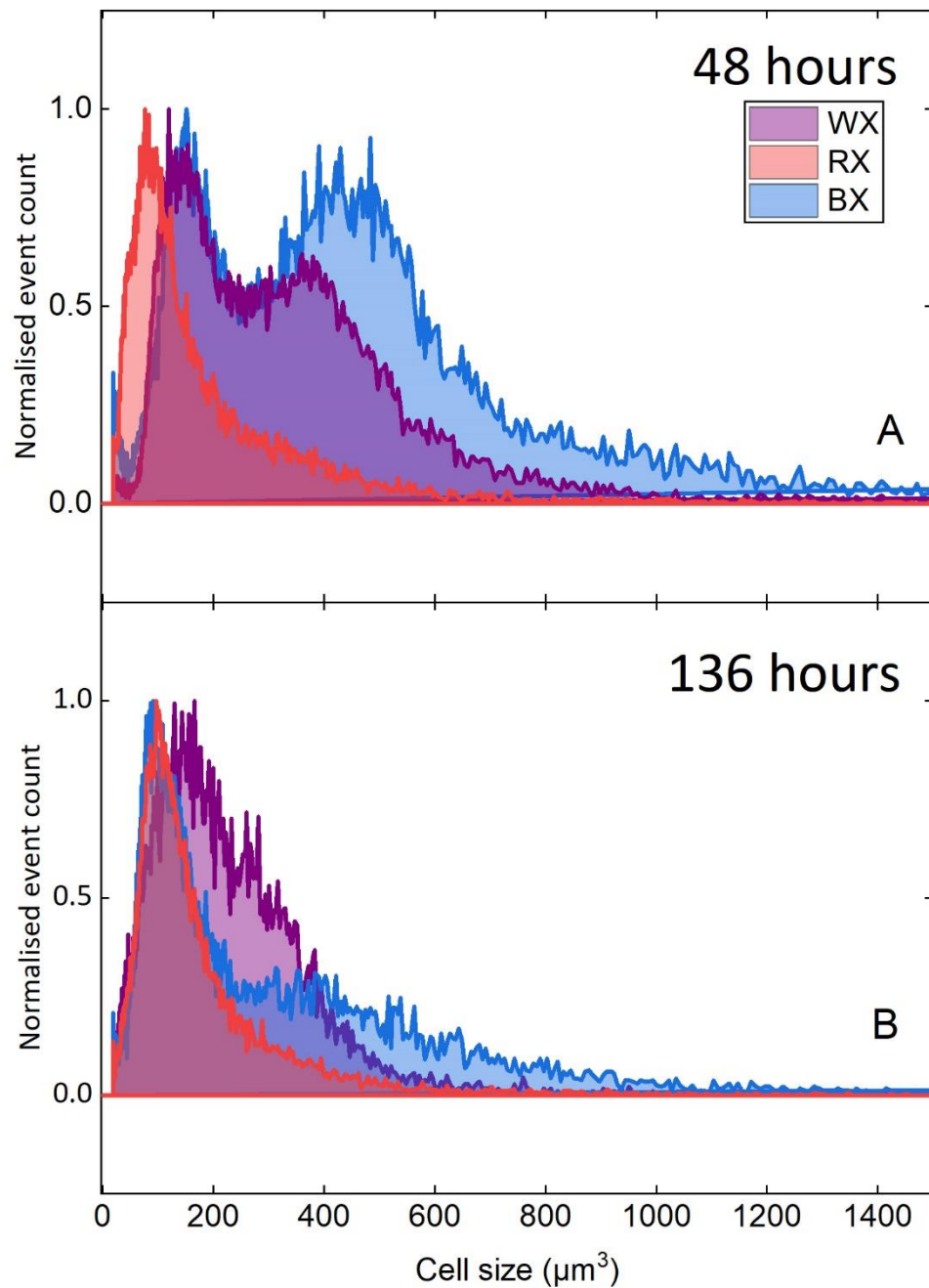


**Figure 3.10.** *C. reinhardtii* cell size distribution at two time-points of a batch culture under a variety of illumination strategies in mixotrophic M8a.Ac media. (A) 48 hours of batch culture corresponding to the mid-exponential growth phase; (B) 136 hours of batch culture corresponding to the late stationary phase. WX, white LED light; RX, red LED light; BX, blue LED light. Single representative sample plotted (N=1).

### 3.4.2. Biochemical composition in phototrophic and mixotrophic batch cultures

The main macromolecular components of *C. reinhardtii* biomass are carbohydrates, lipids and proteins. Most, if not all the carbon fixed in the Calvin-Benson-Bassham cycle or assimilated via the catabolism of acetate will be used as a building block for those macromolecular groups. Nucleic acids also form an essential part of the biochemical make-up but they were assumed to stay constant in all conditions (Chang *et al.*, 2011). Finally, pigments fall under the broad category of lipids, but were measured separately due to their central role in light absorption and the emphasis of this study on the effects of narrow band illumination on biochemical composition.

The following sub-sections present the changes in percentage contribution to the biochemical composition of the cell of each macromolecular group measured throughout the culture under white, red and blue light in two trophic growth modes.

#### Carbohydrate

The main carbohydrate component of *C. reinhardtii* cells is glucose in the form of starch (Choi, Nguyen and Sim, 2010) although a great variety of other monosaccharides are produced by the microalgae as observed in the breakdown of cell wall fractions (Harris, 2001). Starch is a direct sink for photosynthetically fixed carbon exiting the Calvin-Benson cycle via gluconeogenesis and for succinate derived from the glyoxylate cycle during acetate assimilation (Johnson and Alric, 2012). Additionally, just like neutral lipids, starch is an energy storage molecule produced in excess by *C. reinhardtii* under N limitation conditions (Siaut *et al.*, 2011; J Msanne *et al.*, 2012).

Figure 3.11 A shows that the carbohydrate content of the biomass in phototrophic conditions had a pronounced difference in profile for RA, WA and BA cultures. RA cultures maintained a higher carbohydrate content than the other two lights throughout the exponential growth phase. The similar growth and nutrient assimilation profiles for WA and RA cultures (Figure 3.3 A&C and Figure 3.5 A) suggest that similar amounts of carbon were fixed per gDCW in both conditions. As carbohydrate production is intrinsically linked to carbon fixation, it seems like the higher percentage accumulation of carbohydrates in RA cultures could be due to the smaller cell size developed under

those conditions (Figure 3.7 A). Carbohydrate increase and nitrogen depletion occurred concomitantly in WA cultures as expected (Johnson and Alric, 2013). Interestingly, RA cells saw a decrease (from 24% g gDCW<sup>-1</sup> at 48 hours to 10% g gDCW<sup>-1</sup> at 88h) in carbohydrate content coinciding with nitrogen depletion followed by a similar uptick (21% g gDCW<sup>-1</sup>) in the late stationary phase. The carbohydrate content in BA cells was stable during the growth phase (around 10% g gDCW<sup>-1</sup>) and decreased slowly during the stationary phase. BA cells did not exhaust all the ammonia in M8a (Figure 3.5 A) and therefore a large increase in carbohydrate content during the stationary phase would have been unexpected. However, the decline seen (down to 6% g gDCW<sup>-1</sup> at 136 hours) suggests BA cells had to expend their carbohydrate reserves for energy production in lieu of photosynthesis and carbon fixation. This is agreement with the poor growth seen in that experimental condition too.

The carbohydrate content followed very similar patterns WX and BX cultures (Figure 3.11 B). Under both lights, carbohydrates remained stable during the growth phase and increased during the early stationary phase. The path from assimilated carbon to starch is longer in mixotrophic than in autotrophic metabolism due to intracellular localisation of the pathways involved, namely the glyoxylate cycle and the Calvin-Benson cycle respectively (Lauersen *et al.*, 2016). This could explain the lack of carbohydrate content increase during growth seen in WX and BX cultures. As with phototrophic cultures, there was a higher maximum carbohydrate content in the biomass of WX cultures (31% g gDCW<sup>-1</sup> at 112h) compared with BX cultures (11% g gDCW<sup>-1</sup> at 88h), even though the rate of acetate assimilation was the same for both conditions. Such disparity between lights seen in both phototrophic and mixotrophic conditions suggests the effects of light wavelength on carbohydrate content are independent of the growth mode. Given the similar growth patterns between growth modes under each of the two lights, the difference in carbohydrate content could be due to the differences in biomass accumulation seen between white and blue light illuminated cultures. RX cells reached peak carbohydrate content at 16h of culture (26% g gDCW<sup>-1</sup>) after which the carbohydrate content decreased steadily, finally stabilising at the same amount as BX cells at 120h (9% g gDCW<sup>-1</sup>). This contrasts with RA cells which peaked at the end of the



stationary phase, with a carbohydrate percentage fraction of biomass four times larger than BA cultures at 136h.

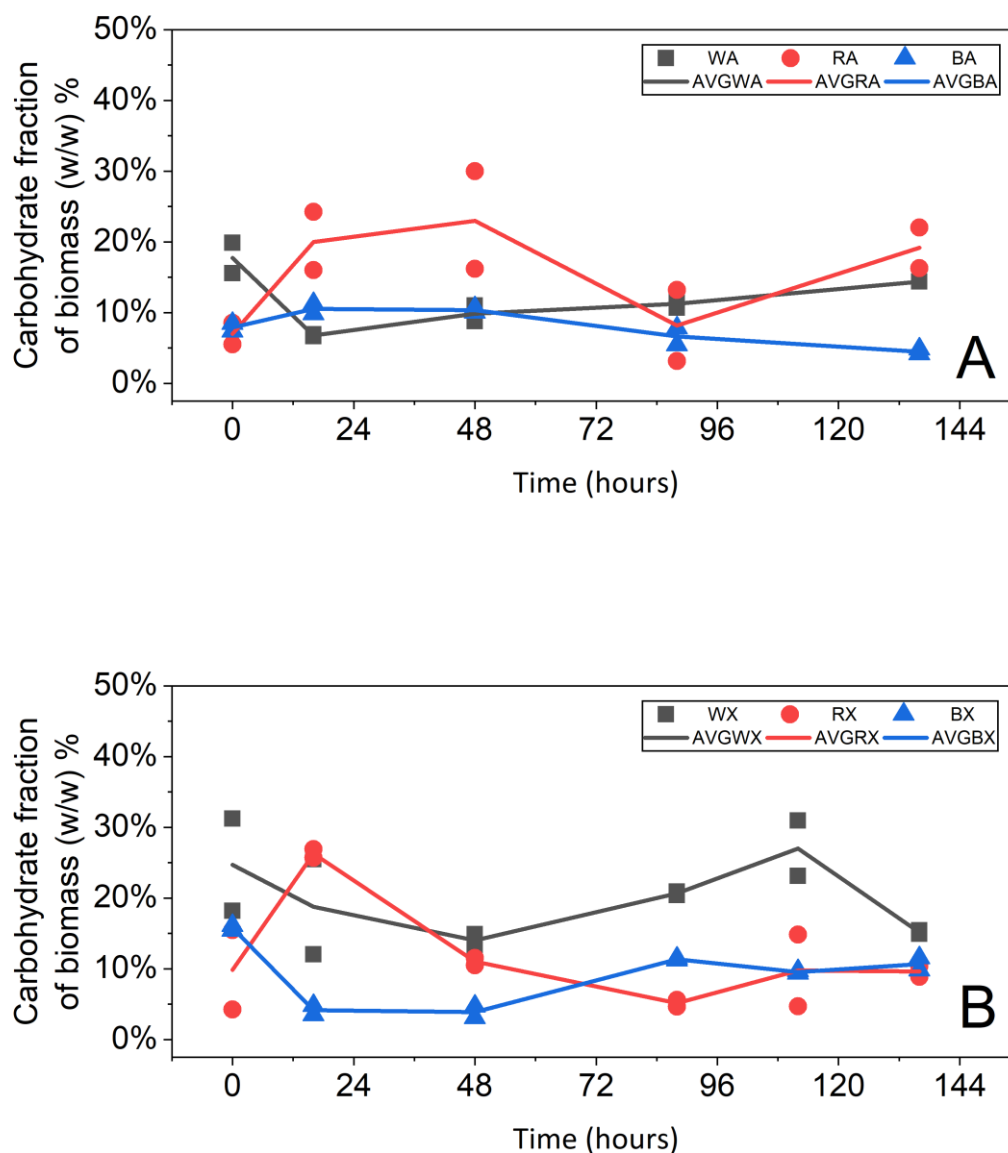


**Figure 3.11.** *C. reinhardtii* carbohydrate fraction as a percentage of biomass dry weight (w/w) over time. (A) Phototrophic batch cultures in M8a. (B) Mixotrophic batch cultures in M8a.Ac. Biological replicates plotted individually (Flask A – squares. Flask B – circles) Average plotted as a continuous line. W, white LED light; R, red LED light; B, blue LED light.

## Lipids

Wild-type *C. reinhardtii* has been shown to turn to autophagous behaviour, breaking down inner membrane structures rich in polar lipids, under N-deprivation conditions in order to produce fatty acid precursors necessary for neutral lipid (triacylglycerides) production (Davey *et al.*, 2014). The study also concluded that the breakdown of polar lipids was mitigated in mixotrophic conditions thanks to the direct production of acetyl-CoA from acetate (Davey *et al.*, 2014). The starting N concentration and the pH at the time of N depletion have been shown to affect final TAG yield (Gardner *et al.*, 2011) therefore the culture strategy chosen to arrive at N depletion is important. A prevalent strategy in literature for studying neutral lipid productivity in N-limited conditions is starting at a low-N concentration as opposed to zero-N; as the negative effects on growth when the latter strategy is employed are too detrimental to TAG yield (Stephenson *et al.*, 2010; Davey *et al.*, 2014; Kamalanathan, Gleadow and Beardall, 2017).

An exceptional increase in lipid as a percentage of dry cell weight was not expected as increases in neutral lipid content have been shown to be offset by the decrease in polar lipid content during nitrogen starvation in photoautotrophic conditions (Davey *et al.*, 2014). WA cultures were the only autotrophic condition that saw an increase in lipid content between the growth phase and the stationary phase (from 20% g gDCW<sup>-1</sup> to 28% g gDCW<sup>-1</sup>). Given that total lipids were measured and assuming the autophagous behaviour described in literature was maintained, the increase seen could be due to neutral lipids produced during the culture in phototrophic conditions (Figure 3.12 A).

The percentage lipid content in WX cultures dipped during the growth phase (from 40% g gDCW<sup>-1</sup> at 0 hours to 12% g gDCW<sup>-1</sup> at 48h) and increased to 20% g gDCW<sup>-1</sup> remaining stable from 88h onwards (Figure 3.12 B). A larger increase was seen in BX cultures (from 8% g gDCW<sup>-1</sup> at 48 hours to 23% g gDCW<sup>-1</sup> at 88h) which coincided with nitrogen and acetate depletion. Considering that BX cultures had a lower carbohydrate percentage than WX in the stationary phase (Figure 3.11 B), it seems that BX cultures directed more carbon towards lipid production whilst WX cells favoured carbohydrates. Just as with carbohydrates, the lipid content in RX cultures followed a similar pattern as in RA cultures showing that under red light the trophic growth mode seems to have less

of an impact on carbon storage allocation than under white and blue light (Figure 3.12 A&B).

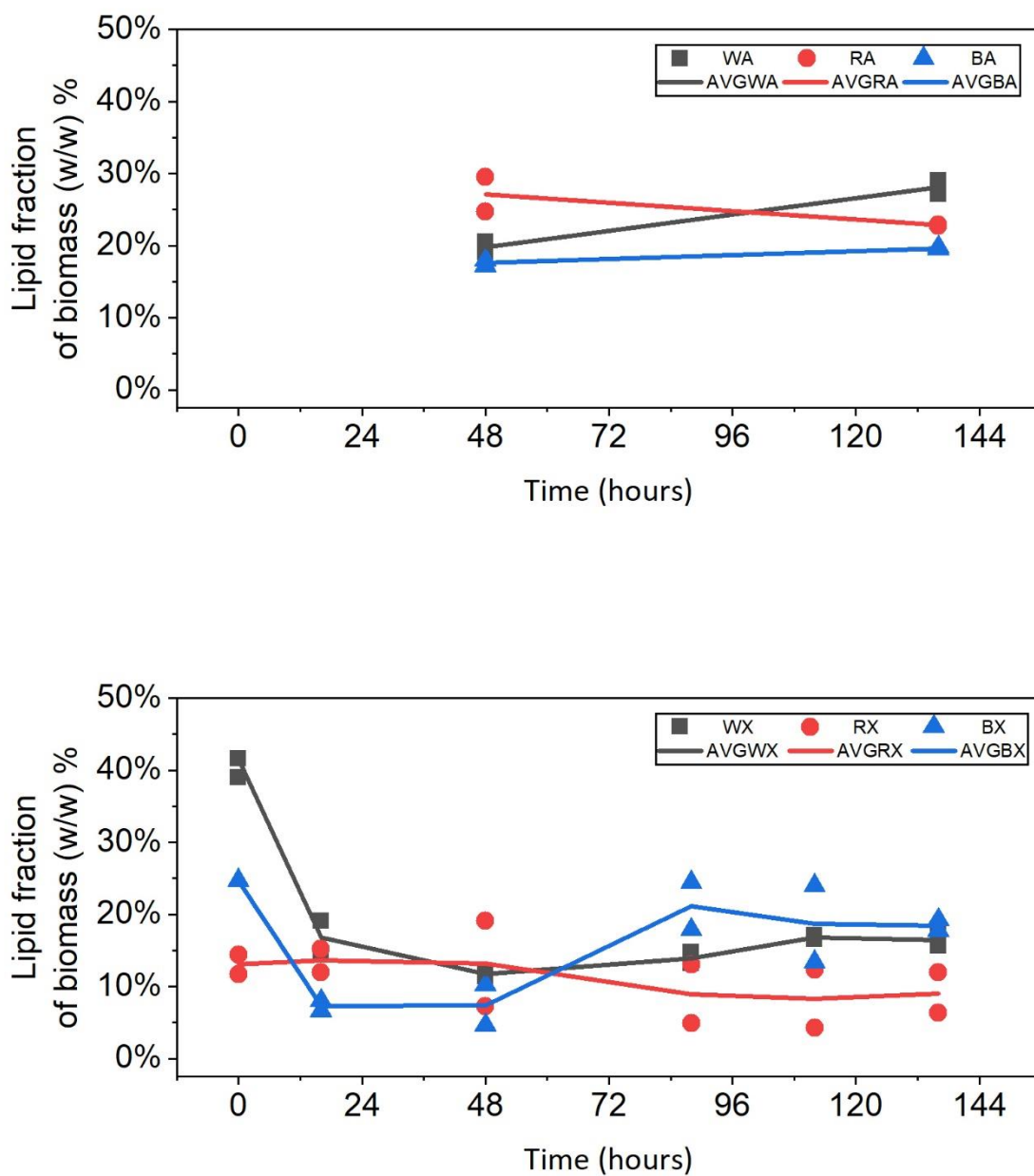


**Figure 3.12.** *C. reinhardtii* lipid fraction as a percentage of biomass dry weight (w/w) over time. (A) Phototrophic batch cultures in M8a. (B) Mixotrophic batch cultures in M8a.Ac. Biological replicates plotted individually (Flask A – squares. Flask B – circles) Average plotted as a continuous line. W, white LED light; R, red LED light; B, blue LED light.

## Protein

Protein content was positively correlated with growth in phototrophic cultures under all three lights (Figure 3.13 A). This was expected as during growth cells need to produce a large quantity of enzymes to maintain all cellular functions operational. Additionally, the *Chlamydomonas* cell wall is made up of glycoproteins rich in hydroxyproline and constantly dividing cells need higher amounts of cell wall components than non-dividing cells (Harris, 2013). Upon entering the stationary phase after depletion of nitrogen and as specific photons available per cell decrease due to the increased biomass concentration (Figure 3.3), overall protein content decreased in all cultures. Mixotrophic experiments had a much more stable protein content under all lights throughout the culture (Figure 3.13 B). This stable profile makes mixotrophic cultures conditions more appealing for microalgae marketed as nutritional supplements as protein content is an important quality attribute of those products (Gellenbeck, 2012). However, a well-controlled autotrophic culture harvested at peak protein content would yield a higher specific protein content and therefore be more beneficial to producers.

It must be noted that the *Chlamydomonas reinhardtii* cell wall has a high content of hydroxyproline-rich glycoproteins (Roberts, Gurney-Smith and Hills, 1972; Adair and Snell, 1990). Due to the lack of an amine linkage of this moiety on cell wall glycoproteins, the assay employed to measure protein content in this chapter would not capture the hydroxyproline content of the cell wall. This limitation of the experimental method chosen may be the reason for the lower than expected protein measurements obtained and could be remedied by employing liquid chromatography mass spectrometry methods (Ichikawa *et al.*, 2010).

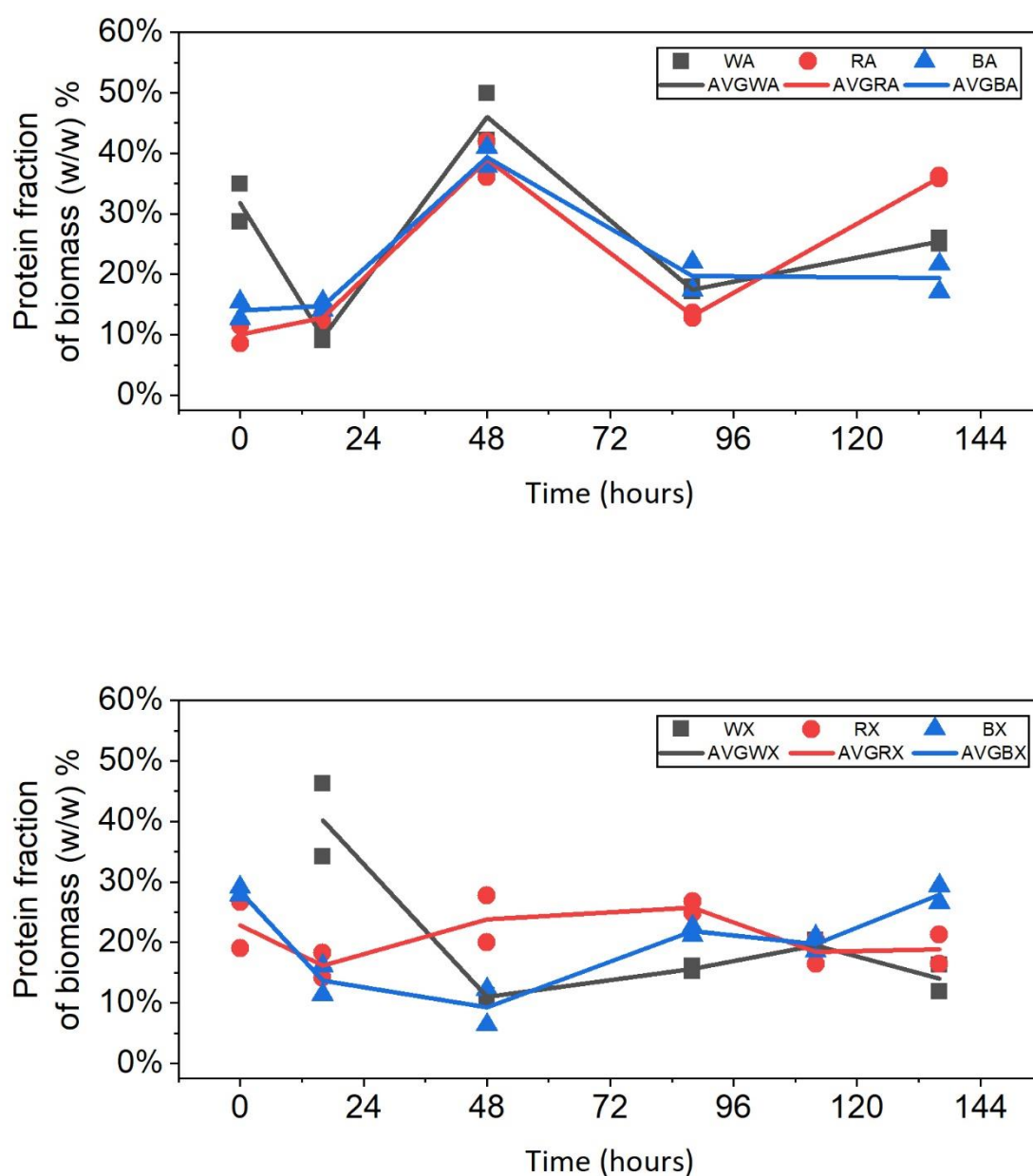


**Figure 3.13.** *C. reinhardtii* protein fraction as a percentage of biomass dry weight (w/w) over time. (A) Phototrophic batch cultures in M8a. (B) Mixotrophic batch cultures in M8a.Ac. Biological replicates plotted individually (Flask A – squares. Flask B – circles) Average plotted as a continuous line. W, white LED light; R, red LED light; B, blue LED light.

## Pigments

Pigments are the biomass component with the most reported data in the context of spectral composition studies. Their light absorbing properties tie them metaphysically to irradiance within a bioreactor and they are the main contributor to mutual shading effects (Burlew, 1953; Zittelli *et al.*, 2013). The functional role of chlorophylls in energy generation via photosynthesis (Perrine, Negi and Sayre, 2012) and of carotenoids in both photosynthesis and photo-protection (Hashimoto *et al.*, 2015) form an intrinsic link between light quality, pigments and microalgae metabolism. When culturing specialist producer species like *D. salina* and *H. pluvialis*, the focus lies on carotenoids like  $\beta$ -carotene and astaxanthin (Katsuda *et al.*, 2004; Xu and Harvey, 2019a) whilst chlorophylls have been primarily monitored in *C. reinhardtii* and *Chlorella vulgaris* studies (Mohsenpour, Richards and Willoughby, 2012; Wagner, Steinweg and Posten, 2016).

During the exponential growth phase, BA cultures produced the highest amount of total pigments per gram of biomass (peaked at 5.5% g gDCW<sup>-1</sup> at 48 hours; Figure 3.14 A&B). Photosynthetic electron flow (EF) is reconfigured between autotrophic and mixotrophic growth, as cyclic EF increases and linear EF decreases. Cyclic EF around PSI recycles NADPH whilst enabling oxidative phosphorylation and the production of ATP for acetate assimilation (Johnson and Alric, 2013). This reconfiguration of photosynthetic stoichiometry is not reflected in the total pigment content of *C. reinhardtii* suggesting that other factors regulate pigment content. Another factor that can affect pigment content is the compatibility of the impinging light spectrum with the cell's specific pigment absorption spectrum as this will dictate how much light is absorbed per cell. Poorly absorbed light wavelengths could lead to an overproduction of pigment to capture as much light as possible. This holds true at a very low light intensity of 25  $\mu\text{mol}_{\text{ph}} \text{m}^{-2} \text{s}^{-1}$  where red and blue light illuminated cultures were shown to accumulate less pigments compared to white light illuminated cultures (Wagner, Steinweg and Posten, 2016). However, chlorophyll a and b have their peak absorption in the blue region (420-450 nm) and blue light cultures in both trophic strategies produced the highest amount of pigment per gram of biomass. Similar results were obtained in cultures that controlled for specific light absorption using a turbidostat,



including no changes in the cross-section absorption spectrum of *C. reinhardtii* between different monochromatic lights (Mooij *et al.*, 2016). Another study with *C. reinhardtii* and monochromatic LEDs obtained the same results (Ajayan *et al.*, 2019). This suggests pigment content is subject to regulation by other factors apart from light quality.

A decrease in total pigment content in the stationary phase of batch cultures is typically linked to the exhaustion of inorganic nitrogen in the media and cessation of cell division leading to the recycling of the photosynthetic apparatus for production of storage macromolecules (Davey *et al.*, 2014; Ajayan *et al.*, 2019). It is interesting to note that even for cultures where ammonium was depleted at the 72h mark (Figure 3.5 A&B), there was no pigment loss registered in the late stationary phase at 136h (Figure 3.14 A&B). Assimilation of inorganic nitrogen in the form of nitrate or ammonia by microalgae results in a net proton imbalance (Scherholz and Curtis, 2013) which leads to significant pH deviations in non-pH controlled autotrophic cultures. The studies that report a loss of pigmentation upon the depletion of nitrogen are not pH controlled so active growth can be assumed to lead to a large pH difference from the start to the end of the culture. Given the tight pH control in our experiments it can be expected that culture conditions are more favourable for cell homeostasis at the 136h mark than they would be in a non-pH-controlled system and this could be linked to the lack of pigment loss. Additionally, BX cultures showed an increased amount of percentage pigments in the late stationary phase compared to the mid-exponential growth phase (from 2.5% g gDCW<sup>-1</sup> at 48 hours to 5.5% g gDCW<sup>-1</sup> at 136h). Overall, the pigments fraction of biomass was different for each light but comparable between trophic modes. This corroborates the maintained relevance of photosynthetic activity during mixotrophic growth discussed in section 3.4.

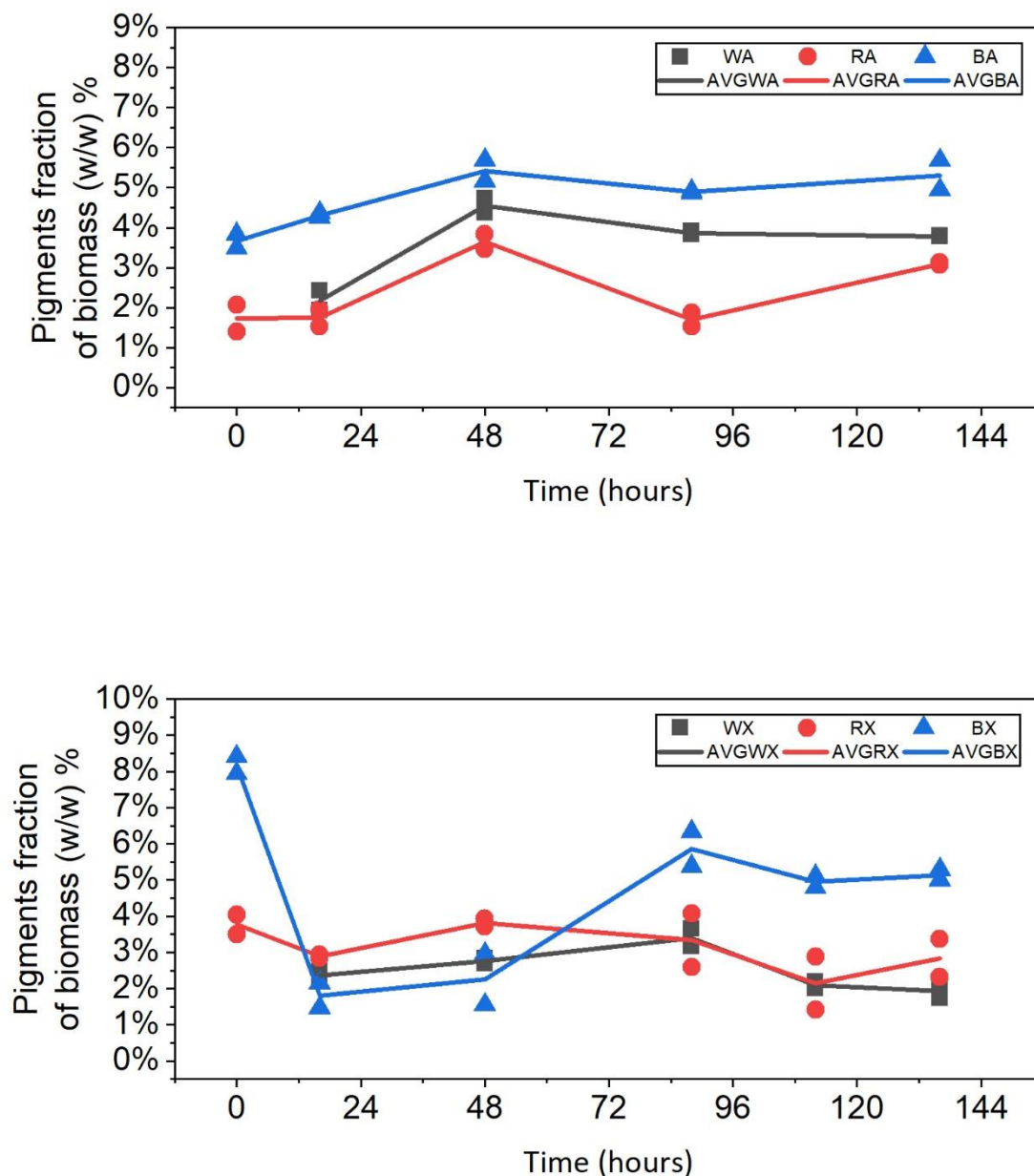


**Figure 3.14.** *C. reinhardtii* pigment fraction as a percentage of biomass dry weight (w/w) over time. (A) Phototrophic batch cultures in M8a. (B) Mixotrophic batch cultures in M8a.Ac. Biological replicates plotted individually (Flask A – squares. Flask B – circles) Average plotted as a continuous line. W, white LED light; R, red LED light; B, blue LED light.

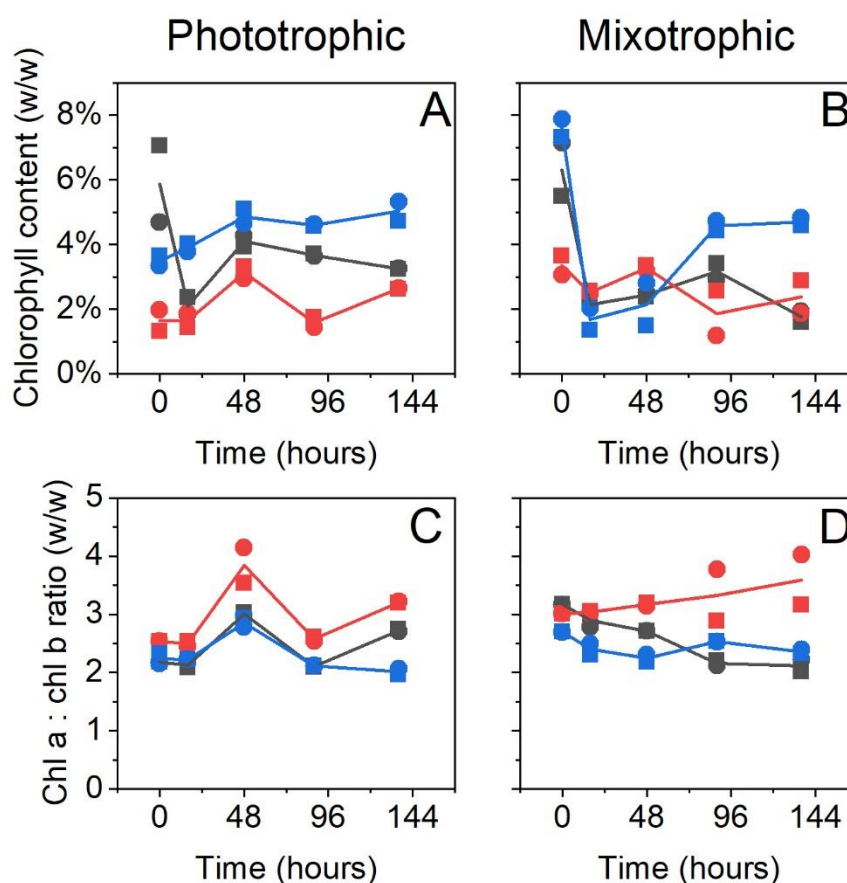


**Figure 3.15.** Chlorophyll content and composition during an entire batch culture. (A,B) Chlorophyll content as a percentage of total biomass. (C,D) Chlorophyll a to chlorophyll b ratio. The two biological replicates (n=2) are indicated by squares (Flask 1) and circles (Flask 2) respectively. Solid lines indicate the average across the biological replicates for each condition. Black symbols and lines used for white light; Red symbols and lines used for red light 640-670nm; Blue symbols and lines used for blue light 440-480nm.

Microalgae have evolved in multi-species habitats where absorbing more light than necessary is a desirable evolutionary trait due to the competition for available light with other species. However, this can lead to the over-absorption of light in high light environments and thus a decrease in photoconversion efficiency (PCE). This is not a desirable trait for industrialisation as maximising PCE should lead to maximised process yields. It has been found in literature that the chlorophyll a to chlorophyll b ratio (chl a/b ratio) is inversely correlated with the percentage of photosystem II (PSII) saturation and therefore light absorption capacity of microalgae (Perrine, Negi and Sayre, 2012). We found the chl a/b ratio in WA cultures (between 2.2 and 2.7; Figure 3.15 A) to be in the

same range as previously published results (Polle, Kanakagiri and Melis, 2003). Interestingly, the chl a/b ratio was higher in RA cells than WA and BA cells throughout the whole batch culture (Figure 3.15 A). This mimics previously published results for *Chlorella sp* (Senge and Senger, 1991) and suggests that the photosynthetic apparatus is altered under a lack of short wavelengths of the PAR spectrum such as narrow band blue LED light. Thus, higher PCE can be expected under red light illumination in mass cultivation conditions. RX cultures maintained a higher chl a/b ratio than cultures under the other two light conditions (Figure 3.15 B). Whilst under phototrophic conditions the chl a/b ratio peaked during exponential growth under all three lights, in mixotrophic conditions each light resulted in a unique pattern.

### 3.5. Discussion

#### Biomass accumulation and nutrient uptake kinetics

The choice of wavelength distribution affected the final biomass accumulated after 136 hours of batch culture in autotrophic conditions (Table 3.2). From an energetic perspective, the wavelength of a photon is inversely proportional to the energy transmitted by said photon. The lowest energy photons in the PAR range are red. Their relatively low energy suffices to drive the required electron excitation at the reaction centres of PSII and PSI for photosynthesis to take place. Therefore, the additional energy supplied by incident light on WA cultures does not explain the increased biomass yield seen in white light cultures (Table 3.5). It could explain the poor performance of blue light cultures as they would have received the largest energetic photon flux per cell at the early stages of the experiment, and this might result in increased photodamage compared to the other two light conditions. However, light is a complex critical process parameter (CPP) and the energetic perspective is not the only facet of import when evaluating the effect of illumination on a microalgal culture. The specific absorption profile of the microalgae pigments as well as biomass concentration will also play a large role in determining the specific amount of energetic photon flux absorbed per cell (Blanken *et al.*, 2013, 2016).

From a metabolic regulation perspective, blue light is a key component of the incident light wavelength-distribution due to the crucial role of phototropin in the expression of pigment biosynthesis-related genes, eyespot size regulation and expression of other photoreceptors (Kianianmomeni and Hallmann, 2014). In a seminal study by Petroutsos and colleagues (2016) it was shown that enhanced thermal dissipation via high-energy quenching (qE) is dependent on detection of blue light by a phototropin in *C. reinhardtii*. The regulatory importance of blue light could explain the increased biomass production of phototrophic *C. reinhardtii* cultures illuminated with the balanced wavelength distribution of white LEDs compared to the narrow wavelength distribution of red LEDs. The balanced wavelength distribution of white LEDs is typically made-up of a blue wavelength peak and a broad shoulder encompassing the remainder of the visible light spectrum, this enables the correct regulation of the aforementioned areas of metabolism improving the viability of a microalgal culture. Interestingly a blue and red-light regulated photoreceptor protein, CrCRYa, has been recently discovered in *C. reinhardtii* (Beel *et al.*, 2012). This newfound cryptochrome is the first evidence of red-light regulated metabolism in the model algae. The discovery of CrCRYa means other red light-regulated photoreceptors might yet remain undiscovered in *C. reinhardtii*. Such red/far-red light activated photoreceptors are typically referred to as phytochromes and are common in both higher plants like *Arabidopsis thaliana* (Clack, Mathews and Sharrock, 1994) and cyanobacteria like *Fremyella diplosiphon* (Wiltbank and Kehoe, 2016).

The reduced influence of light quality in mixotrophic cultures is a novel observation obtained from this set of experiments. The identical acetate uptake rates observed between the three mixotrophic conditions (Figure 3.5 C) indicate they would all reach the same final biomass concentration. However, the lower final biomass concentration of blue light cultures shows that once the organic carbon source is exhausted, the importance of the incident light spectrum on metabolism is re-instated as cells switch to autotrophic metabolism in a very short time just as the switch from cell duplication to energy accumulation observed under stress conditions described in Chapter 2. During the final autotrophic growth phase of mixotrophic cultures the influence of blue light on the cell cycle may also affect the final biomass concentration

in BX. *C. reinhardtii* cells are thought to progress through a cell division commitment check point during the vegetative cell cycle (Münzner and Voigt, 1992; Cross and Umen, 2015). The time taken to reach this commitment point determines the final cell size before cell division as well as the total number of cell divisions within a cell cycle. Blue light has been shown to delay the commitment point, allowing for increased cell size thus extending the total length of the cell cycle too (Oldenhof *et al.*, 2004; Oldenhof, Zachleder and Van Den Ende, 2006).

A slight lag phase up to 16 hours of culture was only observed in the cell concentration measurements of mixotrophic cultures (Figure 3.3 D). This indicates that cells in M8a.Ac took longer to resume their cell division upon inoculation compared to cells inoculated in M8a. This lag also influenced the final cell concentration. The final 24h of the linear growth phase preceding stationary phase were more productive for M8a cultures compared to M8a.Ac cultures. This might be due to the depletion of acetate triggering a more abrupt metabolic reconfiguration, forcing cellular metabolism towards storage molecule production as opposed to a switch towards phototrophic growth metabolism. M8a cultures on the other hand grew phototrophically throughout and as biomass concentration increased and specific light available decreased, they transitioned to stationary phase metabolism.

The reduction in cell proliferation rate after acetate exhaustion could be due to several factors combined. The biomass concentration reached in mixotrophic cultures at 64 hours (Figure 3.3 D) was high enough for light levels to be limiting as demonstrated by autotrophic cultures not growing exponentially at such concentrations (Figure 3.3 C). Additionally, ammonium was also exhausted after up to 64 hours in WX, RX and BX cultures, although there is abundant literature on intracellular nutrient quotas in microalgae and the uncoupling of nutrient depletion and growth arrest (Droop, 1968; Benavides *et al.*, 2015). Another factor could be the metabolic reconfiguration required to switch from mixotrophic to phototrophic metabolism, which would potentially delay the re-initiation of cell proliferation (Johnson and Alric, 2012).

### Linking cell size and biomass distribution to photoprotection

The effect of wavelength selection on cell size of *C. reinhardtii* has been documented in literature in the context of cell cycle regulation (Oldenhof, Zachleder and Van Den Ende, 2004b, 2006). The experiments presented in this chapter corroborate the increase in average cell size of *C. reinhardtii* under blue LED illumination and the decrease in average cell size under red LED illumination compared to white LED illumination (Figures 3.4-3.8). A hypothesis for the increased growth rate observed under red LED light illumination versus blue LED illumination (Table 3.3) is related to cell size and the risk of electron transport chain over-reduction (Hansberg and Aguirre, 1990). The regulatory effects of blue LED light leading to a longer cell cycle and thus a larger average cell size during vegetative growth result in a lower risk of oxygen penetration into the microalgal cell. On the other hand, smaller cells resulting from red LED illumination have a risk of becoming oversaturated with oxygen. Dangerous reactive oxygen species (ROS) are created when oxygen receives energy from excited chlorophyll molecules in the chloroplast leading to the creation of  $^1\text{O}_2$ ; and  $\text{H}_2\text{O}_2$ ,  $(\text{O}_2^{\cdot-})$ , and  $\text{OH}^{\cdot}$  are formed by direct electron transfer from either the photosystem I reaction centre or reducing equivalents like NADPH (Erickson, Wakao and Niyogi, 2015). To avoid over accumulation of ROS, small cells must expend reducing equivalents at a faster rate than larger cells, thus driving faster anabolism and cell growth rate.

As noted above, the influence of wavelength selection on *C. reinhardtii* physiology was dampened under mixotrophic conditions. This dampening was not evident in cell size measurements in the exponential growth phase (Figure 3.9 A). However, it resulted in closer cell sizes between different illumination conditions in the late stationary phase in mixotrophic cultures (Figure 3.10 B) than in autotrophic cultures (Figure 3.9 A). The exhaustion of acetate at 48 hours triggered an early reduction in cell division rate under white and red light (Figure 3.5 C). This resulted in a significant disparity in average final cell concentrations between trophic modes under these two lights (Table 3.8). However, it did not immediately trigger senescence, the OD 750 nm profile attests to continued productivity potentially indicating that a metabolic shift towards increased production of storage molecules occurred. Carbohydrate content increase after 72 hours in WA and RA cultures as did lipids in WA cultures. Lipid production acts as an electron sink

preventing over-reduction of the electron transport chain when nitrogen depletion prevents photosystem repair and there is an over accumulation of reducing equivalents in the chloroplast as not enough ATP is produced to drive the Calvin Benson cycle and drain maintain ETC homeostasis (Hansberg and Aguirre, 1990; Erickson, Wakao and Niyogi, 2015).

### **Limitations of experimental design**

Measurements of the macromolecular components are reported in literature with varying degrees of detail. Biochemical assays like the ones described in the methods section of this chapter are typically employed to obtain estimates for the total amount of each component. Further detail, the molecular composition of said macromolecules, can be obtained with various analytical methods like high-performance liquid chromatography (HPLC), thin layer chromatography (TLC), gas chromatography (GC) and mass spectrometry (MS), each with their own limitations (Lisec *et al.*, 2006; Del Val *et al.*, 2013; Kobayashi *et al.*, 2013). Increased resolution can be informative however a single analytical method does not fit all and the development of protocols for each method fell outside the remit of this thesis. When estimating macromolecular composition, some studies do not attempt a mass balance to reconcile the measured constituents with the total weight per cell as not all constituents are measured (Xia and Gao, 2005; Faraloni *et al.*, 2011). When a mass balance is included, the difference is typically less than 5% (Ike *et al.*, 1997; Wagner *et al.*, 2010). In some cases, not all macromolecular groups are measured. A perfect mass balance is assumed in order to calculate the remainder of the cell's weight (Boyle and Morgan, 2009).

The biochemical assays described in the methods section of this chapter were scaled down from their classical counterparts to reduce biovolume required per assay. This increased the feasible number of assays per experiment whilst keeping sampled volume to a minimum. It also increased throughput as they were performed in 96 well plates, paving the way for automation of these non-trivial techniques. However, the small culture volumes employed were not measurable by standard dry cell weight techniques. In traditional cell culture experiments, obtaining percentage dry weight measurements of macromolecules with these assays was possible due to the large



amount of starting material utilised. The scaled down versions developed in this thesis involved a conversion from g macromolecule per cell to g macromolecule per g dry cell weight. The errors associated with the cell concentration measurement and each of the assays were compounded into relatively large discrepancies compared to those seen in literature between the measured dry cell weight per volume of culture and the sum of each macromolecular component measured as explained in the materials and experimental methods section. Such discrepancies are certainly a limitation of the methods employed and could be remedied in future work by scaling down dry cell weight measurements. Freeze-drying small pelleted aliquots could be a viable alternative to the filtration and oven drying method commonly employed which requires prohibitive amounts of biomass in the context of limited biovolume availability.

### 3.6. Conclusions

The systematic evaluation of the effects of monochromatic illumination and trophic mode on the physiology and biochemical composition of *C. reinhardtii* presented in this chapter offers a well-rounded base line to inform early process development efforts and further monochromatic illumination studies. The balanced light spectrum of white LEDs resulted in a higher maximum growth rate and superior biomass accumulation when compared to either extreme of the PAR range in pH controlled autotrophic conditions. When an organic carbon source was present in the medium, the more energy efficient red LEDs resulted in a final biomass concentration comparable to white LEDs, although the maximum growth rate was 22% higher under white LEDs (Table 3.3). The trade-off between the energy cost savings accrued from red LEDs versus the time taken to reach a high enough biomass concentration could be an important factor to consider when selecting an illumination strategy. The poor performance of BA cultures in terms of  $\mu_{\max}$  (Table 3.3) and final biomass concentration (Figure 3.3 A&C) was remedied in BX cultures where at least  $\mu_{\max}$  was comparable to RA and RX cultures (Table 3.3). Optimisation of mixotrophic culture conditions under blue LED lights could make the illumination strategy a viable option.

There was great similarity in nutrient assimilation rates for both inorganic nitrogen and organic carbon between all conditions. However, there were significant differences

in cell concentration (Figure 3.3 C) and cell size (Figure 3.9) which resulted in the yield of cells on nitrogen ( $Y_{C/NH_4^+}$ ) to vary significantly between WA ( $432 \times 10^6 \text{ cells mgNH}_4^{+1}$ ), RA ( $325 \times 10^6 \text{ cells mgNH}_4^{+1}$ ) and BA ( $107 \times 10^6 \text{ cells mgNH}_4^{+1}$ ) cultures. The holistic perspective achieved by combining the cell concentration, nutrient uptake and cell size data, helps formulate the hypothesis that the effect of illumination wavelength on  $Y_{C/NH_4^+}$  values in autotrophic culture is linked to metabolic differences between the cultures.

The proximal analysis of *C. reinhardtii* biomass throughout a batch culture is seldom reported in a time-dependent manner for all major components. Such granularity uncovered insights into the effects of monochromatic illumination on microalgae metabolism at different stages of the batch culture. Admittedly these experiments performed in batch mode are not the ideal design to answer fundamental questions about the relationship between absorption of light at different wavelengths and its effects on metabolism. Continuous cultures performed in turbidostat mode where specific light absorption per cell is kept constant (Mooij *et al.*, 2016) would provide more comparable conditions from a specific light absorption perspective. However, for the purpose of investigating the effects of constant illumination at a constant intensity these experiments helped identify metabolic differences between the conditions studied as discussed in Section 3.5.

### *Development of reliable tools for the evaluation of key physiological differences at the transcriptional level in *C. reinhardtii**

#### 4.1. Introduction

Freshwater microalgae, like *Chlamydomonas reinhardtii*, have evolved an extensively versatile metabolism that increases their chances of survival in diverse environmental conditions in the presence (mixotrophy) or absence (autotrophy) of a readily available source of nutrients (Grossman *et al.*, 2007). Due to this metabolic plasticity, and despite significant research efforts, our knowledge of algal metabolism remains nascent, relative to other crops, and our control over biomass composition remains rudimentary (Jungandreas *et al.*, 2014). One of the main reasons that fully understanding algal metabolism and how it responds to varying environmental and bioprocessing conditions is far from trivial is the uniqueness of incident light as a critical process parameter. The effects of light on microalgal physiology are mediated by a variety of specialised, light harvesting and light sensing molecules. Chlorophylls, carotenoids, rhodopsins, phototropins and cryptochromes each have a unique absorption spectrum and are involved in different cellular processes like photosynthesis, phototaxis (Sineshchekov, Jung and Spudich, 2002) or cell cycle control (Huang and Beck, 2003; Müller *et al.*, 2017).

In addition, light in and of itself is complex in nature as it can vary in terms of intensity, photoperiod and spectral composition. Light intensity has a well-documented and characterised positive effect on biomass growth both under phototrophic and mixotrophic conditions (Ooms *et al.*, 2016). However, excessively high light intensities have been shown to trigger stress responses, like carotenoid production, in a number of algal species (Steinbrenner and Linden, 2003; Lamers *et al.*, 2008) or even completely inhibit growth

(photoinhibition)(Carvalho *et al.*, 2011). Phototrophic studies on biomass growth of *C. reinhardtii* have shown that below saturating light levels ( $25 - 100 \mu\text{mol}_{\text{ph}} \text{m}^{-2} \text{s}^{-1}$ ), illumination with red and red-blue light can achieve a higher biomass yield on photons compared to white light (Wagner, Steinweg and Posten, 2016). However, at or above saturating light intensities ( $>1500 \mu\text{mol}_{\text{ph}} \text{m}^{-2} \text{s}^{-1}$ ) the yield of biomass on photons was found to be inversely proportional to the specific photon absorption rate. Consequently, illumination at wavelengths considered to be sub-optimal due to their relatively low specific absorption rate (e.g. illumination with yellow and warm white light) has been found to yield higher biomass yields than red or blue light at high light intensities (Mooij *et al.*, 2016).

The advent of light emitting diodes (LEDs) has enhanced our ability to accurately control several properties of incident light, beyond intensity, and investigate their effects on biomass growth and biochemical composition (Pattison *et al.*, 2018). This has enabled in depth investigations of the effects of the frequency and duration of light/dark cycles, spanning timescales from milliseconds to hours (diel-cycle) (Amini Khoeyi, Seyfabadi and Ramezanzpour, 2012; S. K. Wang *et al.*, 2014; Abu-Ghosh *et al.*, 2016). Studies on the impact of light quality on biomass composition, primarily focused on pigment and/or lipid content in specialised producer species like *Haematococcus pluvialis* and *Phaeodactylum tricornutum* [16], have shown a variety of possible responses across species. Therefore, there is a need to understand the diverse and complex effects of the spectral composition of incident light on microalgal physiology and metabolism.

Associating gene expression profiles with changes in microalgal physiology under narrow band illumination can help unravel the specific effects of discrete regions of the photosynthetically active radiation (PAR) region of the visible light spectrum (400 – 750 nm). However, relative quantification of reverse transcription-quantitative real time polymerase chain reaction (RT-qPCR) measurements requires the existence of a set of reference genes with stable expression profiles across a variety of culture conditions. A number of studies have previously proposed candidate reference genes for *C. reinhardtii* with no clear consensus available in the literature due to the limited number of experimental conditions examined in each study (Rosic *et al.*, 2011; Liu *et al.*, 2012; Guo, Lee and Ki, 2013). A comprehensive study

of the stability of four candidate reference genes under nitrogen deprivation both in photoautotrophic and mixotrophic conditions was recently published (Smith and Gilmour, 2018), however is limited to only white light illumination. An extensive transcriptomic analysis of *C. reinhardtii* gene expression under a variety of nutrient depletion conditions has been recently published (Schmollinger *et al.*, 2014).

Given the biotechnological potential of triggering desired responses in a microalgal culture by utilising a tailored spectral composition, this study investigates the effects of wavelength selection and trophic strategy on gene expression in *C. reinhardtii*. The genetic responses elicited by monochromatic LEDs with narrow peak intensities at the two extremes of the PAR range (Blue, 440-480nm and Red, 640-670nm) under phototrophic and mixotrophic conditions were compared against white light control cultures. A set of 10 candidate reference genes was compiled from literature and their stability was assessed across all 6 experimental conditions. The novel reference genes identified herein, coupled with dynamic biomass and pigment content measurements, were used to evaluate the effect of wavelength and trophic strategy induced changes at key metabolic nodes. Finally, the expression levels of promoter genes and/or 5'-/3'-untranslated regions (5'-/3'-UTR) previously targeted for the expression of recombinant proteins in *C. reinhardtii* were characterised to discern favourable illumination conditions and trophic strategies.

## 4.2. Aim & Objectives

The aim of this chapter is to characterise and compare the effect of narrow band illumination at two extremes of the photosynthetically active radiation (PAR) range on the central carbon metabolism gene expression of *C. reinhardtii* in batch cultures with two different trophic strategies (phototrophic and mixotrophic). This can be broken down into the following scientific objectives:

- Optimise the cell lysis step of ribonucleic acid (RNA) extraction from *C. reinhardtii* cell pellets for maximisation of yield, integrity and purity of extracted RNA
- Compare the expression stability of a panel of literature based and novel reference genes (10 in total) to validate future RT-qPCR studies
- Evaluate the effect of wavelength and trophic strategy on gene expression at key metabolic nodes – the Calvin-Benson cycle, tricarboxylic acid (TCA) cycle, glyoxylate cycle and fatty acid synthesis.
- Evaluate the effect of wavelength and trophic strategy on gene expression of commonly used in recombinant protein expression with *C. reinhardtii*

## 4.3. Materials and methods

### 4.3.1. Ribonucleic acid (RNA) extraction

Initial ribonucleic acid extraction efforts were performed with RNeasy spin-column extraction kit (Qiagen, UK) following the manufacturer's instructions. As discussed in section 4.41 extraction yield was lower than expected and optimisation experiments resulted in the final RNA extraction protocol described below.

#### Final RNA extraction protocol

Samples containing  $5 \times 10^6$  cells were centrifuged for 5 minutes at 12,000g (Eppendorf 5415, Cambridge, UK) under constant temperature (4°C). The supernatant was aspirated and discarded, and the cell pellet was stored at -80°C for up to 4 months until further processing. RNA extraction was performed in 2 mL MaXtract High Density Tubes (Qiagen, Venlo,

Netherlands) using TRIzol® (Invitrogen, Carlsbad, US) and following the manufacturer's instructions. GlycoBlue™ Coprecipitant (Invitrogen, Carlsbad, USA), dissolved in 50 µL of RNase-free TE buffer (Sigma-Aldrich®), was used to stain the nucleic acid pellet. Contaminating gDNA was removed with RNase-free DNase (Qiagen, Venlo, Netherlands) according to the manufacturer's protocol. RNA integrity was assessed with a 1% ethidium bromide stained agarose gel in TBE buffer. RNA purity and concentration were assessed using a NanoDrop spectrophotometer (Thermo Fisher). Ratios of absorbance readings at 260/280 nm and 230/260 nm ratios displayed little variability ( $2\pm0.1$ ) and indicated a lack of phenol contamination from the TRIzol based extraction.

#### **4.3.2. Primer design**

Gene primers for RT-qPCR were designed following the Minimum Information for Publication of Quantitative Real-Time PCR Experiments (MIQE) guidelines. Gene sequences were obtained from the *Chlamydomonas reinhardtii* genome v5.5 in the Phytozome database (Goodstein *et al.*, 2011). A custom set of parameters prioritising primer pairs that span intron-exon junctions was used to select primer sequences in primer3 (Untergasser *et al.*, 2012). Primer quality was assessed with PCR Primer Stats (Stothard, 2000). Melt curve analysis with no template controls (NTC), no reverse transcription controls (NRT) and positive controls was used to ensure each primer pair gave rise to a single, well-defined peak from extracted RNA. Serial and linear dilutions were used to establish the log-linear dynamic range for each primer pair and primer efficiency. Starting RNA and primer mix concentrations were optimised over three orders of magnitude ( $1.5\text{-}150\text{ ng }\mu\text{L}^{-1}$  and  $0.9\text{-}90\text{ }\mu\text{M}$  respectively).

#### **4.3.3. Quantitative Reverse Transcription Polymerase Chain Reaction (RT-qPCR)**

RT-qPCR was carried out with a Luna® Universal One-Step RT-qPCR Kit (New England Biolabs, MA, US) on a CFX 96 connect Real-Time PCR System (Bio-Rad, CA, US). Individual RT-qPCR reactions had a total volume of 20 µL made up of 10 µL Luna Universal One-Step Reaction Mix (2X), 1 µL Luna WarmStart® RT Enzyme Mix (20X), 2 µL forward and reverse primer mix (9 µM), 5 µL RNA (75 ng) and 2 µL Nuclease-Free Water. Thermal cycling was programmed according to the kit manufacturer's instructions. In short, 1 cycle of reverse

transcription at 55°C for 10 minutes followed by 1 cycle of initial denaturation at 95°C for 1 minute and 40 cycles of denaturation and extension at 95°C (for 10 seconds) and 60°C (for 30 seconds) respectively. A 60-95°C melt curve was generated to evaluate primer specificity and gDNA contamination.

#### **4.3.4. Reference gene selection and statistical analysis**

A panel of 10 candidate reference genes was compiled from literature (Table 4.1). A set of six diverse experiments including combinations of three different wavelengths and two different trophic strategies was designed to evaluate stability in expression levels. Expression levels of the candidate genes (Table 4.1) were measured by RT-qPCR with samples taken 16, 48 and 136h hours post inoculation and analysed with the qBase+ software package (Biogazelle). The geNorm algorithm (Vandesompele *et al.*, 2002; Hellemans *et al.*, 2007) was used to calculate the coefficient of variation of the normalised reference gene expression levels (CV) and the geNorm stability M-value (M) was used to rank candidate reference genes from least to most stable. Gene expression data were further analysed by performing 3 (W, R, B) by 2 (A, X) factorial ANOVAs to evaluate main and interaction effects of wavelength and trophic strategy on the average relative expression of each gene of interest. Multiple comparisons with Benjamini-Hochberg correction were performed in the statistical software R (version 3.6.1).



**Table 4.1** List of candidate reference genes monitored in this study with RT-qPCR.

Gene	Gene name	Forward Primer (5'-3')	Reverse Primer (5'-3')	Used as reference gene in	Phytozome ID
<b>ATPD</b>	ATP synthase delta chain, chloroplastic	G TTCCTGATCGCCAAGAAGC	GAGTCAATCACGGGCTTCAG	This study	Cre11.g467569.t1.1
<b>RPL-19</b>	Ribosomal protein (large subunit) 19	CCTGAAGAAGTACCGCGACTC	AACACGTTACCCTTGACCTTCA	Liu12	Cre02.g075700.t1.2
<b>RACK1</b>	Receptor of activated protein kinase C	AAGACCATCAAGCTGTGGAACA	TTCCAGACCTTGACCATCTTGT	Siaut07,Beel12	Cre06.g278222.t1.1
<b>RPS-10</b>	Ribosomal protein (small subunit) 10	CTGGTGACTGAGCGCTTCT	GGGCGGTTGGACTTCTTCA	Siaut07,Liu12	Cre09.g411100.t1.2
<b>ch3-II</b>	Histone H3	GAGATTGCCCAGGACTTCAAGA	GATGTCCTTGGGCATGATGGTC	This study	Cre17.g708700.t1.2
<b>psaD</b>	Photosystem I reaction centre subunit II	GACACTCCCAGCCCGATTTC	CCAGGTGATGACGTAGAACTCC	This study	Cre05.g238332.t1.1
<b>ACX1</b>	Acetyl-CoA carboxylase subunit $\alpha$	AGCAAGACTCTGGTTAGCGATG	CCCAAAGCGAGACAGGATAGTG	This study	Cre12.g519100.t1.2
<b>PSRP-</b>	Plastid specific ribosomal protein (small subunit) 1	GCAAGAAGGAGCAGAAGGTAGA	TCCTTGATCTTCTGGAGCTTGG	This study	Cre05.g237450.t1.2
<b>STA1</b>	ADP-glucose pyrophosphorylase large subunit 1	CTCGGTGCTGTCCATCATTCT	GTTGAGGGAGGTCGAGTTGAA	This study	Cre13.g567950.t1.2
<b>DLA3</b>	Dihydrolipoamide acetyltransferase component of pyruvate dehydrogenase	TTCTGTCTCGGTGCTTCTCAGG	TCGTCCTGGTTTTCAAATGCCA	This study	Cre06.g252550.t1.1
<b>RBCS</b>	Ribulose biphosphate carboxylase small subunit	ACCCCGGTCAACAACAAGATG	GTCGTAGTACAGGCAAGACACG	NA	Cre02.g120150.t1.2
<b>FUM1</b>	Fumarate hydratase	AGAACTGCATCAAGAAGGTGGA	AGAAGTCGTTACCCTTGTCGTC	NA	Cre06.g254400.t1.1
<b>MAS1</b>	Malate synthase	CCCAACGGCAAGGTCTACAG	CAGCGTTGTGGAAGAAGAACAG	NA	Cre03.g144807.t1.1
<b>KAS2</b>	3-oxoacyl-[acyl-carrier-protein] synthase	CTCACAAAGTTTCTCGGCAAG	CGCCTTCTCAGTCTTGGAATG	NA	Cre07.g335300.t1.2
<b>atpA</b>	ATP synthase subunit alpha	GCAATGCGTACTCCAGAAGAAC	CGAGCAATACCGTCACCTACTT	NA	2717041 <sup>d</sup>
<b>HSP70A</b>	Heat shock protein 70A	CCAAGAACCAGGTCGCTATGAA	ACCTTCTCCTCGTTCTTGTAGG	NA	Cre08.g372100.t1.2

## 4.4. RNA extraction optimisation

The need to optimise the RNA extraction method employed in this chapter arose from the amount of RNA required to perform the reference gene study and the transcriptional activity study that followed. Initial RNA extraction experiments produced RNA yields 100 times lower than theoretical yields calculated from literature values (Valle, Lien and Knutsen, 1981). Evaluation of the initial results prompted the testing of different streams from the RNeasy spin column extraction kit workflow. No abrupt losses of nucleic acid content were detected between streams of consecutive steps prompting the hypothesis that there was insufficient cell lysis during the incubation with lysis buffer step. Four lysis techniques were initially compared, (a) mechanical lysis with a probe sonicator, (b) mechanical lysis by vortexing with glass beads, (c) sonic lysis with adaptive focused acoustics (AFA), and (d) chemical lysis with phenol- chloroform (Trizol) extraction. The aim of this optimisation study was to maximise RNA yield in a robust and reproducible manner.

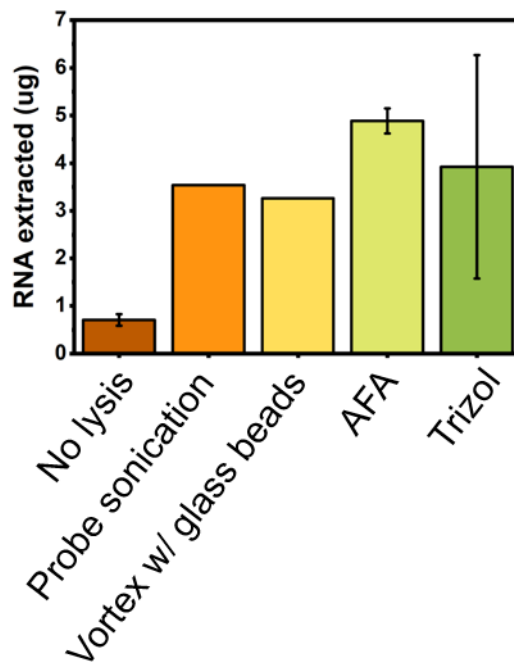


**Figure 4.1** Initial RNA extraction optimisation study focusing on the cell lysis step. RNA was extracted from *C. reinhardtii* cell pellets ( $5 \times 10^6$  cells; N=3).

The highest recovery was achieved with Trizol ( $1.3 \mu\text{gRNA } 1 \times 10^6 \text{ cells}^{-1}$ ) and AFA ( $1 \mu\text{gRNA } 1 \times 10^6 \text{ cells}^{-1}$ ). AFA was more reproducible as it had a significantly smaller CV (17%) than Trizol (60%) (Figure 4.1) however the integrity of the extracted RNA was questionable according to gel electrophoresis results (Figure 4.2). The gel was loaded normalised by RNA quantity according to nanodrop quantification. The streaking seen between the 18S and the 16S bands of the AFA lane suggest nucleic acid fragmentation that should be avoided in RT-qPCR RNA preparations. AFA is commonly used for DNA shearing in NGS sample preparation so this was always a known risk. Meanwhile the well-defined bands seen in the Trizol lane suggest this method does not cause fragmentation issues.

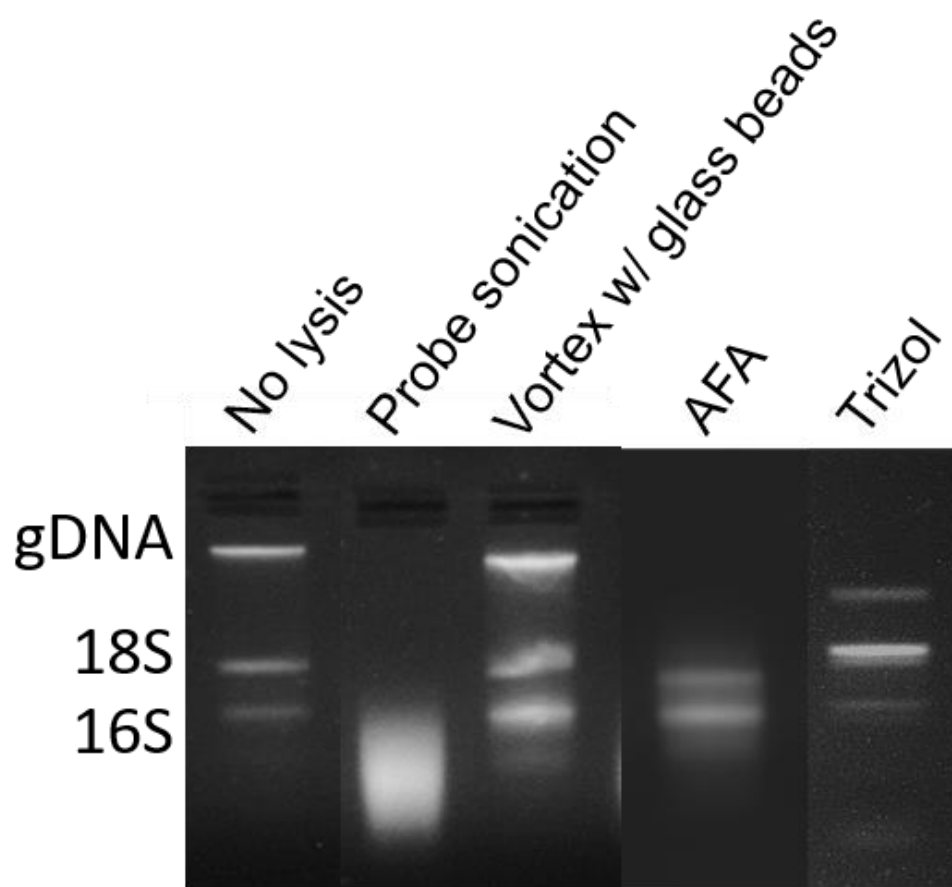


**Figure 4.2** Gel electrophoresis of *C. reinhardtii* RNA extractions employing different lysis techniques. (gDNA, genomic DNA; 18S, 18S rRNA; 16S, 16S rRNA).

The gel electrophoresis integrity check confirmed that probe sonication and vortexing with glass beads are not suitable RNA extraction methods. AFA showed good reproducibility and better integrity than probe sonication. Trizol did not show good reproducibility but it had the highest extraction yield (Figure 4.1) Therefore the second round of optimisation was performed with AFA and Trizol. The AFA treatment time was decreased from 30s to 15s and Trizol extraction was performed in MaXtract tubes specifically designed for this purpose instead of regular Eppendorf tubes. Figure 4.3 shows there was a slight increase in RNA extracted with Trizol ( $1.4 \mu\text{gRNA } 1 \times 10^6 \text{ cells}^{-1}$ ) and the variability decreased significantly down to a CV of 9%. Meanwhile there were no improvements in the AFA assisted extraction.

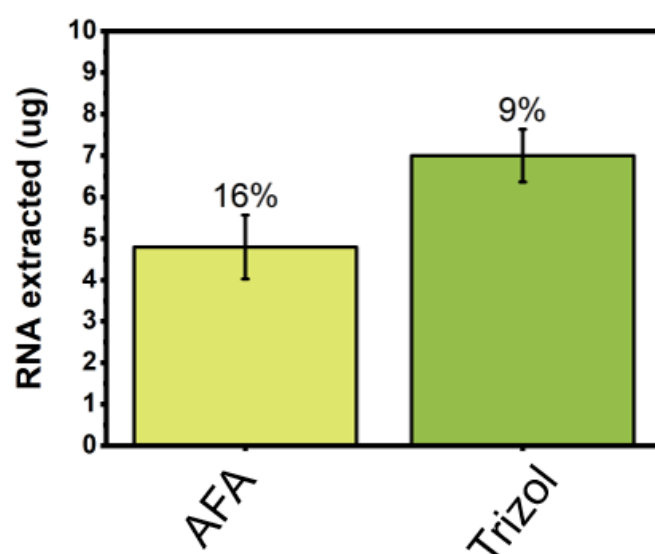


**Figure 4.3** RNA extraction optimisation study focusing on the cell lysis step. RNA was extracted from *C. reinhardtii* cell pellets ( $5 \times 10^6$  cells; N=3).

Finally, the original Trizol extraction method was compared to the Trizol extraction using MaXtract tubes in terms of purity. As can be seen in Figure 4.4 where the RNeasy extraction kit is used a purity standard, the Trizol extraction method using MaXtract tubes produces a much closer purity profile to the standard than the original Trizol extraction. The integrity (Figure 4.2), yield (Figure 4.3) and purity (Figure 4.4) achieved with the Trizol extraction method using MaXtract tubes was considered satisfactory for the following RT-qPCR studies.

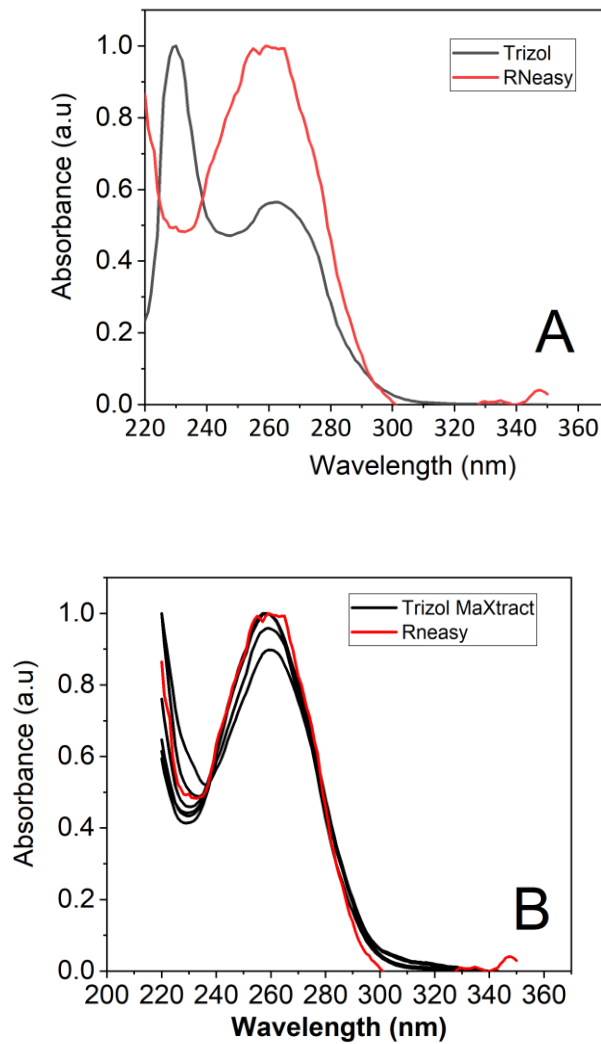


**Figure 4.4** RNA purity analysis. (A) Comparison between Trizol extraction performed in 2 mL Eppendorf tubes and RNA extraction performed with RNeasy spin column kit. (Both extractions N=1) (B) Comparison between Trizol extraction performed in 2 mL MaXtract tubes and RNA extraction performed with RNeasy spin column kit (Trizol extraction N=5; RNeasy extraction N=1). RNA was extracted from *C. reinhardtii* cell pellets ( $5 \times 10^6$  cells).

## 4.5. Expression Stability

Relative quantification of gene expression via RT-qPCR requires the determination of one (or more) reference genes which are expected to maintain a stable expression

level across all experimental conditions examined (Shipley, 2006). The panel of candidate genes (Table 4.1) investigated in the present study reflects three distinct selection criteria: (a) genes extensively used as reference genes in relevant scientific literature (*RACK1*, *RPL19*, *CH3-I* and *RPS10* (Siaut *et al.*, 2007; Beel *et al.*, 2012; Liu *et al.*, 2012; Kianianmomeni and Hallmann, 2013; Adelfi *et al.*, 2014)), (b) genes with functional similarities to widely used reference genes (*PSRP-1*, *psaD* and *ATPD* (Li *et al.*, 2018)) and, novel in this study, (c) genes involved in central carbon metabolism due to its vital role in cellular function under most relevant experimental conditions (*DLA3*, *ACX1* and *STA1*). Gene expression was measured at three time points (16, 48 and 136h post inoculation) for each of the six possible combinations of wavelength (W, R, B) and trophic strategy (A, X).

Raw RT-qPCR data is evaluated in terms of quantification cycle ( $C_q$ ), which is the number of amplification cycles required for a RT-qPCR reaction's fluorescence to surpass a defined threshold. This is inversely correlated to the specific cDNA template present in the reaction. The 10 genes evaluated displayed a wide range of average  $C_q$  values ( $\overline{C_q}$ ) with *ATPD* at the low end ( $\overline{C_q} = 14$ ) and *DLA3* with at the high end of the range ( $\overline{C_q} = 22$ ). An overview of all  $C_q$  ranges measured for candidate reference genes under all experimental conditions examined in this chapter is presented in Figure 4.5. Interestingly the  $C_q$  value for *ATPD* was also found to have lowest variability across all conditions while the  $C_q$  values for *PSRP-1*, chosen for its similarity to canonical ribosomal protein genes utilised as reference genes throughout literature, varied significantly between conditions. Given its exclusively plastidic localisation, it is possible that ribosomal activity in the chloroplast is, at least partially, regulated at the transcriptional level in response to changes in the quality of incident light.

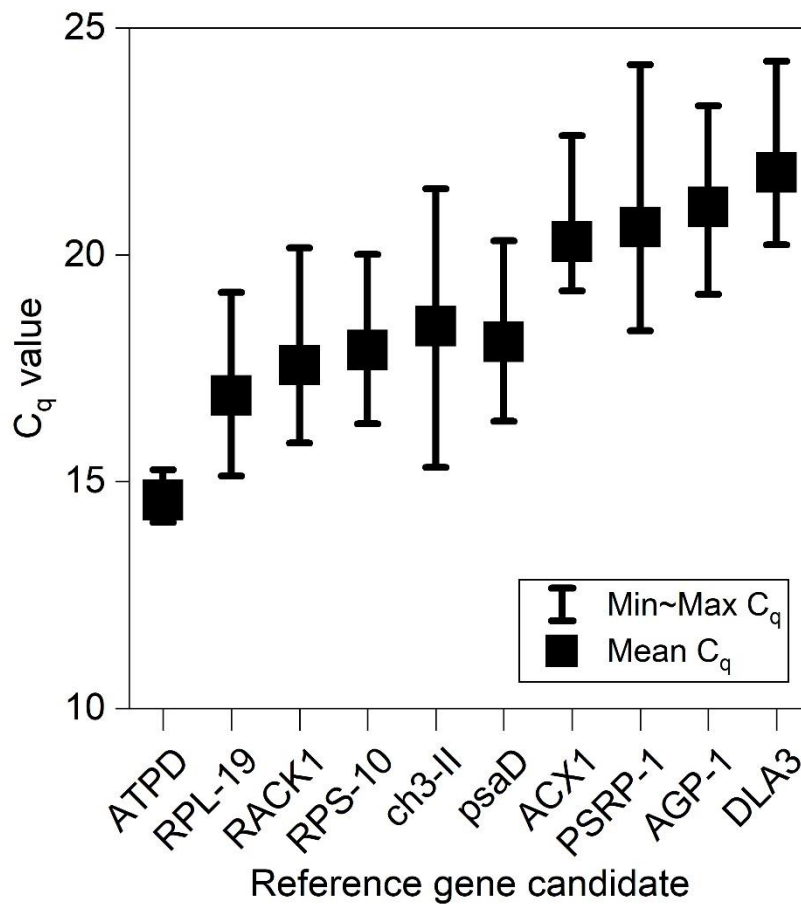


**Figure 4.5.** Mean  $C_q$  of candidate reference genes studied. ( $n = 6$ , error bars represent minimum and maximum  $C_q$ ).

Prior to the development of sophisticated data analysis algorithms and the widespread availability of real-time PCR systems, relative quantification was primarily based on a single reference gene derived either from literature or through simple, yet effective, log-linear models ( $\Delta\Delta C_q$ ) (Livak and Schmittgen, 2001; Pfaffl, 2001). However, current state of the art for comparison of gene expression across widely varying conditions or cell lines involves the use of sophisticated algorithms that employ two or more genes to normalise gene expression measurements (Derveaux, Vandesompele and Hellemans, 2010). The geNorm algorithm, used in the present study, has been successfully applied to a wide variety of organisms (Cortleven *et al.*, 2009; Rosic *et al.*, 2011; Cankorur-Cetinkaya *et al.*, 2012). The algorithm uses pairwise variation ( $V_n/n+1$ ) to evaluate the number of reference genes required to achieve an accurate normalisation factor ( $M$ ) which will remain stable across all experimental conditions and



cell lines studied (Vandesompele *et al.*, 2002; Hellemans *et al.*, 2007). Analysis of the results indicated that *ACX1* and *psaD* form the most stable pair of genes with a  $V_{2/3}$  value lower than the recommended threshold ( $<0.15$ ) (Vandesompele *et al.*, 2002) indicating that additional reference genes are not required.

*ACX1* encodes the  $\alpha$ -carboxyltransferase subunit of the multimeric acetyl coenzyme A (acetyl-CoA) carboxylase (ACCase) and has been shown to be expressed in co-ordination with the other subunits in *Arabidopsis thaliana* (Ke *et al.*, 2000) and *C. reinhardtii* (Goodenough *et al.*, 2014). While significant variations in the expression levels of both the  $\alpha$ - (Goodenough *et al.*, 2014; Smith and Gilmour, 2018) and the  $\beta$ - (Ramanan *et al.*, 2013) carboxyltransferase subunits have been reported in nitrogen starved cells, expression levels of *ACX1* have been shown to remain stable under nitrogen replete conditions, in agreement with the findings in the present study.

The *psaD* gene encodes subunit II of photosystem I (PSI), an essential component for PSI accumulation in *Arabidopsis thaliana* (Ihnatowicz *et al.*, 2004) and key to the efficient functioning of PSI in *Synechocystis sp* (Chitnis, Reilly and Nelson, 1989). A highly expressed constitutive gene, its promoter element has always remained relevant in recombinant protein expression studies in *C. reinhardtii* (Fischer and Rochaix, 2001; Baier, Wichmann, *et al.*, 2018). Light intensity and light quality have been shown to affect the pigment content and composition of microalgal cells but, to the extent of our knowledge, none of the available studies tested the expression levels of *psaD* under monochromatic illumination. It is not particularly surprising that a gene expressing an essential PSI subunit presents robust expression across the conditions studied in the present study as essential photosynthetic components are commonly controlled by post-translational regulatory processes such as epistasis of synthesis (CES) (Choquet and Wollman, 2009).

#### **4.6. Gene expression under different illumination and trophic strategies**

Batch cultures of *C. reinhardtii* 11/32C were grown for 136h under constant illumination at three different wavelengths (W, R, B) using media with (X) and without

(A) a readily available organic carbon source. Daily biomass measurements (OD 750 nm) were used to estimate growth rate during the exponential growth phase ( $\mu_{max}$ , Table 3.3, Figure 3.3 A&B). In agreement with findings from other studies (Mooij *et al.*, 2016), white light illumination was found to have the highest growth rate in both trophic strategies. Interestingly, under the constant environmental conditions considered in the present study (pH, temperature and light intensity), the presence of an organic carbon source had a significant impact on biomass growth only under blue light illumination. In contrast, the addition of a carbon source under white light illumination (WX) resulted in 5% reduction in  $\mu_{exp}$  compared to (WA). The rate of acetate consumption in mixotrophic cultures ( $q_{ac}$ , Table 3.4) was nearly identical under all studied wavelengths irrespective of the observed biomass growth rate. Acetate was fully extinguished from the media within the first 48 hours post inoculation in all mixotrophic conditions.

The expression levels of a panel of genes selected based on their metabolic function (Table 4.1) were measured and analysed for each of the six experimental conditions described above. Gene expression levels for central carbon metabolism genes were estimated by averaging values obtained from two samples taken during the exponential growth phase (16h and 48h). The expression level of promoter genes was evaluated at three different time points (16h, 48h and 136h) throughout the culture. In the sections that follow, gene expression results are presented and discussed grouped by metabolic pathway.

### **Photosynthesis – Inorganic carbon fixation**

The ribulose-1, 5-bisphosphate carboxylase oxygenase (RUBISCO) found in *C. reinhardtii* is a hexadecamer composed of eight small sub-units (SS) and 8 large sub-units (LS). Two variants of the small sub-unit of RUBISCO have been identified in the *Chlamydomonas* nuclear genome (*RBCS1* and *RBCS2*) (Khrebtukova and Spreitzer, 1996). While their peptide products differ by only four amino acids and are functionally redundant (Khrebtukova and Spreitzer, 1996), their expression is dependent both on trophic strategy and the presence or absence of light (Goldschmidt-Clermont, 1986; Goldschmidt-Clermont and Rahire, 1986). The primer pair designed and used in this study (Table 4.1) amplifies both sub-unit variants (*RBCS1* and *RBCS2*) to enable the

evaluation of overall *RBCS* expression irrespective of individual sub-unit related dependences (Figure 4.6). Wavelength selection had a statistically significant effect ( $p < 0.01$ ) on the average expression level of *RBCS* with average expression levels under red light (R) being significantly higher compared to both white (W) and blue (B) light in both trophic conditions (A, X). In addition, the average *RBCS* expression in cultures grown under blue light (B) was significantly higher ( $p < 0.05$ ) than those grown under white light (W) in both trophic conditions. It is worth noting that the macroscopically observed biomass growth rate (Table 3.3) does not appear to be strongly correlated with *RBCS* expression levels. Under both trophic strategies, (R) illuminated cultures displayed statistically significant higher *RBCS* expression levels than (W) illuminated cultures, however resulted in lower growth rate values. Similarly, low levels of *RBCS* expression measured in B and W cultures resulted in substantially different growth rates (Table 3.3). These differences were observed in both trophic conditions and the presence of an external carbon source did not seem to have a significant impact on *RBCS* expression levels.

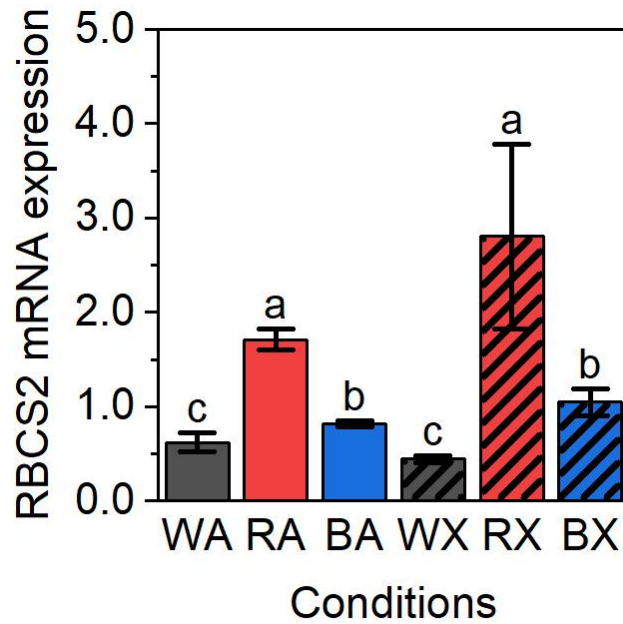


**Figure 4.6.** Carbon fixation related gene expression in the exponential growth phase. Average Ribulose biphosphate carboxylase small subunit (*RBCS*) gene expression from 16 h – 48 h ( $n = 4$ , error bars represent SEM, different error bar labels indicate statistically significant differences between conditions,  $p < 0.05$ ). W: white light, R: red light 640-670nm, B: blue light 440-480nm, A: phototrophic growth in M8a, X: mixotrophic growth in M8a.Ac.

In order to further understand the implications of these results, cell size distribution during the mid-exponential growth phase (48h) was measured for all conditions (Figure 3.9 A and Figure 3.10 A). In both trophic conditions examined, cells grown under constant red light illumination had a smaller average diameter, while cells grown under constant blue light illumination had a larger average diameter when compared to control cultures grown under white light. The growth rate data (Table 3.3), calculated using optical density measurements (750nm), coupled with the cell size distribution data (Figure 3.9 A and Figure 3.10 A). indicate that wavelength selection has an impact on the cell cycle (Oldenhof *et al.*, 2004; Oldenhof, Zachleder and Van Den Ende, 2006). The balanced combination of long- and short-wavelengths making up white light results in the fastest biomass production under both phototrophic (WA) and mixotrophic (WX) conditions. Additionally, an average cell cycle length is maintained and

consequently cell size remains in-between the smaller cells produced by (R) and the larger cells produced by (B) in both trophic strategies. The upregulation of *RBCS* under red light indicates an increased need for energy generation, likely required to operate a shorter cell cycle and maintain a rapid duplication rate. On the other hand, cells grown under blue light had lower *RBCS* expression levels (Figure 4.6), a lower apparent growth rate (Table 3.3) and the largest observed average cell diameter (Figure 3.9 A and Figure 3.10 A). These results suggest that blue light illumination leads to larger cells on average with a longer or arrested cell cycle while red light illumination leads to smaller, rapidly dividing cells. However, in terms of overall biomass yield (in gDCW/L) both extremes of the PAR spectrum underperform when compared to white light illumination.

Chlorophyll (Chl) a/b measurements (Figure 3.15) revealed a statistically significant higher Chl a/b ratio in cultures grown under red light (RA, RX). The Chl a/b ratio has been previously inversely linked to PSII antenna size due to Chl b's preference for binding to peripheral antenna complexes (Perrine, Negi and Sayre, 2012). Moreover, in agreement with previous studies (Wagner, Steinweg and Posten, 2016), the specific amount of Chl b per pg of biomass was significantly lower under red light illumination. Given that incident light intensity was kept constant across all experimental conditions, this further supports the hypothesis stated above, that red light illumination leads to a shortened cell cycle. High values of the Chl a/b ratio, coupled with a smaller antenna (Perrine, Negi and Sayre, 2012) and average cell size (Figure 3.9 A and Figure 3.10 A) result in reduced surface area for absorption of photons and increased photosynthetic efficiency as well as reduced mutual shading across the light path. These effects combine to increase the proportion of cells in the culture receiving enough light to maintain a high growth rate. Consequently, the implied increase in light utilisation efficiency under red light illumination would result in an increased demand for Calvin-Benson cycle (CBC) enzymes like RUBISCO, and potentially increased gene expression as has been observed in the present study (Figure 4.6), to fulfil the increased demand. When considering the monochromatic conditions of this study in isolation, there is a strong positive correlation between biomass growth rate and *RBCS* expression in the autotrophic conditions that is lost in the mixotrophic regime. This suggests that the availability of an organic carbon source and the resulting switch to mixotrophic metabolism reduce the relevance of

photosynthetically generated metabolic resources in biomass growth rate maximisation. This is not apparent in growth under white light, possibly due to its more varied spectral distribution resulting in optimal phototrophic growth at a lower light utilisation efficiency compared to monochromatic illumination.

### **Acetyl Coenzyme A catabolism**

Acetate uptake rates (Table 3.4) were found to be independent of wavelength selection and biomass growth rate. However, when comparing biomass growth across trophic strategies for the same wavelength selection, differences in metabolic behaviour can be observed. In cultures grown under constant white light (WA, WX) and red light (RA, RX) illumination, the addition of acetate as a carbon source resulted in a relatively small change in biomass growth rate (Table 3.3). This suggests that under appropriately controlled conditions phototrophic growth under each of these two lights is nearly optimal. It seems that introducing an organic carbon source under these conditions does not result in an increased rate of biomass production. In contrast, for cultures grown under blue (BA, BX) light, the addition of acetate resulted in a substantial increase of the growth rate. Interestingly, *RBCS* expression levels remained similar across the different trophic strategies (WA, WX, RA, RX and BA, BX; Figure 4.6), indicating no drastic change in the rate of carbon fixation from photosynthesis. Therefore, under white and red illumination the additional carbon uptaken in the form of acetate must be assimilated through a different metabolic pathway, one not directly linked to biomass growth. The presence of acetate is known to trigger a reconfiguration of *C. reinhardtii* metabolism as the inorganic carbon fixation of photosynthesis is complimented by the organic carbon assimilation of acetate via its conversion to acetyl-CoA (Johnson and Alric, 2012).

In nutrient replete mixotrophic conditions acetyl-CoA is preferentially produced in a single enzymatic step catalysed by acetyl-CoA synthase (ACS) (Singh *et al.*, 2014). ACS homologs have been identified in several cellular compartments (ACS1 - cytosol ACS2 - plastid, ACS3 - glyoxysomes and mitochondria) (Terashima *et al.*, 2010; Lauersen *et al.*, 2016). Consequently, this metabolic plasticity enables the cells to repurpose assimilated

acetate to drive different metabolic pathways by channelling it to the appropriate cellular compartments. As can be seen in Figure 4.8, Acetyl-CoA is primarily utilised in fatty acid chain formation (cytoplasm), in the glyoxylate cycle (glyoxysome) and in the TCA cycle (mitochondria). Differences in transcriptional activity between photoautotrophic and mixotrophic metabolism may elucidate the fate of acetate derived carbon assimilated during mixotrophic growth. Therefore, the expression level of enzymes exclusive to each of the three main metabolic pathways that consume acetyl-CoA was evaluated for all experimental conditions.

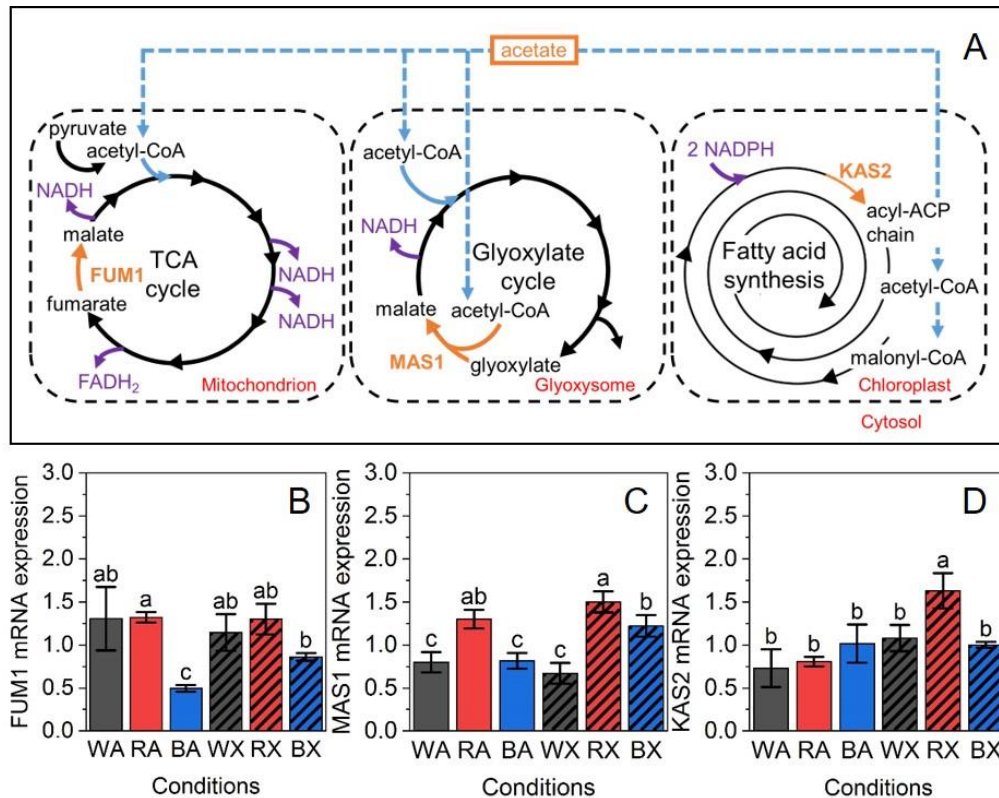


**Figure 4.7.** An overview of acetate metabolism in *C. reinhardtii* and gene expression monitored at key carbon nodes of acetate metabolism. (A) The various subcellular locations and metabolic pathways acetate can be catabolised in. Gene expression of enzymes involved in reactions highlighted in orange and redox cofactors highlighted in purple. (B-D) Average gene expression from 16 h – 48 h of fumarate hydratase (*FUM1*), malate synthase (*MAS1*) and 3-oxoacyl-[acyl-carrier-protein] synthase (*KAS2*) respectively ( $n = 4$ , error bars represent SEM, different error bar labels indicate statistically significant differences between conditions,  $p < 0.05$ ). W: white light, R: red light 640-670nm, B: blue light 440-480nm, A: phototrophic growth in M8a, X: mixotrophic growth in M8a.Ac.

### Tricarboxylic Acid Cycle

The TCA cycle produces reducing equivalents for oxidative phosphorylation and is a vital metabolic process in non-photosynthetic organisms which produce the bulk of their cellular ATP in mitochondria. In contrast mitochondrial respiration rates in nutrient replete phototrophic and mixotrophic conditions average approximately 10-15% of



gross photosynthetic rates across many phyla of microalgae including chlorophytes like *C. reinhardtii* (Raven and Beardall, 2016). In fact, several genes exclusive to the TCA cycle have been reported as non-essential for the growth of photosynthetic organisms (Rubin *et al.*, 2015). Consequently, the availability of an organic carbon source is not expected to have a significant impact on the activity of TCA genes. To verify the validity of the above hypothesis, the expression level of the TCA exclusive *FUM1* gene, which encodes the enzyme fumarate hydratase that catalyses the reversible hydration of fumarate to malate (Figure 4.8A) was measured across all experimental conditions.

The addition of acetate had no impact on *FUM1* expression in cultures grown under white and red light (WA, WX and RA, RX; Figure 4.8B). In fact, *FUM1* expression levels were statistically similar across all four conditions (WA, WX, RA, RX; Figure 4.8B). This indicates, as expected, that there is no correlation between biomass growth (Table 3.3) and TCA cycle activity (assessed through the expression levels of *FUM1* in the present study) in the nutrient replete conditions considered herein. Wavelength selection on the other hand, had a statistically significant effect on the expression level of *FUM1* (Figure 4.8B). Specifically, *FUM1* expression was significantly lower in phototrophic cultures grown under blue light (BA). Interestingly, in cultures grown under blue light (BA, BX; Figure 4.8B) the addition of acetate in the media led to an increased average expression level for *FUM1*. The increased expression level under blue light corresponded to an increased biomass growth rate (BX, Table 3.3) indicating that the additional carbon might be channelled towards mitochondrial respiration and ATP synthesis (Millar *et al.*, 2011). The positive correlation between *FUM1* expression and biomass growth rate for cultures grown under blue light suggests that in the presence of a readily available carbon source cellular growth could rely on TCA cycle activity and heterotrophy.

### **Glyoxylate Cycle**

Algae can preferentially utilize acetate as a carbon source due to the availability of an abbreviated version of the TCA cycle, sharing five of the eight TCA cycle enzymes, known as the glyoxylate cycle. This enables them to bypass the two decarboxylation steps found in the TCA cycle and enables the biosynthesis of macromolecules from

simple C<sub>2</sub> carbon compounds (Silverberg, 1975; Lauersen *et al.*, 2016). The preferential use of the glyoxylate cycle in the presence of a C<sub>2</sub> organic acid has been recently investigated using a genome scale metabolic model of *C. reinhardtii* metabolism under nutrient replete mixotrophic and phototrophic conditions (Chapman *et al.*, 2015). Although qualitative in nature, the results suggested a substantially increased flux through the glyoxylate cycle in the presence of a C<sub>2</sub> organic acid. This theoretical model based approach was able to accurately predict the experimentally observed change in oxygen evolution rate between the two conditions (Chapman *et al.*, 2015). In the present study, the expression of a glyoxylate cycle exclusive gene, *MAS1*, was measured across all experimental conditions. The *MAS1* gene encodes malate synthase, an enzyme that catalyses the formation of malate (C<sub>4</sub>) from glyoxylate (C<sub>2</sub>) and acetyl-CoA (C<sub>23</sub> – Figure 4.8A).

Surprisingly, the presence or absence of acetate had a statistically significant effect on *MAS1* expression levels only in cultures grown under blue light (BA, BX; Figure 4.8C). The 1.5-fold upregulation ( $p < 0.01$ ) of *MAS1* in mixotrophic cultures grown under blue light (BX) did not result in an increased biomass growth rate (Table 3.3). In conjunction with the observed upregulation of the TCA exclusive *FUM1* in mixotrophic growth conditions (BA, BX; Figure 4.8C), these results seem to indicate that carbon derived from acetate can help supplement biomass growth rate in non-optimal light conditions. No significant change in *MAS1* expression levels was detected between phototrophic and mixotrophic conditions for cultures grown under white and red light (WA, WX and RA, RX; Figure 4.8C). This is in contrast to previous studies (Hayashi *et al.*, 2014)(Smith and Gilmour, 2018) where an upregulation of glyoxylate cycle genes was observed following the addition of acetate. One possible explanation is that *MAS1* expression levels are not linked to flux through the glyoxylate cycle in non-growth inhibited, constantly illuminated cultures (WA, WX, RA, RX) due to regulation occurring primarily by enzyme phosphorylation (H. Wang *et al.*, 2014). In fact, no correlation between growth (Table 3.3) and *MAS1* expression (Figure 4.8C) was found for cultures grown under white and red (WA, WX and RA, RX) light in the present study. Finally, wavelength selection was found to have a significant effect on *MAS1* expression levels (Figure 4.8C), with cultures grown under red light having a higher average expression level ( $p < 0.05$ ).

## Fatty Acid Synthesis

Acetyl-CoA derived from assimilated acetate in mixotrophic cultures can be channelled towards fatty acid biosynthesis which is driven by the heterogeneous fatty acid synthase (FAS) enzyme complex in the chloroplast (Riekhof and Benning, 2009). The fatty acids generated can increase the cell's intracellular free fatty acid (FFA) pool or they can be incorporated into one of the many lipid classes produced by *C. reinhardtii* (Li-Beisson, Beisson and Riekhof, 2015). A multi-omics study found that protein levels of enoyl-ACP reductase were reduced during nitrogen deprivation, alongside a transient decrease in all FAS complex related transcripts during the first 12 – 48 hours (Schmollinger *et al.*, 2014). However, in the nutrient replete conditions of this study, where highly differing growth rates were observed between conditions it would be interesting to follow the gene expression of FAS complex related transcripts as a preliminary indicator of changes in macromolecular composition at a cellular level and in the assimilation of acetate derived carbon. The gene *KAS2* encodes 3-ketoacyl-ACP synthase (KAS), the third enzyme in the FAS complex, which adds two carbons per FAS-cycle to the growing acyl-ACP chain using malonyl-ACP as its substrate (Figure 4.8A).

Trophic strategy selection had an impact on *KAS2* expression level in cultures illuminated under white and red light (WA, WX and RA, RX; Figure 4.8D). In both cases, *KAS2* expression was upregulated in the presence of acetate in the media, though the change in expression level was statistically significant only for cultures grown under red light ( $p < 0.05$ ). The highest *KAS2* expression level was observed in mixotrophic cultures grown under red light (RX; Figure 4.8D), while *KAS2* expression levels remained constant across cultures grown in white (WX) and blue (BX) light. In contrast, *KAS2* expression levels remained constant, irrespective of trophic strategy, in cultures grown under blue light (BA, BX; Figure 4.8D).

This suggests that under blue light, an increase in fatty acid production is not required to achieve the observed increase in biomass growth rate (Table 3.3). On the other hand, there was no change in biomass growth rate observed between trophic strategies in cultures grown under red light (R, Table 3.3). Meanwhile a statistically significant increase in *KAS2* expression was observed in red light mixotrophic cultures

(RX; Figure 4.8D). One possible explanation could be that in cultures grown under red light with a smaller average cell size (Figure 3.9 A and Figure 3.10 A) but otherwise comparable biomass growth rate (Table 3.3), the assimilated acetate in the form of acetyl-CoA is preferentially funnelled towards fatty acid production. This would lead to an increased production rate for membrane-lipids, necessary to support the shorter cell-cycle with more cell divisions per unit time for cells grown under red light. Previous studies have shown that the autophagous degradation of membrane lipids for TAG production under nitrogen starvation is less pronounced in mixotrophic *C. reinhardtii* cultures grown in white light (Davey *et al.*, 2014) further hinting at an increased flux of acetyl-CoA towards fatty acid synthesis during mixotrophy.

The gene expression data discussed in the preceding sections is summarised in Figure 4.9. Mixotrophic cultures grown under constant red light illumination had the highest average fold expression for all genes considered thus far. However, this did not translate directly into an increased biomass growth rate as could have been expected given the nature of the genes investigated. This indicates that despite similarities in the observed biomass growth rates across conditions considered herein (Table 3.3), the macromolecular composition of cells will change depending on the utilised trophic and illumination strategy.



**Figure 4.8.** Summary of average gene expression level compared across multiple light and media conditions. The colour scale is normalised in each row as the data reflects average fold change in gene expression and is not directly comparable between genes ( $n = 4$ ). W: white light, R: red light 640-670nm, B: blue light 440-480nm, A: phototrophic growth in M8a, X: mixotrophic growth in M8a.Ac.

### Recombinant protein promoter genes

In recent years, a number of sophisticated genome editing technologies have been adapted to microalgae (Jeon *et al.*, 2017). *C. reinhardtii*, often referred to as the model microalgae, has the most complete algal genome editing toolbox however genetic engineering techniques are being developed for other type of algae as well (Nymark *et al.*, 2016; Taunt, Stoffels and Purton, 2018). Recombinant protein expression in *C. reinhardtii* has been attempted by integration of the recombinant genes into either the chloroplast (Fletcher, Muto and Mayfield, 2007) or the nuclear genome (Rasala and Mayfield, 2015). Each approach has its own benefits and limitations, with no clear consensus on an optimal strategy due to a lack of bioreactor (or larger) scale studies. As

algal genome editing technologies mature, process development for recombinant protein expression will have to explore candidate promoters and culture conditions that lead to optimal transcriptional activity. In order to understand the magnitude of the impact process conditions can exert on transcriptional activity, the expression of a series of genes with promoters and/or 5'/3' UTR(s) that have been previously used to facilitate recombinant gene expression in *C. reinhardtii* (Table 4.1) was evaluated across all experimental conditions. Bearing in mind that transcription and translation do not necessarily correlate well, some high level conclusions can be drawn from the data presented below.

### **Ribulose biphosphate carboxylase small chain (RBCS)**

*RBCS2* is routinely used as a constitutive promoter for nuclear transgene expression in tandem with *HSP70A* (Schroda, Blöcker and Beck, 2000; Rasala *et al.*, 2014; Baier, Kros, *et al.*, 2018). *RBCS* expression was upregulated in both phototrophic and mixotrophic cultures grown under red light illumination (RA, RX; Figure 4.6A). Figure 4.10A presents *RBCS* expression data for an additional time point in the late stationary phase of the culture. In agreement with the results of Figure 4.6, *RBCS* expression is upregulated significantly for cultures grown under red light (RA, RX; Figure 4.10A). Interestingly, there is a large increase in *RBCS* expression during the stationary phase (136h) for both mixotrophic and phototrophic cultures grown in red light. These results suggest that red light illumination would be preferable for recombinant protein synthesis when *RBCS2* is used as a constitutive promoter.

### **Heat shock protein 70A (HSP70A)**

*HSP70A* encodes a heat-shock protein, transcriptionally controlled through elevated temperatures and light (Schroda, Blöcker and Beck, 2000). It has been used as a transcriptional activator of other promoters, most commonly *RBCS2* and recently *RBCS2* with *RBCS2* introns interspersed in the recombinant gene coding sequence (Baier, Wichmann, *et al.*, 2018). In photoautotrophic cultures, a notable increase in expression was only observed during the stationary phase (136 h) of cultures grown in red light (Figure 4.10B). *HSP70A* expression levels were higher in the stationary phase of

mixotrophic cultures across all wavelengths with a notable 6-fold increase ( $p < 0.05$ ) observed in cultures grown under blue light illumination (Figure 4.10B).

### **Adenosine triphosphate synthase subunit alpha (*atpA*)**

Assembly of chloroplastic ATP-synthase requires subunits encoded in both the nuclear and the chloroplast genomes (Finazzi, Drapier and Rappaport, 2009). The gene *atpA* is native to the plastome and encodes sub-unit alpha of the CF<sub>1</sub> complex (Levy, Kindle and Stern, 1997). Its 5'UTR and promoter coding regions have been used to drive both nuclear (Ishikura *et al.*, 1999; Kasai *et al.*, 2003; Michelet *et al.*, 2011) and plastid (Bertalan *et al.*, 2015; Braun-Galleani, Baganz and Purton, 2015) gene expression. Cultures grown under white light illumination had the lowest levels of *atpA* expression across all conditions examined (Figure 4.10C). Interestingly, trophic strategy had a significant impact on *atpA* expression only in cultures grown under red light where a 5.5 fold upregulation was observed in mixotrophic cultures during the mid-exponential phase (16 h and 48 h). These results confirm that culture time, trophic strategy and wavelength selection can all have a significant impact on the transcriptional activity of promoters and should be considered as critical process parameters during process development and optimisation.

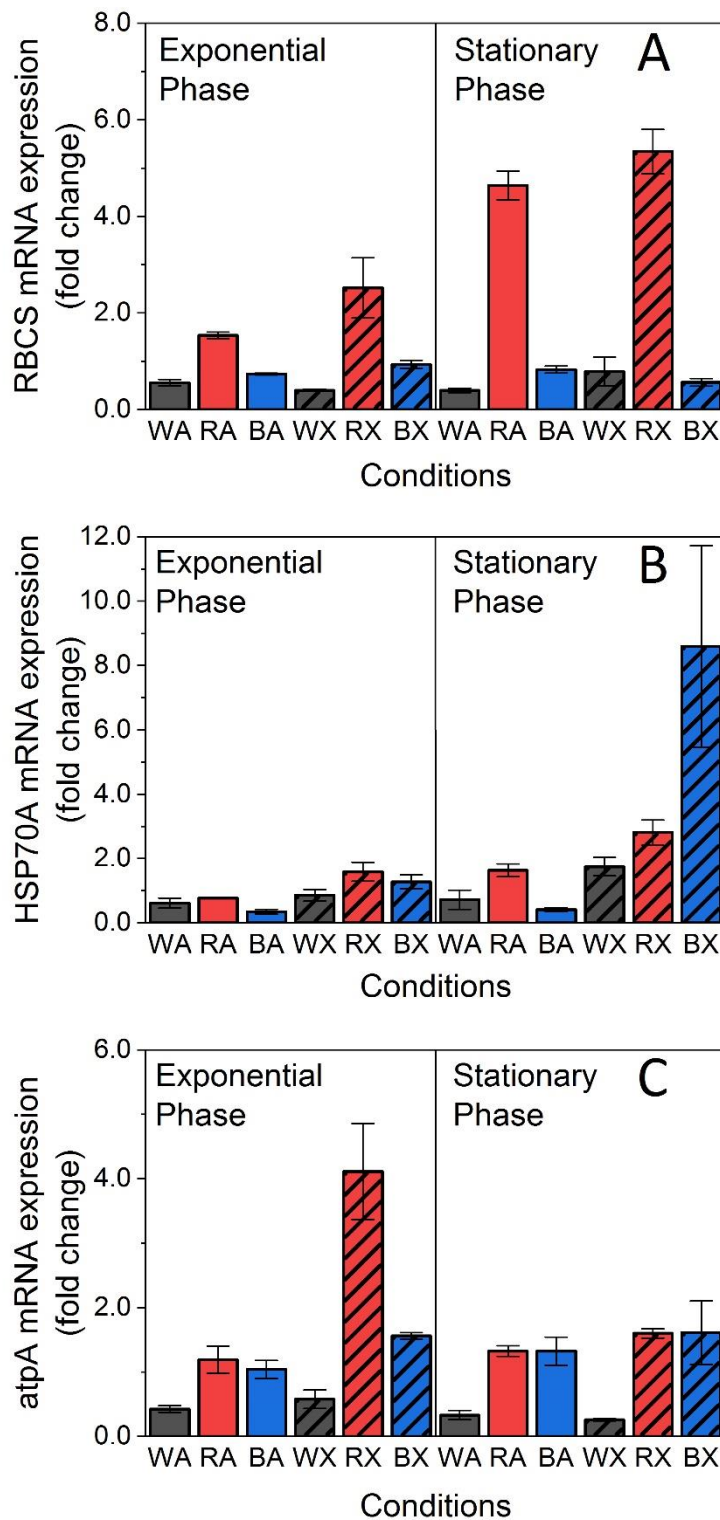


**Figure 4.9** Average gene expression of (A) ribulose biphosphate carboxylase small subunit – *RBCS*, (B) heat-shock protein 70A – *HSP70A* and (C) ATP synthase subunit alpha (*atpA*) respectively, from 16 h –48 h (Exponential Phase, n = 4, error bars represent SEM) and 136 h (Stationary Phase) (n = 2, error bars represent min and max expression). W: white light, R: red light 640-670nm, B: blue light 440-480nm, A: phototrophic growth in M8a, X: mixotrophic growth in M8a.Ac.



## 4.7. Conclusions

The expression profiles of a total of 16 genes (Table 4.1) were monitored across *C. reinhardtii* cultures grown under two different trophic strategies and three different wavelengths. This enabled the identification of novel reference genes (*psaD* and *ACX1*) with significantly improved expression stability compared to commonly used reference genes, across the diverse set of conditions explored herein. The analysis of the expression profiles of representative genes from key metabolic pathways revealed that trophic strategy and wavelength selection have an impact on some (*RBCS* – photosynthesis, *MAS1* – glyoxylate cycle, *KAS2* – fatty acid synthesis) but not all (*MAS1* – TCA cycle) aspects of central carbon metabolism in algae. Specifically, wavelength selection was found to have an impact on photosynthetic efficiency and (as indicated by cell size distribution data) the cell cycle. Moreover, based on the set of gene expression profiles examined in the present study, assimilated acetate was found to be primarily channelled towards fatty acid synthesis, particularly in cultures grown under red light illumination. Finally, the expression profiles of three commonly used promoters for the expression of recombinant proteins was evaluated across all experimental conditions and revealed that culture time, trophic strategy and wavelength selection should be considered as critical process parameters during process development and optimisation. This is the first, to the extent of our knowledge, extensive experimental investigation of the effects of wavelength selection and trophic strategy on gene expression in green algae and will hopefully serve as a baseline reference point for future studies.

## CHAPTER 5

---

### *Model based analysis of the diverse metabolic phenotypes that arise in *C. reinhardtii* under a variety of trophic and illumination strategies*

In Chapters 3 and 4 the effects of wavelength and trophic strategy selection on the biomass productivity, cellular physiology and gene expression of *C. reinhardtii* were evaluated. The choice of narrow wavelength versus broad spectrum illumination, as well as trophic strategy were shown to have a significant impact across all the levels explored. In this chapter, a systematic analysis of the experimental data obtained in Chapters 3 and 4 using an experimentally validated Genome Scale Metabolic model (GeM) for *C. reinhardtii* (iRC1080; Chang *et al.*, 2011) is presented. Initially the GeM is manually curated based on the latest scientific literature and in-house developed computational techniques to update reaction stoichiometries and remove inactive reactions. The curated model is constrained to accurately reflect each of the experimental conditions discussed in Chapters 3 and 4. In order to better capture and analyse changes in biochemical composition using metabolic modelling techniques, a novel biomass curation algorithm is developed and evaluated. Finally, the emergent metabolic configuration for each condition is analysed using Markov-chain based sampling techniques and key metabolic differences between experimental conditions are identified using multivariate data analysis (MVDA).

#### 5.1. Introduction

Metabolism is the amalgamation of all the biochemical reactions occurring in tandem inside a living cell. Genome scale metabolic network models (GeMs) are mathematical reconstructions of all metabolic reactions encoded in an organism's

genome and can be used to simulate specific growth conditions and analyse the resulting cellular phenotype (Orth, Thiele and Palsson, 2010). Additional layers of mechanistic and regulatory information can be incorporated into such models by complementing the reconstructed network with other -omics data like metabolomics, transcriptomics and proteomics (Chang *et al.*, 2010; Lewis *et al.*, 2010; Bonde *et al.*, 2011). Cellular metabolism simulated in a GeM is assumed to be in a quasi-steady state whereby the total sum of any compound being produced must equal the total sum being consumed, resulting in no net accumulation or depletion of metabolites. By assuming that the cell operates towards optimising a particular aspect of its behaviour, usually growth, GeMs can be used to formulate a linear programming (LP) optimisation problem which can be solved to calculate the flow of metabolites throughout the entire network described.

The applications of GeMs are as varied as the types of organisms for which they have been developed. Constraint-based modelling has helped in the identification of a new anti-malarial drug candidate by finding essential enzymes in *Plasmodium falciparum* (Plata *et al.*, 2010) and in further understanding the metabolic differences between white and brown human adipocyte cells (Ramirez *et al.*, 2017). GeMs for photosynthetic organisms have also been published in recent years and a 2015 review article by Baroukh and colleagues reported 19 models for 3 species of cyanobacteria and 2 species of eukaryotic microalgae (Baroukh *et al.*, 2015). The review highlights key differences in the level of metabolic detail and compartmentalisation between published GeMs. The GeM utilised throughout this chapter, iRC1080, is praised for its attention to detail across lipid metabolism and the breakdown of its biomass equation (Chang *et al.*, 2011).

Flux balance analysis (FBA) is a well-established constraint-based modelling approach (Orth, Thiele and Palsson, 2010) in which all mass flow (flux) through a metabolic network is restricted by biomass productivity and extracellular uptake and secretion rates ( $v_{EX}$ ). The backbone of this approach is the mathematical representation of reaction stoichiometry within a GeM in the form of a large and sparse stoichiometric matrix. Under the assumption that all fluxes through the metabolic network are governed by a global cellular objective, a LP optimisation problem is solved to maximise

or minimise the predefined objective. Typically, a hypothesis is formulated based on the metabolic conditions and phenotype being studied to inform the selection of a cellular objective. For example, using FBA to better understand the metabolic effects of antibiotics on *Mycobacterium tuberculosis*, Montezano and colleagues postulated that under antibiotic stress, the cell's objective is survival rather than growth. Therefore they devised a method to align proteomics data to reactions in the GeM and assign percentage contribution of each reaction to the cellular objective (Montezano *et al.*, 2015). Constraint based modelling also accounts for the energetic requirements of a metabolic state. A study of *E. coli* transfected with a  $\beta$ -lactamase expressing plasmid postulated that the unnatural burden exerted by the production of recombinant protein on metabolism results in a change of cellular objective, and concluded that setting maximisation of maintenance energy expenditure as the cellular objective results in a more accurate predictions of the resulting flux distribution (Ow *et al.*, 2009). The diversity of phenotypes studied with FBA has led to the use of many different optimisation objectives and in turn, to the meta-analysis of those objective functions (Feist and Palsson, 2010; García Sánchez and Torres Sáez, 2014). Overall, the appraisal of an objective function is highly dependent on a large number of qualitative and quantitative factors like the number of experimentally determined extra- and intracellular fluxes, as well as the methodologies employed to calculate them (Gianchandani *et al.*, 2008).

Despite the number of different metabolic objectives devised in literature, cell growth remains a relevant objective in many cases. During growth in nutrient replete conditions and in the absence of any extrinsic stress factors, cell proliferation is a universal evolutionary pressure shared by all living organisms. This makes the maximisation of the specific growth rate an obvious candidate to assign in FBA studies. This usually translates into maximisation of the flux through a reaction that incorporates all the building blocks and biosynthetic energy molecules required to generate biomass content from metabolic precursors thus produces the theoretical growth rate predicted by FBA (Feist and Palsson, 2010). Therefore, the level of detail incorporated in the biomass reaction of each GeM will have a huge impact on the quality and accuracy of the resulting flux distributions when cellular growth is set as the objective.

Most GeM simulations assume the primary objective of the cell is biomass production (Price, Reed and Palsson, 2004). This is described in the model by a reaction termed the biomass equation that includes the growth- and non-growth associated maintenance costs as well as a stoichiometric definition of the cell's biochemical composition. Feist and Palsson (2010) described three categories of increasing complexity to describe different levels of granularity in a biomass equation. The basic level incorporates only macromolecular groups and ideally their constituent components. The intermediate level includes the biosynthetic energy required to produce those building blocks as well as polymerisation by-products such as water and diphosphate. A third level of detail termed 'advanced biomass equations' which contains vitamins, elements and cofactors was also described. The authors suggested separating an 'essential biomass' equation, containing the minimally functional content of the cell as inferred from knock-out studies, from non-essential components whenever possible (Feist and Palsson, 2010). Such level of detail is not usually reached in published GeMs. However, if the biomass equation does not accurately represent the cell's biochemical composition, the flux distributions obtained from solving the optimisation problem may not accurately account for the metabolic and energetic costs of producing biomass (Dikicioglu, Kirdar and Oliver, 2015). It was concluded in chapter 3 that the biochemical composition of a *C. reinhardtii* cell changes depending on the growth phase, wavelength choice and trophic growth mode it is in. Therefore, it is necessary to be able to update the model's biomass equation in accordance to the experimentally determined composition in order to maximise the fidelity of the simulated flux distributions.

The effects of modifying the stoichiometry of the biomass equation on predicted flux distributions have been extensively studied in the literature (Senger and Nazem-Bokaei, 2013; Dikicioglu, Kirdar and Oliver, 2015; Levering *et al.*, 2016). Dikicioglu and colleagues (2015) carried out a systematic evaluation of mutant phenotype gene essentiality predictions in a yeast GeM by varying each component of the biomass equation two fold in nutrient replete and various nutrient limited conditions (Dikicioglu, Kirdar and Oliver, 2015). Their analysis demonstrated that experimentally determined changes to the biomass composition of *Saccharomyces cerevisiae* caused by genetic

mutations must be reflected in the biomass equation to accurately predict the metabolic flux distribution of the mutant phenotype.

Senger and Nazem-Bokaei (2013) proposed an unsupervised approach to determine the optimal biomass composition for a given phenotype of *E. coli* by employing a genetic algorithm (Senger and Nazem-Bokaei, 2013). They constrained the *E. coli* GeM with experimentally determined values for all uptake and secretion rates and posited that any additional efflux of metabolites required to satisfy the model's mass balance should be of negligible magnitude. In effect, they termed these additional secretion fluxes as total unconstrained fluxes (TUX) and set minimisation of TUX as the fitness function for the genetic algorithm. This approach diverges from the rest because it does not rely on the variability of experimentally determined biochemical composition data to set the bounds of the optimisation problem. Instead the allowable range for each stoichiometric component arbitrarily to +/-50% of the value in the original biomass equation. However, if any component of the biomass equation differs by more than 50% in the experimental condition studied this method would not be able to capture the real biomass composition.

Levering and colleagues employed Fourier-transform infrared spectroscopy (FTIR) to generate high-throughput measurements of *Phaeodactylum tricornutum* biomass composition at different culture time points and experimental conditions (Levering *et al.*, 2016). These experimental measurements were the basis of condition specific biomass equations substituted into the *P. tricornutum* GeM to simulate different experimental conditions. This is an optimal pipeline, however the number of experiments required to develop and validate high fidelity FTIR linear models for each biomass component is not trivial (Mayers, Flynn and Shields, 2013). Literature values for macromolecular distribution of *C. reinhardtii* biomass grown in nutrient replete conditions vary significantly between publications (Appendix I). Such variability is possibly due to three main factors. Firstly, the wide array of methods available for proximal analysis, secondly the accuracy of the method employed and thirdly the metabolic plasticity of *C. reinhardtii*. Whilst remaining impactful, the true change in biomass composition between experimental conditions may be relatively small and could be hard to determine if the experimental methods are not harmonised between

studies and the accuracy of each method used is not comparable. The lack of full mass balance closure encountered in the results presented in Chapter 3 of this thesis prompted the development of a novel algorithm capable of reconciling the biomass equation in GeMs using a small number of routinely available experimental measurements while accounting for significant levels of experimental uncertainty. The following section details the aim and objectives of this chapter.

## 5.2. Aim & Objectives

The aim of this chapter is to perform a rigorous model based analysis of the effects of illumination and trophic strategy selection on cell physiology and biochemical composition in *Chlamydomonas reinhardtii* in order to maximise the amount of information extracted from the available experimental data presented in Chapters 3 and 4. This can be broken down into the following scientific objectives:

- Manually curate the latest available *C. reinhardtii* GeM (iRC1080, Chan *et al* 2011) to update reaction stoichiometry and remove inactive reactions
- Constrain the GeM using carbon constrained FBA (ccFBA, Lularevic *et al.*, 2019) in order to accurately simulate each of the experimental conditions presented in Chapters 3 and 4
- Develop and validate a novel algorithm able to adapt the stoichiometry of the biomass equation in GeMs to accurately reflect changes in biochemical composition (termed biomass optimisation algorithm or BMO algorithm in the remainder)
- Incorporate the BMO within a comprehensive GeM analysis workflow using Markov-chain based sampling and Multivariate Data Analysis (MVA) techniques to analyse the metabolic phenotype of the curated iRC1080 GeM and identify key metabolic differences between the examined conditions
- Compare the emergent metabolic phenotypes obtained from the FBA studies with previously published data

## 5.3. Methodology

### 5.3.1. Genome-scale metabolic model and experimental data

The latest metabolic network reconstruction for *Chlamydomonas reinhardtii* (iRC1080; Chang *et al.*, 2011) was used in this Chapter so as to guarantee all simulations were performed on an extensively curated and validated Genome Scale Metabolic model (GeM). The iRC1080 pre-processing involved removal of inactive reactions, light reaction stoichiometry adjustment and incorporation of experimental constraints, and is described in further detail in the following sections.

The same experimental conditions evaluated in Chapters 3 and 4 were explored in this Chapter. These were autotrophic growth in M8a medium under white, red and blue LEDs (referred to throughout this chapter as WA, RA and BA respectively) and mixotrophic growth under white, red and blue LEDs (referred to throughout this chapter as WX, RX and BX respectively). Growth rate, nutrient uptake rate and biomass composition data averaged between the 16 and 48 hour timepoints from the experimental cultures described in Chapter 3 were specifically used to constrain the GeM and simulate cells in the mid-exponential growth phase of a batch culture as described below.

### 5.3.2. Flux Balance Analysis

Constraint based methods for metabolic modelling (Bordbar *et al.*, 2014) like flux balance analysis (FBA), condense cellular metabolism into a sparse matrix  $\mathbf{S}$  of size ( $m \times n$ ) referred to as the stoichiometric matrix. Each row ( $m$ ) in  $\mathbf{S}$  stands for a unique metabolite, while each column ( $n$ ) represents an individual reaction. Each matrix element ( $s_{ij}$ ) in  $\mathbf{S}$  is therefore a stoichiometric coefficient of the  $i^{th}$  metabolite in the  $j^{th}$  reaction. Metabolic flux (typically in  $\text{mmol gDCW}^{-1} \text{h}^{-1}$ ) through the metabolic network represented by  $\mathbf{S}$  is represented in a ( $n \times 1$ ) vector  $\mathbf{v}$ . Under the assumption of quasi-steady state, whereby the total amount of any compound being produced in the network is equivalent to the total amount being consumed, a mass balance across  $\mathbf{S}$  yields Equation 5.1 (Orth, Thiele and Palsson, 2010):



$$S \cdot v = 0 \quad (\text{Eq 5.1})$$

The system of equations resulting from Equation 3.1 is underdetermined as there are typically more reactions than metabolites in  $S$ . Consequently, a unique solution cannot be determined. In FBA, it is assumed that cells gear their metabolism towards a singular, overarching metabolic objective such as maximisation of biomass or ATP (Price, Reed and Palsson, 2004). This can be formulated as a linear programming (LP) optimisation problem:

$$\min/\max (Z) \quad (\text{Eq 5.2})$$

$$s. t. \quad S \cdot v = 0 \quad (\text{Eq 5.3})$$

$$v^{ub} \geq v \geq v^{lb} \quad (\text{Eq 5.4})$$

Where  $Z$  corresponds to the flux or fluxes through the reaction or reactions that conform the optimisation objective subject to mass balance (Eq. 5.3) and inequality (Eq. 5.4) constraints. In this Chapter, the biomass objective in all FBA simulations was maximisation of biomass. The set of inequality constraints described in Equation 5.4 determines the minimum or lower bound ( $v^{lb}$ ) and the maximum or upper bound ( $v^{ub}$ ) of flux permissible through each reaction.

In this Chapter, flux balance analysis was performed with the constraint-based reconstruction and analysis toolbox (COBRA) in Matlab R2019b. The experimental constraints applied to iRC1080 are listed in Appendix II.

### 5.3.3. Model pre-processing

#### Adjustment of light reaction stoichiometry

The light input reactions are called PRISM reactions in iRC1080 (Chang *et al.*, 2011). Each reaction describes the spectral distribution of the light source. The visible light spectrum is divided into effective bandwidth regions. The derivation of stoichiometric coefficients for each region corresponds to the ratios of photon flux in the defined

region to the total photon flux in the visible spectrum emitted by a given light source (Figure 5.1 A and B). The PRISM reactions were thus updated to accurately describe the incident light derived from the light source used for the experiments presented in Chapters 3 and 4 (Table 5.1).

**Table 5.1.** Custom PRISM reactions for iRC1080. Stoichiometry derived using Chang *et al.* 2011 methodology and ALGEM LED spectra.

Photon region (nm)	White LED		Red LED		Blue LED	
	iRC1080	Algem	iRC1080	Algem	iRC1080	Algem
	Effective bandwidth coefficient ( $\mu\text{mol}_{\text{ph}} \text{m}^{-2} \text{s}^{-1}$ )					
406-454	0.00711	0.0272		0	-	0.279
378-482	0.0459	0.157		0	-	0.916
417-472	0.0274	0.115		0	-	0.808
451 – 526	0.152	0.262		0	-	0.807
608 – 666	0.257	0.263	0.266	0.266	-	0.00656
659 – 684	0.0703	0.0721	0.660	0.660	-	0.00263
662 - 691	0.0753	0.0813	0.725	0.725	-	0.00296

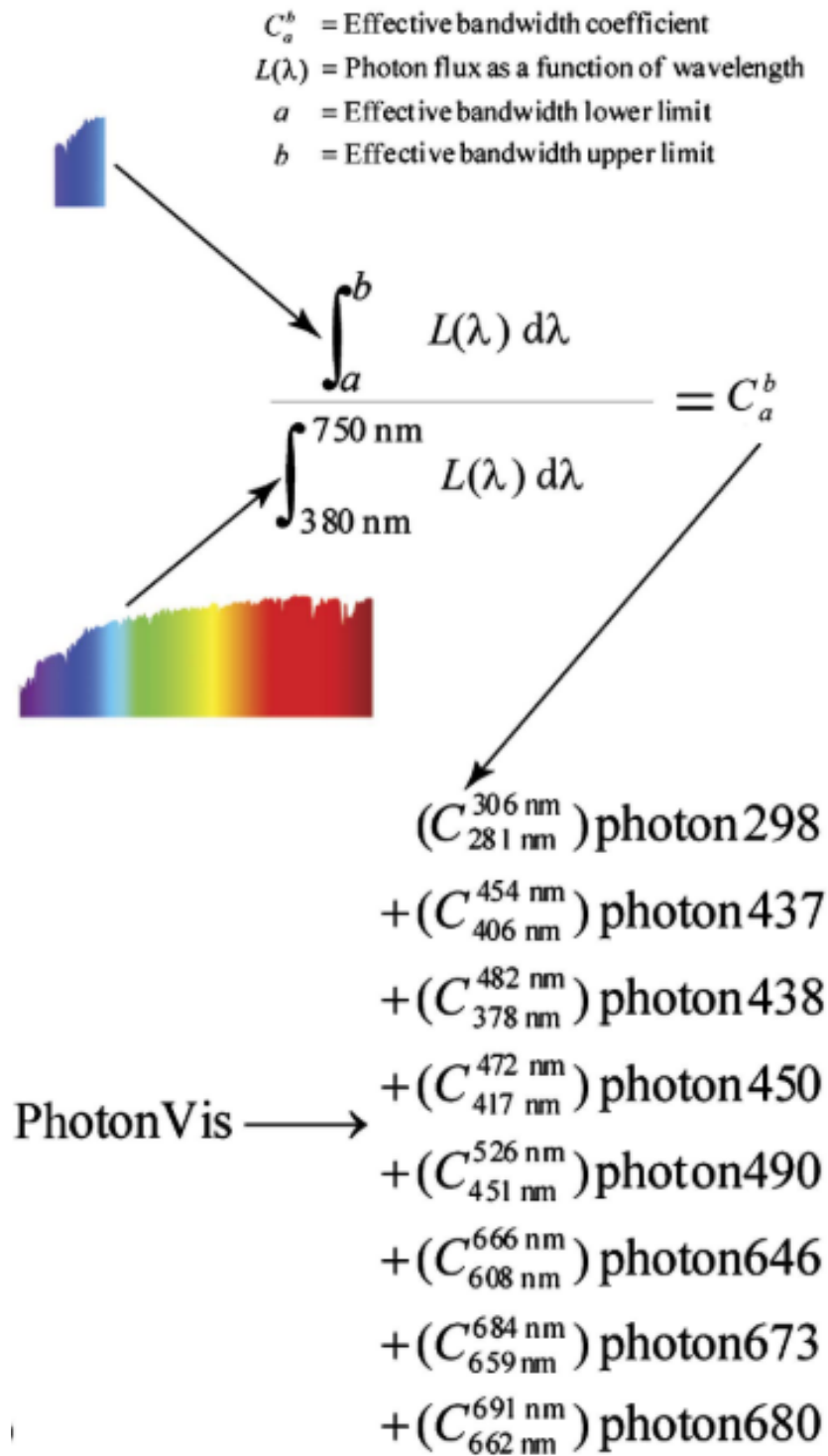


**Figure 5.1** Derivation of light reactions in iRC1080. The photon flux from wavelengths  $a$  to  $b$  is normalized by the total visible photon flux from 380 to 750 nm to yield the effective spectral bandwidth coefficient  $C$ . The coefficients for each range are compiled into a single prism reaction for a given light source, representing the composition of emitted light as defined by photon-utilizing metabolic reactions. Equation variables are defined at the top of the figure (Adapted from Chang *et al.*, 2011).

## Removal of dead-end metabolites and inactive reactions

By design, the application of constraint-based modelling techniques such as FBA leads to underdetermined problem formulations as the number of unknowns (intracellular metabolic fluxes) greatly exceeds the number of known variables (usually a subset of the exchange fluxes  $v_{ex}$ ) (Orth, Thiele and Palsson, 2010). The underdetermined nature of GeMs results in an infinite number of potential flux distributions being able to achieve the same value for the objective function. The lack of a unique solution manifests into a multi-dimensional space of equally optimal solutions, comprising as many dimensions as reactions in the model. The vertices of this multi-dimensional space are delimited by the maximum and minimum flux that each reaction can carry whilst attaining a certain value for the optimisation objective. The larger the solution space, the higher the uncertainty in accurately predicting basic reaction properties including reaction directionality (Kiparissides and Hatzimanikatis, 2017). Therefore, the first step in the GeM analysis workflow followed in this thesis is the removal of so-called blocked reactions (Angeles-Martinez and Theodoropoulos, 2016). These reactions are not able to carry flux when set as the optimisation objective, even when the model is given infinite access to substrates and the ability to secrete an infinite amount of by-products. This is implemented by relaxing the bounds for all extra- and intra- cellular reactions to an arbitrarily large value and performing FVA:

$$Z = c \cdot v \quad (\text{Eq. 5.5})$$

$$\min/\max (Z_i) \quad (\text{Eq. 5.6})$$

$$\text{s.t. } S \cdot v = 0 \quad (\text{Eq. 5.7})$$

$$v^{ub} \geq v \geq v^{lb} \quad (\text{Eq. 5.8})$$

$$v^{ub} = 100, v^{lb} = -100 \quad (\text{Eq. 5.9})$$

Where  $Z$  is the objective function and the index ( $i$ ) indicates the position of a reaction in vectors  $c$ ,  $v$ ,  $v^{ub}$  and  $v^{lb}$ .  $S$  denotes the stoichiometric matrix of the GeM. Vector  $c$  determines the reaction, or combination of reactions, that will be maximised or minimised by the optimisation problem. By default, a value of (1) or a value of (-1) is input in position ( $i$ ) to minimise or maximise the flux through reaction ( $i$ ) respectively. All other entries in vector  $c$  are 0. Vector ( $v^U$ ) contains the upper and vector ( $v^L$ ) contains the lower bound for all reactions in the model. These values are predetermined based on experimental or literature data.

Following this methodology, a total of 544 reactions and consequently 576 metabolites were removed from the model as they were not able to carry any flux. This yielded a new  $S$  composed of 1647 reactions by 1130 metabolites.

#### 5.3.4. Biomass optimisation algorithm

The BMO algorithm developed in this chapter relies on a type of stochastic global optimisation (GO) method called enhanced scatter search (eSS) (Chachuat, Singer and Barton, 2006). The AMIGO2 toolbox (Egea *et al.*, 2009) was used to implement the eSS algorithm in Matlab R2016b. The eSS algorithm requires a fitness function and variable constraints. In brief, maximum and minimum constraints were calculated for each macromolecular group making up the biomass reaction from the experimental data presented in Chapter 3. The fitness function evaluated by the eSS algorithm was the combination of two objectives. First, minimisation of the difference between the experimentally observed maximum specific growth rate ( $\mu_{\max}$ ) and the FBA simulated

$\mu_{\max}$ . Secondly, minimisation of the difference between 1 and the sum of all biomass equation stoichiometric coefficients converted to g gDCW<sup>-1</sup>. The following sub-sections describe these steps in detail.

### Classifying biomass equation constituents

The three original biomass equations in iRC1080 are composed of 171 unique metabolites (See Appendix III for the complete list) plus the energy balance of ATP, ADP, inorganic phosphate and water. These 171 metabolites were divided into 10 macromolecular groups as listed in Table 5.2. The groups were then classified as (a) constant, whereby the proportion of dry cell weight assigned to the group was assumed to not change between the experimental conditions studied, and (b) variable, groups of which experimental data was obtained in Chapter 3 and were found to differ between the experimental conditions studied.

**Table 5.2** Classification of iRC1080 biomass equation constituent metabolites into the macromolecular groups that make up *C. reinhardtii* biomass.

Macromolecular group	Number of constituent metabolites	Type
Carbohydrates	4	Variable
Chlorophyll A	1	Variable
Chlorophyll B	1	Variable
DNA	4	Constant
Glycerol	1	Constant
Lipids	125	Variable
Xanthophylls	8	Variable
Protein	21	Variable
RNA	3	Constant
VFA	3	Constant

### Calculating upper and lower bounds for the eSS algorithm

In the biomass equation, the stoichiometric coefficients of the constituents are mmol gDCW<sup>-1</sup>. These must be converted to g gDCW<sup>-1</sup> for calculating the adjusted stoichiometric coefficient value of each constituent, according to the changes in percentage contribution to the total dry cell weight of the macromolecular group the constituent belongs to:

$$C_{jh} = \frac{MW_j \cdot SC_{jh}}{1000} \quad (\text{Eq. 5.10})$$

Where  $C_{jh}$  is the stoichiometric coefficient of constituent  $j$  in experimental condition  $h$  in g gDCW<sup>-1</sup>;  $MW_j$  is the molecular weight of constituent  $j$  in mol g<sup>-1</sup>;  $SC_{jh}$  is the stoichiometric coefficient of constituent  $j$  in mmol gDCW<sup>-1</sup>.

Within each macromolecular group, all constituents were given equal weighting therefore the original stoichiometric distribution within a group was not altered by the BMO algorithm:

$$d_{jih} = \frac{C_{jh}}{\sum_{k=1}^n C_{kih}} = \frac{C_{jh}}{G_{ih}} \quad (\text{Eq. 5.11})$$

Where  $d_{jih}$  is the proportion of constituent  $j$  in group  $i$  in experimental condition  $h$  (as a % w/w);  $n$  is the total number of constituents in group  $i$ ;  $C_{kih}$  is the sum of the stoichiometric coefficients of all constituents in macromolecular group  $i$  under condition  $h$  also equivalent to  $G_i$  in g gDCW<sup>-1</sup>.

For example, the carbohydrates group is made up of arabinose, galactose, mannose and starch in a g gDCW<sup>-1</sup> ratio of 1.00:1.33:0.63:0.01. Although the percentage contribution of carbohydrates to the total dry cell weight changes between conditions, the ratio of arabinose:galactose:mannose:starch remains constant in all new biomass reactions generated by the BMO algorithm.

The upper and lower bounds used in the BMO algorithm for each  $G$  were calculated from the experimental data in Chapter 3 (Figure 3.11 – 3.14) as follows:

First the sum of macromolecular groups was calculated from the average macromolecular composition at 16 hours of batch culture.

$$\overline{V_{ih}} = \frac{\sum_{k=1}^n V_{kih}}{n} \quad (\text{Eq. 5.12})$$

$$E_{ih} = \sum_{k=1}^z \overline{V_{kih}} \quad (\text{Eq. 5.13})$$

Where  $\overline{V_{ih}}$  is the average quantity of macromolecule  $i$  at 16 hours of batch culture in experimental condition  $h$  in gDCW<sup>-1</sup>;  $n$  is the total number of biological replicates;  $E_{ih}$  is the sum of macromolecular groups in gDCW<sup>-1</sup>;  $z$  is the total number of macromolecular groups.



Next the ghost carbon fraction of each experimental condition was calculated:

$$GC_h = 1 - E_{ih} \quad (\text{Eq. 5.14})$$

Where  $GC_h$  is the ghost carbon fraction in gDCW<sup>-1</sup> in condition  $h$ .

Each  $\overline{V_{ih}}$  was normalised to each  $E_{ih}$  and the normalised  $\overline{V_{ih}}$  were multiplied by their corresponding  $GC_h$  to distribute the  $GC_h$  across each  $\overline{V_{ih}}$  according to their relative measured quantity:

$$GC_{\overline{V_{ih}}} = \left( \frac{\overline{V_{ih}}}{E_{ih}} \right) \cdot GC_h \quad (\text{Eq. 5.15})$$

Where  $GC_{\overline{V_{ih}}}$  is the proportion of GC in condition  $h$  attributable to  $\overline{V_{ih}}$  macromolecular group.

Finally, the upper and lower bounds for each  $G$  was calculated:

$$G_{ihUB} = \overline{V_{ih}} + GC_{\overline{V_{ih}}} \quad (\text{Eq. 5.16})$$

$$G_{ihLB} = \overline{V_{ih}} - GC_{\overline{V_{ih}}} \quad (\text{Eq. 5.17})$$

Where  $G_{ihUB}$  and  $G_{ihLB}$  are the upper and lower bounds set in the BMO algorithm for each macromolecular group in each experimental condition.

### **Fitness function of the eSS algorithm**

The fitness function evaluated by the eSS algorithm was the combination of two objectives. First, minimisation of the difference between the experimentally observed maximum specific growth rate ( $\mu_{\max}$ ) and the FBA simulated  $\mu_{\max}$ . Secondly, minimisation of the difference between 1 and the sum of all biomass equation stoichiometric coefficients converted to gDCW<sup>-1</sup>:

$$\mu_{diff,h} = [(\mu_{exp,h} - \mu_{FBA,h}) \cdot \mu_{exp,h}]^2 \quad (\text{Eq 5.18})$$

$$G_{diff,h} = \left( \sum_{k=1}^n G_{kih} \right) - 1 \quad (\text{Eq 5.19})$$

$$f = \mu_{diff,h} + G_{diff,h} \quad (\text{Eq 5.20})$$

Where  $\mu_{exp,h}$  is the biomass growth rate at 16 hours of batch culture and  $\mu_{FBA,h}$  is the predicted biomass growth rate both in  $\text{h}^{-1}$ ;  $f$  is the fitness function of the eSS algorithm.

### Complete formulation of BMO algorithm

The BMO algorithm is formed by combining the modules described in the previous sections. A GO problem can be formulated and solved with the eSS algorithm (Egea *et al.*, 2007):

$$\min (f) \quad (\text{Eq 5.21})$$

$$s. t. G_{ihLB} \geq G_{ih} \geq G_{ihUB} \quad (\text{Eq 5.22})$$

Every iteration of the eSS algorithm searches through the solution space of  $G_{ih}$  combinations and produces a solution vector of  $G_{ih}$  values that is converted into individual  $C_{jh}$  and then  $SC_{jh}$  used to update the biomass equation of the GeM. The GeM is then solved, and  $f$  is evaluated. Once the value of  $f$  converges on a minimum, a matrix made up of eSS solution vectors is analysed and the solution vector with the smallest  $f$  is selected.

### 5.3.5. Carbon constraining

An algorithm to further constrain the FBA solution space of the GeM by constraining intracellular fluxes of the model based on an elemental balance of carbon (Lularevic *et al.*, 2019) was employed. The aim of carbon constraining is to reduce the size of the resulting solution space by removing physiologically infeasible flux values. This is achieved by imposing a limit on the permissible flux through each intracellular reaction based on the amount of carbon atoms uptaken by the cell under each experimental condition studied. In autotrophic simulations this constraining was governed by the flux through the  $\text{CO}_2$  extracellular exchange ( $\text{EX\_CO}_2$ ) reaction in

iRC1080 whereas in mixotrophic simulations it was the sum of fluxes through EX\_CO<sub>2</sub> and the acetate extracellular exchange reaction (EX\_AC).

### **5.3.6. Model based analysis workflow**

The published version of iRC1080 required curation and reduction pre-processing steps to maximise the efficiency of the solution space sampling and multivariate analysis methods described in the following sections. The workflow summarised in Figure 5.2 was explained in detail in sections 5.3.3, 5.3.4 and 5.3.5. The processed iRC1080 version is referred to from here on with a combination of the experimental condition it simulates and the biomass equation it utilises to do so. For example, the iRC1080 version that simulates white autotrophic growth with the original biomass equation is referred to as *WA OGBM* and the version that simulates the same experimental conditions with the newly generated biomass equation is referred to as *WA BMO*.

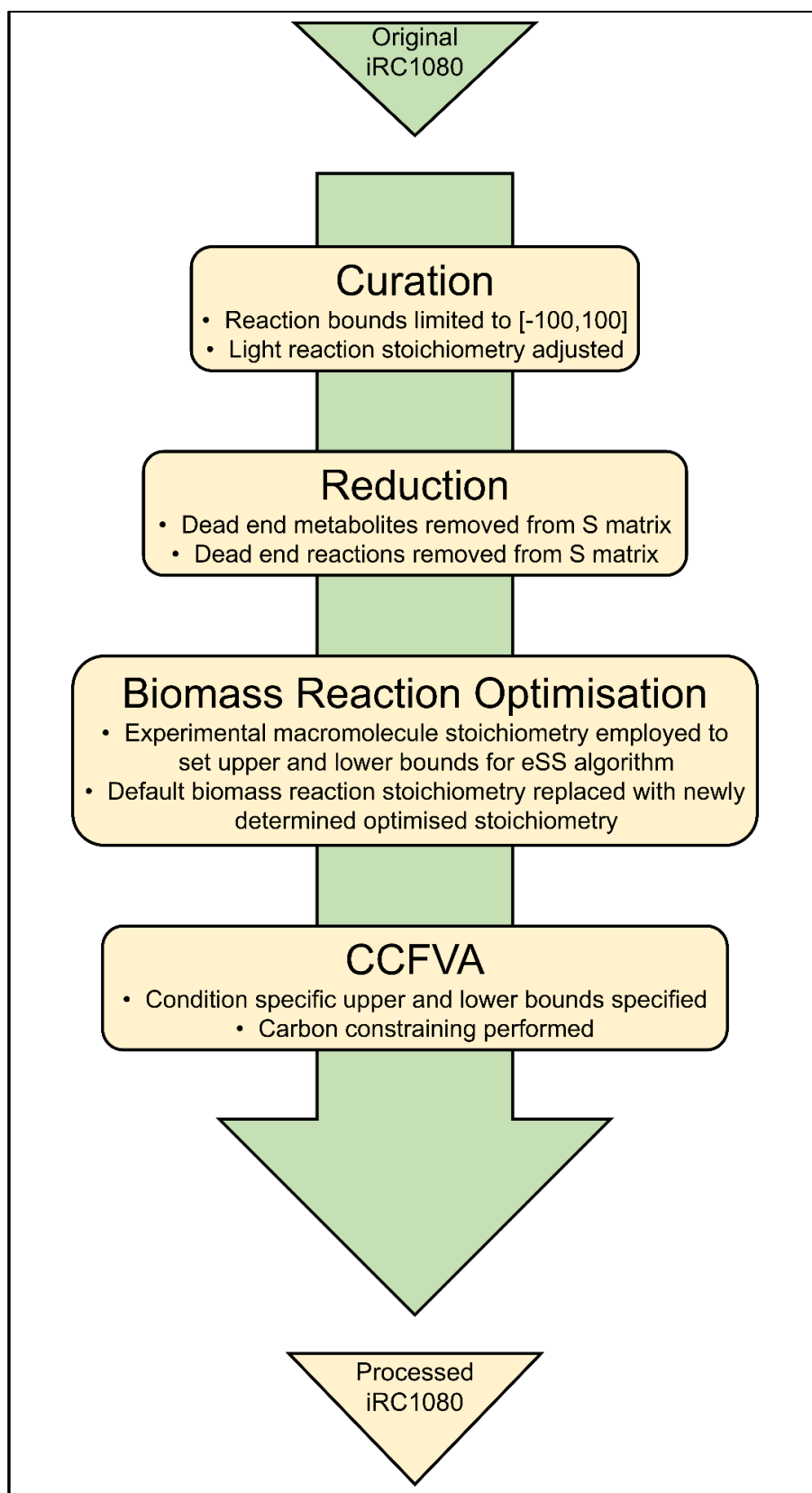


**Figure 5.2**

Complete GeM processing workflow. The original iRC1080 model is first curated and reduced. This is followed by updating of the biomass equation using the BMO algorithm. Finally, the model is carbon constrained using ccFVA and the processed iRC1080 is ready for multivariate analysis.

### 5.3.7. Solution space sampling

After model curation, the application of ccFVA to accurately constrain intra- and extra- cellular reaction bounds and BMO to accurately update the stoichiometry of the biomass reaction the model can be used to simulate metabolism under a given set of experimental conditions. As mentioned above, due to the underdetermined nature of FBA problem formulations a single point solution is of little value. Instead, Markov-chain based random sampling techniques are routinely used to retrieve a statistically representative sample of flux distributions from the resulting optimal solution space. Analysis of this sample of optimal flux distributions is routinely used to enhance behavioural understanding of the metabolic state under a given set of physiological conditions (Mo, Palsson and Herrgard, 2009; Schellenberger and Palsson, 2009; Shlomi *et al.*, 2011). Each of the six experimental conditions presented in Chapters 3 and 4 was uniformly sampled using the ACHR sampler included in the COBRA toolbox (Schellenberger *et al.*, 2011). As ACHR sampling is computationally intensive, prior to sampling all experimental conditions an analysis to determine the minimum number of sampled flux distributions was conducted (Figure 5.3). Computing 500,000 samples is conventionally accepted as sufficient when exploring the solution space of such a GeM. As can be seen in Figure 5., the incremental gain in sample coverage (Sariyar *et al.*, 2006) after 500,000 samples does not justify the additional computational and time expense required to achieve it thus it was decided to perform all sampling at 500,000 samples per condition.

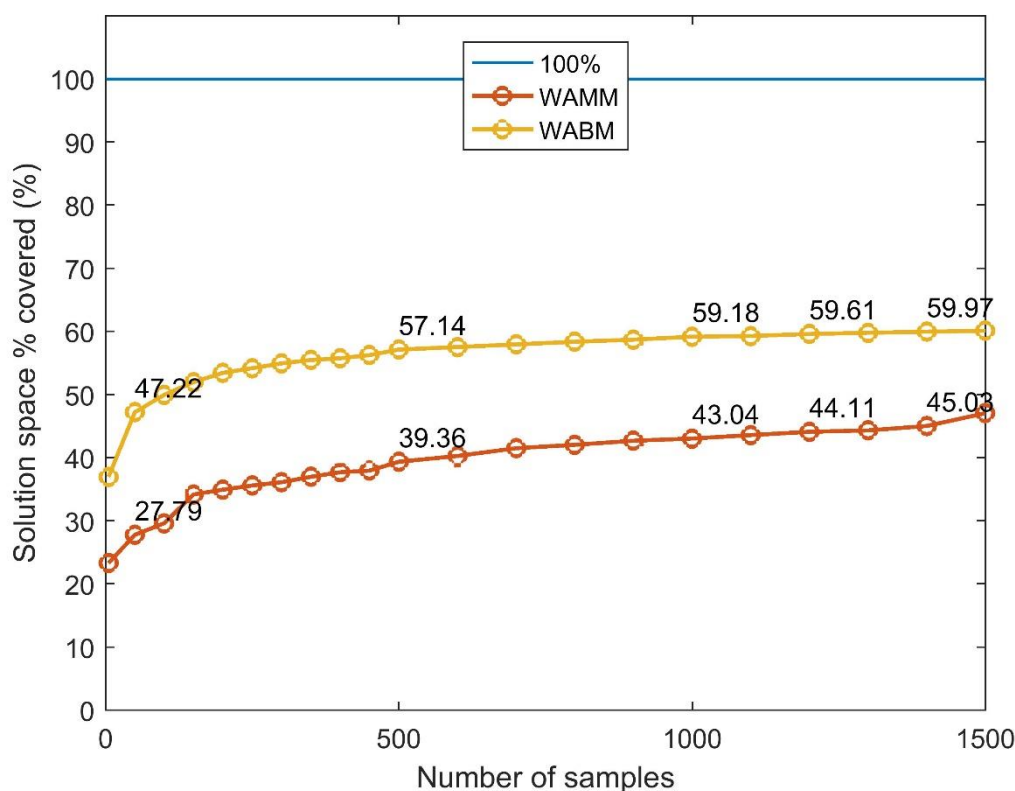


**Figure 5.3** Solution space percentage coverage (Sariyar *et al.*, 2006) as a function of number of samples taken for the flux distribution of a single condition using the GeM iRC1080 model. WAMM, white autotrophic condition constrained with FVA bounds only; WABM, white autotrophic condition constrained with FVA and carbon constraining bounds.

### 5.3.8. Multivariate data analysis by principal component analysis (PCA)

Principal component analysis (PCA) is a multivariate analysis technique that simplifies a K-dimensional dataset by reducing its dimensionality. Standard deviation, covariance and singular value decomposition are employed to do so. This technique produces K new dimensions based on the maximum variance of the original dataset. The new dimensions termed principal components (PCs) and are derived from a linear combination of the original variables. Each PC is made up of K coefficients called loadings and the transformed data points in the new dimensionality are called scores (Sariyar *et al.*, 2006; Worley, Halouska and Powers, 2013). In this chapter, PCA was used on the Monte-Carlo (MC) samples generated with the ACHR algorithm. Each column in the MC samples matrix represents a reaction in the GeM and each row represents a sampled

flux distribution. In this chapter, the MC samples of two or more simulations (i.e. GeMs with different biomass equations or nutrient uptake bounds) were combined into one matrix. The rows (each row is a single sampled flux distribution also referred to as a sample) of the newly constructed matrix were shuffled at random to prevent any systematic errors or bias.

A sample ID vector was generated to preserve each sample's simulation conditions (eg. WA or WX). As PCA problems tend to contain many variables, there is a chance that some variables will have very different scales. The data is commonly mean centred to remove such bias before comparing variables to each other. This was done by subtracting the mean of each column in the MC samples matrix from each respective flux value and dividing the result by the column's standard deviation. The covariance matrix was calculated followed by singular-value decomposition (SVD). In SVD,  $X$  equals  $USV^T$ , where  $X$  is the covariance matrix,  $U$  contains the left singular vectors, the diagonal of the  $S$  matrix is composed of the eigenvalues and  $V^T$  contains the right singular vectors also referred to as loadings. Multiplying the loadings by the original data matrix produces the scores, with  $K$  coordinates according to the number of PCs. A diagram summarising the data processing described above can be seen in Figure 5.4. For more information please refer to *"Multivariate Analysis in Metabolomics"* by Worley and Powers (2013).

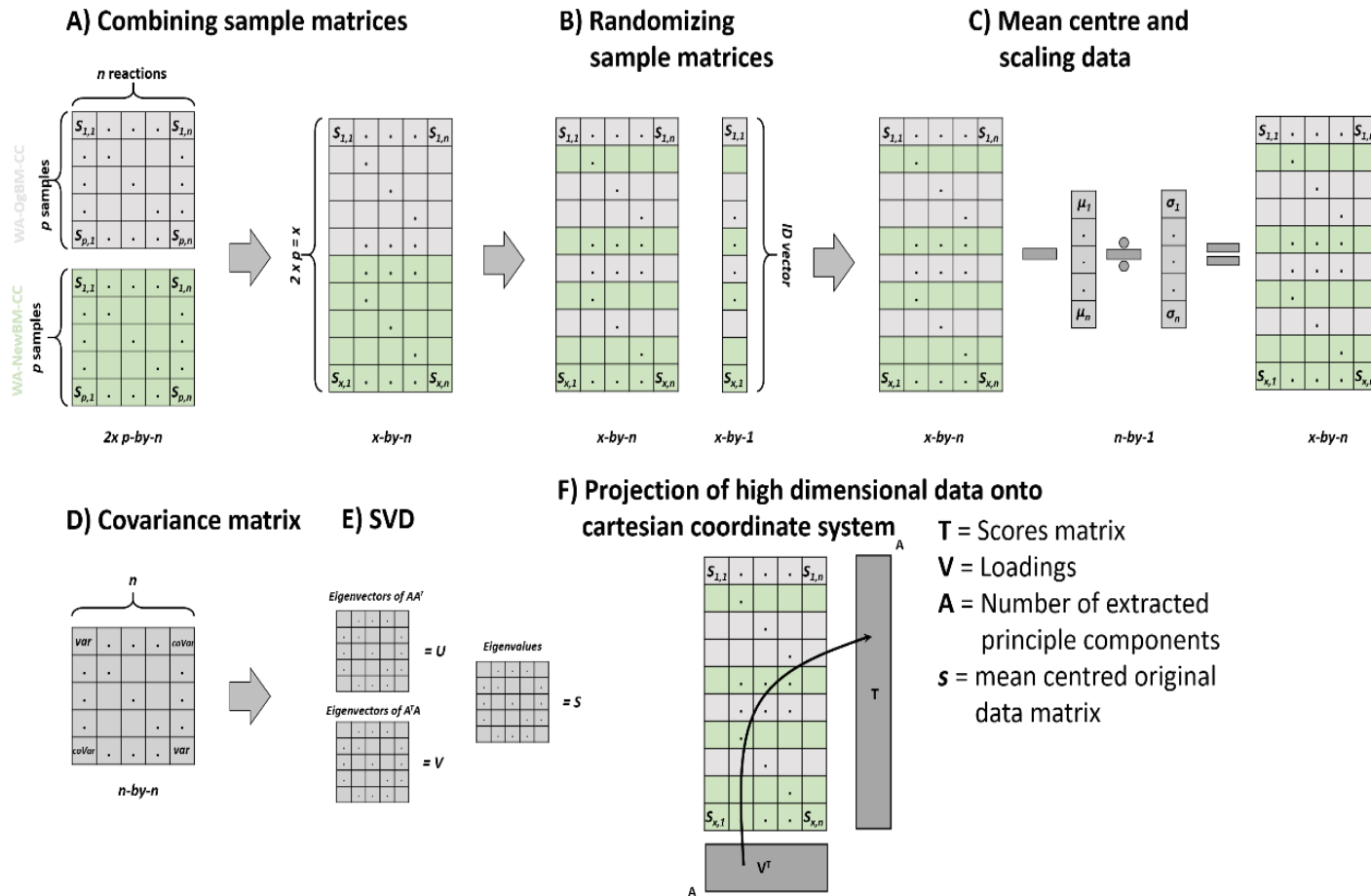


**Figure 5.4.** Schematic overview of PCA and data pre-processing. A) MC samples matrices of size p-by-n (p samples and n reactions) of different simulations. As an example, WA constrained with the original biomass equation (grey) and WA constrained with the newly generated biomass equation (green) are combined into a single matrix. This operation is scalable to any number of experimental conditions. B) Randomizing the full sample matrix by scrambling rows and creation of a sample ID vector (x-by-1) that maintains the connection of each sample to the original matrix it belongs to. C) Data is mean centred and scaled. D) Evaluation of the covariance matrix from the processed samples matrix. E) Singular-value decomposition. F) Loadings are used to project the original mean centred and scaled data onto a new hyperplane where the axes correspond to the generated principal components.



## 5.4. Biomass equation optimisation

Experimental data from Chapter 3 shows *Chlamydomonas reinhardtii* develops different physiologies under monochromatic illumination in autotrophic and in mixotrophic media. Significant alterations to biomass composition during a batch culture could signal some degree of divergence in central carbon metabolism between experimental conditions. The gene expression data from Chapter 4 also shows trophic strategy and wavelength selection have an impact on photosynthesis, the glyoxylate cycle and fatty acid synthesis. In this chapter, the biomass equation of a state-of-the-art genome scale metabolic model (GeM) is adjusted according to experimental measurements (presented in Chapter 3) to reflect the known physiological changes in the model structure; in an effort to corroborate the transcriptional data presented in Chapter 4 and obtain previously unknown insights on the effect of trophic strategy and wavelength selection on the metabolism of *C. reinhardtii*.

The direct and indirect impact of such experimental measurements on seemingly unrelated metabolic subsystems can be predicted by FBA. A recent example of this was showcased in the publication of a GeM of the diatom *Phaeodactylum tricornutum* that predicted a previously unknown glutamine-ornithine shunt that transfers reducing equivalents from the chloroplast to the mitochondria (Levering *et al.*, 2016). However, as explained in the introduction of this chapter, high confidence flux predictions are dependent on the biomass composition being accurately reflected during the simulation.

### Macromolecular composition

Three biomass equations with unique stoichiometries were originally included in the iRC1080 model to describe the cellular biomass composition under autotrophic, mixotrophic and heterotrophic growth. The biomass equations in iRC1080 were derived from literature by the authors of the model using previously reported methods (Förster *et al.*, 2003; Chavali *et al.*, 2008; Chang *et al.*, 2011). The proportion of dry weight biomass attributed to each macromolecular group from carbohydrate, chlorophyll, DNA, volatile fatty acid, glycerol, lipid, protein, RNA and xanthophyll was broken down into

subtypes wherever possible. For example, protein composition was divided into amino acid distribution (Boyle and Morgan, 2009). As such each macromolecular group listed above is represented in the biomass equation by at least two metabolites, except glycerol (see Appendix III for complete breakdown of biomass equation components). The original biomass equations for autotrophic and mixotrophic growth only differed in pigment content.

An updated biomass composition was derived using the BMO algorithm developed herein and presented in section 5.3.2 for each experimental condition. A visual representation of the macromolecular distribution of (a) the original iRC1080 biomass reaction (Figure 5.5A; Figure 5.6A), (b) the experimentally measured macromolecular composition for each experimental condition (Figure 5.5B, D and F; Figure 5.6B, D and F) and (c) the BMO derived biomass reaction (Figure 5.5C, E and G; Figure 5.6C, E and G) is presented in Figures 5.5 and 5.6 for phototrophic and mixotrophic conditions respectively. It is apparent that the original biomass reaction in iRC1080 varies significantly from the experimental data in terms of macromolecular composition.

In the original iRC1080 biomass equation carbohydrates account for 57.52% of the dry cell weight (Figures 5.5A and 5.6A). In contrast, the experimentally measured carbohydrate fraction was found to vary between ~5% and ~33% of DCW under the conditions examined (Figure 3.11). Such a large proportion of the dry cell weight attributed to carbohydrates is usually seen under nitrogen starvation which elicits a stress response that triggers the production of energy storage molecules (James *et al.*, 2011; Davey *et al.*, 2014). Therefore, using the original biomass reaction from iRC1080 to simulate nutrient replete, mid -exponential growth would lead to significant deviations from reality (Joseph Msanne *et al.*, 2012).

Similarly, in terms of protein content, the original iRC1080 biomass reaction accounts for a fixed biochemical composition comprising 14.91% DCW of proteins. However, under the experimental conditions considered in the present thesis, protein content was found to vary significantly with trophic mode, illumination wavelength and culture time ranging from as low as ~15% to as high as ~50% of DCW (Figure 3.13). Therefore, the original iRC1080 biomass reaction was in agreement with experimental

data in terms of the measured fraction of proteins in dry biomass for only one out of the 6 conditions considered (RX, Figure 3.13 B). However, as summarised in Table 3.7, RX had the largest discrepancy between total weight calculated from the sum of proximal analysis measurements ( $36.9 \text{ pg cell}^{-1}$ ) and dry cell weight measurements ( $72.4 \text{ pgDCW cell}^{-1}$ ). Therefore, the BMO algorithm redistributed an additional 48.90% of ghost carbon and protein finally accounted for 37.13% of dry weight in the RX BMO (Figure 5.6E). Growth rate is widely regarded as a good correlate to protein synthesis and expression (Dennis and Bremer, 1974; Scott *et al.*, 2010) and these newly generated BMOs are a representation of actively growing cells therefore an increase in the proportion of protein is not unexpected.

The 12.57% of dry cell weight accounted for by lipids in the original iRC1080 biomass reaction matched 5 out of the 6 experimental conditions considered (WA, BA, Figure 3.11 A; WX, RX, BX, Figure 3.11 B). Consequently, the percentage change in lipids between the OGBM and the BMO biomass reactions was relatively small compared to the other macromolecular groups (Figure 5.5 and Figure 5.6). The close initial agreement between OGBM and experimental results, and the fact that lipid content of *C. reinhardtii* cells is relatively low and stable throughout nutrient replete growth (Davey *et al.*, 2014) was accurately captured by the BMO. Drastic increases in lipid content, particularly neutral lipids, are triggered by continued cultivation in nutrient deplete conditions (Wang *et al.*, 2009), given how the BMO coped with disparate experimental data compared to the OGBM with other macromolecular groups, it should be able to model such nutrient deprived conditions accurately too.

The pigment content is broken down into chlorophyll a, chlorophyll b and xanthophylls for the purposes of this discussion. The chlorophyll a and b proportions of the OGBM were derived (Chang *et al.*, 2011) from a previous study where chlorophyll a and b content was measured in an effort to derive a biomass equation for a smaller GeM that focused on central carbon metabolism (Boyle and Morgan, 2009). The chlorophyll a/b ratio in both iRC1080 and the smaller GeM is 0.60 indicating a larger content of chlorophyll b than chlorophyll a per cell. The opposite is true for our experimental measurements as presented in Figure 3.15, whereby the chlorophyll a/b ratio never dipped below 2. Our experimental results are similar to others published in literature

(Polle *et al.*, 2000; Bonente *et al.*, 2012; Perrine, Negi and Sayre, 2012). The chlorophyll a/b ratio in the BMOs ranges from 1.12 – 2.97. The chlorophyll b content is the same across all BMOs (0.59%, Figure 5.5 B-G and Figure 5.6 B-G), this value may be regarded as an artefact of the model processing workflow. There could be a futile cycle (Santos, Boele and Teusink, 2011) involved in the chlorophyll b synthesis reactions that equivocally constrained the feasible bounds for flux through chlorophyll b synthesis reactions resulting in a narrower solution space leading to the same percentage value in every biomass equation.

The xanthophyll contribution as a percentage of dry cell weight in all BMOs was an order of magnitude larger than expected from experimental results (Appendix IV). This is due to erroneous bounds having been set for the scatter-search algorithm optimisation. Overall, pigments account for less than 6% of the total dry cell weight across all newly generated biomass equations so the impact of such discrepancies on the metabolic network is not expected to overly skew the subsequent analyses. Additionally, the coefficient of variance calculated across all conditions is within the same order of magnitude between the experimental results and the BMOs for every macromolecular group except chlorophyll b. This supports the assumption that the scatter search optimisation is not biased towards any macromolecular group and highlights the error in chlorophyll b content as discussed above.

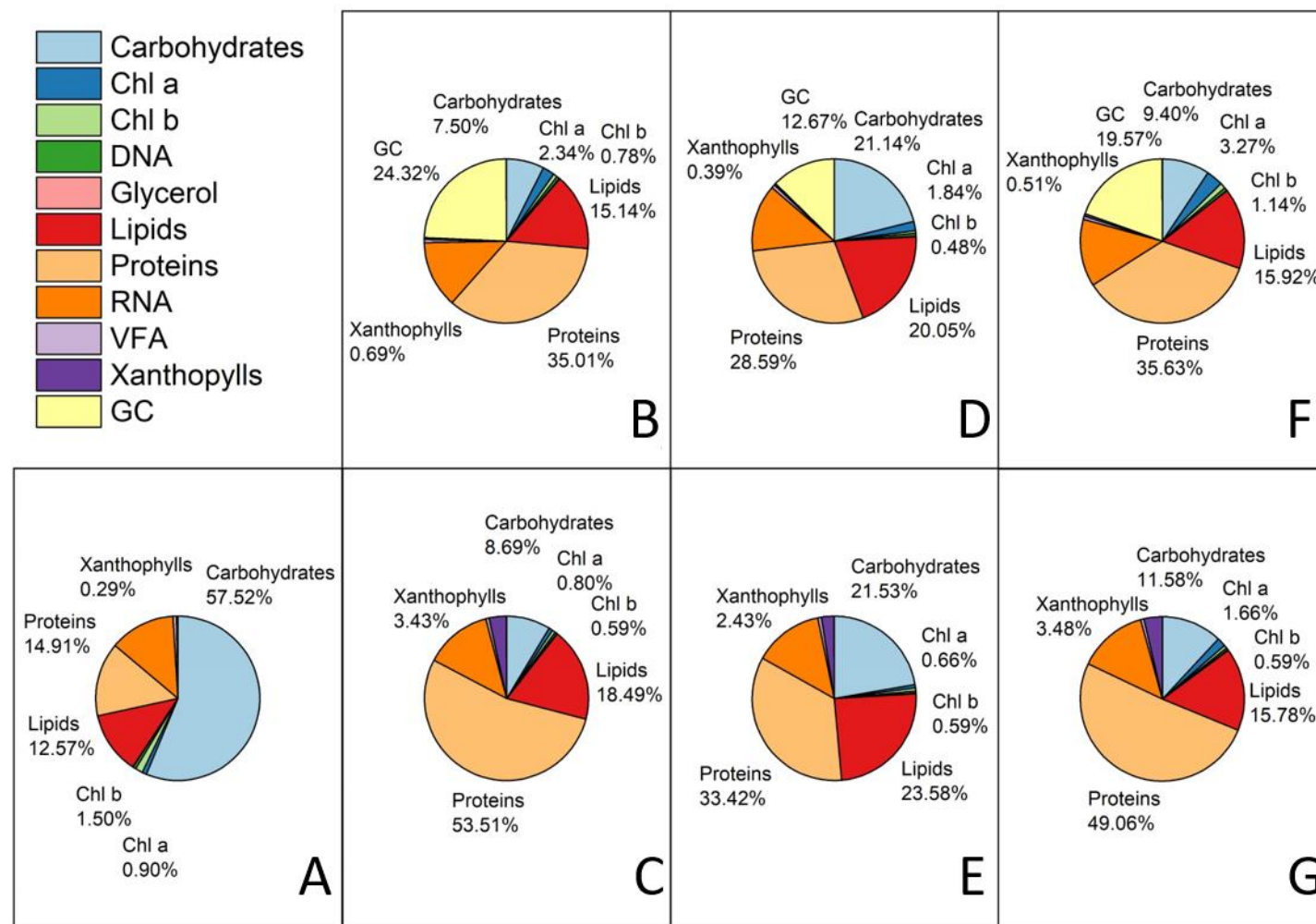


**Figure 5.5**

*C. reinhardtii* biomass composition (g gDCW<sup>-1</sup>) at 16 hours of autotrophic batch culture in M8a under a variety of illumination strategies. (A) Original autotrophic growth iRC1080 biomass equation; (B,D,F) Experimental data for WA, RA and BA respectively; (C,E,G) BMO generated data for WA, RA and BA respectively.

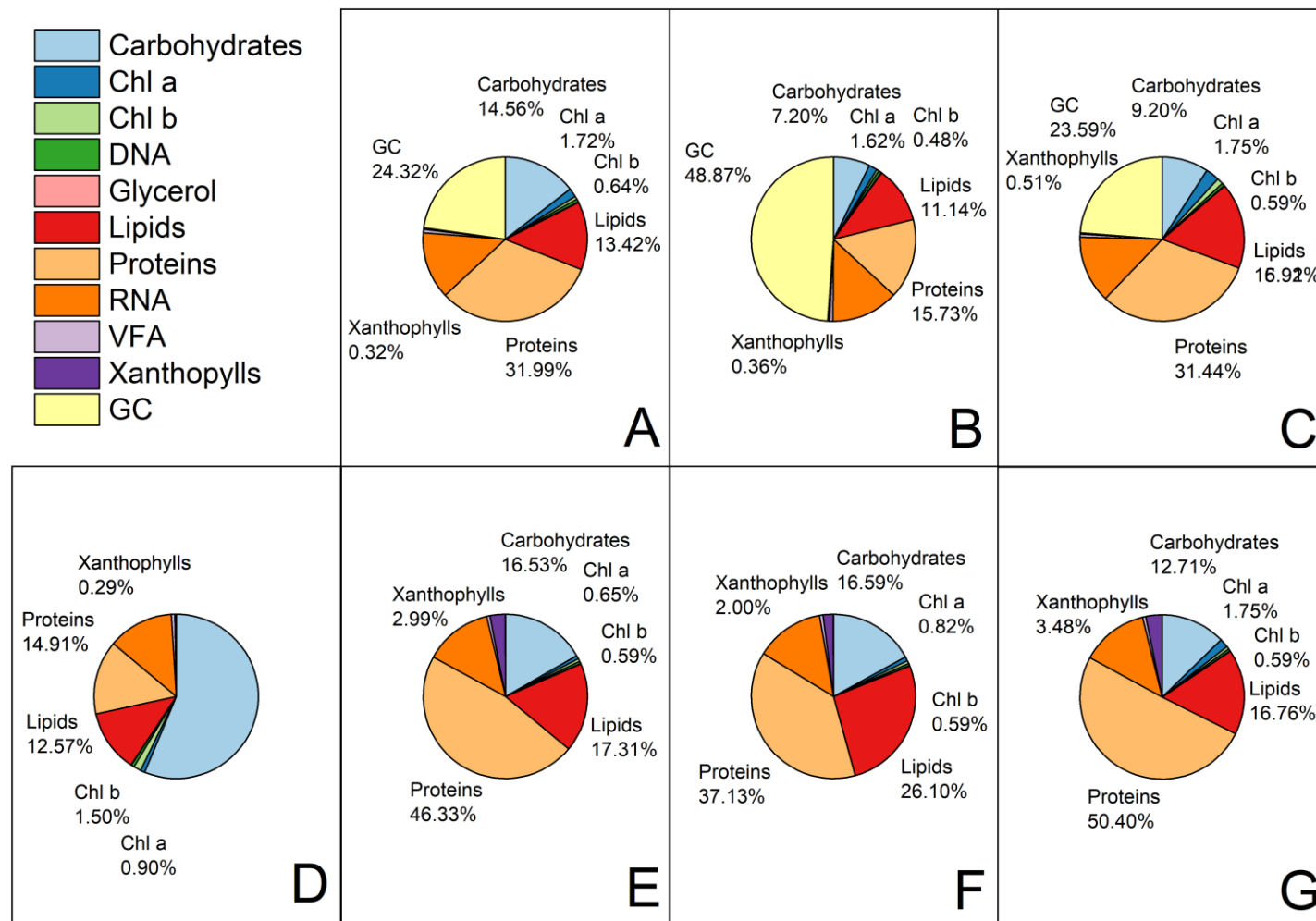


**Figure 5.6**

*C. reinhardtii* biomass composition (g gDCW<sup>-1</sup>) at 16 hours of mixotrophic batch culture in M8a.Ac under a variety of illumination strategies. (A) Original mixotrophic growth iRC1080 biomass equation; (B,D,F) Experimental data for WX, RX and BX respectively; (C,E,G) BMO generated data for WX, RX and BX respectively.

**Table 5.3** *C. reinhardtii* biomass composition (g gDCW<sup>-1</sup>) at 16 hours of batch culture under a variety of trophic and illumination strategies. The original autotrophic and mixotrophic biomass equations are compared to the experimental data and the BMO algorithm generated biomass equations. Only variable macromolecular groups (as defined in Table 5.2) are displayed.

		Carbohydrates		Chlorophyll a		Chlorophyll b		Lipids		Proteins		Xanthophylls		'Ghost carbon'	
Autotrophic iRC1080		57.52		0.90		1.50		12.57		14.91		0.29		-	
WA Exp	WA BMO	7.50	8.69	2.34	0.80	0.78	0.59	15.14	18.49	35.01	53.51	0.69	3.43	24.32	-
RA Exp	RA BMO	21.14	21.53	1.84	0.66	0.48	0.59	20.05	23.58	28.59	33.42	0.39	2.43	12.67	-
BA Exp	BA BMO	9.40	11.58	3.27	1.66	1.14	0.59	15.92	15.78	35.63	49.06	0.51	3.48	19.57	-
Mixotrophic iRC1080		57.52		0.70		1.30		12.57		14.91		0.002		-	
WX Exp	WX BMO	14.56	16.53	1.72	0.65	0.64	0.59	13.42	17.31	31.99	46.33	0.32	2.99	24.32	-
RX Exp	RX BMO	7.20	16.60	1.62	0.82	0.48	0.59	11.14	26.10	15.73	37.13	0.36	2.00	12.67	-
BX Exp	BX BMO	9.20	12.71	2.70	1.75	1.14	0.59	16.91	16.76	31.44	50.40	0.24	3.18	19.57	-

## **Multivariate analysis of flux samples**

### **Separation of the solution space**

After processing the original iRC1080 model and generating condition specific biomass equations, Monte Carlo (MC) sampling of the optimal solution space was performed generating 500,000 solution vectors per condition. Each condition was sampled with the original iRC1080 (OGBM) and the BMO derived biomass equation to determine whether the changes made to biomass composition would impact the resulting flux distributions. The large number of solution vectors obtained is impractical to inspect manually as each of them describes the flux through 1647 unique reactions. Therefore, a multivariate analysis method was chosen to reduce the dimensionality of the problem to a more tractable number in order to be able to identify key differences. Principal component analysis (PCA) was chosen as it is an unbiased way of calculating the contribution of multiple variables to the overall variability of a dataset (Jackson, 1991). PCA can be used to discern whether most of the variability observed is due to model uncertainty or metabolic differences between the conditions compared. Figure 5.7 shows the score plots for each experimental condition. Two distinct clusters can be observed in each score plot where grey points represent samples retrieved using the original iRC1080 biomass reaction, whereas green points represent samples retrieved using the BMO biomass reaction. The BMO updated biomass reaction results in a clearly separated and distinct metabolic configuration in every case. Based on the results of Figures 5.5 and 5.6, this should more closely reflect the experimental conditions being modelled.



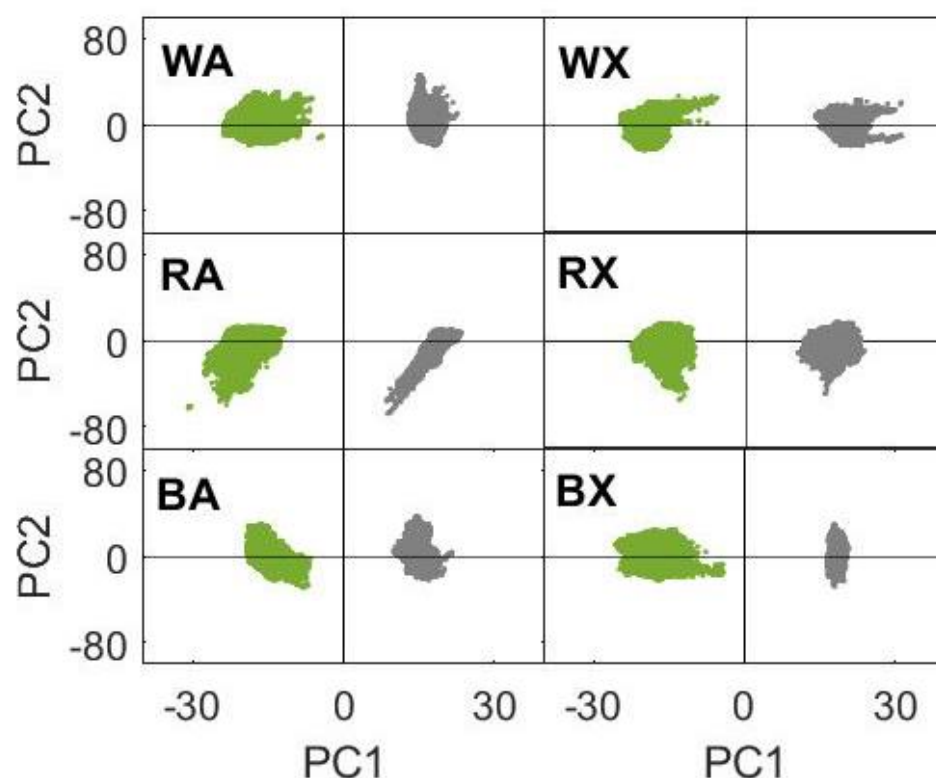


**Figure 5.7** PCA score plots of all experimental conditons. A total of  $1 \times 10^6$  points are plotted on each graph with  $5 \times 10^5$  points per condition. OGBM scores are shown in grey and BMO scores are shown in green. All scores are plotted on principal component 1 (PC1) and principal component 2 (PC2). (-A) Autotrophic growth in M8a; (-X) Mixotrophic growth in M8a.Ac; (W-) White LED light; (R-) Red LED light; (B-) Blue LED light.

Principal components are numbered in order of decreasing variance such that PC1 captures the most variance and this decreases until the total variance is cumulatively described by all components. PC1 captured between 14.63% (BA) and 24.65% (RA) of the total variance (Figure 5.8B illustrates this for the PCA of WA OGBM / WA BMO). 95% of the total variance was captured by the first 290 PCs on average (Figure 5.8A illustrates this for the PCA of WA OGBM / WA BMO). The top 5 PCs were checked for separability but only PC1 showed good separation between scores of each biomass equation. As expected from these observations, the total variance captured by PC1 was an order of magnitude larger than that captured by PC2 in the PCA of WA OGBM / WA BMO.

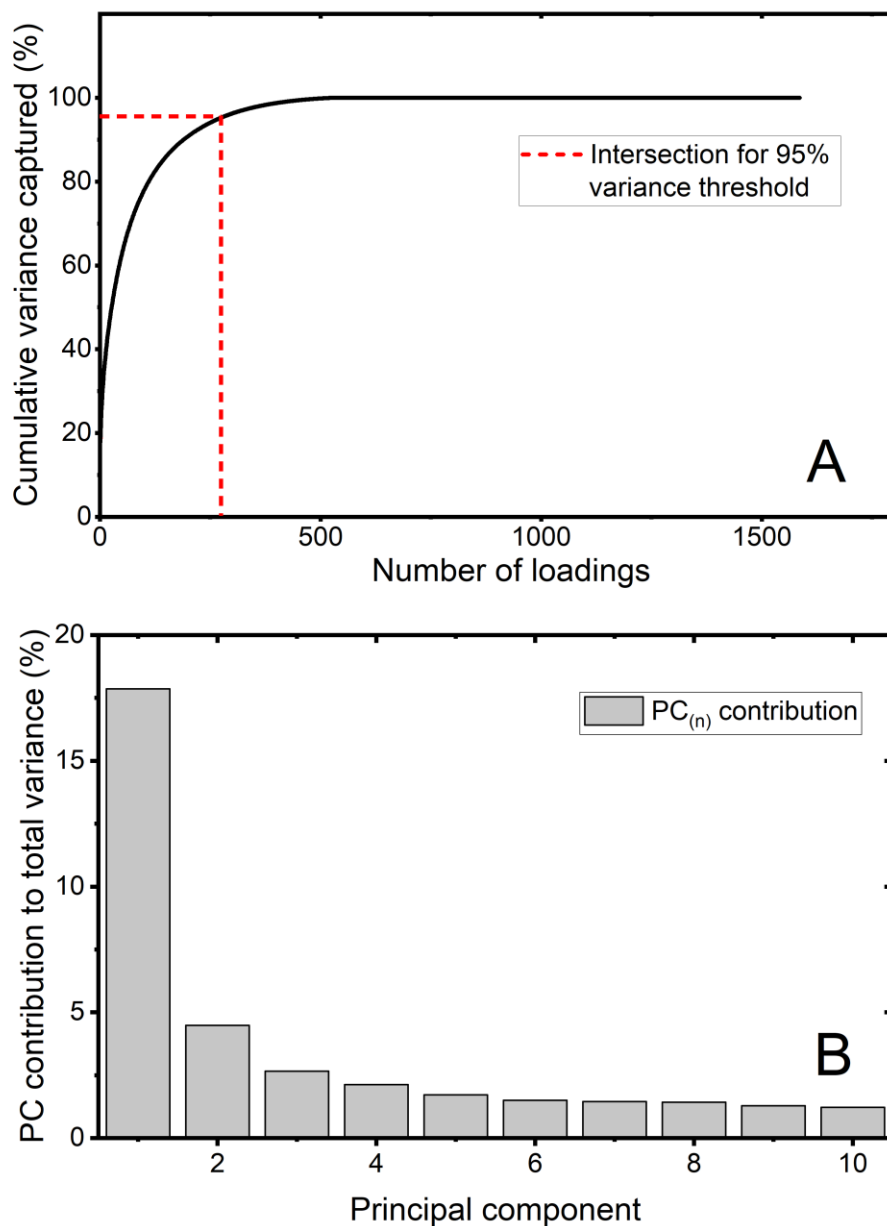


**Figure 5.8** Principal component contribution to total variance. All data plotted were retrieved from the PCA of WA OGBM / WA BMO flux samples. (A) Cumulative variance described by each principal component. (B) The individual contribution of each of the first 10 principal components to the total variance of the flux sample data.

Principal components are vectors generated from linear combinations of the original variables (ie. the model reactions), represented as new axes along which to describe the original variables. The coordinates for each score on these new axes depend on the raw flux values of the score's solution vector and the loadings of each PC used in the plot. Loadings are the coefficients of these new axes (ie. the PCs), their magnitude describes the contribution of the original variable to the new axis. Hence, the larger the numerical value of a loading, the larger the contribution of the represented variable to the separation of the scores on the plot. In Figure 5.7 the scores plotted from samples of the solution space of iRC1080 OGBM and iRC1080 BMO (for all experimental conditions studied; WA, RA, BA, WX, RX, BX) are fully separated along PC1. Therefore, the largest loadings of PC1 correspond to the most important reactions for describing the differences between the metabolic configurations of iRC1080 OGBM and iRC1080 BMO. To define what constitutes a 'large loading', the absolute positive value of all loadings was calculated, and each absolute loading was divided by the largest loading in the PC (Figure 5.9A). This normalisation of the data allowed for the selection of loadings at least 70% as big as the largest loading in each PC. The large loadings in PC1 of the WA OGBM / WA BMO PCA are highlighted inside red boxes in Figure 5.9B.

The analysis of top loadings reduced the number of reactions to investigate from the total 1586 reactions used to build each PCA model to 220 reactions on average across all conditions. Each reaction is part of a subsystem which groups reactions together by metabolic function at the model's authors' discretion. Analysing the top loadings at the subsystem level gives a good overview of the areas of cellular metabolism that are most important in describing the metabolic changes caused by altering the biomass equation of iRC1080. In the top 218 loadings of the PC1 of WA OGBM / WA BMO, there were 37 unique subsystems. Of these 37 subsystems, 20 were directly linked with synthesis of biomass precursor metabolites, accounting for 161 out of the 218 top reactions analysed. This was not entirely unexpected as the only difference between the two models used to generate this PCA was the stoichiometry of the biomass equation. The top loadings of each PCA displayed in Figure 5.6 were analysed. They all contained the same 161 biomass precursor related reactions (Appendix V). This is due to the fact that each PCA was comparing 1,000,000 scores out of which 500,000 used a GeM with

the same biomass equation. Although other condition specific constraints were employed, there was little difference between iRC1080 OGBM scores of different experimental conditions. Therefore, the following section will discuss the results of the WA OGBM / WA BMO PCA and the discussion is representative of the remaining PCAs.

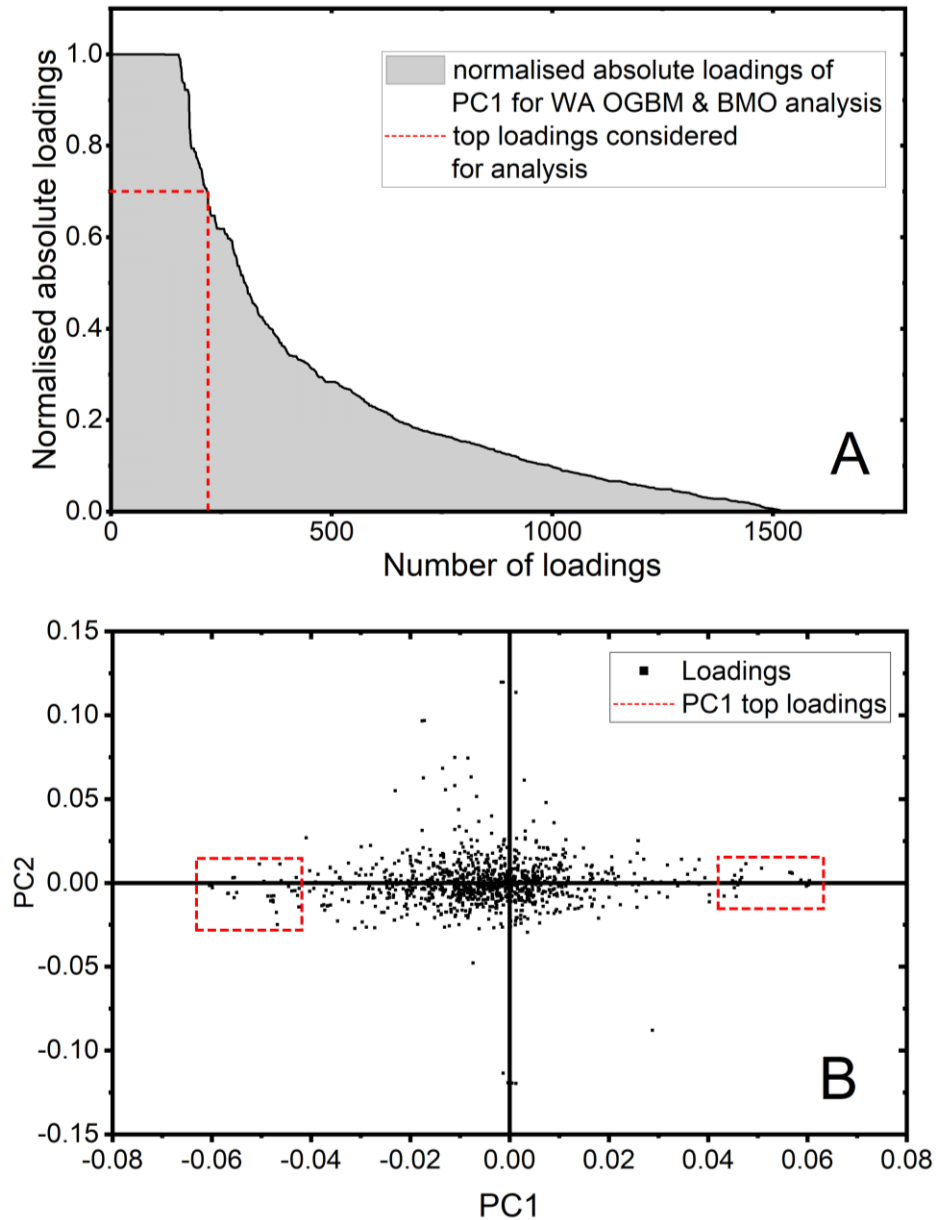


**Figure 5.9** Top loadings analysis. All data plotted were retrieved from the PCA of WA OGBM / WA BMO flux samples. (A) Normalised absolute loadings of principal component 1 (PC1). Loadings with an absolute magnitude at least 70% of the largest loading in PC1 were considered highly influential in the separation of WA OGBM and WA BMO score clusters. (B) Loadings plot where PC1 loadings considered highly influential are termed high loadings and highlighted inside red boxes.

## Analysis of top loadings in PC1 & PC2

The value of a loading within a PC describes the loading's influence on the value of each score plotted along that PC. For example, a large positive loading in PC1 of Figure 5.9B indicates that large positive scores in PC1 (Figure 5.7WA) had a larger than average flux through the reaction described by that loading, and therefore that reaction carried a higher than average flux in WA OGBM simulations compared to WA BMO simulations.

On a loadings scatter plot, each axis corresponds to a PC and the influence of each loading on the scores along those PCs can be easily visualised. Figure 5.10A-D shows the loadings plot for WA OGBM and WA BMO; each panel highlights the loadings for each of the 21 synthesis of biomass precursors (pBM) subsystems. Figure 5.10A highlights the top loadings of carbohydrate constituent synthesis related subsystems like galactose metabolism, fructose and mannose metabolism, and starch metabolism. Most reactions have large positive loadings as expected due to the larger percentage (w/w) carbohydrate in the original biomass equation. The loadings with large negative values highlight the intricacy of top loadings analysis in PCA of GeM models. Reactions in the GeM stoichiometric matrix are made up of rows of stoichiometric coefficients with non-zero values in the rows corresponding to metabolites that participate in the reaction. Irreversible reactions will always have substrates with negative stoichiometric coefficients and products with positive stoichiometric coefficients. However, in reversible reactions, the substrate and product definitions depend on the value of the flux ( $>0$  or  $<0$ ) carried by the reaction. Hence, conclusions cannot be drawn solely from loadings values and must be cross-checked against the stoichiometric matrix  $\mathbf{S}$  to fully contextualise what a larger or smaller than average flux through a reaction means. This was the case across several of the subsystems highlighted in Figure 5.10, and particular examples are further explained next.

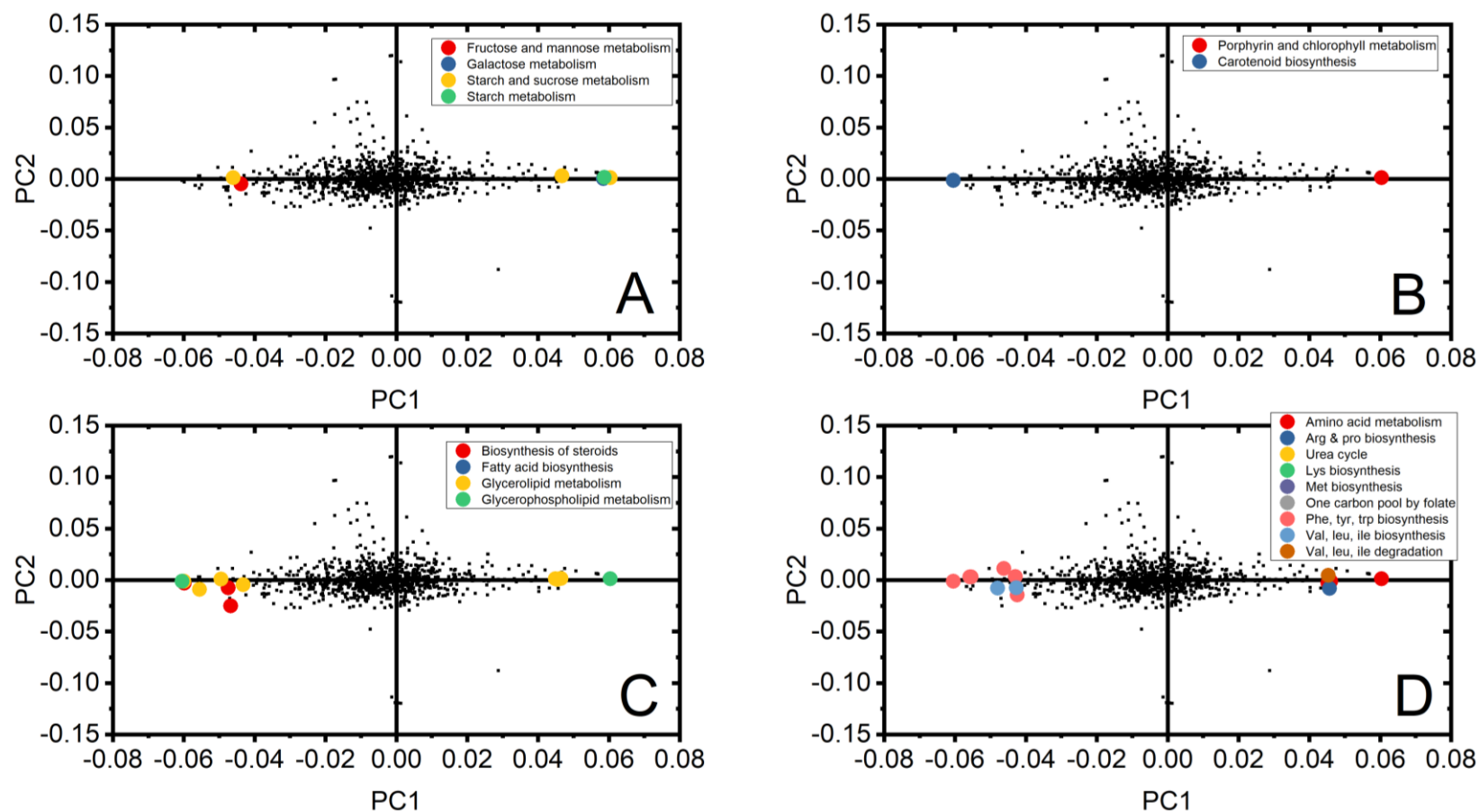
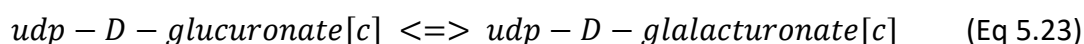


**Figure 5.10** Top loadings analysis. All data plotted were retrieved from the PCA of WA OGBM / WA BMO flux samples. (A-D) Loadings plots where highlighted loadings belong to biomass precursor (pBM) synthesis related subsystems; (A) Carbohydrate pBM synthesis related.

[Figure 5.10 legend continued] subsystems; (B) Pigments pBM synthesis related subsystems; (C) Lipids pBM synthesis related subsystems; (D) Protein pBM synthesis related subsystems

The large negative loading highlighted in the starch and sucrose metabolism subsystem (Figure 5.10A) could be erroneously interpreted as a carbohydrate synthesis related reaction behaving in the opposite manner to the rest and carrying a larger than average flux towards carbohydrate synthesis in the GeM with the newly generated biomass equation. However, it relates to UDP-glucuronate 4-epimerase (UGE) (Equation 5.23), a reversible reaction with a negative median flux value of  $-0.00833 \text{ mmol gDCW}^{-1} \text{ h}^{-1}$  (CC) and  $-0.000209 \text{ mmol gDCW}^{-1} \text{ h}^{-1}$  (BM) calculated from each set of 500,000 solution vectors sampled from each GeM plus biomass equation combination. By examining the flux carried by the reaction and its stoichiometric coefficients in S, it becomes evident that the product of the reaction in the simulations performed is UDP-glucuronate. After a decarboxylation step, UDP-glucuronate is converted into UDP-D-xylose which in turn can be converted into UDP-L-arabinose. UDP-L-arabinose can then be broken down into UDP and L-arabinose thus completing the conversion of UDP-D-glucuronate into a biomass equation precursor metabolite.



Where [c] stands for cytosol localised metabolite. Reaction listed as defined in iRC1080.

The other large negative loading found in the carbohydrate synthesis related subsystems codes for D-mannose aldose-ketose-isomerase (MAKI) (Equation 5.24). A reversible reaction, in this case the left-hand side metabolite is a biomass precursor directly. What makes this reaction more interesting than UDP-glucuronate 4-epimerase is the median flux determined for each GeM plus biomass equation combination. The GeM with the original biomass equation carried a negative median flux of  $-0.00107 \text{ mmol gDCW}^{-1} \text{ h}^{-1}$  and the newly generated biomass equation resulted in a positive median flux of  $0.00359 \text{ mmol gDCW}^{-1} \text{ h}^{-1}$ . This means that the direction of flux through MAKI was reversed in at least 50% of solution vectors generated for WA BMO. Reversing the direction of MAKI results in less mannose being available for the biomass equation

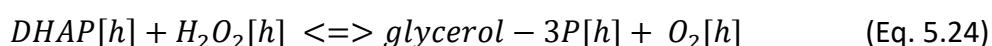


reaction aligning the flux reversal with the lower quantity of carbohydrates in the newly generated biomass equation. It also results in more  $\beta$ -D-fructose being generated which can be transformed directly into D-glucose for glycolysis/gluconeogenesis by  $\alpha$ -D-glucose aldose-ketose-isomerase (AGAKI); or it can enter glycolysis/gluconeogenesis in its phosphorylated form,  $\beta$ -D-fructose 6-phosphate.



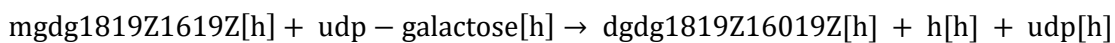
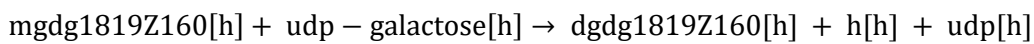
Where [h] stands for chloroplast localised metabolite. Reaction listed as defined in iRC1080.

While the carbohydrate content in the BMO algorithm generated biomass reactions was smaller than in the original iRC1080 biomass reaction, the opposite is true for the lipids proportion of the dry cell weight (Figure 5.5 and 5.6). As expected from this, most reactions in the top loadings of WA BMO / WA OGBM PCA belonging to lipid precursor synthesis subsystems have large negative loadings values showing the flux through lipids synthesis reactions was larger than average in WA BMO (Figure 5.10C). However, there were five exceptions where the loadings had large positive values indicating these lipid related reactions had larger than average fluxes in WA OGBM instead (Equations 5.24 – 5.28). One of them was glycerol-3-phosphate oxidase, a reaction grouped in the glycerophospholipid metabolism subsystem. It is a reversible reaction with a positive median flux in both WA OGBM and WA BMO indicating production of glycerol 3-phosphate from dihydroxyacetone. The larger gluconeogenic fluxes in WA OGBM result in a larger pool of available dihydroxyacetone, enabling a higher flux through glycerol-3-phosphate oxidase explaining its large positive loading value.



Where DHAP is dihydroxyacetone; [h] stands for chloroplast localised metabolite. Reaction listed as defined in iRC1080.

Two digalactosyldiacylglycerol galacto-hydrolase and -synthase reaction pairs (18:1(9Z)/16:0), (18:1(9Z)/16:0(9Z)) all had large positive loading values, but the species of monogalactosyldiacylglycerol lipid (mgdg) involved in these reactions (as a product of hydrolases; as a substrate for synthases) is not a biomass precursor metabolite. However, this mgdg is a substrate in an omega-6 desaturase reaction that produces mgdg-(1829Z12Z160) which is present in the biomass equation. The omega-6 desaturase reaction does have a negative loading value, as expected. In summary, reactions directly linked to biomass equation precursor metabolites follow the expected trend of loadings value and change in percentage contribution of the macromolecule they link to, whilst reactions in the same subsystems but not involved directly with biomass equation metabolites, may not, as other metabolites present may be linked to other metabolic sub-networks and be influenced by multiple macromolecular groups.

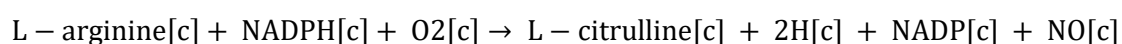


(Eqs 5.25 – 5.28)

Where mgdg stands for monogalactosyldiacylglycerol, dgdg stands for digalactosyldiacylglycerol and [h] stands for chloroplast localised metabolite. Reaction listed as defined in iRC1080.

Percentage (w/w) proteins were higher in the newly generated biomass equation in all cases. Correspondingly, all but one of the top loadings belonging to protein synthesis related subsystems had large negative values (Figure 5.10D). The errant loading corresponds to nitric oxide synthase (Eq 5.29). This reaction degrades L-arginine, a biomass precursor into L-citrulline and nitric oxide. L-citrulline is not a biomass precursor. A large positive flux through this reaction would reduce the amount of L-arginine available for biomass generation and therefore it makes sense for the corresponding loading value to be positive; as the increase in percentage (w/w) protein

in the newly generated biomass equation results in a decrease in flux carried by amino acid degradation reactions like nitric oxide synthase.



(Eq 5.29)

Where [c] stands for cytosol localised metabolite. Reaction listed as defined in iRC1080.

All pigment synthesis related top loadings followed the pattern expected from the decrease in percentage (w/w) chlorophyll a and b and the increase in percentage (w/w) xanthophylls between the original biomass equation and the newly generated biomass equation (Figure 5.10B).

The remaining 16 subsystems accounted for 54 reactions; their loadings values are shown in Figure 5.11. It is of interest to note that at least 25% of the top loadings don't belong to biomass precursor synthesis subsystems. This shows that changing the biomass equation stoichiometry has far reaching effects beyond biomass precursor synthesis subsystems. It is a promising sign for discovering metabolic differences between experimental conditions using the same GeM framework model and condition specific biomass composition data as well as nutrient consumption data.

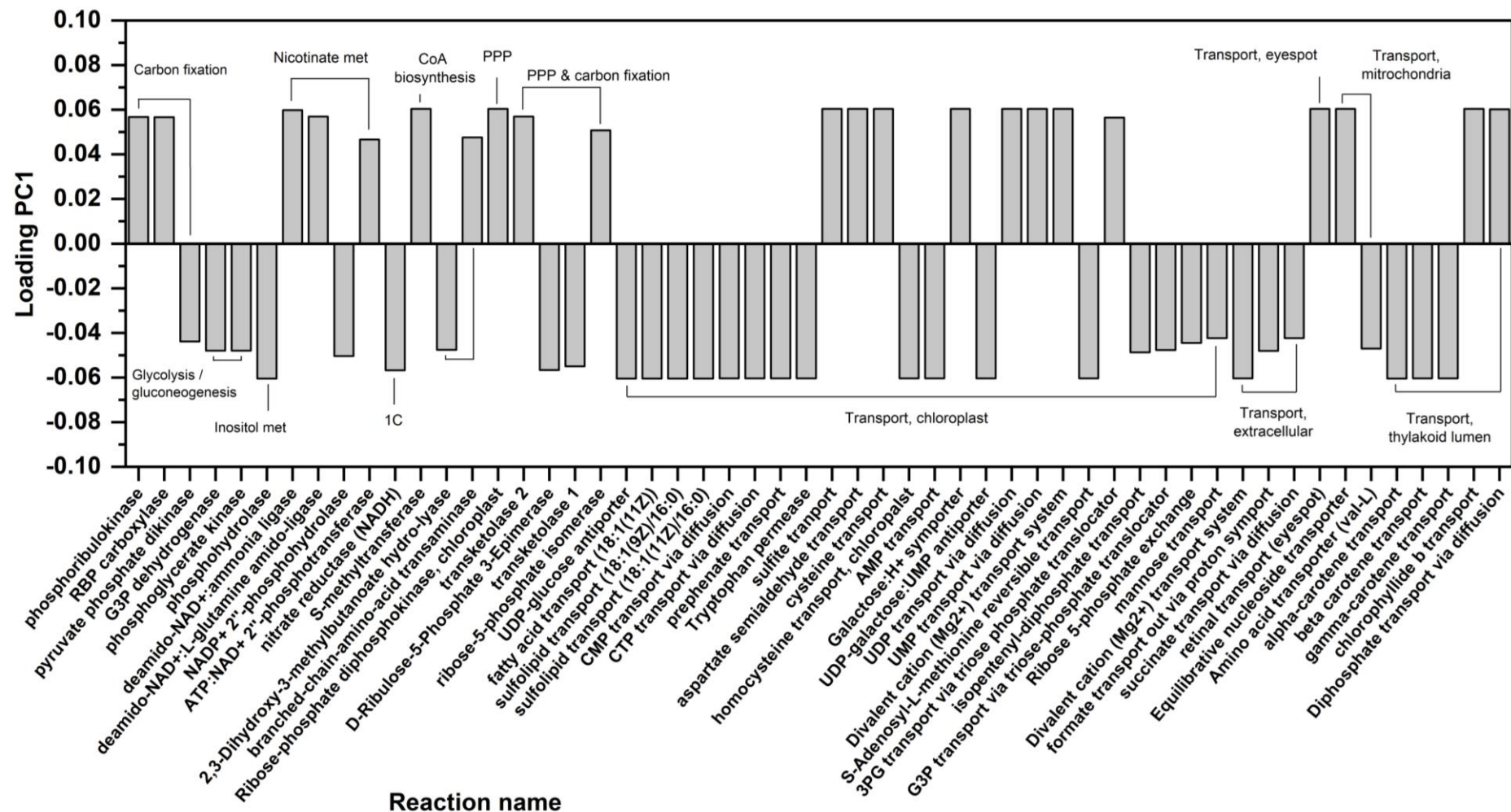


**Figure 5.11** Top loadings bar chart. All data plotted were retrieved from the PCA of WA OGBM / WA BMO flux samples. All 54 top loadings of the 16 non biomass precursor (nBM) synthesis related subsystems found in PC1. PPP, pentose phosphate pathway; 1C, 1-carbon by folate metabolism.

## 5.5. Multivariate analysis of experimental conditions after BMO processing

In the previous section, PCA was used to evaluate the flux distributions of two metabolic networks that only differed in their biomass equation stoichiometry. Clear separation of PCA scores belonging to each network was achieved. In this section, the iRC1080 model is constrained with the newly generated, condition specific biomass equations and experimentally determined nutrient uptake rates. These final iterations of a curated GeM, with experimental condition specific adaptations of the GeM biomass equation are a closer representation of the experiments performed in Chapter 3 and 4 than the published iRC1080 as is. The distinct metabolic configurations sampled capture the macroscopic differences in biomass equation stoichiometry between the experiments. The following analysis explores what other metabolic differences arise between the observed phenotypes by exploring the latent variables (loadings) highlighted in PCA.

### Multivariate analysis of flux samples

#### Separation of the solution space

The autotrophic condition experimentally determined bounds used to constrain iRC1080 were ammonium uptake rate and biomass growth rate between 0 and 48h of batch culture. Figure 5.12 shows the score plot for the three mixotrophic conditions, WA BMO, RA BMO and BA BMO. Three distinct clusters can be observed where grey points represent samples retrieved from WA BMO, red points represent samples retrieved from RA BMO and blue points represent samples retrieved from BA BMO. PC1 clearly separated all conditions whilst PC2 separated WA BMO from BA BMO and RA BMO. This suggests some underlying differences between WA BMO and the other two conditions being captured by PC2.

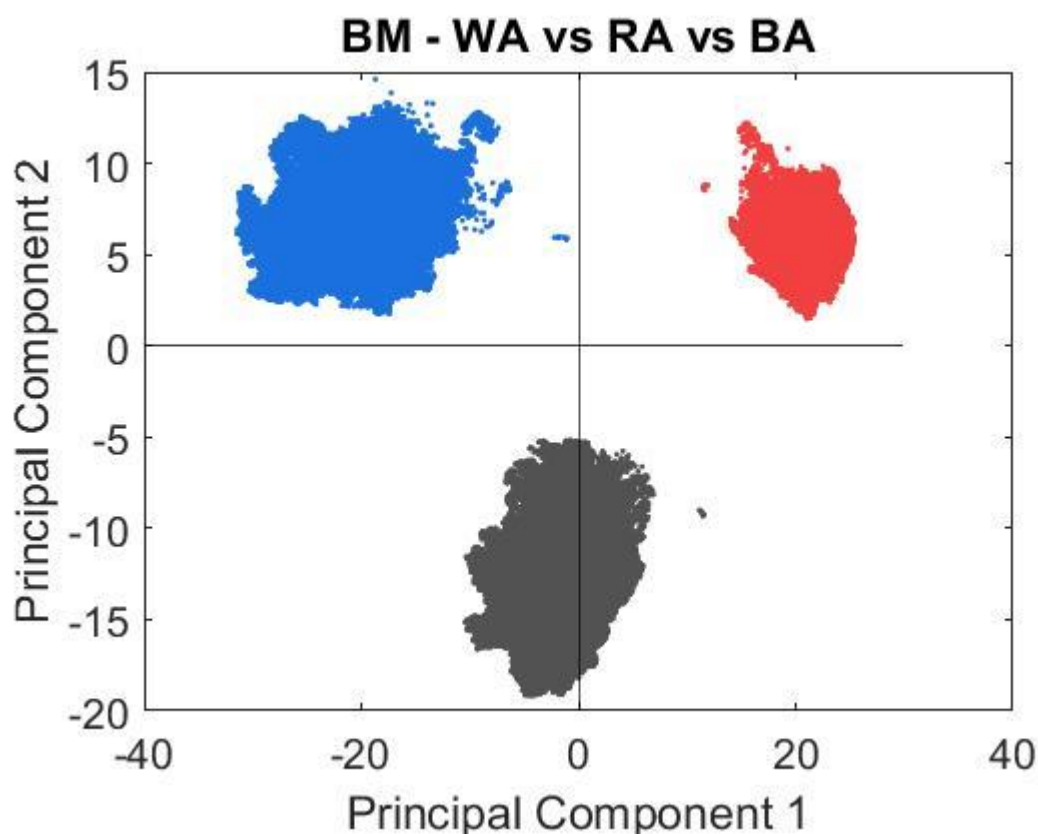


**Figure 5.12** PCA score plots of autotrophic growth simulations under a variety of illumination conditions using BMO algorithm generated biomass equations. A total of  $1.5 \times 10^6$  points are plotted with  $5 \times 10^5$  points per condition. WA BMO scores are shown in grey; RA BMO scores are shown in red; BA BMO scores are shown in blue. All scores are plotted on principal component 1 (PC1) and principal component 2 (PC2). (-A) Autotrophic growth in M8a; (W-) White LED light; (R-) Red LED light; (B-) Blue LED light.

The mixotrophic condition experimentally determined bounds used to constrain iRC1080 were ammonium uptake rate, acetate uptake rate and biomass growth rate between 0 and 48h of batch culture. Figure 5.13 shows the score plot for the three mixotrophic conditions, WX BMO, RX BMO and BX BMO. Three distinct clusters can be observed where grey points represent samples retrieved from WX BMO, orange points represent samples retrieved from RX BMO and blue points represent samples retrieved from BX BMO. PC1 separated BX BMO scores from the other two conditions whilst PC2 separated WX BMO and RX BMO. This suggests some underlying similarity between RX BMO and BX BMO not shared by WX BMO being captured by PC2.

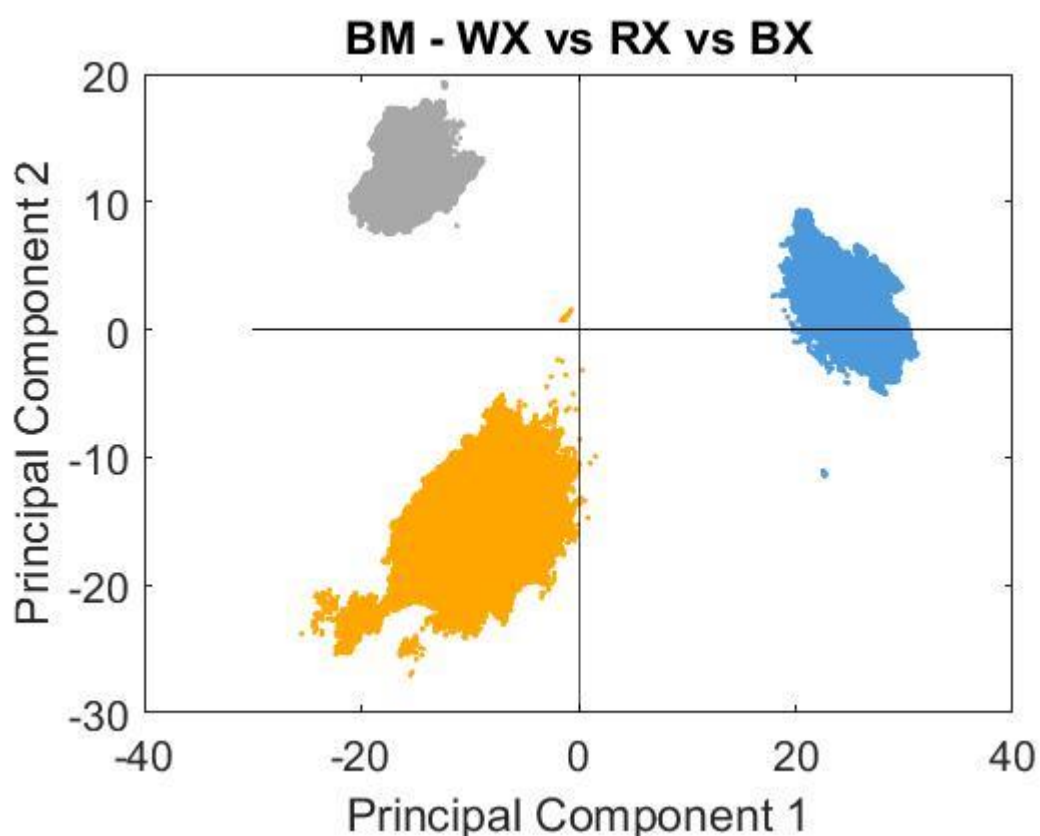


**Figure 5.13** PCA score plots of mixotrophic growth simulations under a variety of illumination conditions using BMO algorithm generated biomass equations. A total of  $1.5 \times 10^6$  points are plotted with  $5 \times 10^5$  points per condition. WX BMO scores are shown in light grey; RX BMO scores are shown in orange; BX BMO scores are shown in light blue. All scores are plotted on principal component 1 (PC1) and principal component 2 (PC2). (-X) mixotrophic growth in M8a.Ac; (W-) White LED light; (R-) Red LED light; (B-) Blue LED light.

#### **Analysis of pBM top loadings in PC1 & PC2**

The loadings of the PCA score plots shown in Figure 5.12 and Figure 5.13 were investigated separately and comparisons between them were drawn when pertinent. Loadings with an absolute value  $\geq 70\%$  of the highest loading in PC1 and PC2 were considered high loadings as in the previous section. High loadings were evaluated as important contributors to the separation of scores along each PC. The total number of high loadings and their association to biomass precursor (pBM) subsystems is summarised in Table 5.4.

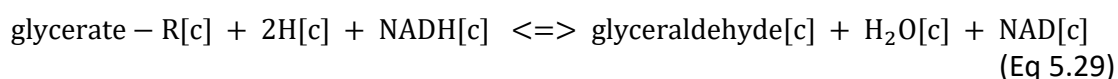
**Table 5.4** Top loadings and subsystems distribution in the first two principal components (PC1 and PC2) of the PCA performed on autotrophic and mixotrophic growth under white, red and blue LED illumination.

Autotrophic PCA				
	Subsystems		High loadings	
	pBM	Other	pBM	Other
PC1	15 (54%)	13 (46%)	151 (77%)	44 (23%)
PC2	12 (60%)	8 (40%)	45 (69%)	20 (31%)
Mixotrophic PCA				
	Subsystems		High loadings	
	pBM	Other	pBM	Other
PC1	28 (54%)	24 (46%)	195 (65%)	103 (35%)
PC2	12 (57%)	9 (43%)	32 (59%)	22 (41%)

The proportion of top loadings belonging to pBM subsystems is dominant along both PC1 and PC2 in the autotrophic PCA (77% and 69%) and mixotrophic PCA (65% and 59%). This indicates that even when comparing across three different experimental conditions with differing constraints across illumination, growth rate and nutrient uptake rates, the majority of the separation of scores along each PC is due to differences in pBM fluxes. This reflects the weight of the biomass reaction when it is selected as the sole biomass optimisation objective.

Most pBM top loadings in PC1 and PC2 of the PCA performed with autotrophic conditions did not show major differences in median flux values beyond the changes in scale expected from the differences in biomass equation composition of each condition. An exception was the redox reaction catalysed by glyceraldehyde oxidoreductase (GLYALDOR, Equation 5.29) found in the 'glycerolipid metabolism' subsystem.





Where [c] stands for cytosol localised metabolite. Reaction listed as defined in iRC1080.

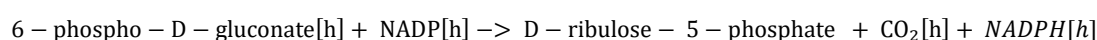
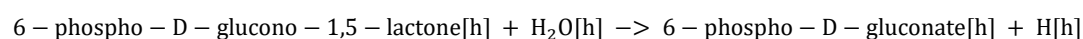
This reversible reaction had a positive median flux in WA BMO and RA BMO samples ( $1.23 \times 10^{-3} \text{ mmol gDCW}^{-1} \text{ h}^{-1}$  and  $4.10 \times 10^{-3} \text{ mmol gDCW}^{-1} \text{ h}^{-1}$ ) and a negative median flux in BA samples ( $-6.27 \times 10^{-6} \text{ mmol gDCW}^{-1} \text{ h}^{-1}$ ). The reversal in directionality suggests glyceraldehyde is used as a substrate to produce reducing power and glycerate carbon backbones under blue light. Glycerate can be phosphorylated to glycerate-2-phosphate in glycolysis or glycerate-3-phosphate in serine synthesis (Bartsch, Hagemann and Bauwe, 2008). Conversely, under white and red light, glycerate serves as precursor for glyceraldehyde biosynthesis. Glyceraldehyde can be converted into glycerol and then glycerol-3-phosphate, a substrate for glycerolipid synthesis (Riekhof and Benning, 2009). The lipid content (w/w) at 48 hours as seen in Figure 3.12 A (WA 20%, RA 27% and BA 17%) matches the preference for a lipid related precursor (glyceraldehyde) in WA BMO and RA BMO samples compared to BA BMO samples. Such insight could inform further experimentation with GLYALDOR mutants under white and red light to determine whether the overexpression of glyceraldehyde oxidoreductase could improve lipid accumulation in nutrient replete conditions.

No pBM top loadings in PC1 and PC2 of the PCA performed with mixotrophic conditions showed any major differences in median flux values beyond the changes in scale expected from the differences in biomass equation composition of each condition. This could be expected from the similarity in biomass composition between WX BMO, RX BMO and BX BMO. Whilst not being equal, there are no drastic differences between the biomass reactions that would prompt a significant change in flux direction across pBM subsystems and reactions.

### **Analysis of nBM top loadings in PC1 & PC2**

All but two of the non-biomass (nBM) high loadings of PC1 in the autotrophic PCA corresponded to transport reactions. Transport reactions are reactions that enable

metabolite transport between compartments without any biochemical transformation occurring. GeM model compartments are formal structures used to distinguish between metabolites located in different intracellular organelles of the modelled cell. Thus, a transport reaction for water is present in the model to allow the movement of water molecules between the cytosol and the chloroplast. Of higher metabolic relevance were the two non-transport reactions found in the non-pBM high loadings of PC1. These were 6-phosphogluconolactonase (PGDh, Equation 5.X) and 6-phosphogluconate dehydrogenase (PGDHh, Equation 5.X).



(Eq 5.30 – 5.31)

Where [h] stands for chloroplast localised metabolite. Reactions listed as defined in iRC1080.

These two reactions form part of the oxidative phase of the pentose phosphate pathway (PPP) which is a secondary source of reducing power in photosynthesising cells grown in autotrophic and mixotrophic conditions (Klein, 1986). The ribulose-5-phosphate (ru5p) produced by PGDHh can feed ribose sugar metabolism for DNA and RNA synthesis as well as amino acid synthesis (Kruger and von Schaewen, 2003). Some portion of the ru5p generated in the PPP is also directed into ribulose-1,5-bisphosphate regeneration in the Calvin Benson cycle. Both reactions had equally high absolute normalised loadings values in the PC1 of the PCA performed on autotrophic conditions (Figure 5.12 A) and the PC2 of the PCA performed on mixotrophic conditions (Figure 5.13 B) of 74.50% of the largest loading.

The large negative value of the loadings in the PC1 of the PCA performed on autotrophic conditions indicates the flux through the reactions was larger than average in BA BMO samples (Figure 5.12). The large negative values of the loadings in the PC2 of the PCA performed on mixotrophic conditions indicate the flux through the reactions was larger than average in RX BMO samples (Figure 5.13). As they comprise a linear pathway, the median flux through both reactions was the same, however it differed per experimental condition as detailed below.

A metabolic flux analysis (MFA) study in *Chlorella pyrenoidosa* found PPP reactions carried a larger flux in cells grown in mixotrophic conditions compared to cells grown in autotrophic conditions (Yang, Hua and Shimizu, 2000). The median flux through PGLh and PGDh mirrored the literature under red light; it was an order of magnitude higher in RX BMO ( $0.053 \text{ mmol gDCW}^{-1} \text{ h}^{-1}$ ) than RA BMO ( $0.0057 \text{ mmol gDCW}^{-1} \text{ h}^{-1}$ ). Flux through the two reactions remained comparable between WA BMO ( $0.016 \text{ mmol gDCW}^{-1} \text{ h}^{-1}$ ) and WX BMO ( $0.014 \text{ mmol gDCW}^{-1} \text{ h}^{-1}$ ). The difference in modelled growth rate under red light between autotrophic (RA BMO -  $0.055 \text{ h}^{-1}$ ) and mixotrophic (RX BMO -  $0.057 \text{ h}^{-1}$ ) simulations was smaller than for white light simulations (WA BMO -  $0.073 \text{ h}^{-1}$ ; WX BMO -  $0.069 \text{ h}^{-1}$ ). Thus, the difference in PPP flux between RA BMO and RX BMO seems to be a result of the distinct metabolic re-configuration generated with each experimental condition. A study on NADPH-producing PPP enzymes in the diatom *Fistulifera solaris* showed that overexpression of such enzymes results in increased lipid accumulation under phototrophic conditions. Equally, RX BMO has 2.52% (w/w) higher lipid content than RA BMO whilst WX BMO has 1.18% (w/w) lower lipid content than WA BMO.

On the other hand, the median flux through PGLh and PGDh in BA BMO ( $0.023 \text{ mmol gDCW}^{-1} \text{ h}^{-1}$ ) was an order of magnitude higher than in BX BMO ( $0.0044 \text{ mmol gDCW}^{-1} \text{ h}^{-1}$ ). The simulated growth rate in BA BMO ( $0.041 \text{ h}^{-1}$ ) was lower than in BX BMO ( $0.053 \text{ h}^{-1}$ ). According to MFA data from literature, the flux through the PPP should be higher in mixotrophic cultures, and a larger growth rate is accompanied by an increased demand for reducing power, DNA, RNA and protein precursors. The reversal of the growth rate to PPP flux correlation in BA BMO and BX BMO demonstrates the unique metabolic configurations captured by the curated GeM and warrants further experimental studies to validate these simulations. Increased flux through PPP would generate a pool of NADPH that could be redirected towards other reduction power requiring pathways like carbon fixation or lipid biosynthesis.

## 5.6. Conclusions

The need for a biomass equation optimisation algorithm is formed of three tenets. Firstly, the metabolic plasticity displayed by microalgae that results in varying biomass

distribution profiles across experimental conditions, and throughout the course of an experiment, makes custom biomass equations essential for maximising GeM simulation fidelity. Secondly, the variance accumulated from the use of different experimental techniques to measure each component of the biomass. Thirdly, the centrality of the biomass equation as a single optimisation objective in FBA simulations, makes it arguably the most important reaction in a GeM model due to its influence in the overall metabolic distribution.

The BMO algorithm developed in this chapter successfully updates the biomass equation of a GeM within the limits set by experimental measurements whilst minimising the difference between simulated and experimental growth rate. The tailored BMOs resulted in distinct metabolic configurations for each experimental condition. The multivariate analysis performed with PCA confirmed each experimental condition with a newly generated BMO gave rise to distinct phenotypes (Figure 5.7, Figure 5.12 and Figure 5.13). In Section 5.4.1, by comparing the original biomass equation to each BMO generated it was demonstrated that the newly generated BMOs affect fluxes related to biomass precursor synthesis. However, the changes observed were proportionally equal across different subsystems of the same macromolecular component due to the available experimental data. To obtain more granularity and insights into metabolic changes of each biomass precursor synthesis subsystem, higher resolution data like that obtained from lipidomics studies (Levering *et al.*, 2016) or amino acid distribution analysis would be required (Kliphuis *et al.*, 2012).

The motivation for engineering highly specific stoichiometric constraints in GeMs is to minimise the number of possible solutions in a simulation. A reduction in solution space is necessary due to the heavily underdetermined nature of this type of models (Schellenberger and Palsson, 2009). To the best of my knowledge this is the first time such separation of solution space between different experimental conditions has been achieved in a microalgal GeM. Previously published work only performed flux balance analysis and flux variability analysis (Kliphuis *et al.*, 2012; Chapman *et al.*, 2015; Levering *et al.*, 2016) which provide a single non-unique solution and extreme (minimum and maximum) values respectively. Central carbon metabolism did not majorly feature in the top loadings of the autotrophic or mixotrophic PCAs. This suggests a high robustness of

central carbon metabolism to the wavelength and trophic strategy choices explored in this thesis. A similar study in *Arabidopsis thaliana* found central carbon metabolism has very little sensitivity between GeMs of the same organism and different biomass equations (Yuan *et al.*, 2016). Nevertheless, the Monte Carlo sampling performed in this chapter produced flux distributions between the maximum and minimum values of the solution space for each reaction in the model. These flux distributions served as the input data for PCA which in turn highlighted otherwise not readily identifiable reactions like GLYALDOR and PGDHh as relevant for distinguishing between the metabolic configurations of each experimental condition. Such insights into the differences in metabolic configuration caused by the choice of wavelength and trophic strategy in a *C. reinhardtii* batch culture serve to inform novel hypotheses and future experimentation efforts.



### *Conclusions & Future directions*

A systematic characterisation of the effects of narrow band monochromatic illumination on microalgae under different trophic strategies was presented in this thesis. A combined experimental and modelling approach was utilised to develop understanding at the physiological, metabolic and gene expression level. Literature observations like the influence of narrow-peak red and blue light emitting diode (LED) illumination on *C. reinhardtii* cell size and cell cycle were confirmed in Chapter 3. Legacy macromolecule quantification assays were scaled-down to reduce biovolume required to generate macromolecular composition data (Chapter 3). These assays enabled novel discoveries like the preferential allocation of carbon towards carbohydrates (RA) or lipids (BA) in the late stationary phase of batch cultures (Chapter 3).

Ribonucleic acid (RNA) extraction from *C. reinhardtii* cells was optimised to improve the yield and purity of the extracted nucleic acids (Chapter 4). This enabled a reference gene evaluation study to determine the suitability of legacy and novel reference genes for real time quantitative polymerase chain reaction (RT-qPCR) studies. Ultimately, the *psaD* (Photosystem I reaction centre subunit II) gene and *ACX1* (Acetyl-CoA carboxylase subunit  $\alpha$ ) gene were chosen as optimal reference genes for RT-qPCR studies of *C. reinhardtii* under different illumination and trophic strategies. The selected reference genes were employed to evaluate differences at the transcriptional level between different illumination and trophic strategies in several areas of central carbon metabolism like photosynthesis (Ribulose biphosphate carboxylase small subunit; *RBCS* gene) or the tricarboxylic acid cycle (fumarate hydratase; *FUM1*) among others (Chapter 4).

After the systematic experimental characterisation, a modelling effort was employed to further discern the metabolic differences between the experimental conditions studied (Chapter 5). The latest genome scale metabolic network model

(GeM) was updated and curated to perform metabolic simulations. A biomass optimisation algorithm (BMO) was developed to adapt the stoichiometry of the biomass equation in the GeM to accurately reflect changes in biochemical composition observed in Chapter 3 (Chapter 5). The resulting metabolic simulations allowed for the clear separation of metabolic configurations resulting under each experimental condition using multivariate analysis.

Every chapter mentioned contains a results and discussion section as well as a conclusions section. This chapter aims to provide the reader with future research directions to further our understanding of the effects of illumination and trophic strategy on microalgae and utilise narrow peak LEDs effectively in microalgal culturing.

## **6.1. Advanced characterisation of the effects of illumination and trophic strategy on microalgae cultivation**

The experimental characterisation carried out in Chapter 3 and Chapter 4 was aimed at providing a baseline of knowledge on the effects of illumination and trophic strategy selection on batch cultures of *C. reinhardtii* and hopefully a representation of such effects on green algae metabolism in general given this species' status as a model algae. To further confirm the relevance of the biomass composition differences observed it would be highly advisable to perform a series of continuous culture experiments in turbidostat mode, hence controlling for the specific photon energy delivered per cell. The biomass composition experiments performed in Chapter 3 were non-targeted assays measuring various molecular groups many conformed by a plethora of intracellular species. A more targeted approach in pre-selected experimental conditions would provide an additional layer of context. For example, a novel illumination strategy that could be designed based on the results presented in Chapter 3 to maximise lipid yield. This strategy would involve initial culture illumination with red LEDs to maximise cellular proliferation rate followed by a switch to blue LEDs once the target cell density has been achieved to maximise lipid content in g gDCW<sup>-1</sup>. Exploring the distribution of lipid species using thin-layer chromatography (TLC) and liquid chromatography mass spectrometry methods (LC-MS) for a comprehensive lipidomic



study would ensure the illumination switch mid-culture did not have a negative impact on the desirability of the lipid species biosynthesised.

There are a plethora of RNA sequencing (RNA-seq) studies on various metabolic shifts in *C. reinhardtii* (Gonzalez-Ballester *et al.*, 2010; Kropat *et al.*, 2012; Blaby *et al.*, 2013; Winck, Pérez Melo and González Barrios, 2013). However, there is a marked gap in literature regarding the adaptation to phototrophic conditions once the organic carbon source is depleted in an otherwise nutrient replete medium. Studies on this topic would provide valuable metabolic information and inform potential commercial cultivation strategies and bioprocessing decisions. With enough knowledge about the mixotrophic to phototrophic metabolic transition, a low organic carbon strategy could be envisaged to minimise costs and risk of contamination whilst allowing a timely arrival at a high enough biomass concentration for phototrophic growth to continue at a similar rate after the depletion of the organic carbon source.

## **6.2. Advanced metabolic modelling of microalgal metabolism**

The GeM processing workflow developed in Chapter 5 successfully updated the biomass equation of the model to accurately represent experimental data and constrained the solution space significantly with carbon constraining (Lularevic *et al.*, 2019). However, elemental constraints based on carbon could be complimented in a future implementation of the workflow by additional constraints based on nitrogen or phosphorous uptake. This would potentially constrain the solution space further, reducing model uncertainty and rendering the Monte Carlo samples derived from it more informative with regards to reaction directionality. The robustness of central carbon metabolism between the simulations of different experimental conditions was surprising due to the physiologic and transcriptional differences found in Chapter 3 and Chapter 4. The BMO algorithm could be further refined by employing more detailed biomass composition data inputs, hence achieving resolution at the intra-macromolecular group level. Such simulations would better conclude whether the robustness of central carbon metabolism observed in the simulations of Chapter 5 was a true result or an artefact of the resolution of the macromolecular data input in the BMO algorithm without resorting to extensive carbon-14 radiolabelling experiments.

Constraining the biomass equation at its most basal level would unlock the predictive power of the GeM further and could provide novel understanding on the effect of illumination and trophic strategy on the metabolic configuration of microalgae. This modelling workflow is not restricted to *C. reinhardtii* and could be applied to other existing microalgae GeMs (*Phaeodactylum tricornutum*, (Levering *et al.*, 2016); *Nannochloropsis gaditana* (Ahmad, Srivastava and Ali, 2017); *N. salina*, (Loira *et al.*, 2017) and; *Chlorella vulgaris* (Zuñiga *et al.*, 2016)).

### 6.3. Concluding remarks

The systematic characterisation of the effects of narrow band monochromatic illumination on microalgae under different trophic strategies presented in this thesis sets a knowledge baseline to be expanded upon. It complements previous works like the studies on *C. reinhardtii* biomass productivity under various illumination strategies in continuous culture (Mooij *et al.*, 2016) and provides tools like the newly identified reference genes for RT-qPCR (Chapter 4) and the BMO algorithm (Chapter 5) that can be easily employed in future studies. As policy reform directs industrial biotechnology efforts towards more sustainable processes, the prominence of microalgae will undoubtedly keep increasing. However, without significant bioprocess optimisation efforts, a repeat of the slow progress and dismal success shown by industrial microalgae-based biofuel efforts is entirely possible. I am hopeful that the results and tools presented in this thesis will add a valuable kernel of knowledge towards advancing microalgal bioprocessing in the future.

# Bibliography

---

Abu-Ghosh, S. *et al.* (2016) 'Flashing light in microalgae biotechnology', *Bioresource Technology*, 203, pp. 357–363. doi: 10.1016/j.biortech.2015.12.057.

Adair, W. S. and Snell, W. J. (1990) 'The *Chlamydomonas reinhardtii* cell wall: structure, biochemistry and molecular biology', *Organization and assembly of plant and animal extracellular matrix*, pp. 15–84.

Adelfi, M. G. *et al.* (2014) 'Selection and validation of reference genes for qPCR analysis in the pennate diatoms *Pseudo-nitzschia multistriata* and *P. arenysensis*', *Journal of Experimental Marine Biology and Ecology*, 451, pp. 74–81. doi: 10.1016/j.jembe.2013.11.003.

Agren, R. *et al.* (2013) 'The RAVEN Toolbox and Its Use for Generating a Genome-scale Metabolic Model for *Penicillium chrysogenum*', *PLOS Computational Biology*, 9(3), pp. 1–16. doi: 10.1371/journal.pcbi.1002980.

Ahmad, A., Srivastava, S. and Ali, B. M. J. (2017) 'Reconstruction and analysis of a genome-scale metabolic model of *Nannochloropsis gaditana*', *Algal research*, 26, pp. 354–364.

Ajayan, K. V. *et al.* (2019) 'Energy efficient technology for enhanced growth and lipid production in *Chlamydomonas reinhardtii* through additional reflector coated LED photo-bioreactor', *Biochemical Engineering Journal*, 144, pp. 81–88. doi: 10.1016/j.bej.2019.01.010.

Al-Kodmany, K. (2018) 'The vertical farm: A review of developments and implications for the vertical city', *Buildings*, 8(2), p. 24.

Allen, J. F. (2003) 'Cyclic, pseudocyclic and noncyclic photophosphorylation: new links in the chain', *Trends in Plant Science*, 8(1), pp. 15–19. doi: [https://doi.org/10.1016/S1360-1385\(02\)00006-7](https://doi.org/10.1016/S1360-1385(02)00006-7).

Amini Khoeyi, Z., Seyfabadi, J. and Ramezanpour, Z. (2012) 'Effect of light intensity and photoperiod on biomass and fatty acid composition of the microalgae, *Chlorella vulgaris*', *Aquaculture International*, 20(1), pp. 41–49. doi: 10.1007/s10499-011-9440-1.

Angeles-Martinez, L. and Theodoropoulos, C. (2016) 'Estimation of flux distribution in metabolic networks accounting for thermodynamic constraints: The effect of equilibrium vs. blocked reactions', *Biochemical Engineering Journal*, 105, pp. 347–357.

Antal, T. K. *et al.* (2003) 'The dependence of algal H<sub>2</sub> production on Photosystem II and O<sub>2</sub> consumption activities in sulfur-deprived *Chlamydomonas reinhardtii* cells', *Biochimica et Biophysica Acta (BBA) - Bioenergetics*, 1607(2), pp. 153–160. doi: <https://doi.org/10.1016/j.bbabi.2003.09.008>.

Arnold, C. G. and Schimmer, O. (1972) 'Die Mitochondrien von *Chlamydomonas reinhardtii*', *Arch. Mikrobiol.*, 81, pp. 50–67.

Baer, S. *et al.* (2016) 'Optimization of spectral light quality for growth and product formation in different microalgae using a continuous photobioreactor', *Algal Research*, 14, pp. 109–115. doi: 10.1016/j.algal.2016.01.011.

Baier, T., Kros, D., *et al.* (2018) 'Engineered Fusion Proteins for Efficient Protein Secretion and Purification of a Human Growth Factor from the Green Microalga *Chlamydomonas reinhardtii*', *ACS Synthetic Biology*, 7(11), pp. 2547–2557. doi: 10.1021/acssynbio.8b00226.

Baier, T., Wichmann, J., *et al.* (2018) 'Intron-containing algal transgenes mediate efficient recombinant gene expression in the green microalga *Chlamydomonas reinhardtii*', *Nucleic Acids Research*, 46(13), pp. 6909–6919. doi: 10.1093/nar/gky532.

Baroukh, C. *et al.* (2015) 'A state of the art of metabolic networks of unicellular microalgae and cyanobacteria for biofuel production', *Metabolic Engineering*, 30, pp. 49–60. doi: 10.1016/j.ymben.2015.03.019.

Bartley, M. L. *et al.* (2014) 'pH effects on growth and lipid accumulation of the biofuel microalgae *Nannochloropsis salina* and invading organisms', *Journal of applied*

*phycology*, 26(3), pp. 1431–1437.

Bartsch, O., Hagemann, M. and Bauwe, H. (2008) 'Only plant-type (GLYK) glycerate kinases produce d-glycerate 3-phosphate', *FEBS Letters*, 582(20), pp. 3025–3028. doi: <https://doi.org/10.1016/j.febslet.2008.07.038>.

Beck, C. F. and Haring, M. A. (1996) 'Gametic Differentiation of *Chlamydomonas*', in Jeon, K. W. (ed.). Academic Press (International Review of Cytology), pp. 259–302. doi: [https://doi.org/10.1016/S0074-7696\(08\)60886-4](https://doi.org/10.1016/S0074-7696(08)60886-4).

Beel, B. *et al.* (2012) 'A Flavin Binding Cryptochrome Photoreceptor Responds to Both Blue and Red Light in *Chlamydomonas reinhardtii*', *The Plant Cell*, 24(7), pp. 2992–3008. doi: 10.1105/tpc.112.098947.

Belay, A. and Fogg, G. E. (1978) 'PHOTOINHIBITION OF PHOTOSYNTHESIS IN *ASTERIONELLA FORMOSA* (BACILLARIOPHYCEAE)1, 2', *Journal of Phycology*, 14(3), pp. 341–347. doi: 10.1111/j.1529-8817.1978.tb00310.x.

Benavides, M. *et al.* (2015) 'Parameter identification of Droop model: an experimental case study', *Bioprocess and biosystems engineering*, 38(9), pp. 1783–1793. doi: 10.1007/s00449-015-1419-2.

Bertalan, I. *et al.* (2015) 'A rapid, modular and marker-free chloroplast expression system for the green alga *Chlamydomonas reinhardtii*', *Journal of Biotechnology*, 195, pp. 60–66. doi: 10.1016/j.jbiotec.2014.12.017.

Bertuccio, A. *et al.* (2015) 'Population balance modeling of a microalgal culture in photobioreactors: Comparison between experiments and simulations', *AIChE Journal*, 61(9), pp. 2702–2710.

Bišová, K. and Zachleder, V. (2014) 'Cell-cycle regulation in green algae dividing by multiple fission', *Journal of Experimental Botany*, 65(10), pp. 2585–2602. doi: 10.1093/jxb/ert466.

Blaby-Haas, C. E. and Merchant, S. S. (2019) 'Comparative and Functional Algal Genomics', *Annual Review of Plant Biology*, 70(1), pp. 605–638. doi: 10.1146/annurev-

arplant-050718-095841.

Blaby, I. K. *et al.* (2013) 'Systems-level analysis of nitrogen starvation-induced modifications of carbon metabolism in a *Chlamydomonas reinhardtii* starchless mutant.', *The Plant cell*, 25(11), pp. 4305–23. doi: 10.1105/tpc.113.117580.

Blaby, I. K. *et al.* (2014) 'The *Chlamydomonas* genome project: A decade on', *Trends in Plant Science*, 19(10), pp. 672–680. doi: 10.1016/j.tplants.2014.05.008.

Blank, R. and Arnold, C. G. (1980) 'Variety of mitochondrial shapes, sizes, and volumes in *Chlamydomonas reinhardtii*', *Protoplasma*, 104(1), pp. 187–191. doi: 10.1007/BF01279382.

Blanken, W. *et al.* (2013) 'Cultivation of microalgae on artificial light comes at a cost', *Algal Research*, 2(4), pp. 333–340. doi: 10.1016/j.algal.2013.09.004.

Blanken, W. *et al.* (2016) 'Predicting microalgae growth', *Algal Research*, 14, pp. 28–38. doi: 10.1016/j.algal.2015.12.020.

Bonde, B. K. *et al.* (2011) 'Differential Producibility Analysis (DPA) of Transcriptomic Data with Metabolic Networks: Deconstructing the Metabolic Response of *M. tuberculosis*', *PLoS Computational Biology*. Edited by J. A. Papin, 7(6), p. e1002060. doi: 10.1371/journal.pcbi.1002060.

Bonente, G. *et al.* (2012) 'Acclimation of *Chlamydomonas reinhardtii* to different growth irradiances.', *The Journal of biological chemistry*, 287(8), pp. 5833–5847. doi: 10.1074/jbc.M111.304279.

Bordbar, A. *et al.* (2014) 'Constraint-based models predict metabolic and associated cellular functions.', *Nature reviews. Genetics*, 15(2), pp. 107–20. doi: 10.1038/nrg3643.

Borowitzka, L. J. and Borowitzka, M. A. (1990) 'Commercial production of B-Carotene by *Dunaliella Salina* in open ponds', *Bulletin of Marine Science*, 47(1), pp. 244–252.

Borowitzka, M. A. (1999) 'Commercial production of microalgae: ponds, tanks,

tubes and fermenters', *Journal of Biotechnology*, 70(1–3), pp. 313–321. doi: 10.1016/S0168-1656(99)00083-8.

Borowitzka, Michael A (2013) 'Energy from Microalgae: A Short History', in Borowitzka, M. A. and Moheimani, N. R. (eds) *Algae for Biofuels and Energy*. Dordrecht: Springer Netherlands, pp. 1–15. doi: 10.1007/978-94-007-5479-9\_1.

Borowitzka, Michael A. (2013) 'High-value products from microalgae-their development and commercialisation', *Journal of Applied Phycology*, 25(3), pp. 743–756. doi: 10.1007/s10811-013-9983-9.

Bowler, C., Vardi, A. and Allen, A. E. (2010) 'Oceanographic and biogeochemical insights from diatom genomes.', *Annual review of marine science*, 2, pp. 333–365. doi: 10.1146/annurev-marine-120308-081051.

Boyle, N. R. and Morgan, J. A. (2009) 'Flux balance analysis of primary metabolism in *Chlamydomonas reinhardtii*', *BMC Systems Biology*, 3(1), p. 4. doi: 10.1186/1752-0509-3-4.

Braun-Galleani, S., Baganz, F. and Purton, S. (2015) 'Improving recombinant protein production in the *Chlamydomonas reinhardtii* chloroplast using vivid Verde Fluorescent Protein as a reporter', *Biotechnology Journal*, 10(8), pp. 1289–1297. doi: 10.1002/biot.201400566.

Brindley Alías, C. *et al.* (2004) 'Influence of Power Supply in the Feasibility of *Phaeodactylum tricornutum* Cultures', *Biotechnology and Bioengineering*, 87(6), pp. 723–33. doi: 10.1002/bit.20179.

Broddrick, J. (2016) *Available predictive genome-scale metabolic network reconstructions (UCSD Website)*. Available at: <http://systemsbiology.ucsd.edu/InSilicoOrganisms/OtherOrganisms> (Accessed: 19 October 2016).

Broddrick, J. T. *et al.* (2019) 'Predicting the metabolic capabilities of *Synechococcus elongatus* PCC 7942 adapted to different light regimes', *Metabolic Engineering*, 52(August 2018), pp. 42–56. doi: 10.1016/j.ymben.2018.11.001.

Buder, J. (1919) 'Zur Kenntnis der phototaktischen Richtungsbewegungen', *Jahrb. Wiss. Bot.*, 58, pp. 105–220.

Burlew, J. S. (1953) *Current status of the large-scale culture of algae*. 1st edn, *Algal culture, From laboratory to pilot plant*. 1st edn. Edited by J. S. Burlew. Carnegie Institution of Washington.

Çakmak, Z. E. *et al.* (2014) 'Induction of triacylglycerol production in *Chlamydomonas reinhardtii*: Comparative analysis of different element regimes', *Bioresource Technology*, 155, pp. 379–387. doi: 10.1016/j.biortech.2013.12.093.

Cankorur-Cetinkaya, A. *et al.* (2012) 'A Novel Strategy for Selection and Validation of Reference Genes in Dynamic Multidimensional Experimental Design in Yeast', *PLOS ONE*, 7(6), pp. 1–14. doi: 10.1371/journal.pone.0038351.

Carvalho, A. P. *et al.* (2011) 'Light requirements in microalgal photobioreactors: An overview of biophotonic aspects', *Applied Microbiology and Biotechnology*, 89(5), pp. 1275–1288. doi: 10.1007/s00253-010-3047-8.

Celewicz-Gołdyn, S. and Kuczyńska-Kippen, N. (2017) 'Ecological value of macrophyte cover in creating habitat for microalgae (diatoms) and zooplankton (rotifers and crustaceans) in small field and forest water bodies', *PLOS ONE*, 12(5), p. e0177317. Available at: <https://doi.org/10.1371/journal.pone.0177317>.

Chachuat, B., Singer, A. B. and Barton, P. I. (2006) 'Global Methods for Dynamic Optimization and Mixed-Integer Dynamic Optimization', *Industrial & Engineering Chemistry Research*, 45(25), pp. 8373–8392. doi: 10.1021/ie0601605.

Chang, R. L. *et al.* (2010) 'Drug Off-Target Effects Predicted Using Structural Analysis in the Context of a Metabolic Network Model', *PLOS Computational Biology*, 6(9), p. e1000938. Available at: <https://doi.org/10.1371/journal.pcbi.1000938>.

Chang, R. L. *et al.* (2011) 'Metabolic network reconstruction of *Chlamydomonas* offers insight into light-driven algal metabolism', *Molecular Systems Biology*, 7(1), pp. 518–518. doi: 10.1038/msb.2011.52.



Chapman, D. and Dodd, G. H. (1971) 'Physicochemical probes of membrane structure', in ROTHFIELD, L. I. B. T.-S. and F. of B. M. (ed.) *Structure and Function of Biological Membranes*. Academic Press, pp. 13–81. doi: <https://doi.org/10.1016/B978-0-12-598650-2.50007-7>.

Chapman, S. J. and Gray, T. R. G. (1981) 'Endogenous metabolism and macromolecular composition of *Arthrobacter globiformis*', *Soil Biology and Biochemistry*, 13(1), pp. 11–18. doi: 10.1016/0038-0717(81)90095-X.

Chapman, S. P. *et al.* (2015) 'Flux balance analysis reveals acetate metabolism modulates cyclic electron flow and alternative glycolytic pathways in *Chlamydomonas reinhardtii*', *Frontiers in Plant Science*, 6(June), pp. 1–14. doi: 10.3389/fpls.2015.00474.

Chapman, S. P. *et al.* (2017) 'Cyclic decomposition explains a photosynthetic down regulation for *Chlamydomonas reinhardtii*', *BioSystems*, 162, pp. 119–127. doi: 10.1016/j.biosystems.2017.09.014.

Chavali, A. K. *et al.* (2008) 'Systems analysis of metabolism in the pathogenic trypanosomatid *Leishmania major*', *Molecular Systems Biology*, 4(177), p. 177. doi: 10.1038/msb.2008.15.

Chiaramonti, D. *et al.* (2013) 'Review of energy balance in raceway ponds for microalgae cultivation: Re-thinking a traditional system is possible', *Applied Energy*, 102, pp. 101–111. doi: <http://dx.doi.org/10.1016/j.apenergy.2012.07.040>.

Chisti, Y. (2007) 'Biodiesel from microalgae', *Biotechnol Adv*, 25. doi: 10.1016/j.biotechadv.2007.02.001.

Chisti, Y. (2013) 'Constraints to commercialization of algal fuels', *Journal of Biotechnology*, 167(3), pp. 201–214. doi: 10.1016/j.jbiotec.2013.07.020.

Chitnis, P. R., Reilly, P. A. and Nelson, N. (1989) 'Insertional inactivation of the gene encoding subunit II of photosystem I from the cyanobacterium *Synechocystis* sp. PCC 6803.', *The Journal of biological chemistry*, 264(31), pp. 18381–18385.

Choi, S. P., Nguyen, M. T. and Sim, S. J. (2010) 'Enzymatic pretreatment of

Chlamydomonas reinhardtii biomass for ethanol production', *Bioresource Technology*, 101(14), pp. 5330–5336. doi: <https://doi.org/10.1016/j.biortech.2010.02.026>.

Choquet, Y. and Wollman, F.-A. (2009) 'The CES Process', in *The Chlamydomonas Sourcebook: Organellar and Metabolic Processes*, pp. 1027–1064.

Clack, T., Mathews, S. and Sharrock, R. A. (1994) 'The phytochrome apoprotein family in Arabidopsis is encoded by five genes: the sequences and expression of PHYD and PHYE', *Plant Molecular Biology*, 25(3), pp. 413–427. doi: 10.1007/BF00043870.

Cope, K. R., Snowden, M. C. and Bugbee, B. (2014) 'Photobiological Interactions of Blue Light and Photosynthetic Photon Flux: Effects of Monochromatic and Broad-Spectrum Light Sources', *Photochemistry and Photobiology*, 90(3), pp. 574–584. doi: 10.1111/php.12233.

Cortleven, A. *et al.* (2009) 'Selection of plastid- and nuclear-encoded reference genes to study the effect of altered endogenous cytokinin content on photosynthesis genes in Nicotiana tabacum', *Photosynthesis Research*, 102(21), pp. 1–9. doi: 10.1007/s11120-009-9470-y.

Cross, F. R. (2020) 'Regulation of Multiple Fission and Cell-Cycle-Dependent Gene Expression by CDKA1 and the Rb-E2F Pathway in Chlamydomonas', *Current Biology*, 30(10), pp. 1855–1865.e4. doi: <https://doi.org/10.1016/j.cub.2020.03.019>.

Cross, F. R. and Umen, J. G. (2015) 'The Chlamydomonas cell cycle', *Plant Journal*, 82(3), pp. 370–392. doi: 10.1111/tpj.12795.

Dangeard, P. (1888) 'Recherches sur les algues inferieures', *Ann Sci Nat 7th Ser Bot*, 4(1), pp. 105–175.

Davey, M. P. *et al.* (2014) 'Triacylglyceride Production and Autophagous Responses in Chlamydomonas reinhardtii Depend on Resource Allocation and Carbon Source', *Eukaryotic Cell*, 13(3), pp. 392–400. doi: 10.1128/EC.00178-13.

Davies, D. R. and Plaskitt, A. (1971) 'Genetical and structural analyses of cell-wall formation in Chlamydomonas reinhardtii', *Genetics Research*, 17(1), pp. 33–43.

Dennis, P. P. and Bremer, H. (1974) 'Macromolecular composition during steady-state growth of *Escherichia coli* B/r', *Journal of bacteriology*, 119(1), pp. 270–281.

Derveaux, S., Vandesompele, J. and Hellemans, J. (2010) 'How to do successful gene expression analysis using real-time PCR', *Methods*, 50(4), pp. 227–230. doi: 10.1016/j.ymeth.2009.11.001.

Dikicioglu, D., Kirdar, B. and Oliver, S. G. (2015) 'Biomass composition: the "elephant in the room" of metabolic modelling', *Metabolomics*, pp. 1690–1701. doi: 10.1007/s11306-015-0819-2.

Domozych, D. *et al.* (2012) 'The Cell Walls of Green Algae: A Journey through Evolution and Diversity', *Frontiers in Plant Science*, 3, p. 82. doi: 10.3389/fpls.2012.00082.

Donnan, L. and John, P. C. L. (1983) 'Cell cycle control by timer and sizer in *Chlamydomonas*', *Nature*, 304(5927), pp. 630–633. doi: 10.1038/304630a0.

Doran, P. M. (2013) *Bioprocess Engineering Principles*. 2nd edn. Waltham, MA: Academic Press.

Droop, M. R. (1968) 'Vitamin B<sub>12</sub> and marine ecology. IV. The kinetics of uptake, growth and inhibition in *Monochrysis lutheri*', *J. Mar. Biol. Ass. U.K.*, 48, pp. 689–733. doi: 10.1017/S0025315400019238.

Dubois, M. *et al.* (1956) 'Colorimetric Method for Determination of Sugars and Related Substances', *Analytical Chemistry*, 28(3), pp. 350–356. doi: 10.1021/ac60111a017.

Dyo, Y. M. and Purton, S. (2018) 'The algal chloroplast as a synthetic biology platform for production of therapeutic proteins', *Microbiology Society*, 164(2), pp. 113–121. doi: 10.1099/mic.0.000599.

Egea, J. A. *et al.* (2007) 'Scatter search for chemical and bio-process optimization', *Journal of Global Optimization*, 37(3), pp. 481–503. doi: 10.1007/s10898-006-9075-3.

Egea, J. A. *et al.* (2009) 'Dynamic Optimization of Nonlinear Processes with an

Enhanced Scatter Search Method', *Industrial & Engineering Chemistry Research*, 48(9), pp. 4388–4401. doi: 10.1021/ie801717t.

Erickson, E., Wakao, S. and Niyogi, K. K. (2015) 'Light stress and photoprotection in *Chlamydomonas reinhardtii*', *The Plant Journal*, 82(3), pp. 449–465. doi: <https://doi.org/10.1111/tpj.12825>.

Ermilova *et al.* (1996) 'Isolation and Characterization of Chemotaxis Mutants of *Chlamydomonas reinhardtii*', *Current microbiology*, 32(6), pp. 357–359.

Ermilova, E. V., Zalutskaya, Z. M. and Gromov, B. V. (1993) 'Chemotaxis towards sugars in *Chlamydomonas reinhardtii*', *Current Microbiology*, 27(1), pp. 47–50. doi: 10.1007/BF01576833.

EY (2017) *Beyond borders: Biotechnology report*.

Fábregas, J. *et al.* (2003) 'Interactions between irradiance and nutrient availability during astaxanthin accumulation and degradation in *Haematococcus pluvialis*', *Applied Microbiology and Biotechnology*, 61(5–6), pp. 545–551. doi: 10.1007/s00253-002-1204-4.

Faraloni, C. *et al.* (2011) 'Enhanced hydrogen production by means of sulfur-deprived *Chlamydomonas reinhardtii* cultures grown in pretreated olive mill wastewater', *International Journal of Hydrogen Energy*, 36(10), pp. 5920–5931. doi: <https://doi.org/10.1016/j.ijhydene.2011.02.007>.

Fasaei, F. *et al.* (2018) 'Techno-economic evaluation of microalgae harvesting and dewatering systems', *Algal Research*, 31, pp. 347–362.

FDA (2011) *Guidance for Industry, Process Validation: General Principles and Practices, Revision 1*. Rockville, MD.

Feist, A. M. and Palsson, B. O. (2010) 'The biomass objective function', *Current Opinion in Microbiology*, 13(3), pp. 344–349. doi: 10.1016/j.mib.2010.03.003.

Fernandez, E., Llamas, A. and Galvan, A. (2009) 'Nitrogen assimilation and its regulation', in Stern, D. B. (ed.) *The Chlamydomonas Sourcebook: Organellar and*

*Metabolic Processes*. Elsevier, pp. 69–114.

Field *et al.* (1998) 'Primary production of the biosphere: integrating terrestrial and oceanic components', *Science (New York, N.Y.)*, 281(5374), pp. 237–240. doi: 10.1126/science.281.5374.237.

Fields, F. J., Ostrand, J. T. and Mayfield, S. P. (2018) 'Fed-batch mixotrophic cultivation of *Chlamydomonas reinhardtii* for high-density cultures', *Algal Research*, 33(March 2017), pp. 109–117. doi: 10.1016/j.algal.2018.05.006.

Finazzi, G., Drapier, D. and Rappaport, F. (2009) 'The CF<sub>0</sub>F<sub>1</sub> ATP Synthase Complex of Photosynthesis', in Stern, D. B. (ed.) *The Chlamydomonas Sourcebook: Organellar and Metabolic Processes*. 2nd edn. Elsevier, pp. 639–670. doi: 10.1016/0092-8674(90)90467-S.

Finkel, Z. V *et al.* (2005) 'Climatically driven macroevolutionary patterns in the size of marine diatoms over the Cenozoic', *Proceedings of the National Academy of Sciences*, 102(25), pp. 8927–8932. doi: 10.1073/pnas.0409907102.

Finnegan, P. M., Soole, K. L. and Umbach, A. L. (2004) 'Alternative mitochondrial electron transport proteins in higher plants', in *Plant mitochondria: from genome to function*. Springer, pp. 163–230.

Fischer, B. B., Wiesendanger, M. and Eggen, R. I. L. (2006) 'Growth Condition-Dependent Sensitivity, Photodamage and Stress Response of *Chlamydomonas reinhardtii* Exposed to High Light Conditions', *Plant and Cell Physiology*, 47(8), pp. 1135–1145. doi: 10.1093/pcp/pcj085.

Fischer, N. and Rochaix, J. D. (2001) 'The flanking regions of Psad drive efficient gene expression in the nucleus of the green alga *Chlamydomonas reinhardtii*', *Molecular Genetics and Genomics*, 265(5), pp. 888–894. doi: 10.1007/s004380100485.

Flassig, R. J. *et al.* (2016) 'Dynamic flux balance modeling to increase the production of high-value compounds in green microalgae', *Biotechnology for Biofuels*, 9(1), pp. 1–12. doi: 10.1186/s13068-016-0556-4.

Fletcher, S. P., Muto, M. and Mayfield, S. P. (2007) 'Optimization of Recombinant Protein Expression in the Chloroplasts of Green Algae', in León, R., Galván, A., and Fernández, E. (eds) *Transgenic Microalgae as Green Cell Factories*. New York, NY: Springer New York, pp. 90–98. doi: 10.1007/978-0-387-75532-8\_8.

Focsan, A., Polyakov, N. and Kispert, L. (2017) 'Photo Protection of Haematococcus pluvialis Algae by Astaxanthin: Unique Properties of Astaxanthin Deduced by EPR, Optical and Electrochemical Studies', *Antioxidants*, 6(4), p. 80. doi: 10.3390/antiox6040080.

Förster, J. *et al.* (2003) 'Genome-scale reconstruction of the *Saccharomyces cerevisiae* metabolic network.', *Genome research*, 13(2), pp. 244–253. doi: 10.1101/gr.234503.

Foster, K. W. and Smyth, R. D. (1980) 'Light Antennas in phototactic algae.', *Microbiological Reviews*, 44(4), pp. 572 LP – 630. Available at: <http://mmbr.asm.org/content/44/4/572.abstract>.

Fredrickson, A. G., Mcgee III, R. D. and Tsuchiya, H. . (1970) 'Mathematical Models in Fermentation Processes', *Adv. Appl. Microbiol*, 23, pp. 419–465.

Gaffal, K. P. (1987) 'Mitosis-specific oscillations of mitochondrial morphology in *Chlamydomonas reinhardtii*', *Endocytobiosis Cell Res*, 4(1), pp. 41–61.

García Sánchez, C. E. and Torres Sáez, R. G. (2014) 'Comparison and analysis of objective functions in flux balance analysis', *Biotechnology Progress*, 30(5), pp. 985–991. doi: 10.1002/btpr.1949.

Gardner, R. *et al.* (2011) 'Medium pH and nitrate concentration effects on accumulation of triacylglycerol in two members of the chlorophyta', *Journal of Applied Phycology*, 23(6), pp. 1005–1016. doi: 10.1007/s10811-010-9633-4.

Gavrilescu, M. and Chisti, Y. (2005) 'Biotechnology—a sustainable alternative for chemical industry', *Biotechnology advances*, 23(7–8), pp. 471–499.

Gellenbeck, K. W. (2012) 'Utilization of algal materials for nutraceutical and

cosmeceutical applications-what do manufacturers need to know?', *Journal of Applied Phycology*, 24(3), pp. 309–313. doi: 10.1007/s10811-011-9722-z.

Ghirardi, M. L. *et al.* (2000) 'Microalgae: A green source of renewable H<sub>2</sub>', *Trends in Biotechnology*, 18(12), pp. 506–511. doi: 10.1016/S0167-7799(00)01511-0.

Gianchandani, E. P. *et al.* (2008) 'Predicting biological system objectives de novo from internal state measurements', *BMC Bioinformatics*, 9(1), p. 43. doi: 10.1186/1471-2105-9-43.

Gimpel, J. A. *et al.* (2015) 'Production of recombinant proteins in microalgae at pilot greenhouse scale', *Biotechnology and Bioengineering*, 112(2), pp. 339–345. doi: 10.1002/bit.25357.

Goldman, J. C. (1979) 'Outdoor algal mass cultures-II. Photosynthetic yield limitations', *Water Research*, 13(2), pp. 119–136. doi: 10.1016/0043-1354(79)90083-6.

Goldschmidt-Clermont, M. (1986) 'The two genes for the small subunit of RuBP Carboxylase/oxygenase are closely linked in *Chlamydomonas reinhardtii*', *Plant Molecular Biology*, 6(1), pp. 13–21. doi: 10.1007/BF00021302.

Goldschmidt-Clermont, M. and Rahire, M. (1986) 'Sequence, evolution and differential expression of the two genes encoding variant small subunits of ribulose biphosphate carboxylase/oxygenase in *Chlamydomonas reinhardtii*', *Journal of Molecular Biology*, 191(3), pp. 421–432. doi: 10.1016/0022-2836(86)90137-3.

Gonzalez-Ballester, D. *et al.* (2010) 'RNA-Seq Analysis of Sulfur-Deprived *Chlamydomonas* Cells Reveals Aspects of Acclimation Critical for Cell Survival', *The Plant cell*, 22(6), pp. 2058–2084. doi: 10.1105/tpc.109.071167.

Goodenough, U. *et al.* (2014) 'The path to triacylglyceride obesity in the sta6 strain of *Chlamydomonas reinhardtii*', *Eukaryotic Cell*, 13(5), pp. 591–613. doi: 10.1128/EC.00013-14.

Goodenough, U. W. and Heuser, J. E. (1985) 'The *Chlamydomonas* cell wall and its constituent glycoproteins analyzed by the quick-freeze, deep-etch technique', *Journal*

*of Cell Biology*, 101(4), pp. 1550–1568. doi: 10.1083/jcb.101.4.1550.

Goodstein, D. M. *et al.* (2011) 'Phytozome: a comparative platform for green plant genomics', *Nucleic Acids Research*, 40(D1), pp. D1178–D1186. doi: 10.1093/nar/gkr944.

Gould, K. S. (2004) 'Nature's Swiss army knife: The diverse protective roles of anthocyanins in leaves', *Journal of Biomedicine and Biotechnology*, 2004(5), pp. 314–320. doi: 10.1155/S1110724304406147.

GreenSea (2016) *GreenSea Company Website*. Available at: <http://www.greensea.fr/> (Accessed: 11 February 2016).

Grilo, A. L. and Mantalaris, A. (2019) 'The Increasingly Human and Profitable Monoclonal Antibody Market', *Trends in Biotechnology*, 37(1), pp. 9–16. doi: 10.1016/j.tibtech.2018.05.014.

Grossman, A. R. *et al.* (2007) 'Novel metabolism in *Chlamydomonas* through the lens of genomics', *Current Opinion in Plant Biology*, 10(2), pp. 190–198. doi: 10.1016/j.pbi.2007.01.012.

Guiry, M. D. (2012) 'How many species of algae are there?', *Journal of Phycology*, 48(5), pp. 1057–1063. doi: 10.1111/j.1529-8817.2012.01222.x.

Guo, R., Lee, M. A. and Ki, J. S. (2013) 'Normalization genes for mRNA expression in the marine diatom *Ditylum brightwellii* following exposure to thermal and toxic chemical stresses', *Journal of Applied Phycology*, 25(4), pp. 1101–1109. doi: 10.1007/s10811-012-9908-z.

Gupta, R., Sharma, R. and Beg, Q. K. (2013) 'Revisiting microbial keratinases: next generation proteases for sustainable biotechnology', *Critical reviews in biotechnology*, 33(2), pp. 216–228.

Hamilton, J. J. and Reed, J. L. (2014) 'Software platforms to facilitate reconstructing genome-scale metabolic networks', *Environmental Microbiology*, 16(1), pp. 49–59. doi: 10.1111/1462-2920.12312.

Van Handel, E. (1985) 'Rapid determination of total lipids in mosquitoes', *Journal*



of the American Mosquito Control Association, 1(3), pp. 302–304.

Hansberg, W. and Aguirre, J. (1990) 'Hyperoxidant states cause microbial cell differentiation by cell isolation from dioxygen', *Journal of Theoretical Biology*, 142(2), pp. 201–221. doi: [https://doi.org/10.1016/S0022-5193\(05\)80222-X](https://doi.org/10.1016/S0022-5193(05)80222-X).

Harder, R. and von Witsch, H. (1942) 'Über Massenkultur von Diatomeen', *Berichte der Deutschen Botanischen Gesellschaft*, 60(11), pp. 146–152. doi: <https://doi.org/10.1111/j.1438-8677.1942.tb03902.x>.

Harris, E. H. (2001) 'Chlamydomonas as a model organism', *Molecular Biology*, 52(1), pp. 363–406. doi: 10.1146/annurev.arplant.52.1.363.

Harris, E. H. (2009) 'Chapter 6 - The Life of an Acetate Flagellate', in Harris, E. H., Stern, D. B., and Witman, G. B. B. T.-T. C. S. (Second E. (eds) *The Chlamydomonas Sourcebook (Second Edition) Volume 1*. London: Academic Press, pp. 159–210. doi: <https://doi.org/10.1016/B978-0-12-370873-1.00006-X>.

Harris, E. H. (2013) *The Chlamydomonas Sourcebook Volume1: Introduction to Chlamydomonas and Its Laboratory Use, Journal of Chemical Information and Modeling*. Edited by Elizabeth H. Harris. doi: 10.1017/CBO9781107415324.004.

Harris, E. H., Stern, D. B. and Witman, G. B. (eds) (2009) 'Chapter 1 - The Genus Chlamydomonas', in *The Chlamydomonas Sourcebook (Second Edition)*. Second Edi. London: Academic Press, pp. 1–24. doi: <https://doi.org/10.1016/B978-0-12-370873-1.00001-0>.

Hashimoto, H. *et al.* (2015) 'Natural and artificial light-harvesting systems utilizing the functions of carotenoids', *Journal of Photochemistry and Photobiology C: Photochemistry Reviews*, 25, pp. 46–70. doi: <https://doi.org/10.1016/j.jphotochemrev.2015.07.004>.

Hayashi, Y. *et al.* (2014) 'Increase in peroxisome number and the gene expression of putative glyoxysomal enzymes in Chlamydomonas cells supplemented with acetate', *Journal of Plant Research*, 128(1), pp. 177–185. doi: 10.1007/s10265-014-0681-8.

Hegemann, P. and Marwan, W. (1988) 'SINGLE PHOTONS ARE SUFFICIENT TO TRIGGER MOVEMENT RESPONSES IN *Chlamydomonas reinhardtii*', *Photochemistry and Photobiology*, 48(1), pp. 99–106. doi: 10.1111/j.1751-1097.1988.tb02793.x.

Heifetz, P. B. *et al.* (2000) 'Effects of acetate on facultative autotrophy in *Chlamydomonas reinhardtii* assessed by photosynthetic measurements and stable isotope analyses.', *Plant physiology*, 122(4), pp. 1439–45. doi: 10.1104/pp.122.4.1439.

Heldt, F. S. *et al.* (2020) 'A single light-responsive sizer can control multiple-fission cycles in *Chlamydomonas*', *Current Biology*, 30(4), pp. 634–644.

Hellemans, J. *et al.* (2007) 'qBase relative quantification framework and software for management and automated analysis of real-time quantitative PCR data', *Genome Biology*, 8(2), p. R19. doi: 10.1186/gb-2007-8-2-r19.

Hendry, J. I. *et al.* (2016) 'Metabolic model of *Synechococcus* sp. PCC 7002: Prediction of flux distribution and network modification for enhanced biofuel production', *Bioresource Technology*, 213, pp. 190–197. doi: <https://doi.org/10.1016/j.biortech.2016.02.128>.

Herdman, M. and Stanier, R. Y. (1977) 'The cyanelle: Chloroplast or endosymbiotic prokaryote?', *FEMS Microbiology Letters*, 1(1), pp. 7–11. doi: 10.1111/j.1574-6968.1977.tb00568.x.

Hu, Q. and Sommerfeld, M. (2010) 'Photobioreactor and uses therefore. U.S. Patent Application US2010/0028976 A1'.

Huang, K. and Beck, C. F. (2003) 'Phototropin is the blue-light receptor that controls multiple steps in the sexual life cycle of the green alga *Chlamydomonas reinhardtii*', *Proceedings of the National Academy of Sciences*, 100(10), pp. 6269–6274. doi: 10.1073/pnas.0931459100.

Huntley, M. E. and Redalje, D. G. (2007) *CO<sub>2</sub> mitigation and renewable oil from photosynthetic microbes: A new appraisal, Mitigation and Adaptation Strategies for Global Change*. doi: 10.1007/s11027-006-7304-1.

ICH (2006) *Q9 Harmonized Tripartite Guideline, Quality Risk Management*.

ICH (2009a) *Q10, Harmonized Tripartite Guideline, Pharmaceutical Quality System*.

ICH (2009b) *Q8(R2) Harmonized Tripartite Guideline, Pharmaceutical Development, Step 4 version*.

Ichikawa, S. *et al.* (2010) 'Hydroxyproline-containing dipeptides and tripeptides quantified at high concentration in human blood after oral administration of gelatin hydrolysate', *International Journal of Food Sciences and Nutrition*, 61(1), pp. 52–60. doi: 10.3109/09637480903257711.

Ihnatowicz, A. *et al.* (2004) 'Mutants for photosystem I subunit D of *Arabidopsis thaliana*: Effects on photosynthesis, photosystem I stability and expression of nuclear genes for chloroplast functions', *Plant Journal*, 37(6), pp. 839–852. doi: 10.1111/j.1365-313X.2004.02011.x.

Ike, A. *et al.* (1997) 'Hydrogen photoproduction from CO<sub>2</sub>-fixing microalgal biomass: application of halotolerant photo synthetic bacteria', *Journal of Fermentation and Bioengineering*, 84(6), pp. 606–609. doi: 10.1016/S0922-338X(97)81921-6.

Inskeep, W. P. and Bloom, P. R. (1985) 'Extinction coefficients of chlorophyll-a and chlorophyll-b in N,N-dimethylformamide and 80-percent acetone', *Plant Physiology*, 77, pp. 483–485.

Ishikura, K. *et al.* (1999) 'Expression of a foreign gene in *Chlamydomonas reinhardtii* chloroplast', *Journal of Bioscience and Bioengineering*, 87(3), pp. 307–314. doi: 10.1016/S1389-1723(99)80037-1.

Jackson, J. E. (1991) 'PCA with more than two variables', in *A User's Guide to Principal Components*. Hoboken: Wiley-Interscience, pp. 26–62.

James, G. O. *et al.* (2011) 'Fatty acid profiling of *Chlamydomonas reinhardtii* under nitrogen deprivation', *Bioresource Technology*, 102(3), pp. 3343–3351. doi: 10.1016/j.biortech.2010.11.051.

James, G. O. *et al.* (2013) 'Temperature modulation of fatty acid profiles for biofuel

production in nitrogen deprived *Chlamydomonas reinhardtii*', *Bioresour Technol*, 127. doi: 10.1016/j.biortech.2012.09.090.

Jeon, S. *et al.* (2017) 'Current status and perspectives of genome editing technology for microalgae', *Biotechnology for Biofuels*, 10(1), pp. 1–18. doi: 10.1186/s13068-017-0957-z.

Johnson, X. and Alric, J. (2012) 'Interaction between starch breakdown, acetate assimilation, and photosynthetic cyclic electron flow in *Chlamydomonas reinhardtii*', *Journal of Biological Chemistry*, 287(31), pp. 26445–26452. doi: 10.1074/jbc.M112.370205.

Johnson, X. and Alric, J. (2013) 'Central carbon metabolism and electron transport in *Chlamydomonas reinhardtii*: Metabolic constraints for carbon partitioning between oil and starch', *Eukaryotic Cell*, 12(6), pp. 776–793. doi: 10.1128/EC.00318-12.

Jungandreas, A. *et al.* (2014) 'The acclimation of *Phaeodactylum tricornutum* to blue and red light does not influence the photosynthetic light reaction but strongly disturbs the carbon allocation pattern', *PLoS ONE*, 9(8). doi: 10.1371/journal.pone.0099727.

Kalantari, F. *et al.* (2017) 'A review of vertical farming technology: A guide for implementation of building integrated agriculture in cities', in *Advanced Engineering Forum*. Trans Tech Publ, pp. 76–91.

Kamalanathan, M. *et al.* (2016) 'Impacts of nitrogen and phosphorus starvation on the physiology of *Chlamydomonas reinhardtii*', *Journal of Applied Phycology*, 28(3), pp. 1509–1520.

Kamalanathan, M., Gleadow, R. and Beardall, J. (2017) 'Use of a chemical inhibitor as an alternative approach to enhance lipid production in *Chlamydomonas reinhardtii* (Chlorophyceae)', *Phycologia*, 56(2), pp. 159–166. doi: 10.2216/16-49.1.

Kasai, S. *et al.* (2003) 'Effect of coding regions on chloroplast gene expression in *Chlamydomonas reinhardtii*', *Journal of Bioscience and Bioengineering*, 95(3), pp. 276–282. doi: 10.1016/s1389-1723(03)80029-4.

Katsuda, T. *et al.* (2004) 'Astaxanthin production by *Haematococcus pluvialis* under illumination with LEDs', *Enzyme and Microbial Technology*, 35(1), pp. 81–86. doi: <https://doi.org/10.1016/j.enzmictec.2004.03.016>.

Kaye, Y. *et al.* (2019) 'The mitochondrial alternative oxidase from *Chlamydomonas reinhardtii* enables survival in high light.', *The Journal of biological chemistry*, 294(4), pp. 1380–1395. doi: 10.1074/jbc.RA118.004667.

Ke, J. *et al.* (2000) 'Coordinate regulation of the nuclear and plastidic genes coding for the subunits of the heteromeric acetyl-coenzyme A carboxylase', *Plant Physiology*, 122(4), pp. 1057–1071. doi: 10.1104/pp.122.4.1057.

Kebelmann, K. *et al.* (2013) 'Intermediate pyrolysis and product identification by TGA and Py-GC/MS of green microalgae and their extracted protein and lipid components', *Biomass and Bioenergy*, 49, pp. 38–48. doi: <https://doi.org/10.1016/j.biombioe.2012.12.006>.

Keskiaho, K. *et al.* (2007) '*Chlamydomonas reinhardtii* Has Multiple Prolyl 4-Hydroxylases, One of Which Is Essential for Proper Cell Wall Assembly', *The Plant Cell*, 19(1), pp. 256 LP – 269. doi: 10.1105/tpc.106.042739.

Ketheesan, B. and Nirmalakhandan, N. (2012) 'Feasibility of microalgal cultivation in a pilot-scale airlift-driven raceway reactor', *Bioresource Technology*, 108, pp. 196–202. doi: <http://dx.doi.org/10.1016/j.biortech.2011.12.146>.

Khrebtukova, I. and Spreitzer, R. J. (1996) 'Elimination of the *Chlamydomonas* gene family that encodes the small subunit of ribulose-1,5-bisphosphate carboxylase/oxygenase', *Proceedings of the National Academy of Sciences*, 93(24), pp. 13689–13693. doi: 10.1073/pnas.93.24.13689.

Kianianmomeni, A. and Hallmann, A. (2013) 'Validation of reference genes for quantitative gene expression studies in *Volvox carteri* using real-time RT-PCR', *Molecular Biology Reports*, 40(12), pp. 6691–6699. doi: 10.1007/s11033-013-2784-z.

Kianianmomeni, A. and Hallmann, A. (2014) 'Algal photoreceptors: In vivo functions and potential applications', *Planta*, 239(1), pp. 1–26. doi: 10.1007/s00425-

Kim, D. G. *et al.* (2014) 'Manipulation of light wavelength at appropriate growth stage to enhance biomass productivity and fatty acid methyl ester yield using *Chlorella vulgaris*', *Bioresource Technology*, 159, pp. 240–248. doi: 10.1016/j.biortech.2014.02.078.

Kindle, K. L. (1990) 'High-frequency nuclear transformation of *Chlamydomonas reinhardtii*.' , *Proceedings of the National Academy of Sciences*, 87(3), pp. 1228–1232.

Kiparissides, A. and Hatzimanikatis, V. (2017) 'Thermodynamics-based Metabolite Sensitivity Analysis in metabolic networks', *Metabolic Engineering*, 39, pp. 117–127. doi: 10.1016/j.ymben.2016.11.006.

Kirk, J. T. O. (1994) *Light and Photosynthesis in Aquatic Ecosystems*. Cambridge University Press (Light and Photosynthesis in Aquatic Ecosystems). Available at: <https://books.google.co.uk/books?id=lt5GePwa2EIC>.

Klein, U. (1986) 'Compartmentation of glycolysis and of the oxidative pentose-phosphate pathway in *Chlamydomonas reinhardtii*', *Planta*, 167(1), pp. 81–86. doi: 10.1007/BF00446372.

Kliphuis, A. M. J. *et al.* (2010) 'Photosynthetic efficiency of *Chlorella sorokiniana* in a turbulently mixed short light-path photobioreactor', *Biotechnology Progress*, 26(3), pp. 687–696. doi: 10.1002/btpr.379.

Kliphuis, A. M. J. *et al.* (2011) 'Effect of O<sub>2</sub>:CO<sub>2</sub> ratio on the primary metabolism of *Chlamydomonas reinhardtii*', *Biotechnology and Bioengineering*, 108(10), pp. 2390–2402. doi: 10.1002/bit.23194.

Kliphuis, A. M. J. *et al.* (2012) 'Metabolic modeling of *Chlamydomonas reinhardtii*: energy requirements for photoautotrophic growth and maintenance', *Journal of Applied Phycology*, 24(2), pp. 253–266. doi: 10.1007/s10811-011-9674-3.

Kobayashi, N. *et al.* (2013) 'Rapid detection and quantification of triacylglycerol by HPLC-ELSD in *chlamydomonas reinhardtii* and *chlorella* strains', *Lipids*, 48(10), pp. 1035–

1049. doi: 10.1007/s11745-013-3828-9.

Kong, F. *et al.* (2017) 'Chlamydomonas carries out fatty acid  $\beta$ -oxidation in ancestral peroxisomes using a bona fide acyl-CoA oxidase', *Plant Journal*, 90(2), pp. 358–371. doi: 10.1111/tpj.13498.

Kropat, J. *et al.* (2012) 'A revised mineral nutrient supplement increases biomass and growth rate in *Chlamydomonas reinhardtii*', 66(5), pp. 770–780. doi: 10.1111/j.1365-313X.2011.04537.x.A.

Kruger, N. J. and von Schaewen, A. (2003) 'The oxidative pentose phosphate pathway: structure and organisation', *Current Opinion in Plant Biology*, 6(3), pp. 236–246. doi: [https://doi.org/10.1016/S1369-5266\(03\)00039-6](https://doi.org/10.1016/S1369-5266(03)00039-6).

Kubo, T. *et al.* (2009) 'The chlamydomonas hatching enzyme, sporangin, is expressed in specific phases of the cell cycle and is localized to the flagella of daughter cells within the sporangial cell wall', *Plant and Cell Physiology*, 50(3), pp. 572–583. doi: 10.1093/pcp/pcp016.

Lababpour, A. *et al.* (2004) 'Effects of nutrient supply methods and illumination with blue light emitting diodes (LEDs) on astaxanthin production by *Haematococcus pluvialis*', *Journal of Bioscience and Bioengineering*, 98(6), pp. 452–456. doi: 10.1016/S1389-1723(05)00311-7.

Lamers, P. P. *et al.* (2008) 'Exploring and exploiting carotenoid accumulation in *Dunaliella salina* for cell-factory applications', *Trends in Biotechnology*, 26(11), pp. 631–638. doi: <https://doi.org/10.1016/j.tibtech.2008.07.002>.

Lauersen, K. J. *et al.* (2016) 'Peroxisomal microbodies are at the crossroads of acetate assimilation in the green microalga *Chlamydomonas reinhardtii*', *Algal Research*, 16, pp. 266–274. doi: 10.1016/j.algal.2016.03.026.

León-Saiki, G. M. *et al.* (2018) 'The impact of day length on cell division and efficiency of light use in a starchless mutant of *Tetrademus obliquus*', *Algal Research*, 31, pp. 387–394. doi: <https://doi.org/10.1016/j.algal.2018.02.027>.

Levering, J. *et al.* (2016) 'Genome-Scale Model Reveals Metabolic Basis of Biomass Partitioning in a Model Diatom.', *PloS one*, 11(5), p. e0155038. doi: 10.1371/journal.pone.0155038.

Levy, H., Kindle, K. L. and Stern, D. B. (1997) 'A Nuclear Mutation That Affects the 3[prime] Processing of Several mRNAs in Chlamydomonas Chloroplasts.', *The Plant Cell*, 9(5), pp. 825 LP – 836. doi: 10.1105/tpc.9.5.825.

Lewis, N. E. *et al.* (2010) 'Large-scale in silico modeling of metabolic interactions between cell types in the human brain.', *Nature biotechnology*, 28(12), pp. 1279–1285. doi: 10.1038/nbt.1711.

Li-Beisson, Y., Beisson, F. and Riekhof, W. (2015) 'Metabolism of acyl-lipids in Chlamydomonas reinhardtii', *Plant Journal*, 82(3), pp. 504–522. doi: 10.1111/tpj.12787.

Li, J. *et al.* (2018) 'Selection of reference genes for real-time RT-PCR normalization in brown alga Undaria pinnatifida', *Journal of Applied Phycology*, 31(1), pp. 787–793. doi: 10.1007/s10811-018-1576-1.

Lin, Z. *et al.* (2019) 'Alternative Oxidase Is Involved in the Pathogenicity, Development, and Oxygen Stress Response of Botrytis cinerea', *Phytopathology*®, 109(10), pp. 1679–1688. doi: 10.1094/PHYTO-01-19-0012-R.

Lisec, J. *et al.* (2006) 'Gas chromatography mass spectrometry–based metabolite profiling in plants', *Nature Protocols*, 1(1), pp. 387–396. doi: 10.1038/nprot.2006.59.

Liu, C. *et al.* (2012) 'Validation of housekeeping genes for gene expression studies in an ice alga Chlamydomonas during freezing acclimation', *Extremophiles*, 16(3), pp. 419–425. doi: 10.1007/s00792-012-0441-4.

Liu, K. (2019) 'Effects of sample size, dry ashing temperature and duration on determination of ash content in algae and other biomass', *Algal Research*, 40, p. 101486. doi: <https://doi.org/10.1016/j.algal.2019.101486>.

Livak, K. J. and Schmittgen, T. D. (2001) 'Analysis of relative gene expression data using real-time quantitative PCR and the 2(- $\Delta\Delta C(T)$ ) Method', *Methods*, 25(4), pp. 402–



408. doi: 10.1006/meth.2001.1262.

Loira, N. *et al.* (2017) 'Reconstruction of the microalga *Nannochloropsis salina* genome-scale metabolic model with applications to lipid production', *BMC systems biology*, 11(1), p. 66.

Lowry, O. H. *et al.* (1951) 'Protein measurement with the Folin phenol reagent.', *The Journal of biological chemistry*, 193(1), pp. 265–75. Available at: <http://www.ncbi.nlm.nih.gov/pubmed/14907713>.

Lularevic, M. *et al.* (2019) *Improving the accuracy of flux balance analysis through the implementation of carbon availability constraints for intracellular reactions*, *Biotechnology and Bioengineering*. doi: 10.1002/bit.27025.

Mackinder, L. C. M. *et al.* (2016) 'A repeat protein links Rubisco to form the eukaryotic carbon concentrating organelle', *Pnas*, pp. 2–7. doi: 10.1073/pnas.1522866113.

Madagan, K. L. (1998) *Tools for nuclear transformation in Chlamydomonas reinhardtii*. UCL (University College London).

Majidian, P. *et al.* (2018) 'Metabolic engineering of microorganisms for biofuel production', *Renewable and Sustainable Energy Reviews*, 82(July 2017), pp. 3863–3885. doi: 10.1016/j.rser.2017.10.085.

Marañón, E. *et al.* (2013) 'Unimodal size scaling of phytoplankton growth and the size dependence of nutrient uptake and use', *Ecology Letters*, 16(3), pp. 371–379. doi: 10.1111/ele.12052.

Markou, G., Chatzipavlidis, I. and Georgakakis, D. (2012) 'Carbohydrates production and bio-flocculation characteristics in cultures of *Arthrospira* (*Spirulina*) *platensis*: improvements through phosphorus limitation process', *BioEnergy research*, 5(4), pp. 915–925.

Martino, A. De *et al.* (2007) 'Genetic and phenotypic characterization of *Phaeodactylum tricornutum* (Bacillariophyceae) accessions', *Journal of Phycology*, 43(5),

pp. 992–1009. doi: 10.1111/j.1529-8817.2007.00384.x.

Matsuda, Y. *et al.* (1985) 'Cell wall lytic enzyme released by mating gametes of *Chlamydomonas reinhardtii* is a metalloprotease and digests the sodium perchlorate-insoluble component of cell wall.', *Journal of Biological Chemistry*, 260(10), pp. 6373–6377.

Matsumura, K., Yagi, T. and Yasuda, K. (2003) 'Role of timer and sizer in regulation of *Chlamydomonas* cell cycle', *Biochemical and Biophysical Research Communications*, 306(4), pp. 1042–1049. doi: [https://doi.org/10.1016/S0006-291X\(03\)01089-1](https://doi.org/10.1016/S0006-291X(03)01089-1).

Mayers, J. J., Flynn, K. J. and Shields, R. J. (2013) 'Rapid determination of bulk microalgal biochemical composition by Fourier-Transform Infrared spectroscopy', *Bioresource Technology*, 148, pp. 215–220. doi: 10.1016/j.biortech.2013.08.133.

McCloskey, D., Palsson, B. Ø. and Feist, A. M. (2013) 'Basic and applied uses of genome-scale metabolic network reconstructions of *Escherichia coli*.', *Molecular systems biology*, 9(1), p. 661. doi: 10.1038/msb.2013.18.

McCree, K. J. (1971) 'The action spectrum, absorptance and quantum yield of photosynthesis in crop plants', *Agricultural Meteorology*, 9, pp. 191–216. doi: [https://doi.org/10.1016/0002-1571\(71\)90022-7](https://doi.org/10.1016/0002-1571(71)90022-7).

McIntosh, L. (1994) 'Molecular biology of the alternative oxidase', *Plant physiology*, 105(3), pp. 781–786. doi: 10.1104/pp.105.3.781.

McKay, R. M. L., Gibbs, S. P. and Vaughn, K. (1991) 'RuBisCo activase is present in the pyrenoid of green algae', *Protoplasma*, 162, pp. 38–45.

Merchant, S. S. *et al.* (2007) 'The *Chlamydomonas* Genome Reveals the Evolution of Key Animal and Plant Functions', *Science*, 318(5848), pp. 245–250. doi: 10.1126/science.1143609.The.

Michelet, L. *et al.* (2011) 'Enhanced chloroplast transgene expression in a nuclear mutant of *Chlamydomonas*.', *Plant biotechnology journal*, 9(5), pp. 565–74. doi: 10.1111/j.1467-7652.2010.00564.x.

Millar, A. H. *et al.* (2011) 'Organization and Regulation of Mitochondrial Respiration in Plants', *Annual Review of Plant Biology*, 62(1), pp. 79–104. doi: 10.1146/annurev-arplant-042110-103857.

Milne, B. F. *et al.* (2015) 'Unraveling the Intrinsic Color of Chlorophyll', *Angewandte Chemie International Edition*, 54(7), pp. 2170–2173. doi: <https://doi.org/10.1002/anie.201410899>.

Mo, M. L., Palsson, B. Ø. and Herrgard, M. J. (2009) 'Connecting extracellular metabolomic measurements to intracellular flux states in yeast.', *BMC systems biology*, 3, p. 37. doi: 10.1186/1752-0509-3-37.

Mohan, S. V. *et al.* (2016) 'Waste biorefinery: a new paradigm for a sustainable bioelectro economy', *Trends in Biotechnology*, 34(11), pp. 852–855.

Mohsenpour, S. F., Richards, B. and Willoughby, N. (2012) 'Spectral conversion of light for enhanced microalgae growth rates and photosynthetic pigment production', *Bioresource Technology*, 125, pp. 75–81. doi: 10.1016/j.biortech.2012.08.072.

Montezano, D. *et al.* (2015) 'Flux Balance Analysis with Objective Function Defined by Proteomics Data—Metabolism of Mycobacterium tuberculosis Exposed to Mefloquine', *PLOS ONE*, 10(7), pp. 1–19. doi: 10.1371/journal.pone.0134014.

Mooij, T. De *et al.* (2016) 'Impact of light color on photobioreactor productivity', *Algal Research*, 15, pp. 32–42. doi: 10.1016/j.algal.2016.01.015.

Msanne, J *et al.* (2012) 'Metabolic and gene expression changes triggered by nitrogen deprivation in the photoautotrophically grown microalgae *Chlamydomonas reinhardtii* and *Coccomyxa* sp. C-169', *Phytochemistry*, 75. doi: 10.1016/j.phytochem.2011.12.007.

Msanne, Joseph *et al.* (2012) 'Metabolic and gene expression changes triggered by nitrogen deprivation in the photoautotrophically grown microalgae *Chlamydomonas reinhardtii* and *Coccomyxa* sp. C-169', *Phytochemistry*, 75, pp. 50–59. doi: 10.1016/j.phytochem.2011.12.007.

Muller-Feuga, A. *et al.* (2012) 'Appraisal of a horizontal two-phase flow photobioreactor for industrial production of delicate microalgae species', *Journal of Applied Phycology*, 24(3), pp. 349–355. doi: 10.1007/s10811-012-9820-6.

Müller, N. *et al.* (2017) 'A Plant Cryptochrome Controls Key Features of the *Chlamydomonas* Circadian Clock and Its Life Cycle', *Plant Physiology*, 174(1), pp. 185–201. doi: 10.1104/pp.17.00349.

Münzner, P. and Voigt, J. (1992) 'Blue Light Regulation of Cell Division in *Chlamydomonas reinhardtii*.', *Plant physiology*, 99(4), pp. 1370–1375. doi: 10.1104/PP.99.4.1370.

Nama, S. *et al.* (2019) 'Non-photochemical quenching-dependent acclimation and thylakoid organization of *Chlamydomonas reinhardtii* to high light stress', *Photosynthesis Research*, 139(1), pp. 387–400. doi: 10.1007/s11120-018-0551-7.

NOVAgreen (2016) *NOVAgreen Company Website*. Available at: <http://www.novagreen-microalgae.de/> (Accessed: 11 February 2016).

Nymark, M. *et al.* (2016) 'A CRISPR/Cas9 system adapted for gene editing in marine algae', *Scientific Reports*, 6(April), pp. 6–11. doi: 10.1038/srep24951.

Oldenhof, H. *et al.* (2004) 'Effect of red and blue light on the timing of cyclin-dependent kinase activity and the timing of cell division in *Chlamydomonas reinhardtii*', *Plant Physiology and Biochemistry*, 42(4), pp. 341–348. doi: 10.1016/j.plaphy.2004.02.002.

Oldenhof, H., Zachleder, V. and Van Den Ende, H. (2004a) 'Blue light delays commitment to cell division in *Chlamydomonas reinhardtii*', *Plant Biology*, 6(6), pp. 689–695. doi: 10.1055/s-2004-821341.

Oldenhof, H., Zachleder, V. and Van Den Ende, H. (2004b) 'Blue light delays commitment to cell division in *Chlamydomonas reinhardtii*', *Plant Biology*, 6(6), pp. 689–695. doi: 10.1055/s-2004-821341.

Oldenhof, H., Zachleder, V. and Van Den Ende, H. (2006) 'Blue- and red-light

regulation of the cell cycle in *Chlamydomonas reinhardtii* (Chlorophyta)', *European Journal of Phycology*, 41(3), pp. 313–320. doi: 10.1080/09670260600699920.

Oltra, C. (2011) 'Stakeholder perceptions of biofuels from microalgae', *Energy Policy*, 39(3), pp. 1774–1781. doi: <https://doi.org/10.1016/j.enpol.2011.01.009>.

Ooms, M. D. *et al.* (2016) 'Photon management for augmented photosynthesis', *Nature Communications*, 7, p. 12699. doi: 10.1038/ncomms12699.

Oren-Shamir, M., Pick, U. and Avron, M. (1990) 'Plasma membrane potential of the alga *Dunaliella*, and its relation to osmoregulation', *Plant physiology*, 93(2), pp. 403–408.

Oren, A. (2014) 'The ecology of *Dunaliella* in high-salt environments', *Journal of biological research (Thessalonike, Greece)*, 21(1), p. 23. doi: 10.1186/s40709-014-0023-y.

Orosa, M. *et al.* (2001) 'Comparison of the accumulation of astaxanthin in *Haematococcus pluvialis* and other green microalgae under N-starvation and high light conditions', *Biotechnology Letters*, 23(13), pp. 1079–1085.

Orth, J. D., Thiele, I. and Palsson, B. Ø. (2010) 'What is flux balance analysis?', *Nature Biotechnology*, 28(3), pp. 245–248. doi: 10.1038/nbt.1614.

Ow, D. S.-W. *et al.* (2009) 'Identification of cellular objective for elucidating the physiological state of plasmid-bearing *Escherichia coli* using genome-scale in silico analysis', *Biotechnology Progress*, 25(1), pp. 61–67. doi: 10.1002/btpr.51.

Panagopoulou, T. I. and Rafiq, Q. A. (2019) 'CAR-T immunotherapies: Biotechnological strategies to improve safety, efficacy and clinical outcome through CAR engineering', *Biotechnology Advances*, [In press]. doi: 10.1016/j.biotechadv.2019.06.010.

Park, J. B. K., Craggs, R. J. and Shilton, A. N. (2011) 'Wastewater treatment high rate algal ponds for biofuel production', *Bioresource Technology*, 102(1), pp. 35–42. doi: <http://dx.doi.org/10.1016/j.biortech.2010.06.158>.

Pattison, P. M. *et al.* (2018) 'LEDs for photons, physiology and food', *Nature*, 563(7732), pp. 493–500. doi: 10.1038/s41586-018-0706-x.

Peers, G. *et al.* (2009) 'An ancient light-harvesting protein is critical for the regulation of algal photosynthesis', *Nature*, 462(7272), pp. 518–521. doi: 10.1038/nature08587.

Pérez-López, P. *et al.* (2014) 'Life cycle assessment of the production of the red antioxidant carotenoid astaxanthin by microalgae: from lab to pilot scale', *Journal of Cleaner Production*, 64, pp. 332–344. doi: <https://doi.org/10.1016/j.jclepro.2013.07.011>.

Perrine, Z., Negi, S. and Sayre, R. T. (2012) 'Optimization of photosynthetic light energy utilization by microalgae', *Algal Research*, 1(2), pp. 134–142. doi: 10.1016/j.algal.2012.07.002.

Pfaffl, M. W. (2001) 'A new mathematical model for relative quantification in real-time RT-PCR.', *Nucleic acids research*, 29(9), p. e45. doi: 10.1093/nar/29.9.e45.

Plata, G. *et al.* (2010) 'Reconstruction and flux-balance analysis of the Plasmodium falciparum metabolic network', *Molecular Systems Biology*, 6(1), p. 408. doi: 10.1038/msb.2010.60.

Polle, J. E. W. *et al.* (2000) 'Photosynthetic apparatus organization and function in the wild type and a chlorophyll b-less mutant of Chlamydomonas reinhardtii. Dependence on carbon source', *Planta*, 211(3), pp. 335–344. doi: 10.1007/s004250000279.

Polle, J. E. W., Kanakagiri, S.-D. and Melis, A. (2003) 'tla1, a DNA insertional transformant of the green alga Chlamydomonas reinhardtii with a truncated light-harvesting chlorophyll antenna size', *Planta*, 217(1), pp. 49–59. doi: 10.1007/s00425-002-0968-1.

Price, N. D., Reed, J. L. and Palsson, B. Ø. (2004) 'Genome-scale models of microbial cells: evaluating the consequences of constraints', *Nature Reviews Microbiology*, 2(11), pp. 886–897. doi: 10.1038/nrmicro1023.

Proschold, T. *et al.* (2001) 'Molecular phylogeny and taxonomic revision of Chlamydomonas (Chlorophyta). I. Emendation of Chlamydomonas Ehrenberg and Chloromonas Gobi, and description of Oogamochlamys gen. nov. and Lobo-chlamys gen. nov.', *Protist*, 152(4), pp. 265–300. doi: 10.1078/1434-4610-00068.

Pröschold, T., Harris, E. H. and Coleman, A. W. (2005) 'Portrait of a species: Chlamydomonas reinhardtii', *Genetics*, 170(4), pp. 1601–1610. doi: 10.1534/genetics.105.044503.

Pushkareva, E., Johansen, J. R. and Elster, J. (2016) 'A review of the ecology, ecophysiology and biodiversity of microalgae in Arctic soil crusts', *Polar Biology*, 39(12), pp. 2227–2240. doi: 10.1007/s00300-016-1902-5.

Pyo Kim, J. *et al.* (2006) 'Enhanced hydrogen production by controlling light intensity in sulfur-deprived Chlamydomonas reinhardtii culture', *International Journal of Hydrogen Energy*, 31(11), pp. 1585–1590. doi: <https://doi.org/10.1016/j.ijhydene.2006.06.026>.

Qiu, R. *et al.* (2017) 'Effects of pH on cell growth, lipid production and CO<sub>2</sub> addition of microalgae Chlorella sorokiniana', *Algal Research*, 28, pp. 192–199. doi: <https://doi.org/10.1016/j.algal.2017.11.004>.

Raheem, A. *et al.* (2018) 'A review on sustainable microalgae based biofuel and bioenergy production: Recent developments', *Journal of cleaner production*, 181, pp. 42–59.

Ramanan, R. *et al.* (2013) 'Lipid droplet synthesis is limited by acetate availability in starchless mutant of Chlamydomonas reinhardtii', *FEBS Letters*, 587(4), pp. 370–377. doi: 10.1016/j.febslet.2012.12.020.

Ramirez, A. K. *et al.* (2017) 'Integrating Extracellular Flux Measurements and Genome-Scale Modeling Reveals Differences between Brown and White Adipocytes', *Cell Reports*, 21(11), pp. 3040–3048. doi: <https://doi.org/10.1016/j.celrep.2017.11.065>.

Rasala, B. A. *et al.* (2014) 'Enhanced genetic tools for engineering multigene traits into green algae', *PLoS ONE*, 9(4), p. e94028. doi: 10.1371/journal.pone.0094028.

Rasala, B. A. and Mayfield, S. P. (2015) 'Photosynthetic biomanufacturing in green algae; production of recombinant proteins for industrial, nutritional, and medical uses', *Photosynthesis research*, 123(3), pp. 227–239. doi: 10.1007/s11120-014-9994-7.

Rasala, B. a and Mayfield, S. P. (2010) 'The microalga *Chlamydomonas reinhardtii* as a platform for the production of human protein therapeutics.', *Bioengineered bugs*, 2(1), pp. 50–4. doi: 10.4161/bbug.2.1.13423.

Raven, J. A. (1974) 'Carbon dioxide fixation', in Stewart, W. D. P. (ed.) *Algal physiology and biochemistry*. 1st edn, pp. 434–449.

Raven, J. A. and Beardall, J. (2016) 'Dark Respiration and Organic Carbon Loss', in Borowitzka, M. A. and Raven, J. A. (eds) *The Physiology of Microalgae*. 1st edn. Springer, pp. 129–142.

Rayat, A. C. M. E. *et al.* (2016) 'Ultra scale-down approaches to enhance the creation of bioprocesses at scale: impacts of process shear stress and early recovery stages', *Current opinion in chemical engineering*, 14, pp. 150–157.

Rayat, A. C. M. E., Micheletti, M. and Lye, G. J. (2010) 'Evaluation of cell disruption effects on primary recovery of antibody fragments using microscale bioprocessing techniques.', *Biotechnology progress*, 26(5), pp. 1312–21. doi: 10.1002/btpr.450.

Reijnders, M. J. M. F. *et al.* (2014) 'Green genes: Bioinformatics and systems-biology innovations drive algal biotechnology', *Trends in Biotechnology*, 32(12), pp. 617–626. doi: 10.1016/j.tibtech.2014.10.003.

Richardson, J. W. *et al.* (2014) 'A financial assessment of two alternative cultivation systems and their contributions to algae biofuel economic viability', *Algal Research*, 4, pp. 96–104. doi: <http://dx.doi.org/10.1016/j.algal.2013.12.003>.

Riekhof, W. R. and Benning, C. (2009) 'Glycerolipid Biosynthesis', in Stern, D. B. (ed.) *The Chlamydomonas Sourcebook: Organellar and Metabolic Processes*. 2nd edn. Elsevier, pp. 41–69. doi: 10.1016/0092-8674(90)90467-S.

Roach, T., Sedoud, A. and Krieger-Liszkay, A. (2013) 'Acetate in mixotrophic growth



medium affects photosystem II in *Chlamydomonas reinhardtii* and protects against photoinhibition', *Biochimica et Biophysica Acta - Bioenergetics*, 1827(10), pp. 1183–1190. doi: 10.1016/j.bbabbio.2013.06.004.

Roberts, K. (1974) 'Crystalline Glycoprotein Cell Walls of Algae: Their Structure, Composition and Assembly', *Philosophical Transactions of the Royal Society B: Biological Sciences*, 268(891), pp. 129–146. doi: 10.1098/rstb.1974.0021.

Roberts, K., Gurney-Smith, M. and Hills, G. J. (1972) 'Structure, composition and morphogenesis of the cell wall of *Chlamydomonas reinhardtii*: I. Ultrastructure and preliminary chemical analysis', *Journal of ultrastructure research*, 40(5–6), pp. 599–613.

Rosic, N. N. *et al.* (2011) 'Validation of Housekeeping Genes for Gene Expression Studies in *Symbiodinium* Exposed to Thermal and Light Stress', *Marine Biotechnology*, 13(3), pp. 355–365. doi: 10.1007/s10126-010-9308-9.

Rubin, B. E. *et al.* (2015) 'The essential gene set of a photosynthetic organism', *Proceedings of the National Academy of Sciences*, 112(48), pp. E6634–E6643. doi: 10.1073/pnas.1519220112.

Sack, L. *et al.* (1994) 'Note. Isolation of four new strains of *Chlamydomonas reinhardtii* (chlorophyta) from soil samples.', *Journal of phycology*, 30(4), pp. 770–773.

Sager, R. and Granick, S. (1953) 'Nutritional studies with *Chlamydomonas reinhardtii*', *Annals of the New York Academy of Sciences*, 56(5), pp. 831–838. doi: 10.1111/j.1749-6632.1953.tb30261.x.

Santos, F., Boele, J. and Teusink, B. (2011) 'A Practical Guide to Genome-Scale Metabolic Models and Their Analysis', in *Methods in Systems Biology*. 1st edn. Elsevier Inc., pp. 509–532. doi: 10.1016/B978-0-12-385118-5.00024-4.

Sariyar, B. *et al.* (2006) 'Monte Carlo sampling and principal component analysis of flux distributions yield topological and modular information on metabolic networks', *Journal of Theoretical Biology*, 242(2), pp. 389–400. doi: 10.1016/j.jtbi.2006.03.007.

Sato, N. *et al.* (1996) 'Contribution of lowered unsaturation levels of chloroplast

lipids to high temperature tolerance of photosynthesis in *Chlamydomonas reinhardtii*', *Journal of Photochemistry and Photobiology B: Biology*, 36(3), pp. 333–337. doi: [https://doi.org/10.1016/S1011-1344\(96\)07389-7](https://doi.org/10.1016/S1011-1344(96)07389-7).

Schellenberger, J. and Palsson, B. (2009) 'Use of randomized sampling for analysis of metabolic networks', *Journal of Biological Chemistry*, 284(9), pp. 5457–5461. doi: 10.1074/jbc.R800048200.

Scherholz, M. L. and Curtis, W. R. (2013) 'Achieving pH control in microalgal cultures through fed-batch addition of stoichiometrically-balanced growth media.', *BMC biotechnology*, 13(1), p. 39. doi: 10.1186/1472-6750-13-39.

Schmollinger, S. *et al.* (2014) 'Nitrogen-sparing mechanisms in *Chlamydomonas* affect the transcriptome, the proteome, and photosynthetic metabolism', *Plant Cell*, 26(4), pp. 1410–1435. doi: 10.1105/tpc.113.122523.

Schroda, M., Blöcker, D. and Beck, C. F. (2000) 'The HSP70A promoter as a tool for the improved expression of transgenes in *Chlamydomonas*', *Plant Journal*, 21(2), pp. 121–131. doi: 10.1046/j.1365-3113X.2000.00652.x.

Schuetz, R., Kuepfer, L. and Sauer, U. (2007) 'Systematic evaluation of objective functions for predicting intracellular fluxes in *Escherichia coli*', *Molecular Systems Biology*, 3(119). doi: 10.1038/msb4100162.

Schulze, P. S. C. *et al.* (2014) 'Light emitting diodes (LEDs) applied to microalgal production', *Trends in Biotechnology*, 32(8), pp. 422–430. doi: 10.1016/j.tibtech.2014.06.001.

Scott, M. *et al.* (2010) 'Interdependence of cell growth and gene expression: origins and consequences', *Science*, 330(6007), pp. 1099–1102.

Sekimoto, H. (2017) 'Sexual reproduction and sex determination in green algae', *Journal of Plant Research*, 130(3), pp. 423–431. doi: 10.1007/s10265-017-0908-6.

Senge, M. and Senger, H. (1991) 'Adaptation of the Photosynthetic Apparatus of *Chlorella* and *Ankistrodesmus* to Blue and Red Light', *Botanica Acta*, 104(2), pp. 139–

143. doi: 10.1111/j.1438-8677.1991.tb00209.x.

Senger, R. S. (2010) 'Biofuel production improvement with genome-scale models: The role of cell composition', *Biotechnology Journal*, 5(7), pp. 671–685. doi: 10.1002/biot.201000007.

Senger, R. S. and Nazem-Bokaei, H. (2013) 'Resolving Cell Composition Through Simple Measurements, Genome-Scale Modeling, and a Genetic Algorithm', in Alper, H. S. (ed.) *Systems Metabolic Engineering: Methods and Protocols*. Totowa, NJ: Humana Press, pp. 85–101. doi: 10.1007/978-1-62703-299-5\_5.

Shastri, A. A. and Morgan, J. A. (2005) 'Flux balance analysis of photoautotrophic metabolism', *Biotechnology Progress*, 21(6), pp. 1617–1626. doi: 10.1021/bp050246d.

Shipley, G. L. (2006) 'An introduction to real-time PCR', in M, D. T. (ed.) *Real-Time PCR*. 1st edn. Taylor & Francis (Advanced Methods), pp. 1–37.

Shlomi, T. *et al.* (2011) 'Genome-scale metabolic modeling elucidates the role of proliferative adaptation in causing the Warburg effect', *PLoS Comput Biol*, 7(3), p. e1002018.

Siaut, M. *et al.* (2007) 'Molecular toolbox for studying diatom biology in *Phaeodactylum tricornutum*', *Gene*, 406(1–2), pp. 23–35. doi: 10.1016/j.gene.2007.05.022.

Siaut, M. *et al.* (2011) 'Oil accumulation in the model green alga *Chlamydomonas reinhardtii*: characterization, variability between common laboratory strains and relationship with starch reserves.', *BMC biotechnology*, 11(1), p. 7. doi: 10.1186/1472-6750-11-7.

Silverberg, B. A. (1975) 'An ultrastructural and cytochemical characterization of microbodies in the green algae', *Protoplasma*, 83(3), pp. 269–295. doi: 10.1007/BF01282559.

Sineshchekov, O. A., Jung, K.-H. and Spudis, J. L. (2002) 'Two rhodopsins mediate phototaxis to low- and high-intensity light in *Chlamydomonas reinhardtii*', *Proceedings*

of the *National Academy of Sciences*, 99(13), pp. 8689–8694. doi: 10.1073/pnas.122243399.

Singh, H. *et al.* (2014) 'Acetate and bicarbonate assimilation and metabolite formation in *Chlamydomonas reinhardtii*: A <sup>13</sup>C-NMR study', *PLoS ONE*, 9(9). doi: 10.1371/journal.pone.0106457.

Slocombe, S. P. *et al.* (2013) 'A rapid and general method for measurement of protein in micro-algal biomass', *Bioresource Technology*, 129, pp. 51–57. doi: 10.1016/j.biortech.2012.10.163.

Smith, R. T. and Gilmour, D. J. (2018) 'The influence of exogenous organic carbon assimilation and photoperiod on the carbon and lipid metabolism of *Chlamydomonas reinhardtii*', *Algal Research*, 31(January), pp. 122–137. doi: 10.1016/j.algal.2018.01.020.

Steinbrenner, J. and Linden, H. (2003) 'Light induction of carotenoid biosynthesis genes in the green alga *Haematococcus pluvialis*: regulation by photosynthetic redox control', *Plant Molecular Biology*, 52(2), pp. 343–356. doi: 10.1023/A:1023948929665.

Stephanopoulos, G. N., Aristidou, A. a and Nielsen, J. (1998) 'Chapter 10 - Applications of Metabolic Flux Analysis', *Metabolic Engineering: Principles and Methodologies*, pp. 411–459. doi: <http://dx.doi.org/10.1016/B978-012666260-3/50011-X>.

Stephenson, A. L. *et al.* (2010) 'Influence of nitrogen-limitation regime on the production by *Chlorella vulgaris* of lipids for biodiesel feedstocks', *Biofuels*, 1. doi: 10.4155/bfs.09.1.

Stothard, P. (2000) 'The Sequence Manipulation Suite: JavaScript programs for analyzing and formatting protein and DNA sequences', *Biotechniques*, 28, pp. 1102–1104.

Su, Yujie *et al.* (2017) 'Progress of microalgae biofuel's commercialization', *Renewable and Sustainable Energy Reviews*, 74, pp. 402–411. doi: <https://doi.org/10.1016/j.rser.2016.12.078>.

Suzuki, L. and Johnson, C. (2002) 'Photoperiodic control of germination in the unicell *Chlamydomonas*', *Naturwissenschaften*, 89(5), pp. 214–220. doi: 10.1007/s00114-002-0302-6.

Takache, H. *et al.* (2010) 'Experimental and theoretical assessment of maximum productivities for the microalgae *Chlamydomonas reinhardtii* in two different geometries of photobioreactors', *Biotechnology Progress*, 26(2), pp. 431–440. doi: 10.1002/btpr.356.

Takahashi, H. *et al.* (2013) 'Cyclic electron flow is redox-controlled but independent of state transition', *Nature Communications*, 4(1), p. 1954. doi: 10.1038/ncomms2954.

Taunt, H. N., Stoffels, L. and Purton, S. (2018) 'Green biologics: The algal chloroplast as a platform for making biopharmaceuticals', 5979. doi: 10.1080/21655979.2017.1377867.

Terashima, M. *et al.* (2010) 'Characterizing the Anaerobic Response of *Chlamydomonas reinhardtii* by Quantitative Proteomics', *Molecular & Cellular Proteomics*, 9(7), pp. 1514 LP – 1532. doi: 10.1074/mcp.M900421-MCP200.

Tibocha-Bonilla, J. D. *et al.* (2018) 'Advances in metabolic modeling of oleaginous microalgae', *Biotechnology for biofuels*, 11, p. 241. doi: 10.1186/s13068-018-1244-3.

Tollete, D. *et al.* (2011) 'Control of Hydrogen Photoproduction by the Proton Gradient Generated by Cyclic Electron Flow in *Chlamydomonas reinhardtii*', *The Plant Cell*, 23(7), pp. 2619 LP – 2630. doi: 10.1105/tpc.111.086876.

Tredici, M. R. and Rodolfi, L. (2004) 'Reactor for industrial culture of photosynthetic micro-organisms. PCT Patent WO2004/074423'. PCT Patent.

Turmel, M., Lemieux, C. and Lee, R. W. (1980) 'Net synthesis of chloroplast DNA throughout the synchronized vegetative cell-cycle of *Chlamydomonas*', *Current genetics*, 2(3), pp. 229–232.

Umen, J. G. and Goodenough, U. W. (2001) 'Chloroplast DNA methylation and inheritance in *Chlamydomonas*', *Genes & development*, 15(19), pp. 2585–2597. doi: 10.1101/gad.906701.

Untergasser, A. *et al.* (2012) 'Primer3-new capabilities and interfaces', *Nucleic Acids Research*, 40(15). doi: 10.1093/nar/gks596.

Del Val, I. J. *et al.* (2013) 'An optimized method for extraction and quantification of nucleotides and nucleotide sugars from mammalian cells', *Analytical Biochemistry*, 443(2), pp. 172–180. doi: 10.1016/j.ab.2013.09.005.

Valle, O., Lien, T. and Knutsen, G. (1981) 'Fluorometric determination of DNA and RNA in *Chlamydomonas* using ethidium bromide', *Journal of Biochemical and Biophysical Methods*, 4, pp. 271–277.

Vandesompele, J. *et al.* (2002) 'Accurate normalization of real-time quantitative RT-PCR data by geometric averaging of multiple internal control genes.', *Genome biology*, 3(7), p. research0034.1. doi: 10.1186/gb-2002-3-7-research0034.

Vitova, M. *et al.* (2011) '*Chlamydomonas reinhardtii*: Duration of its cell cycle and phases at growth rates affected by light intensity', *Planta*, 233(1), pp. 75–86. doi: 10.1007/s00425-010-1282-y.

Vladimirova, M. G., Markelova, A. G. and Semenenko, B. E. (1982) 'Use of the cytoimmunofluorescent method to clarify localization of ribulose biphosphate carboxylase in pyrenoids of unicellular algae', *Sov. Plant Physiol*, 29, pp. 725–734.

Vothknecht, U. C. and Westhoff, P. (2001) 'Biogenesis and origin of thylakoid membranes', *Biochimica et Biophysica Acta (BBA) - Molecular Cell Research*, 1541(1–2), pp. 91–101. doi: [http://dx.doi.org/10.1016/S0167-4889\(01\)00153-7](http://dx.doi.org/10.1016/S0167-4889(01)00153-7).

Voulgaris, I. *et al.* (2016) 'Evaluation of options for harvest of a recombinant E. Coli fermentation producing a domain antibody using ultra scale-down techniques and pilot-scale verification', *Biotechnology Progress*, 32(2), pp. 382–392.

Wagner, H. *et al.* (2010) 'The use of FTIR spectroscopy to assess quantitative

changes in the biochemical composition of microalgae', *Journal of Biophotonics*, 3(8–9), pp. 557–566. doi: 10.1002/jbio.201000019.

Wagner, I. and Posten, C. (2017) 'Pressure reduction affects growth and morphology of *Chlamydomonas reinhardtii*', *Engineering in Life Sciences*, 17(5), pp. 552–560. doi: 10.1002/elsc.201600131.

Wagner, I., Steinweg, C. and Posten, C. (2016) 'Mono- and dichromatic LED illumination leads to enhanced growth and energy conversion for high-efficiency cultivation of microalgae for application in space', *Biotechnology Journal*, 11(8), pp. 1060–1071. doi: 10.1002/biot.201500357.

Wang, H. *et al.* (2014) 'The global phosphoproteome of *chlamydomonas reinhardtii* reveals complex organellar phosphorylation in the flagella and thylakoid membrane', *Molecular and Cellular Proteomics*, 13(9), pp. 2337–2353. doi: 10.1074/mcp.M114.038281.

Wang, S. K. *et al.* (2014) 'Microalgae cultivation in photobioreactors: An overview of light characteristics', *Engineering in Life Sciences*, 14(6), pp. 550–559. doi: 10.1002/elsc.201300170.

Wang, Z. T. *et al.* (2009) 'Algal Lipid Bodies: Stress Induction, Purification, and Biochemical Characterization in Wild-Type and Starchless *Chlamydomonas reinhardtii*', *Eukaryotic Cell*, 8(12), pp. 1856–1868. doi: 10.1128/EC.00272-09.

Wellburn, A. R. (1987) 'Plastids A2 - BOURNE, G.H. BT - Cytology and Cell Physiology (Fourth Edition)', in. San Diego: Academic Press, pp. 149–210. doi: <http://dx.doi.org/10.1016/B978-0-08-091882-2.50009-9>.

Wellburn, A. R. (1994) 'The spectral determination of chlorophylls a and b, as well as total carotenoids, using various solvents with spectrophotometers of different resolution', *Journal of Plant Physiology*, 144, pp. 307–313.

Wichmann, J., Baier, T., Wentnagel, E., Lauersen, Kyle J., *et al.* (2018) 'Tailored carbon partitioning for phototrophic production of (E)- $\alpha$ -bisabolene from the green microalga *Chlamydomonas reinhardtii*', *Metabolic Engineering*, 45(November 2017), pp.

211–222. doi: 10.1016/j.ymben.2017.12.010.

Wichmann, J., Baier, T., Wentnagel, E., Lauersen, Kyle J, *et al.* (2018) 'Tailored carbon partitioning for phototrophic production of (E)- $\alpha$ -bisabolene from the green microalga *Chlamydomonas reinhardtii*', *Metabolic Engineering*, 45, pp. 211–222. doi: <https://doi.org/10.1016/j.ymben.2017.12.010>.

Wilhelm, C., Kramer, P. and Wild, a (1985) 'Effect of Different Light Qualities on the Ultrastructure, Thylakoid Membrane-Composition and Assimilation Metabolism of *Chlorella-Fusca*', *Physiologia Plantarum*, 64(3), pp. 359–364.

Williams, P. J. le B. and Laurens, L. M. L. (2010) 'Microalgae as biodiesel & biomass feedstocks: Review & analysis of the biochemistry, energetics & economics', *Energy & Environmental Science*, 3(5), p. 554. doi: 10.1039/b924978h.

Wiltbank, L. B. and Kehoe, D. M. (2016) 'Two cyanobacterial photoreceptors regulate photosynthetic light harvesting by sensing teal, green, yellow, and red light', *mBio*, 7(1), pp. 1–8. doi: 10.1128/mBio.02130-15.

Winck, F. V., Páez Melo, D. O. and González Barrios, A. F. (2013) 'Carbon acquisition and accumulation in microalgae *Chlamydomonas*: Insights from “omics” approaches', *Journal of Proteomics*, 94, pp. 207–218. doi: 10.1016/j.jprot.2013.09.016.

de Winter, L. *et al.* (2017) 'The influence of day/night cycles on biomass yield and composition of *Neochloris oleoabundans*', *Biotechnology for biofuels*, 10(1), p. 104.

Winwood, R. J. (2013) 'Recent developments in the commercial production of DHA and EPA rich oils from micro-algae', *Oilseeds and fats Crops and Lipids*, 20(6).

Worley, B., Halouska, S. and Powers, R. (2013) 'Utilities for quantifying separation in PCA/PLS-DA scores plots', *Analytical biochemistry*, 433(2), pp. 102–104.

Wu, C. *et al.* (2015) 'Genome-based metabolic mapping and  $^{13}\text{C}$  flux analysis reveal systematic properties of an oleaginous microalga *Chlorella protothecoides*.', *Plant physiology*, 167(2), pp. 586–99. doi: 10.1104/pp.114.250688.

Xia, J.-R. and Gao, K.-S. (2005) 'Impacts of Elevated  $\text{CO}_2$  Concentration on



Biochemical Composition, Carbonic Anhydrase, and Nitrate Reductase Activity of Freshwater Green Algae', *Journal of Integrative Plant Biology*, 47(6), pp. 668–675. doi: 10.1111/j.1744-7909.2005.00114.x.

Xu, Y. and Harvey, P. J. (2019a) 'Carotenoid production by *Dunaliella salina* under red light', *Antioxidants*, 8(5). doi: 10.3390/antiox8050123.

Xu, Y. and Harvey, P. J. (2019b) 'Red Light Control of  $\beta$ -Carotene Isomerisation to 9-cis  $\beta$ -Carotene and Carotenoid Accumulation in *Dunaliella salina*', *Antioxidants*, 8(5), p. 148. doi: 10.3390/antiox8050148.

Yadav, G., Dubey, B. K. and Sen, R. (2020) 'A comparative life cycle assessment of microalgae production by CO<sub>2</sub> sequestration from flue gas in outdoor raceway ponds under batch and semi-continuous regime', *Journal of Cleaner Production*, 258, p. 120703. doi: <https://doi.org/10.1016/j.jclepro.2020.120703>.

Yan, C. *et al.* (2016) 'The effects of various LED (light emitting diode) lighting strategies on simultaneous biogas upgrading and biogas slurry nutrient reduction by using of microalgae *Chlorella* sp.', *Energy*, 106, pp. 554–561. doi: <https://doi.org/10.1016/j.energy.2016.03.033>.

Yang, C., Hua, Q. and Shimizu, K. (2000) 'Energetics and carbon metabolism during growth of microalgal cells under photoautotrophic, mixotrophic and cyclic light-autotrophic/dark-heterotrophic conditions', *Biochemical Engineering Journal*, 6(2), pp. 87–102. doi: [https://doi.org/10.1016/S1369-703X\(00\)00080-2](https://doi.org/10.1016/S1369-703X(00)00080-2).

Yuan, H. *et al.* (2016) 'Flux balance analysis of plant metabolism: the effect of biomass composition and model structure on model predictions', *Frontiers in plant science*, 7, p. 537.

Yusa, F., Steiner, J. M. and Löffelhardt, W. (2008) 'Evolutionary conservation of dual Sec translocases in the cyanelles of *Cyanophora paradoxa*', *BMC Evolutionary Biology*, p. 304. doi: 10.1186/1471-2148-8-304.

Zittelli, G. C. *et al.* (2013) 'Photobioreactors for Mass Production of Microalgae', in John Wiley & Sons Ltd (ed.) *Handbook of Microalgal Culture: Applied Phycology and*

*Biotechnology*. 2nd edn. Blackwell Publishing Ltd, pp. 225–266. doi: 10.1002/2F9781118567166.

Zones, J. M. *et al.* (2015) 'High-resolution profiling of a synchronized diurnal transcriptome from *Chlamydomonas reinhardtii* reveals continuous cell and metabolic differentiation', *Plant Cell*, 27(10), pp. 2743–2769. doi: 10.1105/tpc.15.00498.

Zuñiga, C. *et al.* (2016) 'Genome-scale metabolic model for the green alga *Chlorella vulgaris* UTEX 395 accurately predicts phenotypes under autotrophic, heterotrophic, and mixotrophic growth conditions', *Plant physiology*, 172(1), pp. 589–602.

## Appendix I

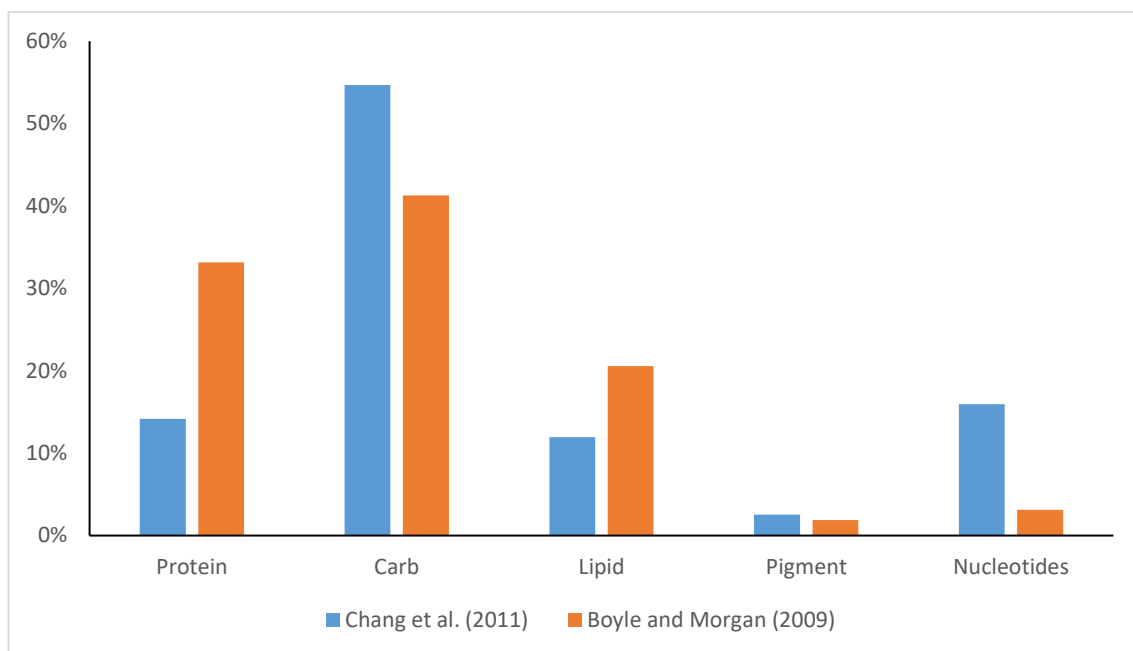


**Figure I.1** Disparity in published *C. reinhardtii* GeM biomass equation compositions.

## Appendix II

**Table II.1** FBA constraints used to simulate autotrophic conditions under different illumination conditions.

Reaction	Lower bound	Upper bound
	(mmol gDW <sup>-1</sup> h <sup>-1</sup> ) (μmax in h <sup>-1</sup> )	
White Phototrophic		
White_Light	115	202
'EX_nh4(e)'	-0.306	-0.291
'EX_co2(e)'	-4.06	-3.32
Biomass_Chlamy_auto	0.069	0.076
Red Phototrophic		
Red_Light	45.0	116
'EX_nh4(e)'	-0.238	-0.211
'EX_co2(e)'	-4.06	-3.32
Biomass_Chlamy_auto	0.054	0.056
Blue Phototrophic		
Blue_Light	89.9	398
'EX_nh4(e)'	-0.451	-0.418
'EX_co2(e)'	-4.06	-3.32
Biomass_Chlamy_auto	0.040	0.042

**Table II.2** FBA constraints used to simulate mixotrophic conditions under different illumination conditions.

Reaction name	Lower bound	Upper bound
	(mmol gDW <sup>-1</sup> h <sup>-1</sup> ) (μmax in h <sup>-1</sup> )	
White Mixotrophic		
White_Light	130	380
'EX_nh4(e)'	-2.87	-2.36
'EX_co2(e)'	-4.06	-3.32
EX_ac(e)	-4.38	-2.39
Biomass_Chlamy_mixo	0.064	0.074
Red Mixotrophic		
Red_Light	42.4	117
'EX_nh4(e)'	-1.27	-1.08
'EX_co2(e)'	-4.06	-3.32
EX_ac(e)	-0.730	-0.717
Biomass_Chlamy_mixo	0.055	0.056
Blue Mixotrophic		
Blue_Light	38.8	124
'EX_nh4(e)'	-1.78	-1.24
'EX_co2(e)'	-4.06	-3.32
EX_ac(e)	-3.00	-2.43
Biomass_Chlamy_mixo	0.050	0.056

## Appendix III

**Table III.1** Original autotrophic and mixotrophic growth biomass equations in iRC1080.

MetID	Stoich Auto	StoichMixo	Group
arab-L[c]	-5.2E-01	-5.2E-01	Carbohydrate
gal[c]	-7.0E-01	-7.0E-01	Carbohydrate
man[c]	-3.3E-01	-3.3E-01	Carbohydrate
starch300[h]	-6.4E-03	-6.4E-03	Carbohydrate
chla[u]	-1.0E-02	-7.8E-03	Chlorophyll A
chlb[u]	-1.7E-02	-1.4E-02	Chlorophyll B
datp[c]	-2.2E-03	-2.2E-03	DNA
dctp[c]	-3.9E-03	-3.9E-03	DNA
dgtp[c]	-3.9E-03	-3.9E-03	DNA
dttp[c]	-2.2E-03	-2.2E-03	DNA
glyc[c]	-1.2E-02	-1.2E-02	Glycerol
asqdca18111Z160[c]	-1.2E-03	-1.2E-03	Lipid
asqdca1819Z160[c]	-1.2E-03	-1.2E-03	Lipid
asqdca1829Z12Z160[c]	-1.2E-03	-1.2E-03	Lipid
asqdca1839Z12Z15Z160[c]	-1.2E-03	-1.2E-03	Lipid
asqdpa18111Z160[c]	-1.2E-03	-1.2E-03	Lipid
asqdpa1819Z160[c]	-1.2E-03	-1.2E-03	Lipid
asqdpa1829Z12Z160[c]	-1.2E-03	-1.2E-03	Lipid
asqdpa1839Z12Z15Z160[c]	-1.2E-03	-1.2E-03	Lipid
dgdg1819Z160[h]	-1.7E-03	-1.7E-03	Lipid
dgdg1819Z1617Z[h]	-3.0E-04	-3.0E-04	Lipid
dgdg1819Z1619Z[h]	-3.0E-04	-3.0E-04	Lipid
dgdg1819Z1627Z10Z[h]	-4.0E-04	-4.0E-04	Lipid
dgdg1819Z1634Z7Z10Z[h]	-2.0E-04	-2.0E-04	Lipid
dgdg1819Z1637Z10Z13Z[h]	-2.0E-04	-2.0E-04	Lipid
dgdg1829Z12Z160[h]	-3.3E-03	-3.3E-03	Lipid
dgdg1829Z12Z1617Z[h]	-3.0E-04	-3.0E-04	Lipid
dgdg1829Z12Z1619Z[h]	-3.0E-04	-3.0E-04	Lipid
dgdg1829Z12Z1627Z10Z[h]	-5.4E-04	-5.4E-04	Lipid
dgdg1829Z12Z1634Z7Z10Z[h]	-2.7E-04	-2.7E-04	Lipid
dgdg1829Z12Z1637Z10Z13Z[h]	-2.7E-04	-2.7E-04	Lipid
dgdg1839Z12Z15Z160[h]	-2.4E-03	-2.4E-03	Lipid

dgdg1839Z12Z15Z1627Z10Z[h]	-5.4E-04	-5.4E-04	Lipid
dgdg1839Z12Z15Z1634Z7Z10Z[h]	-7.4E-04	-7.4E-04	Lipid
dgdg1839Z12Z15Z1637Z10Z13Z[h]	-7.4E-04	-7.4E-04	Lipid
dgdg1839Z12Z15Z1644Z7Z10Z13Z[h]	-2.7E-04	-2.7E-04	Lipid
dgts16018111Z[c]	-7.7E-05	-7.7E-05	Lipid
dgts1601819Z[c]	-7.7E-05	-7.7E-05	Lipid
dgts1601829Z12Z[c]	-1.1E-03	-1.1E-03	Lipid
dgts1601835Z9Z12Z[c]	-3.9E-03	-3.9E-03	Lipid
dgts1601845Z9Z12Z15Z[c]	-2.1E-03	-2.1E-03	Lipid
dgts18111Z18111Z[c]	-7.4E-05	-7.4E-05	Lipid
dgts18111Z1819Z[c]	-7.4E-05	-7.4E-05	Lipid
dgts18111Z1829Z12Z[c]	-2.0E-04	-2.0E-04	Lipid
dgts18111Z1835Z9Z12Z[c]	-4.0E-04	-4.0E-04	Lipid
dgts18111Z1845Z9Z12Z15Z[c]	-2.7E-04	-2.7E-04	Lipid
dgts1819Z18111Z[c]	-7.4E-05	-7.4E-05	Lipid
dgts1819Z1819Z[c]	-7.4E-05	-7.4E-05	Lipid
dgts1819Z1829Z12Z[c]	-2.0E-04	-2.0E-04	Lipid
dgts1819Z1835Z9Z12Z[c]	-4.0E-04	-4.0E-04	Lipid
dgts1819Z1845Z9Z12Z15Z[c]	-2.7E-04	-2.7E-04	Lipid
dgts1829Z12Z18111Z[c]	-7.5E-05	-7.5E-05	Lipid
dgts1829Z12Z1819Z[c]	-7.5E-05	-7.5E-05	Lipid
dgts1829Z12Z1829Z12Z[c]	-4.0E-04	-4.0E-04	Lipid
dgts1829Z12Z1835Z9Z12Z[c]	-1.6E-03	-1.6E-03	Lipid
dgts1829Z12Z1845Z9Z12Z15Z[c]	-7.5E-05	-7.5E-05	Lipid
dgts1839Z12Z15Z18111Z[c]	-3.4E-04	-3.4E-04	Lipid
dgts1839Z12Z15Z1819Z[c]	-3.4E-04	-3.4E-04	Lipid
dgts1839Z12Z15Z1835Z9Z12Z[c]	-1.1E-03	-1.1E-03	Lipid
dgts1839Z12Z15Z1845Z9Z12Z15Z[c]	-4.1E-04	-4.1E-04	Lipid
mgdg1829Z12Z160[h]	-2.0E-04	-2.0E-04	Lipid
mgdg1829Z12Z1617Z[h]	-2.0E-04	-2.0E-04	Lipid
mgdg1829Z12Z1619Z[h]	-2.0E-04	-2.0E-04	Lipid
mgdg1829Z12Z1627Z10Z[h]	-4.0E-04	-4.0E-04	Lipid
mgdg1829Z12Z1634Z7Z10Z[h]	-4.0E-04	-4.0E-04	Lipid
mgdg1829Z12Z1637Z10Z13Z[h]	-4.0E-04	-4.0E-04	Lipid
mgdg1829Z12Z1644Z7Z10Z13Z[h]	-3.2E-03	-3.2E-03	Lipid
mgdg1839Z12Z15Z160[h]	-2.0E-04	-2.0E-04	Lipid
mgdg1839Z12Z15Z1627Z10Z[h]	-4.0E-04	-4.0E-04	Lipid
mgdg1839Z12Z15Z1634Z7Z10Z[h]	-3.2E-03	-3.2E-03	Lipid
mgdg1839Z12Z15Z1637Z10Z13Z[h]	-3.2E-03	-3.2E-03	Lipid
mgdg1839Z12Z15Z1644Z7Z10Z13Z[h]	-2.8E-02	-2.8E-02	Lipid

pail18111Z160[c]	-1.9E-03	-1.9E-03	Lipid
pail1819Z160[c]	-2.6E-04	-2.6E-04	Lipid
pe1801835Z9Z12Z[c]	-2.3E-03	-2.3E-03	Lipid
pe1801845Z9Z12Z15Z[c]	-6.5E-04	-6.5E-04	Lipid
pe18111Z1835Z9Z12Z[c]	-3.1E-03	-3.1E-03	Lipid
pe18111Z1845Z9Z12Z15Z[c]	-1.3E-04	-1.3E-04	Lipid
pe1819Z1835Z9Z12Z[c]	-9.4E-05	-9.4E-05	Lipid
pe1819Z1845Z9Z12Z15Z[c]	-3.9E-06	-3.9E-06	Lipid
pe1829Z12Z1835Z9Z12Z[c]	-2.0E-04	-2.0E-04	Lipid
pg18111Z160[h]	-6.1E-04	-6.1E-04	Lipid
pg18111Z1613E[h]	-4.5E-04	-4.5E-04	Lipid
pg1819Z160[h]	-6.1E-04	-6.1E-04	Lipid
pg1819Z1613E[h]	-4.5E-04	-4.5E-04	Lipid
pg1829Z12Z160[h]	-7.4E-04	-7.4E-04	Lipid
pg1829Z12Z1613E[h]	-3.4E-03	-3.4E-03	Lipid
pg1839Z12Z15Z160[h]	-7.4E-04	-7.4E-04	Lipid
pg1839Z12Z15Z1613E[h]	-1.2E-03	-1.2E-03	Lipid
sqdg160[h]	-2.4E-03	-2.4E-03	Lipid
sqdg18111Z160[h]	-4.8E-04	-4.8E-04	Lipid
sqdg1819Z160[h]	-4.8E-04	-4.8E-04	Lipid
sqdg1829Z12Z160[h]	-7.3E-04	-7.3E-04	Lipid
sqdg1839Z12Z15Z160[h]	-7.8E-04	-7.8E-04	Lipid
tag16018111Z160[c]	-1.3E-03	-1.3E-03	Lipid
tag16018111Z180[c]	-1.3E-03	-1.3E-03	Lipid
tag16018111Z18111Z[c]	-1.3E-03	-1.3E-03	Lipid
tag16018111Z1819Z[c]	-1.3E-03	-1.3E-03	Lipid
tag16018111Z1835Z9Z12Z[c]	-1.3E-03	-1.3E-03	Lipid
tag16018111Z1845Z9Z12Z15Z[c]	-1.3E-03	-1.3E-03	Lipid
tag1601819Z160[c]	-1.3E-03	-1.3E-03	Lipid
tag1601819Z180[c]	-1.3E-03	-1.3E-03	Lipid
tag1601819Z18111Z[c]	-1.3E-03	-1.3E-03	Lipid
tag1601819Z1819Z[c]	-1.3E-03	-1.3E-03	Lipid
tag1601819Z1835Z9Z12Z[c]	-1.3E-03	-1.3E-03	Lipid
tag1601819Z1845Z9Z12Z15Z[c]	-1.3E-03	-1.3E-03	Lipid
tag1801819Z160[c]	-1.3E-03	-1.3E-03	Lipid
tag1801819Z180[c]	-1.2E-03	-1.2E-03	Lipid
tag1801819Z18111Z[c]	-1.2E-03	-1.2E-03	Lipid
tag1801819Z1819Z[c]	-1.2E-03	-1.2E-03	Lipid
tag1801819Z1835Z9Z12Z[c]	-1.3E-03	-1.3E-03	Lipid
tag1801819Z1845Z9Z12Z15Z[c]	-1.3E-03	-1.3E-03	Lipid



tag18111Z18111Z160[c]	-1.3E-03	-1.3E-03	Lipid
tag18111Z18111Z180[c]	-1.2E-03	-1.2E-03	Lipid
tag18111Z18111Z18111Z[c]	-1.3E-03	-1.3E-03	Lipid
tag18111Z18111Z1819Z[c]	-1.3E-03	-1.3E-03	Lipid
tag18111Z18111Z1835Z9Z12Z[c]	-1.3E-03	-1.3E-03	Lipid
tag18111Z18111Z1845Z9Z12Z15Z[c]	-1.3E-03	-1.3E-03	Lipid
tag18111Z1819Z160[c]	-1.3E-03	-1.3E-03	Lipid
tag18111Z1819Z180[c]	-1.2E-03	-1.2E-03	Lipid
tag18111Z1819Z18111Z[c]	-1.3E-03	-1.3E-03	Lipid
tag18111Z1819Z1819Z[c]	-1.3E-03	-1.3E-03	Lipid
tag18111Z1819Z1835Z9Z12Z[c]	-1.3E-03	-1.3E-03	Lipid
tag18111Z1819Z1845Z9Z12Z15Z[c]	-1.3E-03	-1.3E-03	Lipid
tag1819Z18111Z160[c]	-1.3E-03	-1.3E-03	Lipid
tag1819Z18111Z180[c]	-1.2E-03	-1.2E-03	Lipid
tag1819Z18111Z18111Z[c]	-1.3E-03	-1.3E-03	Lipid
tag1819Z18111Z1819Z[c]	-1.3E-03	-1.3E-03	Lipid
tag1819Z18111Z1835Z9Z12Z[c]	-1.3E-03	-1.3E-03	Lipid
tag1819Z18111Z1845Z9Z12Z15Z[c]	-1.3E-03	-1.3E-03	Lipid
tag1819Z1819Z160[c]	-1.3E-03	-1.3E-03	Lipid
tag1819Z1819Z180[c]	-1.2E-03	-1.2E-03	Lipid
tag1819Z1819Z18111Z[c]	-1.3E-03	-1.3E-03	Lipid
tag1819Z1819Z1819Z[c]	-1.3E-03	-1.3E-03	Lipid
tag1819Z1819Z1835Z9Z12Z[c]	-1.3E-03	-1.3E-03	Lipid
tag1819Z1819Z1845Z9Z12Z15Z[c]	-1.3E-03	-1.3E-03	Lipid
acaro[h]	-5.0E-04	-4.0E-06	Pigment
anxan[u]	-1.0E-04	-7.9E-07	Pigment
caro[u]	-1.4E-03	-1.1E-05	Pigment
loroxan[u]	-6.6E-04	-5.1E-06	Pigment
lut[u]	-1.3E-03	-9.9E-06	Pigment
neoxan[u]	-5.5E-04	-4.3E-06	Pigment
vioxan[u]	-3.5E-04	-2.8E-06	Pigment
zaxan[u]	-3.0E-04	-2.4E-06	Pigment
ala-L[c]	-2.7E-01	-2.8E-01	Protein
arg-L[c]	-1.5E-01	-9.4E-02	Protein
asn-L[c]	-6.8E-02	-7.0E-02	Protein
asp-L[c]	-6.8E-02	-7.0E-02	Protein
cys-L[c]	-2.4E-03	-1.2E-02	Protein
gln-L[c]	-8.1E-02	-9.2E-02	Protein
glu-L[c]	-8.1E-02	-9.2E-02	Protein
gly[c]	-1.0E-01	-1.1E-01	Protein

his-L[c]	-1.2E-03	-1.3E-02	Protein
ile-L[c]	-3.3E-02	-3.8E-02	Protein
leu-L[c]	-8.2E-02	-9.3E-02	Protein
lys-L[c]	-1.8E-02	-3.1E-02	Protein
met-L[c]	-2.4E-03	-1.3E-02	Protein
phe-L[c]	-3.4E-02	-4.0E-02	Protein
pro-L[c]	-4.7E-02	-5.2E-02	Protein
rhodopsin[s]	-1.0E-06	-1.0E-06	Protein
ser-L[c]	-2.1E-02	-2.1E-02	Protein
thr-L[c]	-8.2E-02	-3.5E-02	Protein
trp-L[c]	-1.2E-03	-1.6E-03	Protein
tyr-L[c]	-1.2E-03	-1.6E-03	Protein
val-L[c]	-5.9E-02	-6.4E-02	Protein
ctp[c]	-1.0E-01	-1.0E-01	RNA
gtp[c]	-1.0E-01	-1.0E-01	RNA
utp[c]	-5.9E-02	-5.9E-02	RNA
ac[c]	-3.7E-02	-3.7E-02	VFA
but[c]	-2.5E-02	-2.5E-02	VFA
ppa[c]	-3.0E-02	-3.0E-02	VFA

## Appendix IV

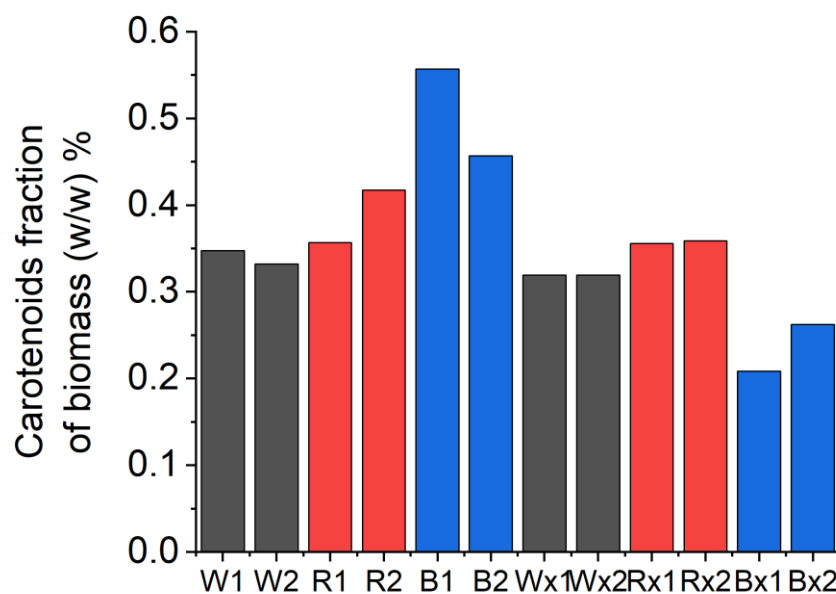


**Figure IV.1** *C. reinhardtii* carotenoids fraction as a percentage of biomass dry weight (w/w) at 48 hours of batch culture. (A) Phototrophic batch cultures in M8a. (B) Mixotrophic batch cultures in M8a.Ac. Biological replicates plotted individually (Flask A – 1. Flask B – 2). W, white LED light; R, red LED light; B, blue LED light.

## Appendix V

**Table V.1** All 161 biomass precursor synthesis related reactions identified in the top loadings of PCA of WA OGBM / WA BMO.

SS	RXNname
Fatty acid biosynthesis	'3-hydroxyacyl-[acyl-carrier-protein] dehydratase (n-C18:0)'
Fatty acid biosynthesis	'3-hydroxyacyl-[acyl-carrier-protein] dehydratase ((11Z)-n-C18:1)'
Fatty acid biosynthesis	'3-oxoacyl-[acyl-carrier-protein] reductase (n-C18:0)'
Fatty acid biosynthesis	'3-oxoacyl-[acyl-carrier-protein] reductase ((11Z)-n-C18:1)'
Fatty acid biosynthesis	'3-oxoacyl-[acyl-carrier-protein] synthase (n-C18:0)'
Fatty acid biosynthesis	'3-oxoacyl-[acyl-carrier-protein] synthase ((11Z)-n-C18:1)'
Fatty acid metabolism	'Acetyl-CoA:acetyl-CoA C-acetyltransferase'
Fatty acid metabolism	'butanoyl-CoA:acetyl-CoA C-butanoyltransferase'
Fatty acid metabolism	'Hexanoyl-CoA:acetyl-CoA C-acyltransferase'
Fatty acid metabolism	'Octanoyl-CoA:acetyl-CoA C-acyltransferase'
Fatty acid metabolism	'Decanoyl-CoA:acetyl-CoA C-acyltransferase'
Fatty acid metabolism	'Lauroyl-CoA:acetyl-CoA C-acyltransferase'
Fatty acid metabolism	'myristoyl-CoA:acetylCoA C-myristoyltransferase'
Fatty acid metabolism	'Decanoyl-CoA:(acceptor) 2,3-oxidoreductase'
Fatty acid metabolism	'Lauroyl-CoA:(acceptor) 2,3-oxidoreductase'
Fatty acid metabolism	'Tetradecanoyl-CoA:(acceptor) 2,3-oxidoreductase'
Fatty acid metabolism	'Palmitoyl-CoA:oxygen 2-oxidoreductase'
Fatty acid metabolism	'Butanoyl-CoA:oxygen 2-oxidoreductase'
Fatty acid metabolism	'Hexanoyl-CoA:(acceptor) 2,3-oxidoreductase'
Fatty acid metabolism	'Octanoyl-CoA:oxygen 2-oxidoreductase'
Fatty acid biosynthesis	'acyl-[acyl-carrier-protein] delta9-desaturase ((9Z)-n-C16:1)'
Fatty acid biosynthesis	'stearoyl-[acyl-carrier-protein] delta9-desaturase ((9Z)-n-C18:1)'
Glycerolipid metabolism	'betaine lipid synthase (3-amino-3-carboxypropyltransferase) (16:0/18:1(11Z))'
Glycerolipid metabolism	'betaine lipid synthase (3-amino-3-carboxypropyltransferase) (16:0/18:1(9Z))'
Glycerolipid metabolism	'betaine lipid synthase (3-amino-3-carboxypropyltransferase) (18:1(11Z)/18:1(11Z))'
Glycerolipid metabolism	'betaine lipid synthase (3-amino-3-carboxypropyltransferase) (18:1(11Z)/18:1(9Z))'
Glycerolipid metabolism	'betaine lipid synthase (3-amino-3-carboxypropyltransferase) (18:1(9Z)/18:1(11Z))'

Glycerolipid metabolism	'betaine lipid synthase (3-amino-3-carboxypropyltransferase) (18:1(9Z)/18:1(9Z))'
Riboflavin metabolism	'ATP:FMN adenylyltransferase'
Glycerolipid metabolism	'1-hexadecanoyl-sn-glycerol 3-phosphate O-acyltransferase (n-C16:0) (ACP substrate)'
Glycerolipid metabolism	'1-octadec-11-enoyl-sn-glycerol 3-phosphate O-acyltransferase (n-C16:0) (ACP substrate)'
Glycerolipid metabolism	'1-octadec-9-enoyl-sn-glycerol 3-phosphateO-acyltransferase (n-C16:0) (ACP substrate)'
Glycerolipid metabolism	'1-octadec-9-enoyl-sn-glycerol 3-phosphateO-acyltransferase ((9Z)-C16:1) (ACP substrate)'
Purine metabolism	'1-(5''-Phosphoribosyl)-5-amino-4-(N-succinocarboxamide)-imidazole AMP-lyase'
Pyrimidine metabolism	'aspartate carbamoyltransferase, mitochondria'
Glycerolipid metabolism	'oleate desaturase (2''-18:4(5Z,9Z,12Z,15Z)/18:2(9Z,12Z)/16:0)'
Glycerolipid metabolism	'linoleate desaturase (2''-18:4(5Z,9Z,12Z,15Z)/18:3(9Z,12Z,15Z)/16:0)'
Glycerolipid metabolism	'oleate desaturase (2''-18:3(5Z,9Z,12Z)/18:2(9Z,12Z)/16:0)'
Glycerolipid metabolism	'linoleate desaturase (2''-18:3(5Z,9Z,12Z)/18:3(9Z,12Z,15Z)/16:0)'
Purine metabolism	'allantoin synthetase'
Butanoate metabolism	'butanoyl-CoA:acetate CoA transferase'
Glycerophospholipid metabolism	'CDP-diacylglycerol: myo-inositol 3-phosphatidyltransferase (18:1(11Z)/16:0)'
Glycerophospholipid metabolism	'CDP-diacylglycerol: myo-inositol 3-phosphatidyltransferase (18:1(9Z)/16:0)'
Glycerophospholipid metabolism	'CDP-diacylglycerol synthetase (18:1(11Z)/16:0)'
Glycerophospholipid metabolism	'CDP-diacylglycerol synthetase (18:1(11Z)/16:0), chloroplast'
Glycerophospholipid metabolism	'CDP-diacylglycerol synthetase (18:1(9Z)/16:0)'
Glycerophospholipid metabolism	'CDP-diacylglycerol synthetase (18:1(9Z)/16:0), chloroplast'
Porphyrin and chlorophyll metabolism	'chlorophyllide a oxidase'
Biosynthesis of steroids	'4-(cytidine 5''-diphospho)-2-C-methyl-D-erythritol kinase'
Biosynthesis of steroids	'2-C-methyl-D-erythritol 4-phosphate cytidyltransferase'
Purine metabolism	'2''-Deoxyadenosine 5''-diphosphate:oxidized-thioredoxin 2''-oxidoreductase'

Glycerolipid metabolism	'digalactosyldiacylglycerol palmitate delta7-desaturase (18:1(9Z)/16:1(7Z))'
Glycerolipid metabolism	'digalactosyldiacylglycerol synthase (18:1(9Z)/16:0)'
Glycerolipid metabolism	'omega-3 desaturase (18:3(9Z,12Z,15Z)/16:0) (DGDG)'
Glycerolipid metabolism	'omega-6 desaturase (18:1(9Z)/16:2(7Z,10Z)) (DGDG)'
Glycerolipid metabolism	'omega-6 desaturase (18:2(9Z,12Z)/16:0) (DGDG)'
Glycerolipid metabolism	'omega-6 desaturase (18:2(9Z,12Z)/16:1(9Z)) (DGDG)'
Glycerolipid metabolism	'delta5 desaturase (16:0/18:3(5Z,9Z,12Z))'
Glycerolipid metabolism	'delta5 desaturase (18:1(11Z)/18:3(5Z,9Z,12Z)) (DGTS)'
Glycerolipid metabolism	'delta5 desaturase (18:2(9Z,12Z)/18:3(5Z,9Z,12Z))'
Glycerolipid metabolism	'oleate desaturase (16:0/18:2(9Z,12Z))'
Glycerolipid metabolism	'linoleate desaturase (16:0/18:4(5Z,9Z,12Z,15Z))'
Glycerolipid metabolism	'oleate desaturase (18:1(11Z)/18:2(9Z,12Z)) (DGTS)'
Glycerolipid metabolism	'linoleate desaturase (18:1(11Z)/18:4(5Z,9Z,12Z,15Z)) (DGTS)'
Glycerolipid metabolism	'oleate desaturase (18:1(9Z)/18:2(9Z,12Z)) (DGTS)'
Glycerolipid metabolism	'linoleate desaturase (18:1(9Z)/18:4(5Z,9Z,12Z,15Z)) (DGTS)'
Glycerolipid metabolism	'oleate desaturase (18:2(9Z,12Z)/18:1(11Z))'
Glycerolipid metabolism	'linoleate desaturase (18:3(9Z,12Z,15Z)/18:1(11Z))'
Glycerolipid metabolism	'linoleate desaturase (18:3(9Z,12Z,15Z)/18:1(9Z))'
Glycerolipid metabolism	'linoleate desaturase (18:3(9Z,12Z,15Z)/18:3(5Z,9Z,12Z))'
Glycerolipid metabolism	'linoleate desaturase (18:3(9Z,12Z,15Z)/18:4(5Z,9Z,12Z,15Z))'
Pyrimidine metabolism	'dihydroorotase'
Pyrimidine metabolism	'dihydroorotate oxidase'
Biosynthesis of steroids	'1-deoxy-D-xylulose-5-phosphate reductoisomerase'

Biosynthesis of steroids	'1-deoxy-D-xylulose-5-phosphate synthase'
Fatty acid biosynthesis	'enoyl-[acyl-carrier-protein] reductase (NADH) (n-C18:0)'
Fatty acid metabolism	'(S)-3-Hydroxybutanoyl-CoA hydro-lyase'
Fatty acid metabolism	'(S)-Hydroxyhexanoyl-CoA hydro-lyase'
Fatty acid metabolism	'(S)-Hydroxyoctanoyl-CoA hydro-lyase'
Fatty acid metabolism	'(S)-Hydroxydecanoyl-CoA hydro-lyase'
Fatty acid metabolism	'(S)-3-Hydroxydodecanoyl-CoA hydro-lyase'
Fatty acid metabolism	'(S)-3-Hydroxytetradecanoyl-CoA hydro-lyase'
Fatty acid metabolism	'(S)-3-Hydroxyhexadecanoyl-CoA hydro-lyase'
Purine metabolism	'phosphoribosylaminoimidazolecarboxamide formyltransferase'
Purine metabolism	'phosphoribosylglycinamide formyltransferase, cytosol'
Glycerolipid metabolism	'glycerol-3-phosphate acyltransferase (C16:0)'
Glycerolipid metabolism	'glycerol-3-phosphate acyltransferase ((9Z)-C18:1)'
Glycerolipid metabolism	'glycerol-3-phosphate acyltransferase ((11Z)-C18:1)'
Biosynthesis of steroids	'geranylgeranyl diphosphate synthase'
Starch metabolism	'glucose-1-phosphate adenylyltransferase (chloroplast)'
Glycerolipid metabolism	glyceraldehyde oxidoreductase (NAD)'
Glutathione metabolism	'glutathione:protein-disulfide oxidoreductase'
Fatty acid metabolism	'(S)-3-Hydroxybutanoyl-CoA:NAD oxidoreductase'
Fatty acid metabolism	'(S)-hydroxyhexanoyl-CoA:NAD oxidoreductase'
Fatty acid metabolism	'(S)-hydroxyoctanoyl-CoA:NAD oxidoreductase'
Fatty acid metabolism	'(S)-hydroxydecanoyl-CoA:NAD oxidoreductase'
Fatty acid metabolism	'(S)-3-hydroxydodecanoyl-CoA:NAD oxidoreductase'
Fatty acid metabolism	'(S)-3-Hydroxytetradecanoyl-CoA:NAD oxidoreductase'
Fatty acid metabolism	'(S)-3-Hydroxyhexadecanoyl-CoA:NAD oxidoreductase'
Biosynthesis of steroids	'4-hydroxy-3-methylbut-2-en-1-yl diphosphate synthase'
Purine metabolism	'hydroxyisourate hydrolase'
Purine metabolism	'IMP cyclohydrolase'
Carotenoid biosynthesis	'lycopene cyclase (alpha-carotene producing)'
Carotenoid biosynthesis	'lycopene cyclase (delta-carotene producing)'
Carotenoid biosynthesis	'lutein hydroxylase'
Fructose and mannose metabolism	'D-mannose aldose-ketose-isomerase'

Biosynthesis of steroids	'2-C-methyl-D-erythritol 2,4-cyclodiphosphate synthase'
Glycerolipid metabolism	'monogalactosyldiacylglycerol synthase (18:1(9Z)/16:0)'
Glycerolipid metabolism	'monogalactosyldiacylglycerol synthase (18:1(9Z)/16:1(9Z))'
Glycerolipid metabolism	'omega-6 desaturase (18:2(9Z,12Z)/16:2(7Z,10Z)) (MGDG)'
Carotenoid biosynthesis	'neoxanthin synthase'
Pyrimidine metabolism	'orotidine-5''-phosphate decarboxylase'
Pyrimidine metabolism	'orotate phosphoribosyltransferase'
Glycerophospholipid metabolism	'phosphatidylglycerol palmitate-delta3t-desaturase (18:1(11Z)/16:1(3E))'
Glycerophospholipid metabolism	'phosphatidylglycerol palmitate-delta3t-desaturase (18:1(9Z)/16:1(3E))'
Glycerophospholipid metabolism	'phosphatidylglycerol palmitate-delta3t-desaturase (18:2(9Z,12Z)/16:1(3E))'
Glycerophospholipid metabolism	'phosphatidylglycerol palmitate-delta3t-desaturase (18:3(9Z,12Z,15Z)/16:1(3E))'
Glycerophospholipid metabolism	'phosphatidylglycerol phosphate phosphatase (18:1(11Z)/16:0), chloroplast'
Glycerophospholipid metabolism	'phosphatidylglycerol phosphate phosphatase (18:1(9Z)/16:0), chloroplast'
Glycerophospholipid metabolism	'phosphatidylglycerolphosphate synthase (18:1(11Z)/16:0), chloroplast'
Glycerophospholipid metabolism	'phosphatidylglycerolphosphate synthase (18:1(9Z)/16:0), chloroplast'
Glycerophospholipid metabolism	'omega-3 desaturase (18:3(9Z,12Z,15Z)/16:0) (PG)'
Glycerophospholipid metabolism	'omega-6 desaturase (18:2(9Z,12Z)/16:0) (PG)'
Purine metabolism	'phosphoribosylamine---glycine ligase'
Purine metabolism	'phosphoribosylaminoimidazole carboxylase, cytosol'
Purine metabolism	'phosphoribosylaminoimidazolesuccinocarboxamide synthase, cytosol'
Purine metabolism	'5-phosphoribosylamine:diphosphate phospho-alpha-D-ribosyltransferase (glutamate-amidating)'
Purine metabolism	'phosphoribosylformylglycinamide cyclo-ligase'
Purine metabolism	'phosphoribosylformylglycinamide synthase'
Glycerophospholipid metabolism	'serine decarboxylase'
Glycerolipid metabolism	'sulfolipid 2''-O-acyltransferase (2''-18:3(5,9,12,15)/18:1(11Z)/16:0)'



Glycerolipid metabolism	'sulfolipid 2''-O-acyltransferase (2''-18:4(5,9,12,15)/18:1(9Z)/16:0)'
Glycerolipid metabolism	'sulfolipid 2''-O-acyltransferase (2''-18:3(5,9,12)/18:1(11Z)/16:0)'
Glycerolipid metabolism	'sulfolipid 2''-O-acyltransferase (2''-18:3(5,9,12)/18:1(9Z)/16:0)'
Glycerolipid metabolism	'sulfolipid synthase (16:0/16:0)'
Glycerolipid metabolism	'sulfolipid synthase (18:1(11Z)/16:0)'
Glycerolipid metabolism	'sulfolipid synthase (18:1(9Z)/16:0)'
Glycerolipid metabolism	'omega-3 desaturase (18:3(9Z,12Z,15Z)/16:0) (SQDG)'
Glycerolipid metabolism	'omega-6 desaturase (18:2(9Z,12Z)/16:0) (SQDG)'
Starch metabolism	'starch synthase (300 glc units) (chloroplast)'
Pyrimidine metabolism	'thioredoxin-disulfide reductase, cytosol'
Glycerolipid metabolism	'betaine lipid synthase (trimethylase) (16:0/18:1(11Z))'
Glycerolipid metabolism	'betaine lipid synthase (trimethylase) (16:0/18:1(9Z))'
Glycerolipid metabolism	'betaine lipid synthase (trimethylase) (18:1(11Z)/18:1(11Z))'
Glycerolipid metabolism	'betaine lipid synthase (trimethylase) (18:1(11Z)/18:1(9Z))'
Glycerolipid metabolism	'betaine lipid synthase (trimethylase) (18:1(9Z)/18:1(11Z))'
Glycerolipid metabolism	'betaine lipid synthase (trimethylase) (18:1(9Z)/18:1(9Z))'
Glycerolipid metabolism	'UDP-sulfoquinovose synthase'
Galactose metabolism	'UDP-glucose 4-epimerase'
Purine metabolism	'urate oxidase'
Purine metabolism	'xanthine dehydrogenase'